Important Notice

THE UNIVERSITY OF CALGARY

Crosswell Seismic Processing: Automatic Velocity Analysis, Filtering, and Reflection Imaging

by

Guoping Li

A THESIS

SUBMITTED TO THE FACULTY OF GRADUATE STUDIES

IN PARTIAL FULFILLMENT OF THE REQUIREMENTS FOR THE

DEGREE OF MASTER OF SCIENCE

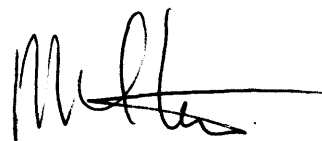DEPARTMENT OF GEOLOGY AND GEOPHYSICS
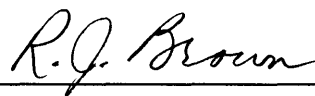
CALGARY, ALBERTA

OCTOBER, 1994

THE UNIVERSITY OF CALGARY

FACULTY OF GRADUATE STUDIES

The undersigned certify that they have read, and recommend to the Faculty of Graduate Studies for acceptance, a thesis entitled "Crosswell Seismic Processing: Automatic Velocity Analysis, Filtering, and Reflection Imaging" submitted by Guoping Li in partial fulfillment of the requirements for the degree of Master of Science.

_____

Supervisor, Dr. Robert R. Stewart
Dept. of Geology and Geophysics

_____

Dr. R. James Brown
Dept. of Geology and Geophysics

_____

Dr. Edward S. Krebes
Dept. of Geology and Geophysics

_____

Dr. C. John Bland
Dept. of Physics and Astronomy

October 3, 1994

ABSTRACT

A study on crosswell seismic data processing is presented. Three surveys from Texas and Alberta, using downhole airgun or explosive charges and geophone or hydrophone streamers, are analyzed. Strong tube waves generally obscure useful but weak reflections. To suppress them, f-k, median and alpha-trimmed mean filters are used. The median filter works best. A new velocity analysis technique is developed, assuming velocity increasing linearly with depth, to automatically derive a one-dimensional velocity profile from first-arrival traveltimes. Tests show encouraging results. Different methods of extracting reflection information from crosswell data are discussed. An imaging technique using common-reflection-point stacking is developed and tested with synthetic and field data. This technique enables one to take advantage of the high-fold subsurface coverage of crosswell reflections and process crosswell data like surface seismic CDP data. The stacked reflection images constructed show high resolution that is difficult to obtain from surface seismic or VSP data.

ACKNOWLEDGMENTS

TABLE OF CONTENTS

LIST OF FIGURES

LIST OF SYMBOLS AND ABBREVIATIONS

AGC	Automatic gain control
CDP	Common depth point
CI	Common interval
CMD	Common mid-depth
CPU	Central processor unit
CR	Common receiver
CRB	Common reflection bin
CRP	Common reflection point
CS	Common source
HMO	Horizontal moveout
NMO	Normal moveout
RVSP	Reverse vertical seismic profiling
S/N ratio	Signal-to-noise ratio
VMO	Vertical moveout
VSP	Vertical seismic profiling
Xwell	Crosswell
n-C	n-component; $n = 1, 2,$ or 3
n-D	n-dimension; $n = 1, 2,$ or 3
θ	Reflection angle
f	Temporal frequency
ft	foot (or feet)
g	Receiver (geophone) depth
h	Half of source and receiver depth difference (interval)

Hz	Hertz (cycles per second); unit of frequency
k	Wavenumber or spatial frequency
kHz	Kilohertz
m	Mid-depth (half of the sum of source and receiver depths)
ms	Millisecond
P	Compressional wave
r	Reflector depth
s	Source depth
S	Shear wave
s	Second
t	Two-way traveltime
t_0	Two-way vertical traveltime
V	Velocity
x	Well-to-well distance (offset)
z	Depth

Chapter 1

Introduction

1.1   Terminology

Over the last decade, there have been many advances in the new geophysical technology of recording seismic data using two wells: one well for downhole seismic sources and the other for downhole receivers. Various terms such as "crosswell", "crosshole", "cross-borehole", and "interwell" have appeared in the geophysical literature to describe the geometry involved in this technology. In this thesis, the term *crosswell* is adopted.

The term *crosswell seismology* is used to refer to the branch of applied seismology that studies the physical properties of the rocks between and below the two boreholes. It consists of acquisition, processing, and interpretation of crosswell seismic data.

When the term *crosswell seismic surveying* is used, the aspects of field techniques and processes of crosswell seismic data acquisition are emphasized. Although it has been used in the literature and, to some degree confused with crosswell seismology, *crosswell tomography* refers specifically in this thesis to the processes that reconstruct the interwell images of various rock properties from crosswell seismic direct waves, using

tomographic inversion techniques. *Crosswell reflection imaging*, however, is a technique that stresses the use of later events contained in crosswell seismic data to provide an image of the subsurface reflectivity between and below the boreholes. Thus, crosswell seismology should include crosswell seismic surveying, crosswell tomography and crosswell reflection imaging.

1.2   Background review

Crosswell seismic data have been acquired in North America and elsewhere in the world. Many applications in petroleum activities and geotechnical engineering studies have been published and examples include: in-situ remote monitoring of the changing reservoir conditions associated with enhanced oil recovery processes (Laine, 1987; Macrides et al., 1988; Bregman et al., 1989) and cyclic steam stimulation for bitumen production (Eastwood et al., 1994); delineating the location and size of subsurface fracture systems at a hot dry rock geothermal site (Fehler and Pearson, 1984); and tracing of fractures during characterization of disposal sites for hazardous wastes (Wong et al., 1987). The use of crosswell reflection imaging and its correlation with geology in oilfield development has been reported recently (Khalil et al., 1993).

Crosswell seismic data promise to provide higher resolution than the surface seismic and VSP data. During crosswell data collection, both the source and receiver are typically located beneath the strongly attenuative overburden and weathering zone, and seismic signals usually travel a short distance from the source to the receiver in the Earth. Therefore, very high-frequency short-wavelength seismic waves capable of resolving fine geologic features can be recorded.

The history of recording crosswell seismic measurements may date back to as

early as the 1910 era. According to Hardage (1985), the first documented seismic application involving buried sources and geophones can be found in a U.S. patent claimed in 1917 by Fessenden, who used a dual-hole (crosswell) geometry for locations of borehole acoustic energy sources and borehole acoustic receivers, respectively, to record seismic signals for imaging the geologic region between the boreholes. This early borehole seismic work represents a starting point in the course of modern crosswell seismic technology development. After Fessenden's work, a few other geophysical pioneers continued to make contributions to the development of crosswell seismology. Barton (1929) analyzed the possible uses of seismic measurements in boreholes to map geological structures. In the 1950s, crosswell seismic surveys were made in eastern Colorado, where dynamite charges of one pound were shot in boreholes a few hundred feet deep and the seismic signals were detected in similar boreholes a few hundred feet away (Ricker, 1953; McDonal et al., 1958). The purposes of these surveys were to study the form and laws of propagation of seismic wavelets (Ricker, 1953) and to investigate the attenuation effect of shear and compressional waves in the subsurface rocks (McDonal et al., 1958). In the 1960s, similar surveys were carried out again in the United States, in order to determine the elastic properties of salt domes and to define suitable sites for atomic explosions. Bois et al. (1972) reported some experiments for crosswell seismology conducted in oilfields in southwest France and its application in a hydrocarbon reservoir study. They used well-to-well seismic measurements to infer elastic properties (velocity structure) between the wells and thus to locate the reservoirs. Their work appears to be the earliest attempt to combine crosswell acquisition geometry with tomographic inversion techniques for seismic imaging. Bernabini and Borelli (1974) also inferred the elastic parameters of a corridor of near-surface rocks from the crosswell seismic data measured in a multiple borehole situation.

Since the early 1980s, there have been various types of high-quality

nondestructive downhole seismic sources (such as air guns, piezoelectrical transducers, vibrators, sparkers, explosives, and the drill bit), and high-sensitivity downhole detectors (locking geophones, hydrophones, and accelerometers) both available for borehole seismic surveys. In modern crosswell acquisition, the downhole source and receiver can be lowered into deep wells to record multichannel data from many depth positions. It is important to note that, when many depth positions along the boreholes are occupied by the sources and receivers, detailed high-fold coverage of the interwell rock section is achievable, allowing for seismic imaging with high S/N ratio. Many such multi-fold crosswell seismic surveys were recorded by oil companies recently, and three of them will be described in this thesis.

With more crosswell seismic data recorded, data processing requires greater attention. Various processing and imaging methods have been proposed, tested, and applied. Two types of signals from field crosswell seismic data have been used: direct arrivals (first breaks) and reflections.

Most past efforts have concentrated on inversion of traveltimes (or amplitudes) measured from direct arrivals (or transmitted waves) in crosswell data. Direct arrivals usually are strong, coherent energy, and they are easily identified and picked. In contrast, reflections are often weak in raw crosswell data, and sometimes impossible to extract from the recorded wavefield because of the strong interference of unwanted noise such as tube waves. Direct arrivals provide the most robust observations for crosswell imaging. Therefore in the early stage of crosswell seismic studies, it was natural and straightforward to use direct arrivals, instead of reflections, in image reconstruction.

The techniques of tomographic reconstruction have been used for crosswell traveltime inversion. The word, "tomography", is from the Greek language and it means a picture of a slice or section. The basic idea behind this technique is "using the data measured outside an object to infer the interior properties inside that object" — that is, to

obtain the image of an interior slice of that object (Stewart, 1991). To achieve this, the interior region has to be measured with broad angular coverage. The mathematical basis of tomographic inversion is the well-known Radon transform (Dines and Lytle, 1979). Various tomographic inversion methods have been successfully used to reconstruct images of the subsurface (e.g., distribution of velocity or attenuation) from measured direct arrivals. Widely used methods include: the back-projection method (East et al., 1988; Ho-Liu et al., 1989), the algebraic reconstruction techniques (ART) (Mason, 1981; Peterson et al., 1985), the simultaneous iterative reconstruction techniques (SIRT) (Ivansson, 1985), and the diffraction tomography method (Lo et al., 1988; Pratt and Worthington, 1988; Williamson, 1991). Crosswell tomography has proved a useful tool in hydrocarbon reservoir development and engineering applications. Yet, a few drawbacks have been found. Tomographic traveltime inversion is limited by poor coverage near the bottom of the wells and no coverage below them (Khalil et al., 1993). Tomographic images can suffer from non-uniqueness (Bregman et al., 1989) and artifact contamination. Since the inversion tries to yield estimates of the smoothly varying components of the subsurface velocity distribution, the images produced sometimes fail to resolve discontinuities in the velocities (Pratt and Goulty, 1991).

Crosswell seismic data contain a diversity of wave types. Direct arrivals represent only a small fraction of the total information recorded in the crosswell data. Reflections, mode-converted waves, diffractions, head waves, interface waves, tube waves, and other waves are often found in field crosswell data. Real crosswell data studies (Khalil et al., 1993; Lazaratos et al., 1993; also in this thesis) reveal that crosswell data frequently display a great richness of later events such as reflections. These reflections are significant in imaging the subsurface, because they carry useful information about acoustic impedance contrasts of geologic objects. If processed properly, high-resolution crosswell reflections should allow for detailed lithologic correlation and precise location

of the lateral discontinuities under the ground. Also important is that from the reflections an image can be produced that provides not only coverage of the interwell space, but also coverage of the region near the bottom of the boreholes and below it, where the geologic zone of interest is often located.

Over the last decade, researchers and development geophysicists have been making great strides in taking advantage of the reflection information in crosswell seismic data. The earliest effort of applying crosswell reflection data perhaps is the work of Hawkins et al. (1982). They developed a so-called Yo-Yo system, by which they vertically traversed a seismic source in one well and a receiver in an adjacent well, simultaneously, to provide horizontally moving reflection points on interfaces between two wells. With this system, they were able to obtain a high-resolution crosswell reflection profile and use it to resolve detailed coal-seam structures.

A variety of crosswell reflection imaging approaches have been proposed, including crosswell-CDP mapping (Baker and Harris, 1984; Iverson, 1988; Abdalla et al., 1990; Lazaratos et al., 1993), migration (Hu et al., 1988; Zhu and McMechan, 1988; Findlay et al., 1991; Qin and Schuster, 1993; Zhou and Qin, 1993), combined migration/inversion (Beydoun et al., 1989; Pratt and Goulty, 1991), and common mid-depth (CMD) stacking (Stewart et al., 1991; Stewart and Marchisio, 1991).

Crosswell reflection data were first processed by treating them as VSP data. Baker and Harris (1984), Iverson (1988), and Abdalla et al. (1990) discussed processing flows for crosswell reflection imaging, based on some VSP processing techniques. Reflections are extracted from the crosswell wavefield, and then separated in upgoing and downgoing directions. The upgoing and downgoing wavefields are mapped into two images of the interwell area, by applying a variation of the VSP-CDP mapping algorithm (Wyatt and Wyatt, 1984). To emphasize that the algorithm was applied to the crosswell geometry, relevant names such as XHL/CDP or XSP/CDP mapping were used (it is called Xwell-

CDP mapping in this thesis). This mapping algorithm maps every data sample to a possible reflection point based on reflection point locations and traveltimes calculated by ray tracing. Synthetic crosswell data were generated by Abdalla and Stewart (1989) using numerical modeling software and processed through the mapping algorithm for a final image of reflectors. The result was encouraging. Two real-data studies were presented using reflection data in a 2.5 to 17 kHz frequency range from the Midale oilfield of southeastern Saskatchewan (Khalil et al., 1993) and in the frequency band of 300-4000 Hz from a test site in Devine, Texas (Lazaratos et al., 1993). Both studies used the Xwell-CDP mapping algorithm to generate high-resolution reflection images. These studies show a good correlation between the crosswell reflection image and the sonic log-based synthetics, and demonstrate that vertical resolution of the order of 3-5 ft (1.0-1.5 m) from crosswell reflections with frequencies of a few kilohertz is feasible.

However, some technical difficulties associated with the Xwell-CDP mapping technique exist. It is found that the most reliable part of the images is the portion close to the source well and in a range of depths around the source/receiver depth; however, when moving away from the source well, the signal-to-noise ratio and the image quality degrade (Lazaratos et al., 1993). It should be noted, though, that the real objective of crosswell seismology is to image the medium away from the wells. Besides, redundancy of reflections due to high fold in modern crosswell data acquisition is not optimally used in this mapping method because it maps reflection data from a single gather only. Single-gather mapping provides single-fold images, which are often unreliable because of the complexity of the crosswell wavefield. One remedial measure to overcome this problem, as suggested by Khalil et al. (1993), is to sum all the individual reflection images from each receiver-gather map to produce a final section. Although the lateral coverage of the image in the final stacked section is extended, it is found also that misregistration or dissimilarity of partial images will degrade the stack (Khalil et al., 1993).

Migration algorithms have been used to generate migrated depth sections. The reverse-time finite-difference migration was tested with prestack and post-stack synthetic crosswell data (Hu et al., 1988; Zhu and McMechan, 1988) and real data (Zhou and Qin, 1993). Findlay et al. (1991) and Qin and Schuster (1993) applied a Kirchhoff migration to real crosswell data. Beydoun et al. (1989) applied an elastic migration/inversion technique to crosswell data. Pratt and Goulty (1991) proposed combining wave-equation imaging with traveltime tomography to form high-resolution images from crosswell data. In general, these methods can provide high-resolution crosswell reflection images, and a reasonably good lithologic correlation with sonic logs. However, these algorithms are expensive because they demand a great deal of CPU time, even on supercomputers. Despite the fact that these methods work very well for synthetic data, results of migrating real crosswell data show dipping artifacts, edge effects, and some unexpected discontinuity of reflectors.

One important fact is that modern crosswell seismic acquisition geometry provides a multi-fold coverage of the subsurface reflectors. This suggests the potential treatment of crosswell reflection data as surface CDP data. The CDP stacking procedure has been proven successful and cost-effective for surface seismic imaging, because the advantage of multi-fold coverage is fully exploited during the data processing.

Recently, a few efforts have been made to produce a stacked section from crosswell data. In a physical modeling study, Stewart et al. (1991) and Stewart and Marchisio (1991) proposed processing crosswell seismic data like CDP reflection data. This CDP-type procedure includes trace gathering around a common source-receiver mid-depth (CMD gathering) as well as a linear vertical moveout correction (VMO) between the various CMD locations. The VMO-corrected traces are then sorted into their correct lateral bins and stacked. Their study shows that the CDP-type procedure (called the CMD stacking method in this thesis) produces a better image in the zone of interest

than the Xwell-CDP mapping procedure. An important aspect of the CMD stacking method is that it requires less analyst intervention, compared to the Xwell-CDP mapping procedure. This new processing procedure works well for a medium with little velocity variation. In such a medium, reflections in CMD gathers are flat, which makes stacking possible.

However, this CMD stacking method is not ideal. Further research reveals that the linear VMO function is only an approximation which may cause residual moveout in the data, and that the CMD gathering may be unnecessary. Instead, reflection data can be stacked directly in common-reflection-point (or bin) gathers without using the CMD gathers, and provide better images.

To summarize, crosswell seismic data have drawn much attention from the petroleum industry and geotechnical engineering world, because they promise to provide very high-resolution images of the subsurface structure. Modern crosswell acquisition technology produces multi-fold crosswell seismic data. Crosswell direct-arrival traveltimes provide a reliable data set for tomographic inversion to reconstruct a velocity image. Previous studies show crosswell data also contain much useful reflection information, which can be used to generate high-resolution reflection images, through processing procedures such as Xwell-CDP mapping, migration or inversion, and CMD stacking. Still, more research is required for these processing techniques to become a fast, cost-effective, reliable, and flexible imaging tool in seismic applications.

1.3 Thesis objectives

The main objective of this thesis is to develop a complete processing procedure to make an image from multi-fold crosswell seismic data. The emphasis will be placed on

how to process crosswell reflection data more effectively and from there generate better stacked sections in a rapid manner with minimum analyst intervention. To achieve this objective, two approaches will be taken. First, necessary new algorithms will be developed to facilitate solving the specific crosswell imaging problems. Second, concepts and ideas, which have been used by other reflection imaging techniques published previously (such as the CMD stacking method) and which can be incorporated into the new methods developed in this thesis, will be fully used. It is hoped that, through this thesis study, a general and standard procedure for crosswell processing and imaging can be generated, by which crosswell reflection data will be treated as surface seismic CDP data, and they can be processed with existing software available for surface seismic processing.

1.4   Thesis structure

This thesis is composed of eight chapters. Chapter 2 will describe the crosswell geometry used in three field surveys carried out recently in North America, along with some important field parameters, such as well-to-well distances, surveying depths, and sources and receivers used. An analysis of the wavefield in a typical shot record from each survey will also be given.

Crosswell seismic data are often contaminated by strong tube waves. Sometimes reflection imaging is impossible without suppressing these disturbing tube waves first. Chapter 3 will deal with the tube wave problem by giving a theoretical and experimental analysis of how these waves are generated, then taking a close look at their basic characteristics in the field crosswell data from the surveys described in Chapter 2, and

finally investigating several multichannel filtering methods that may be useful in suppressing tube waves.

In Chapter 4, a method for automatic derivation of velocity information from first arrivals of crosswell data will be proposed. A mathematical framework for this method will be given, followed by tests with different data sets.

In Chapter 5, there will be a review of some important concepts and ideas that can be used in crosswell reflection imaging. Specifically, the modified CMD stacking method, together with a few variations that help supplement this method, will be discussed.

Based on the concepts and techniques shown in Chapter 5, a new imaging method, common-reflection-point stacking, will be described in Chapter 6. A complete processing procedure will be proposed and tested with synthetic data.

A case study will be discussed in Chapter 7, where field crosswell seismic data from one of the surveys in Chapter 2 will be used to generate a stacked section. Details regarding every processing step and results will be provided. A brief interpretation of the final images produced and correlation with synthetic seismograms and other seismic data will be given.

Chapter 8 will conclude this thesis with a number of remarks drawn from this study as well as future work suggested to improve the crosswell reflection imaging techniques discussed.

1.5   Software and hardware

Most crosswell signal analysis and data processing carried out here was done by using existing seismic processing software, including Landmark/ITA INSIGHT® 4.0 and

Advance Geophysical Corporation's ProMAX® processing systems. Algorithms necessary for crosswell reflection imaging were implemented with computer code written in FORTRAN in the INSIGHT® programming environment. Numerical crosswell modeling was done by using the Uniseis® modeling package on Landmark workstations. Hardware used is SUN SPARC 2 workstations with reasonably large disk space appropriate for large crosswell data sets.

Chapter 2

Crosswell seismic surveys and wavefield analysis

2.1   Introduction

Three crosswell seismic surveys, shot recently in North America by major oil companies, will be described in this chapter. In these surveys, different downhole sources and downhole receiving tools were used. The surveying geometries used were different. Single- and/or multi-component seismic data were recorded. The data quality varies from one survey to another. In addition to a description of the surveys, an analysis of a representative shot record of the field data from each survey will be given.

2.2   Humble survey

2.2.1   Survey geometry and field parameters

In 1989, Texaco Inc. (USA) conducted an experimental crosswell and reverse VSP survey in the Humble area of Texas. The purpose was to test downhole seismic sources and receivers. Three wells were used as source and receiver holes, and three-

component (3-C) crosswell and single-component (1-C) RVSP data were collected.

Figure 2.1 shows the geometry of the survey. Wells *C30* and *K22* served as the source well and receiver well in turn. That is, as the one-level 3-C VSP geophone was in *K22*, *C30* was the source well, and vice versa. A third hole, *D1*, was used as detector well only, in which thirty 3-C geophones were permanently buried at various depths from 35 ft (10.7 m) to 1485 ft (452.6 m) at 50-ft (15.2 m) increments. *D1* is 355 ft (108.2 m) away from *C30*, and 1015 ft (309.4 m) from *K22*. *K22* and *C30* are 815 ft (248.4 m) apart. In addition, a surface seismic line, consisting of 80 stations each having six 1-C geophones in a 50-ft (15.2 m) linear array, was laid out nearly across *C30* to record RVSP data.

The downhole source was a Bolt air gun with an 80-cubic-inch air chamber, operated at air pressures of 2000 to 3200 psi. This gun was shot in wells *C30* and *K22*, respectively. The recording system was an EG&G 2420 instrument, with 90 channels plus 3 auxiliary channels. The frequency band of the filter was 10-1440 Hz. The pre-amplifier gain was set to 30 dB. Crosswell data were recorded at a sample interval of 0.25 ms. A Texaco WAVE III system was used to record the RVSP data. All the seismic data were written on magnetic tape in SEG-D format.

The whole experiment was conducted in two steps. In step one, the air gun was lowered into *C30*, shooting from 300 ft (91.4 m) to 2340 ft (713.2 m) at a 10-ft (3.0 m) spacing. The recording systems WAVE III and EG&G 2420 were hooked up in a master-slave relationship in order to simultaneously record the data from each shot. Three-component crosswell data were recorded, through 30 3-C geophones buried in well *D1*, on the EG&G 2420 system, with channels 1-30 recording the vertical component, channels 31-60 recording one horizontal component, and channels 61-90 recording the other horizontal component. A 3-C crosswell common-receiver gather was also recorded from a 3-C VSP tool located at a 1500-ft (457.2 m) depth in *K22* , which was now the
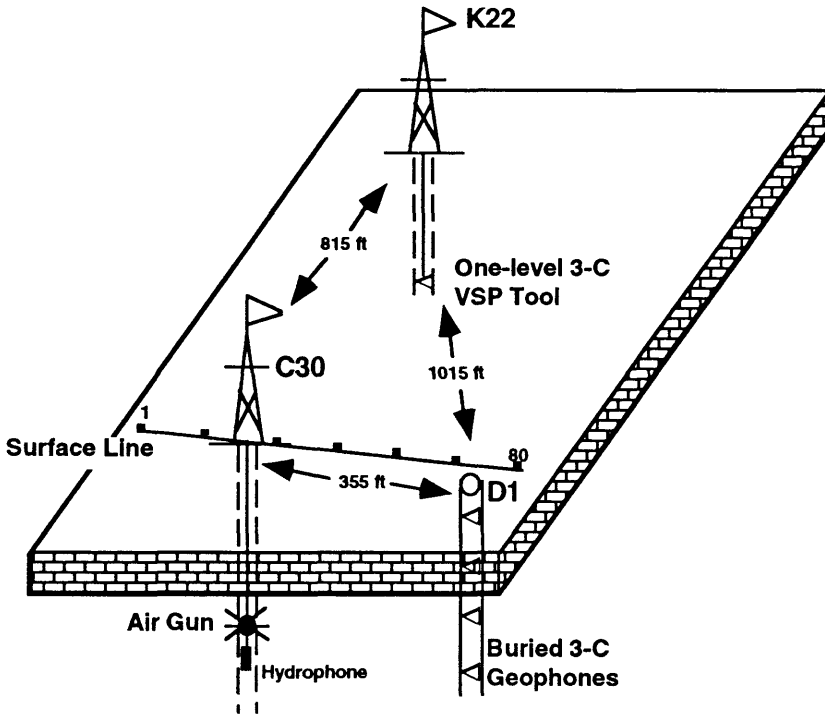
FIG. 2.1. The Humble, Texas crosswell survey. Wells *C30* and *K22* were used both as source and receiver wells. The detector well *D1* had 30 buried 3-C geophones. A surface seismic line was laid close to wells *C30* and *D1*. (Modified from Z. Sun, Pers. Comm.)

---

receiver well. The three components were recorded on the auxiliary channels of the EG&G 2420 system. In addition, the 80 stations along the surface line recorded the RVSP data from the source well *C30*.

During the second step of the experiment, the air gun was moved from *C30* into *K22*, and the VSP tool moved from *K22* into *C30*. Now, the gun was fired in *K22*, every 20 ft (6.1 m), from 300 ft (91.4 m) until 2540 ft (774.2 m). Crosswell and RVSP seismic data were recorded in a similar manner as in step one.

A hydrophone, which was hung below the air gun, was used to monitor the near-field signatures of the source every time it was excited.

2.2.2 Wavefield analysis

Figure 2.2 shows a common-receiver gather. The data were recorded when the air gun was shot from 300 ft (91.4 m) to 2540 ft (774.2 m) in well *K22*, while the 3-C VSP tool was in *C30*, 1500 ft (457.2 m) deep. The data shown in Figure 2.2 are from one of the horizontal components.

Analysis of this gather reveals a few basic features. Strong linear events, with different dips, dominate the whole wavefield. They are the tube waves which were generated within the source hole *K22*, converted into *P* and *S* body waves, and propagated toward the geophone in *C30*. A detailed discussion of these tube waves will be given in Chapter 3. A direct *P* wave arrives earliest, but it is weak. From 0.3 s to 0.6 s, there is some indication of a weak direct *S* wave, which is hardly visible on shallower traces, probably due to the interference of the strong tube waves. In this data set, there are *no* visible reflections.

An *f-k* spectrum of this gather is plotted in Figure 2.3. In the left half of the *f-k* domain, there are two dipping events (contours) that start from the origin. The event labeled *T1* has an apparent velocity of 4600 ft/s (1402.1 m/s), while event *T2* is 1530 ft/s (466.3 m/s), both calculated by using the equation of $V = f/k$, where f is the frequency, and k the wavenumber. These two events are the tube waves, corresponding to *T1* and *T2* in Figure 2.2. In the *f-k* domain, the *T1* event is spatially aliased at frequencies of about 115 Hz and 350 Hz, where they are wrapped around the wavenumber axis. Event *T2* is aliased at lower frequencies of 40 Hz and 120 Hz. Except for the aliased component, there is not much energy around the zero-wavenumber axis, indicating lack of often higher-velocity reflections.

Depth (ft)
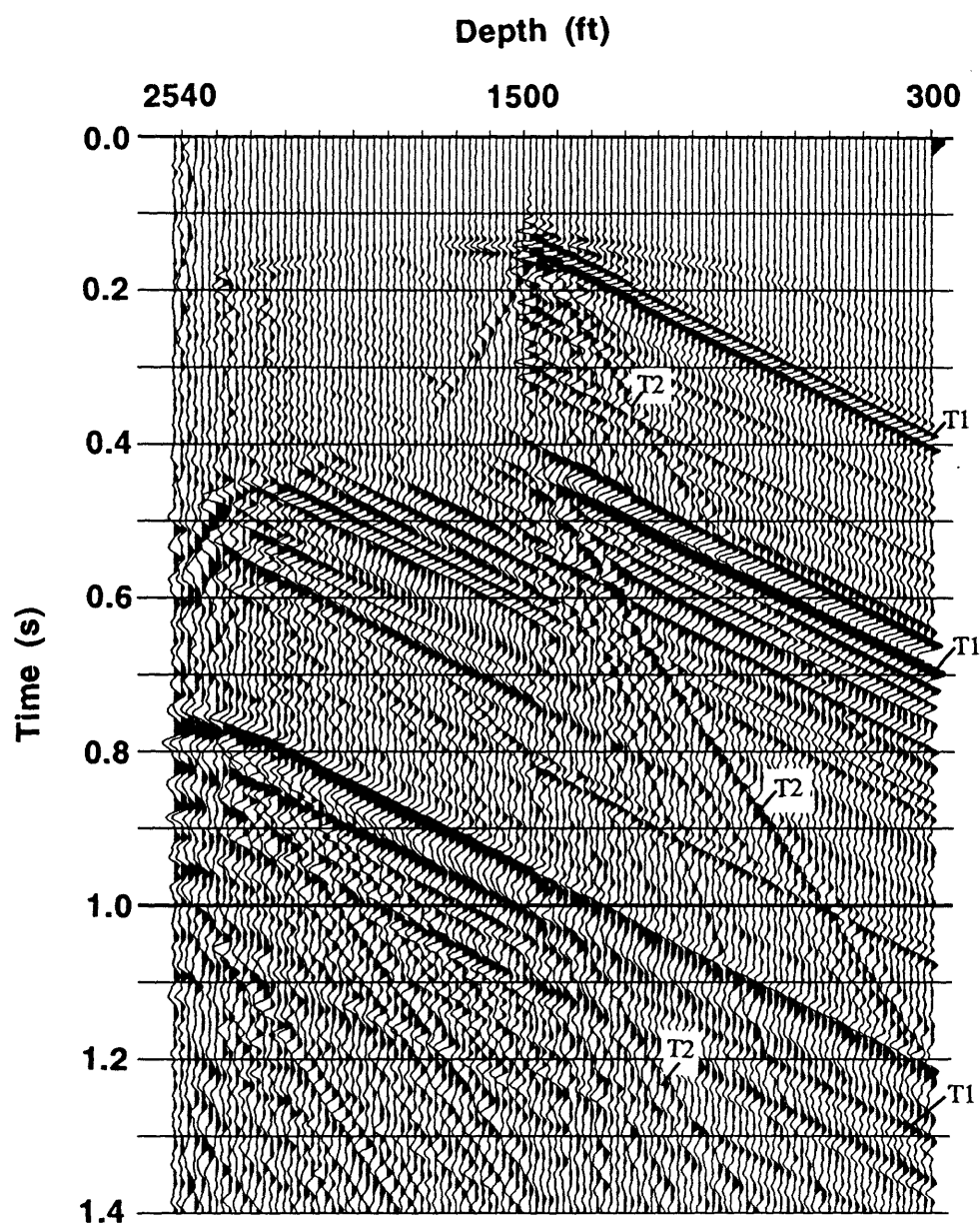
FIG. 2.2 Common-receiver gather, Humble, Texas. The air gun was shot in *K22* from 300 ft (91.4 m) to 2540 ft (774.2 m). A three-component geophone was located in *C30*, 1500 ft (457.2 m) deep. The offset between the wells was 815 ft (248.4 m). This is a horizontal-component record. Events *T1* and *T2* are tube waves.
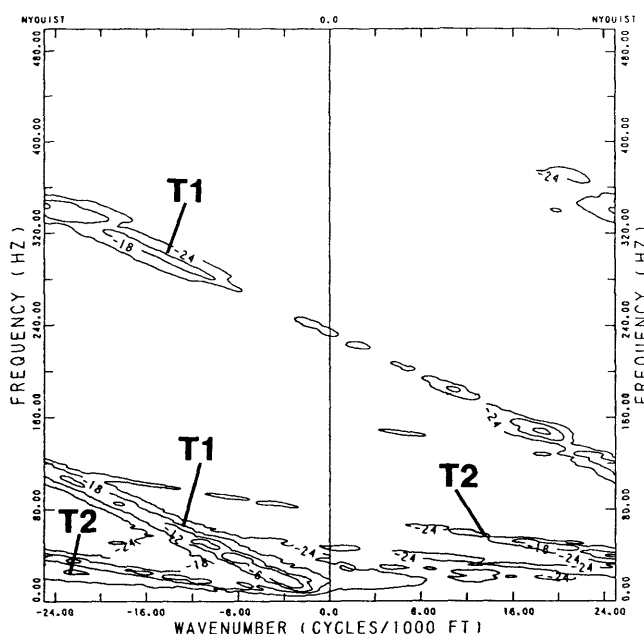
FIG. 2.3 An *f-k* spectral display of the common-receiver gather shown in Figure 2.2. The tube waves with different dips (*T1* and *T2*) are spatially aliased at different frequencies.

2.3 Friendswood survey

2.3.1 Survey geometry and field parameters

This survey was shot by Exxon Production Research Company at their test site near Friendswood, Texas (Chen et al., 1990). It was part of a combined seismic experiment consisting of crosswell, VSP, reverse VSP, and surface CDP seismic data, all of which were collected at the same location. Two 1000-ft (304.8 m) cased wells, separated by 600 ft (182.9 m), were used as the source and receiver wells respectively. The maximum deviation in both wells was less than 7 ft (2.1 m). The surface seismic line was shot across the two wells, recording the CDP data.

Shown in Figure 2.4 is the recording geometry used, along with a sonic log from
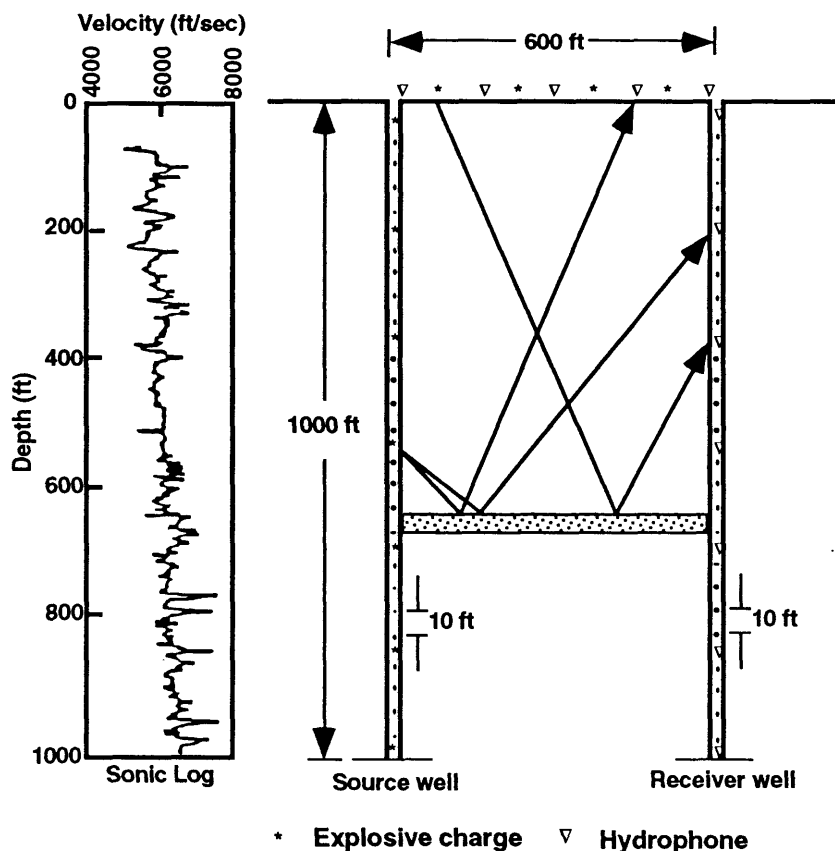
FIG. 2.4. The Friendswood, Texas combined seismic experiment. Crosswell seismic, VSP, and reverse VSP data were recorded from the two boreholes separated by 600 ft (182.9 m). A surface seismic line across the wells recorded CDP data. The sonic log is adapted from Zhou and Qin (1993).

the source well. Three groups of borehole data were recorded: crosswell data (sources shot from the source well into the receiver well); RVSP data (sources in the source well shot into receivers along the surface line); and VSP data (sources located on the surface shot into the receiver well).

In the crosswell case, downhole explosive sources of 10-gram charges were fired every 10 ft (3.0 m) from a depth of 1000 ft (304.8 m) upwards to 30 ft (9.1 m). The 10-gram charge provided high-quality data and did not damage the well (Chen and Eriksen, 1989; Chen et al., 1990). A 24-channel hydrophone streamer served as the downhole

receiver. The spacing between receiver stations was 10 ft (3.0 m). Each station consisted of 10 hydrophones for improved sensitivity. Four streamer positions were needed to cover the receiver well from depths of 960 ft (292.6 m) to 10 ft (3.0 m). The analog signals from all 24 stations were transmitted uphole simultaneously through tow leaders. The digitizer had a 16-bit dynamic range. In this experiment, the data were recorded at a 1/4 ms sample rate for 4000 points. The digitized data were written on magnetic tape in SEG-D format.

I have processed the first 0.5 second of data from the first 95 shot gathers. Details of data processing will be given in Chapter 7.

2.3.2 Data examples and wavefield analysis

Examples of the crosswell data collected in Friendswood, Texas are illustrated by a common-source gather [from a depth of 330 ft (100.6 m)] and a common-receiver gather [from a receiver depth of 460 ft (140.2 m)], respectively displayed in Figures 2.5 and 2.6. This complexity of wavefields contained in the crosswell data was analyzed by Chen et al. (1990). The following wave identification is based on their analysis. In the common-source gather (Figure 2.5), a number of events can be identified. The strong hyperbolic wave labeled D is the direct P wave. SR is the downgoing P-wave reflection. This wave is radiated from the source well upwards to the surface and reflected into the receiver well. Events like DR are P-wave reflections generated from deep layers between the two boreholes. A few upgoing reflections such as UR are weak but still visible. In addition to the high-amplitude 60-Hz power-line noise, the common-source gather are dominated also by strong tube waves such as $T1$ and $T2$. These tube waves have a similar generation mechanism, but travel in different directions. $T1$ is a P wave radiated from the source well to the bottom of the receiver well, converted into a tube wave, and then transmitted uphole. Tube wave $T2$, however, is a P wave radiated from the source

Depth (ft)
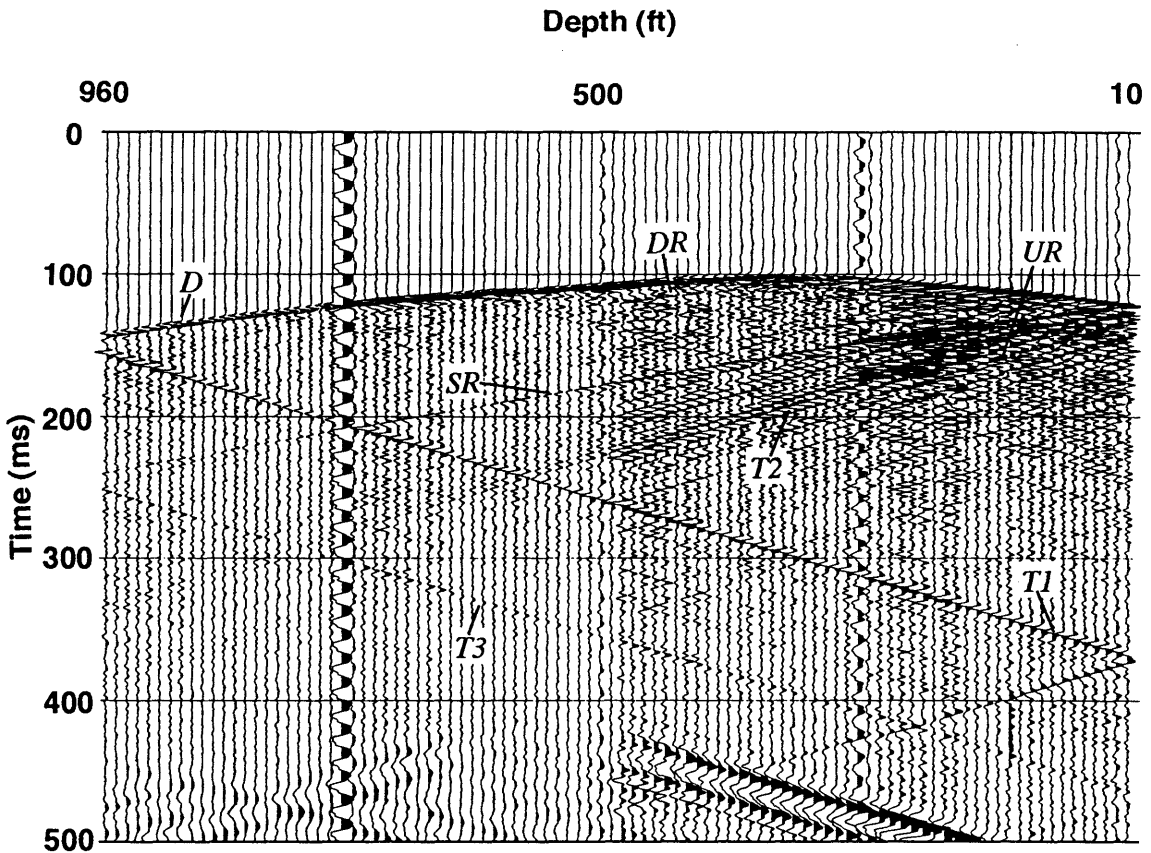
FIG. 2.5. Common-source gather, Friendswood, Texas. The source depth is 330 ft (100.6 m). Receivers are positioned between 10 ft (3.0 m) and 960 ft (292.6 m), spaced at 10 ft (3.0 m). The well-to-well distance is 600 ft (182.9 m). A number of events are identified, after Chen et al. (1990). *D* - The direct *P* wave from the source well to the receiver well; *SR* - A *P*-wave radiated from the source well up to the surface and reflected into receivers in the receiver well; *DR* - A downgoing *P*-wave reflection generated from subsurface layers between the wells; *UR* - An upgoing *P*-wave reflection from layers between the wells; *T1* - A *P*-wave radiated from the source well to the bottom of the receiver well, converted into a tube wave, and traveled uphole; *T2* - A *P*-wave radiated from the source well to the top of the receiver well, converted into a tube wave, and traveled downhole; and, *T3* - A tube wave converted from the reflection *SR* at the bottom of the receiver well and transmitted uphole.
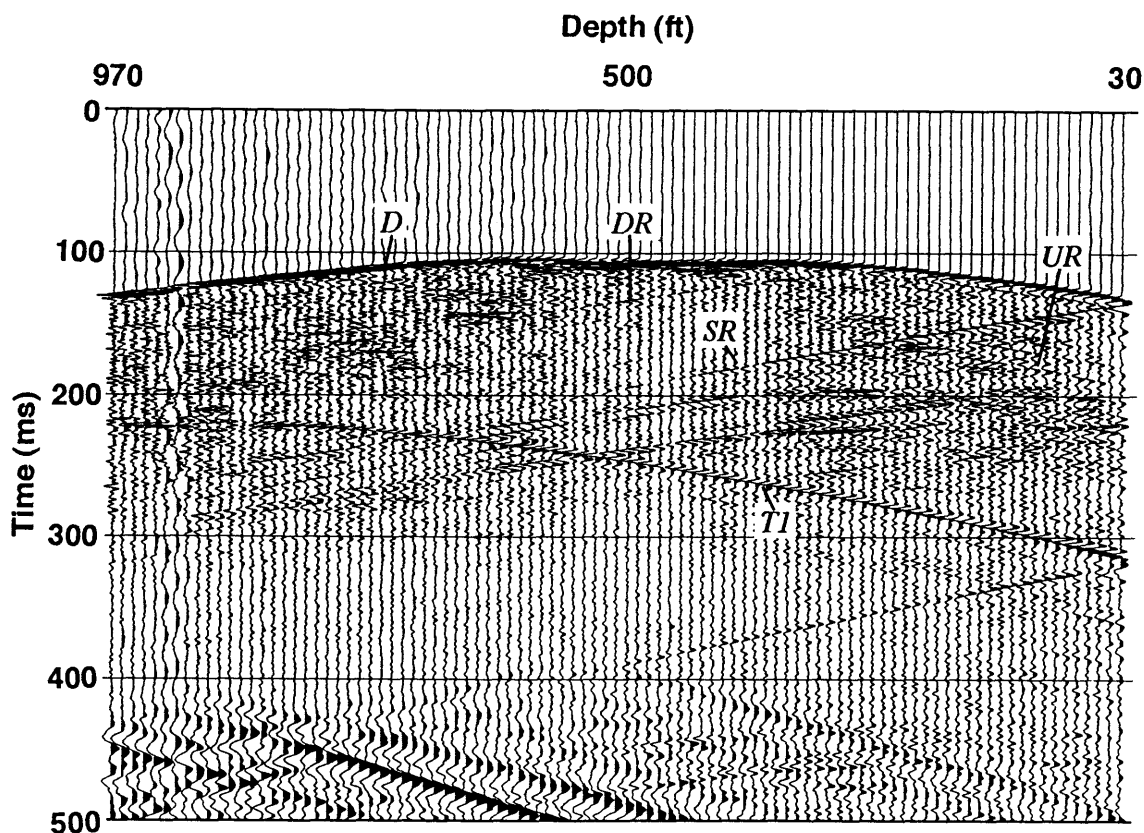
FIG. 2.6. Common-receiver gather, Friendswood, Texas. The receiver depth is 460 ft (140.2 m). Sources are shot between 30 ft (9.1 m) and 1000 ft (304.8 m), at every 10 ft (3.0 m), from the source well 600 ft (182.9 m) apart. (The last three traces are not displayed here.) *D* - The direct *P* wave from the source well to the receiver well; *SR* - A *P*-wave radiated from the source well up to the surface and reflected into receivers in the receiver well; *DR* - A downgoing *P*-wave reflection generated from subsurface layers between the wells; *UR* - An upgoing *P*-wave reflection from layers between the wells; and *T1* - A *P*-wave radiated from the source well to the bottom of the receiver well and converted into a tube wave.

well to the top of the receiver well, converted into a tube wave, and transmitted downhole. Reflections can be converted into tube waves, too. For example, event *T3* is the tube wave converted from the downgoing reflection *SR* at the bottom of the receiver well, and then travels uphole. Generally speaking, tube waves constitute severe noise that needs to be removed. Because of their linear nature in the common-source gather, they may be suppressed by using velocity filters in this gather. This subject will be discussed in Chapter 3.

The sonic log shows many obvious velocity changes with depth, where reflections that can be seen in the shot gather may be generated.

The data have a more complicated wavefield in the common-receiver gather (Figure 2.6). Although direct *P* wave *D*, downgoing reflection from the surface *SR*, downgoing reflections from layers *DR*, and upgoing reflections *UR*, are still identifiable in this gather, tube waves become more difficult to trace, because some of them have a non-linear moveout like that of reflections.

Now let us look at the data in the frequency domain. Shown in Figure 2.7 is an average amplitude spectrum for the 96 traces of the record in Figure 2.5 within the first 500 ms. The frequency band is quite broad. The high-energy power-line noise is evident at 60 Hz. Between 20 Hz and 60 Hz, there is relatively high energy that is largely due to tube waves and partly to other noise. A useful signal bandwidth may be from 70 Hz to 650 Hz. In the *f-k* domain, the tube waves are severely spatially aliased. The aliased energy of the tube waves in both directions (such as T1 and T2) is wrapped around the wavenumber axis, and therefore overlaps the zone of reflections. Despite various types of noise and unwanted waves, properly processed crosswell data provide much significant reflection information, as will be seen in the following chapters.
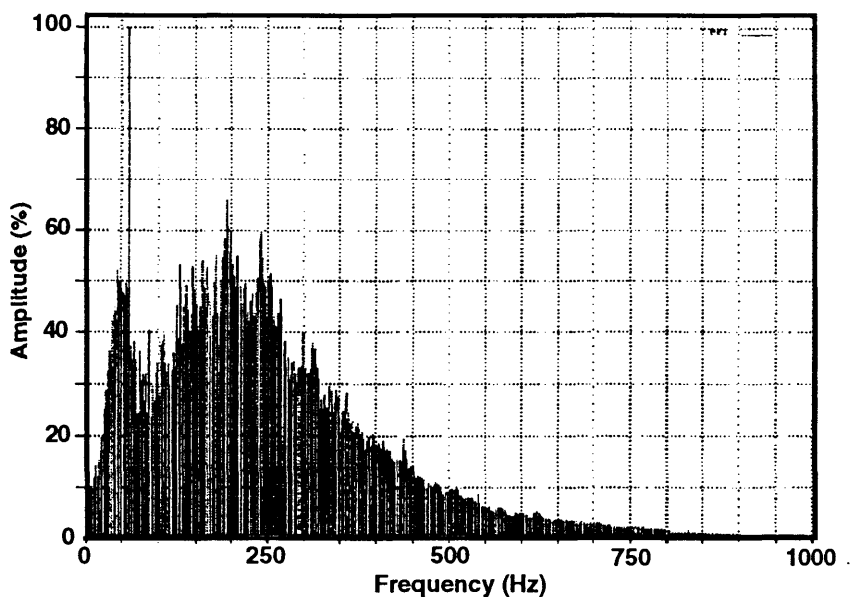
FIG. 2.7. Average amplitude spectrum of the raw shot record in Figure 2.5.

2.4　Cold Lake survey

2.4.1　Background

A recovery process, called cyclic steam stimulation (CSS), has been used since 1985 by Imperial Oil near Cold Lake, Alberta (Figure 2.8), to commercially produce extremely viscous bitumen from the unconsolidated porous sandstone reservoir in the Clearwater Formation (Eastwood et al., 1994). This recovery process involves injection of steam at high temperatures and pressures (310° C and 10 MPa), followed by the production of bitumen from the same wells. Twenty wells are directionally drilled from a single surface location or pad. To acquire knowledge regarding the volume of reservoir affected by the CSS and the displacement efficiency, a comprehensive seismic monitoring program has been undertaken to map steam-heated zones in the reservoir.

The CSS process was initiated in 1986 at D3 pad, where six observation wells were drilled around well D3-8 (Figure 2.9). In 1990, a seismic monitoring program was initiated, which included monitoring temperature and pressure in the 6 observation wells, rock physics, four crosswell tomograms, two 3-D seismic reflection surveys, geological modeling, and thermal numerical reservoir simulation. Figure 2.9 indicates the location of 15 CSS wells and 6 observation wells, the area coverage of the 3-D seismic, the location of crosswell seismic planes, and the location of the thermal simulation model. In this chapter, I will show the results of the crosswell seismic surveys only.

2.4.2   Survey geometry and field parameters

Wells OB2 and OB4 were used as source wells. Wells OB3 and OB5 were used as receiver wells. Therefore, crosswell seismic data were collected from 4 crosswell planes including OB2->OB3, OB2->OB5, OB4->OB3, and OB4->OB5. The offsets between wells range from 180 ft (54.9 m) (OB2-OB3, and OB4-OB5) to about 320 ft (97.5 m) (OB2-OB5, and OB4-OB3). I will use the crosswell plane of OB2-OB3 as an example for further analysis below.

During the crosswell surveys, Exxon's 32-shot downhole explosive source (Figure 2.10) was used to shoot into a 36-level hydrophone streamer (Figure 2.11). In well OB-2, the source tool was fired at 10-ft (3.0 m) increments from 400 ft (121.9 m) to 2030 ft (618.7 m), while in well OB-3, the hydrophone streamer was positioned between 240 ft (73.2 m) and 1560 ft (475.5 m), spaced at 10 ft (3.0 m) (Figure 2.12). Due to streamer length constraints and the desire to have the highest fold possible in the data, the source tool was shot in the source well OB2 in four passes, for each of four different streamer locations in the receiver well OB3.

26
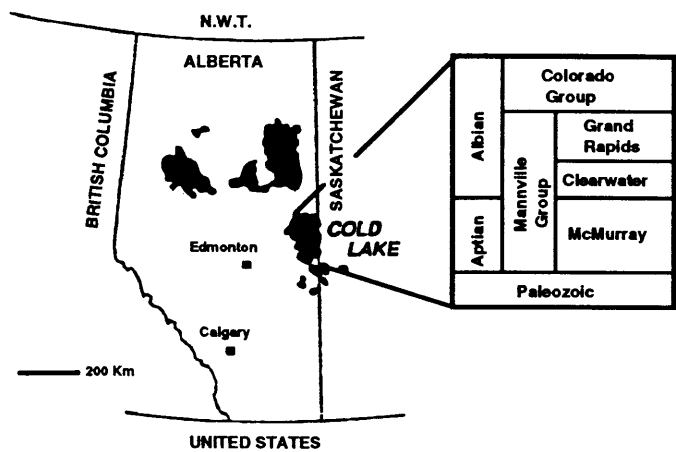
FIG. 2.8 The location of Cold Lake survey area and strati-graphic chart (after Eastwood et al., 1994).
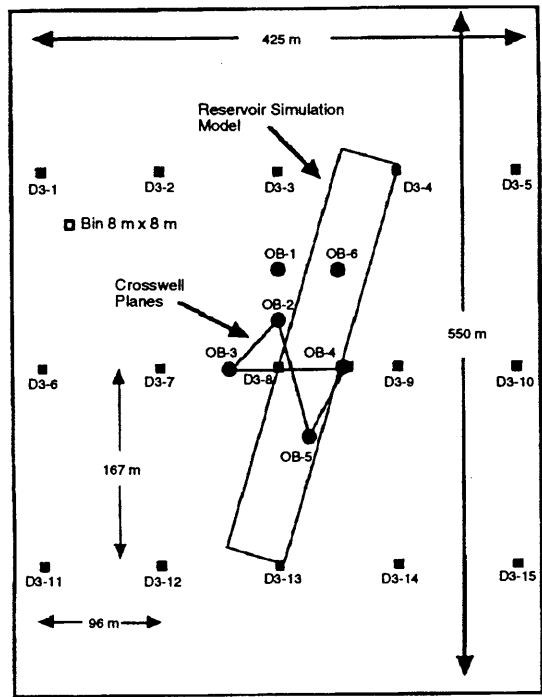
FIG. 2.9. Site map showing bottom hole locations of cyclic steam stimulation wells (D3-1 to D3-15), observation wells (OB-1 to OB-6), four crosswell planes, areal coverage of 3-D seismic, and the three-well reservoir simulator model (after Eastwood et al., 1994).

27
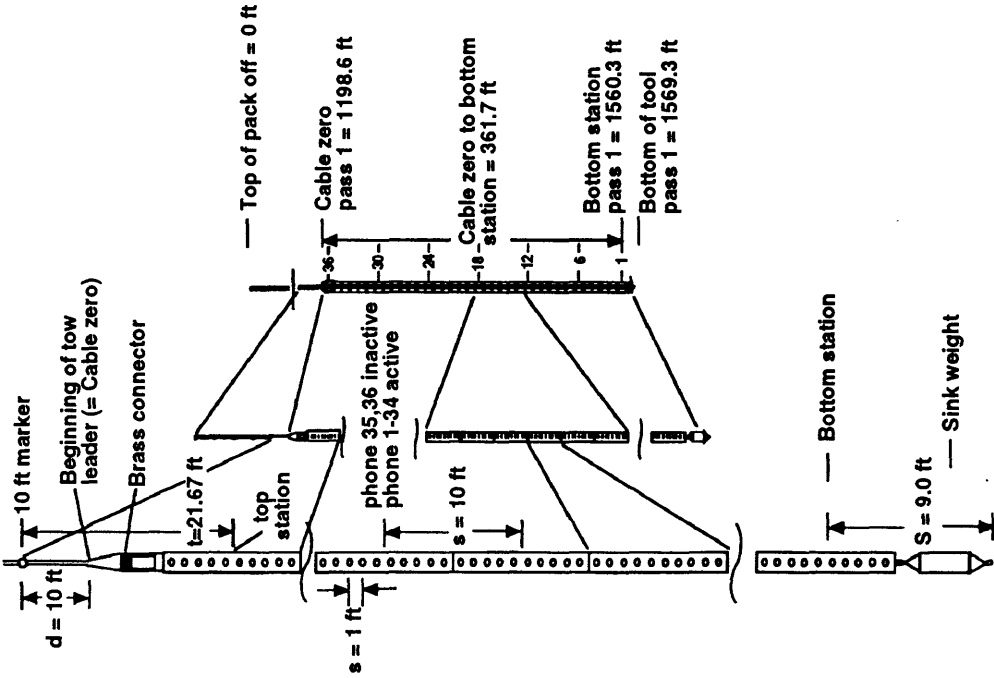
FIG. 2.11. A downhole 36-level hydrophone streamer used in the Cold Lake crosswell surveys (Courtesy of Imperial Oil Resources Ltd.).
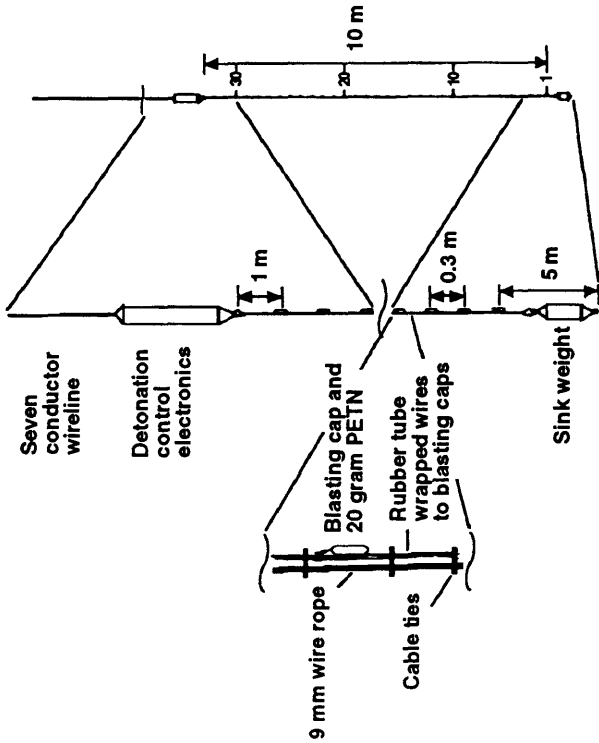
FIG 2.10 A 32-level downhole explosive seismic source tool used in the Cold Lake crosswell surveys (Courtesy of Imperial Oil Resources Ltd.).
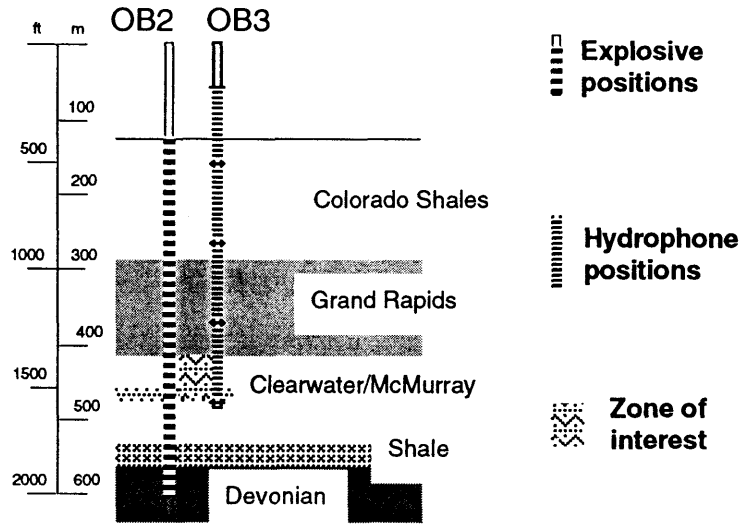
FIG. 2.12. Cold Lake crosswell data acquisition geometry in source well OB2 and receiver well OB3. The wells are offset by 180 ft (54.9 m). (Courtesy of Imperial Oil Resources Ltd.)

2.4.3 Data examples and wavefield analysis

A shot record from the crosswell plane OB2-OB3 is displayed in Figure 2.13. This record is from the source location at depth 470 ft (143.3 m) in the source well OB2. The receiver depths range from 240 ft (73.2 m) to 1560 ft (475.5 m), at intervals of 10 ft (3.0 m). The frequency spectrum of this record is shown in Figure 2.14.

The data below 150 ms are almost occupied with strong low-frequency tube waves appearing in two different directions. The tube waves have a low velocity of about 4600 ft/s (1402.1 m/s). However, above 150 ms, there are a few reflections whose velocity is around 6800 ft/s (2072.6 m/s). These reflections are noticeable in the shallow section, although in the same area there are tube waves as well. It is interesting to note that, in the shallow part of the data, the tube waves have similar frequency content to that of the reflections. The whole wavefield has a dominant frequency of about 90 Hz in the spectrum. But the frequency of the reflections may be higher than 150 Hz.

Depth (ft)

240   **900**   **1560**
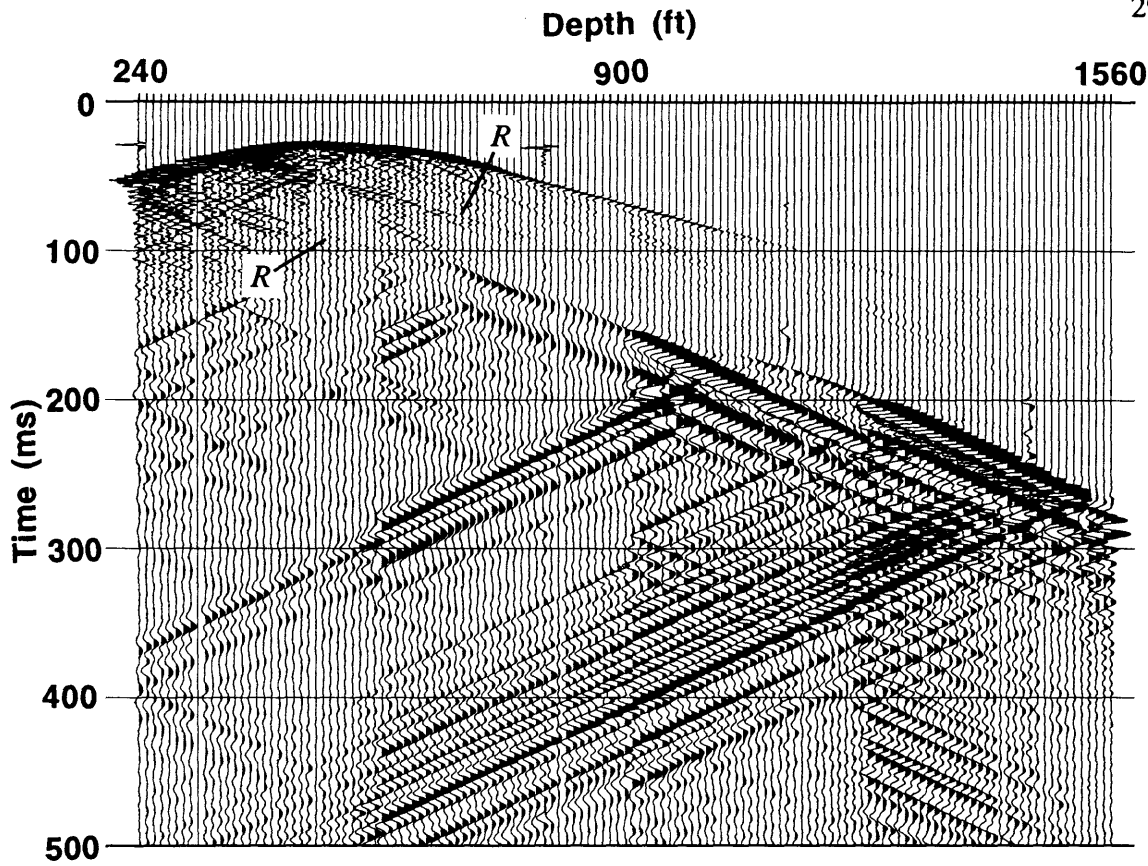
FIG. 2.13. Common-source gather, Cold Lake, Alberta. This gather was collected from the source well *OB2* and the receiver well *OB3*, 180 ft (54.9 m) apart. Source depth is 470 ft (143.3 m), and receiver depths are from 240 ft (73.2 m) to 1560 ft (475.5 m), at spacing 10 ft (3.0 m). *R* represents reflections.
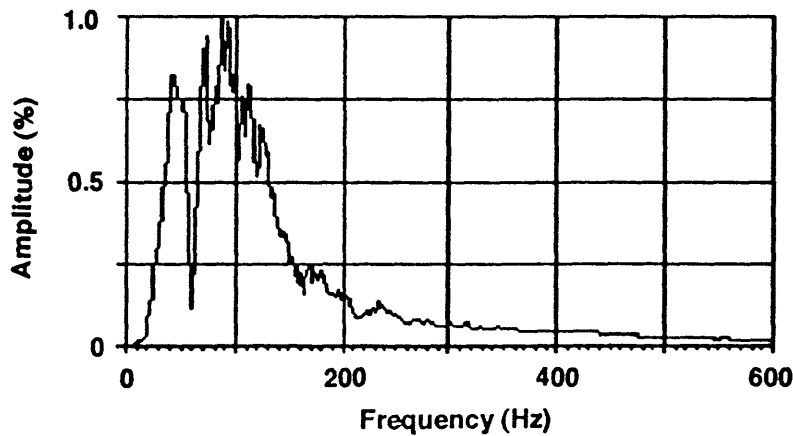
FIG. 2.14. Amplitude spectrum of the common-source gather in Figure 2.13.

2.5 Summary

Crosswell seismic data from 3 different surveys in North America are presented in this chapter. The well-to-well distances used range from 180 ft (54.9 m) to 1015 ft (309.4 m). The survey depth is generally shallow and varies in a range of 10 ft (3.0 m) to 2540 ft (774.2 m). In all three cases, vertical or nearly vertical boreholes were used as source and receiver wells.

Two different types of downhole seismic sources were used. They are downhole air gun and downhole explosive sources. Hydrophone streamers and geophones (either one-component or three-component) were used downhole to receive the crosswell data.

In all cases, tube waves were recorded. They are strong coherent events in the data, and usually dominate the recorded wavefield. Their frequency content can vary from very low to as high as that of the reflections. The tube waves can be generated in the source well as well as in the receiver well.

The purposes of these crosswell surveys extend from seismic monitoring of a cyclic steam stimulation recovery process (Cold Lake) to testing downhole sources and receivers (Humble). All crosswell seismics were shot in conjunction with other seismic data sets (VSP, reverse VSP, 2-D or 3-D surface seismics).

The Friendswood survey [10-g explosive source, hydrophone streamer, and 600-ft (182.9 m) well offset] provides the best reflection information. There are some reflection events visible in the Cold Lake crosswell data [20-g explosive source, hydrophone streamer, and 180-ft (54.9 m) well offset]. But no reflections are found in the Humble data [air gun, 3-C geophone, and 815-ft (248.4 m) well offset]. Therefore, it is decided that the Friendswood data are chosen for reflection data processing and imaging in later chapters.

Chapter 3

Tube waves and digital filtering

3.1 Introduction

Strong tube waves can dominate the wavefield in crosswell seismic data, as has been seen before. Compared to these tube waves, reflections are often very weak and, in some cases, almost invisible. This situation makes it difficult, and even impossible sometimes, to image the subsurface geology with reflections recorded in the field crosswell data.

There have been a number of relevant theoretical and experimental studies on how a tube wave is generated within a borehole and how it propagates in the surrounding medium. A detailed discussion of these studies is beyond the scope of this thesis. However, a brief review may be useful for a better understanding of the tube waves observed in the field data. This review will thus be given in this chapter, followed by an examination of the near-field and far-field records of the data from the Humble, Texas survey. Near-field and far-field data are defined as wavefields that are recorded close to and far away from the energy source, respectively. A few tube waves were identified in the previous chapter. The discussion will be extended in this chapter, with the purpose of relating the theoretical predictions and experimental observations to the real-data results. It

is important to effectively suppress the tube waves through digital filtering before crosswell reflection imaging. In this chapter, several filters will be tested and the results will be analyzed.

3.2   Theoretical and experimental studies

The problem of radiation patterns of a seismic source located in a fluid-filled borehole and the associated tube-wave propagation has been studied by a number of authors. Lee and Balch (1982) and Winbow (1989) presented the theory for the far-field radiation of P and S waves from an air gun source in an open fluid-filled borehole into the surrounding medium and tube waves propagating along the borehole. Winbow (1989) also discussed the problem in cased boreholes.

The energy radiated directly from a borehole source into the surrounding medium is defined as primary radiation (Lee et al., 1984). The primary radiation is direction dependent and its amplitude decreases with distance (due to spherical divergence) as a function of $1/R$, where R is the distance from the source. The radiation pattern for body waves depends not only on the wave velocities of the surrounding medium, but also on the velocity of the fluid inside the borehole.

According to these studies, a seismic source in a fluid-filled borehole can cause not only P- and S-wave primary radiation, but also a tube wave within the hole. Actually, as much as 99% of the energy produced by the borehole source can transmit as tube waves in the fluid-filled borehole, with only a small fraction of the energy going into the surrounding medium in the form of body waves (Winbow, 1989). A tube wave traveling in a borehole can cause secondary radiation (conversion from tube waves into P and S waves).

Unlike primary radiation, tube waves are not directional, and they do not suffer

much energy loss from geometrical spreading. Tube waves within the borehole have a significant impact on the body waves propagating in the surrounding medium. When the tube-wave velocity is close to the S-wave velocity in the surrounding medium, the borehole fluid has a substantial effect on the S-wave radiation. Also, the effect of the borehole fluid on the S-wave radiation is much more pronounced than on the P-wave radiation.

Observations from field borehole seismic experiments have been published. Winbow (1989) stated that a tube wave hitting the bottom of the source hole or any other discontinuities within it (such as a washed-out zone), theoretically represents an equivalent point source and thus causes secondary radiation. Winbow (1989) also found that tube waves are trapped in a cased borehole more than an uncased hole. Lee et al. (1984) observed that the amplitudes of secondary radiation can be much stronger than the primary radiation. Chen et al. (1990) reported that an air gun produces more tube waves and less direct P waves. P-wave amplitude is approximately linearly proportional to the size of the source while tube-wave amplitude increases only slightly with the size. However, the energy partition between P waves and tube waves is found dependent on charge size, open or cased hole, and lithology. A larger charge produces a higher P-wave/tube-wave ratio. An open hole produces a higher P-wave/tube-wave ratio than does a cased hole. Soft rocks (lower P- and S-wave velocities) produce a higher P-wave/tube-wave ratio than hard rocks.

3.3   Tube waves in field data

3.3.1 Near-field data

Figure 3.1 shows a common-receiver gather from the crosswell survey in Humble, Texas (see Chapter 2). The data are from a hydrophone hung closely below the air gun. They were located in the same source well, $K22$. When the air gun was shot from 300 ft (91.4 m) to 2540 ft (774.2 m), the hydrophone went downhole with it to record the near-

Source Depth (ft)
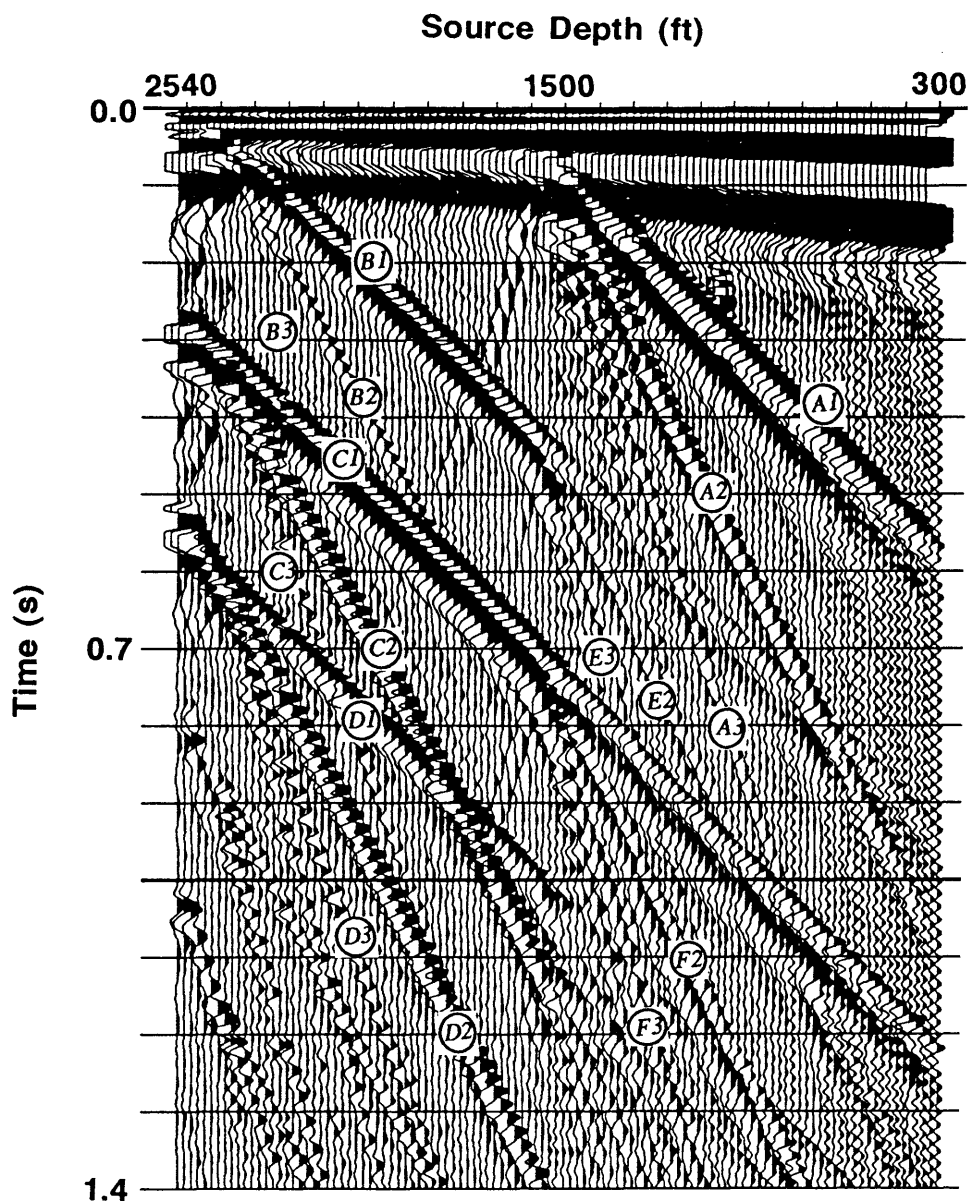
FIG. 3.1. Near-field waves in a hydrophone record from the crosswell seismic survey in Humble, Texas. The hydrophone is located in the source well *K22*, where an air gun, above the receiver, is shot down from 300 ft (91.4 m) to 2540 ft (774.2 m).

field signatures.

The near-field gather recorded the air gun bubbles, which appear just after time zero, and a number of tube-wave packages, which generally are strong, coherent, and linear. Some evident tube waves have been marked with symbols. Based on their dips, they are divided into three groups, and in each group, the tube waves are parallel. Group one (*A1*, *B1*, *C1*, *D1*, etc.) has an apparent velocity of 4600 ft/s (1402.1 m/s), which is close to the typical mud velocity in the borehole. The velocity of group two (*A2*, *B2*, *C2*, *D2*, *E2*, *F2*, etc.) is 1530 ft/s (466.3 m/s). The last group (*A3*, *B3*, *C3*, *D3*, *E3*, *F3*, etc.) has a velocity of 750 ft/s (228.6 m/s).

Tube waves in group one, such as *A1*, *B1*, *C1*, and *D1*, are stronger than the tube waves in the other two groups. Tube waves *A1*, *A2*, and *A3* appear to be generated from the same origin at the depth of 1500 ft (457.2 m). Therefore, an interpretation that *A2* and *A3* are multiples of *A1* can be made. In the same way, *B2* and *B3*, *C2* and *C3*, *D2* and *D3* are likely multiples of *B1*, *C1*, and *D1*, respectively.

From the hydrophone gather in Figure 3.1, it is inferred that around the borehole there are discontinuities, a few of which appear at 1500 ft (457.2 m), 2300 ft (701.0 m), and below 2540 ft (774.2 m). These discontinuities may be due to casing changes, and form significant impedance contrasts. Figure 3.2 explains the mechanism of how the selected tube waves (*A1~A3*, and *E2~E3*) were generated within the borehole. Every time the air gun was excited at a depth in the source well, the energy produced would radiate outwards. A large amount of the energy would travel downward in the form of a tube wave. When it encountered a discontinuity, the tube wave would be reflected back to the hydrophone above, where the reflected tube wave like *A1* was recorded. Since the bottom of the hydrophone (or possibly, of the air gun) is also an interface of large impedance contrast, the reflected tube-wave energy would be reflected again, travel downwards, hit the discontinuity once more, and bounce back to the hydrophone to generate the twice-

reflected tube wave, i.e., *A2*. In the same way, *A3* is the tube wave reflected three times. Higher order multiply reflected tube waves would also be generated within the hole.

Tube waves may not necessarily be reflected from the same discontinuity. Figure 3.2 also depicts another situation where tube wave, *B1* (not shown), that was reflected from a deep discontinuity, was traveling once more between the hydrophone and a shallower discontinuity to form tube wave *E2*, and twice more to form *E3*. The similar interpretation applies to the rest of tube waves not explained in Figure 3.2.

The amplitudes of all the tube waves in Figure 3.1 are fairly uniform, indicating that there is little energy loss due to geometric spreading. This agrees with the theoretical
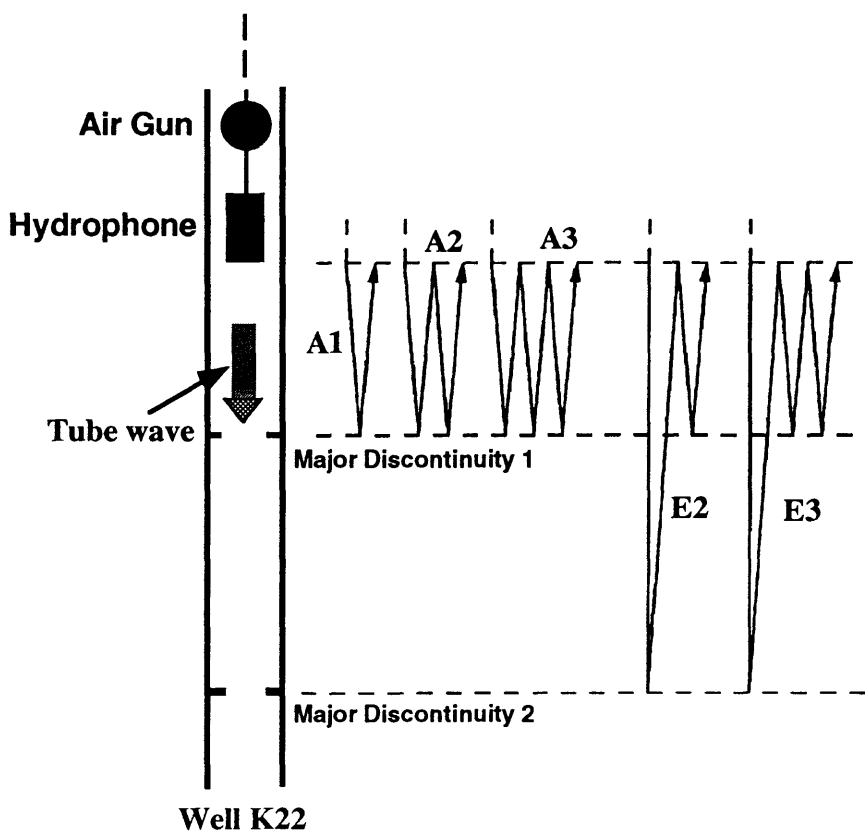
FIG. 3.2. Explanation of tube waves received by the hydrophone in the source well *K22* where the air gun is shot. Tube waves can be reflected from discontinuities more than once.

analysis in the preceding section. However, reflecting interfaces have some transmission loss. So higher-order multiply reflected tube waves are weaker than tube waves reflected only once.

3.3.2 Far-field data

Figure 3.3 shows a common-receiver gather of the Humble crosswell data shot in well *K22* and received in well *C30*, 815 ft (248.4 m) far away. The air gun was shot from 300 ft (91.4 m) to 2540 ft (774.2 m). The receiver was a 3-C VSP tool at a depth of 1500 ft (457.2 m). The data in Figure 3.3 are the far-field record from one of the horizontal component channels on the 3-C geophone.

Many tube-wave events are evident in this gather. The tube-wave energy is coherent, dips linearly, and dominates the gather. The body-wave energy, either *P*- or *S*-wave direct arrival, is very weak. Indeed, the *S* wave is so weak that it is hardly visible. It supports the theory mentioned in section 3.2, that only a small fraction of the total energy produced by the downhole source can radiate out into the medium and that most of it is trapped as tube waves in the borehole.

When the strong tube waves encounter a discontinuity in the source well (sudden acoustic impedance change such as casing change, the top or bottom of the borehole), secondary radiation occurs. Such secondary radiation will cause conversion of tube waves into body waves (*P* or *S*). The strong dipping events in Figure 3.3 are interpreted as body waves converted from tube waves, as a result of secondary radiation in the source well *K22*.

Figure 3.4 shows a number of major events picked from Figure 3.3. They include a *P*-wave direct arrival (*P*), an *S*-wave direct arrival (*S*), a converted *P* wave (*T-P*), and a few converted *S* waves (*T-S*). The converted *S* waves include the waves converted from tube waves which are multiply reflected for the same reason as discussed in section 3.3.1.
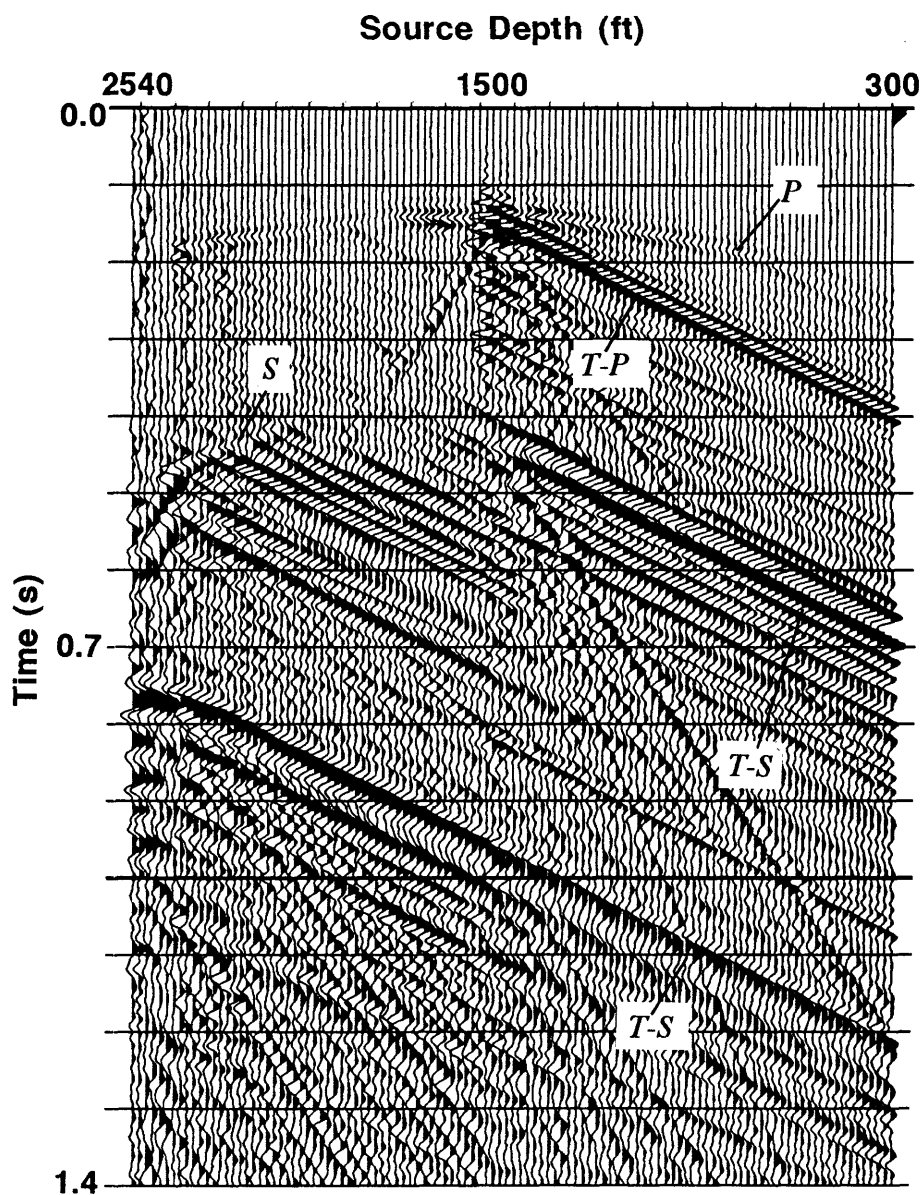
FIG. 3.3. Far-field waves in a common-receiver gather from the crosswell survey in Humble, Texas. The three-component VSP tool was 1500 ft (457.2 m) deep in well *C30*, while the downhole air gun was shot from 300 ft (91.4 m) to 2540 ft (774.2 m) in well *K22*. Well separation was 815 ft (248.4 m). This gather is from one of the horizontal components recorded. The annotated events are described in Figure 3.4.
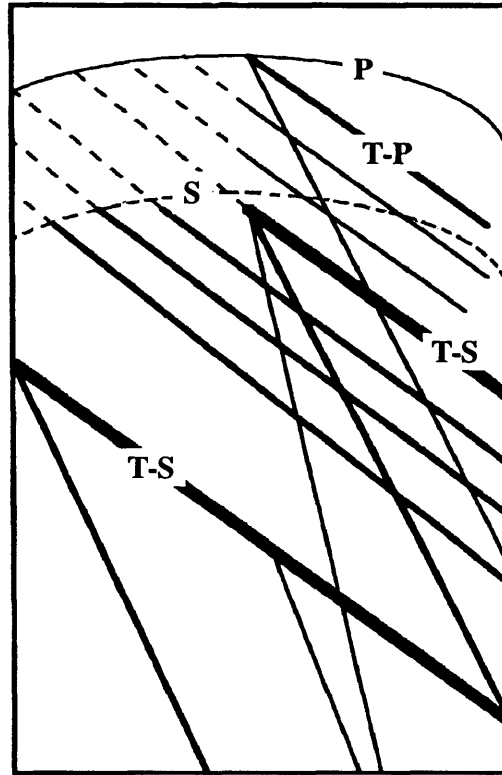
FIG. 3.4. Events identified from Figure 3.3. *P*: *P*-wave direct arrival; *S*: *S*-wave direct arrival; *T-P*: *P* wave converted from a tube wave; *T-S*: *S* wave converted from a tube wave.

Figure 3.5 schematically illustrates how tube waves (including multiply reflected versions) are converted into body waves. From Figure 3.3, it can be seen that the horizontal-component channel recorded more *S*-wave energy converted from the tube waves than the converted *P*-wave energy.

The *P* or *S* converted waves do parallel each other. The time delay of the *T-S* wave with respect to the *T-P* wave is the longer transit time of the *S* wave across the interwell distance. Although the secondary radiation can happen at discontinuities of any depths, the traveltime of the converted waves is a linear function of the source depth from which the tube wave begins to travel. The intercept of this linear function is the traveltime from the
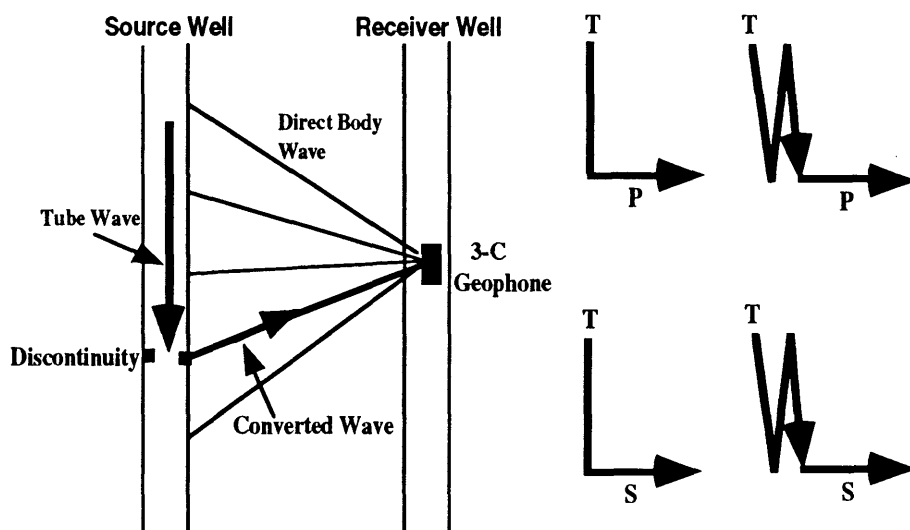
FIG. 3.5. Conversion of tube waves into body waves can happen at discontinuities in the source well.

---

secondary source (a discontinuity) to the receiver (which is constant for every shot), and the slope is the velocity of the tube wave. This is why these dipping tube-wave events are parallel to each other and have the same apparent velocity.

3.4   Tube wave suppression

3.4.1   Test data

Having analyzed tube waves in field crosswell data, I will now discuss the application of filtering methods to suppress them. Three types of filters will be considered below. They are *f-k* filter, median filter, and alpha-trimmed mean filter.

A shot record from the Friendswood crosswell survey as shown in Figure 2.5 is selected for the filtering test. There are two reasons why the Friendswood data are

selected. First, the Friendswood data contain both tube waves and good reflections. It is desirable to examine the effect of those filters on the reflected waves remained in the filtered record. Second, after the tube waves are removed, the filtered Friendswood data will be used in reflection imaging, which will be elaborated in Chapter 7.

3.4.2 *f-k* filtering

The *f-k* filter is a multichannel operator, implemented in the frequency-wavenumber (*f-k*) domain, through 2-D Fourier transformations (Yilmaz, 1987). Often, signals and noise in the recorded seismic data exhibit different characteristics, such as dip or moveout, which can be distinguished from trace to trace. Events that dip in the time-distance (*t-x*) domain can be separated in the *f-k* domain by their velocity. In our case, coherent strong tube waves generally have a lower velocity than reflections, and thus have a larger moveout (or dip). Because of this, the tube waves can be isolated from the reflections in the *f-k* domain, so they can be suppressed by designing a rejection zone. Typically, a rejection zone is designed with a fan or pie-slice or arbitrary polygon shape. One or more filters can be specified in the *f-k* domain by their frequency and velocity limits. The data within the specified zones can be either rejected or passed.

Figure 3.6 compares the results before and after *f-k* filtering of the Friendswood crosswell record. Prior to *f-k* filtering, the data were trace-equalized to avoid possible spurious noise in the *k*-direction. Polygons were designed around the linear tube waves in the *f-k* domain. Since the low-velocity tube waves in the Friendswood data are severely spatially aliased in the *f-k* domain, and the aliased components overlap the reflections, the use of the filter in the overlapping zones causes loss of some reflection energy. Components within the selected polygons (mostly tube waves) were rejected, and components outside the polygons were kept. Figure 3.6a shows the input shot record, with the passed wavefield shown in (b), and the rejected tube waves in (c).
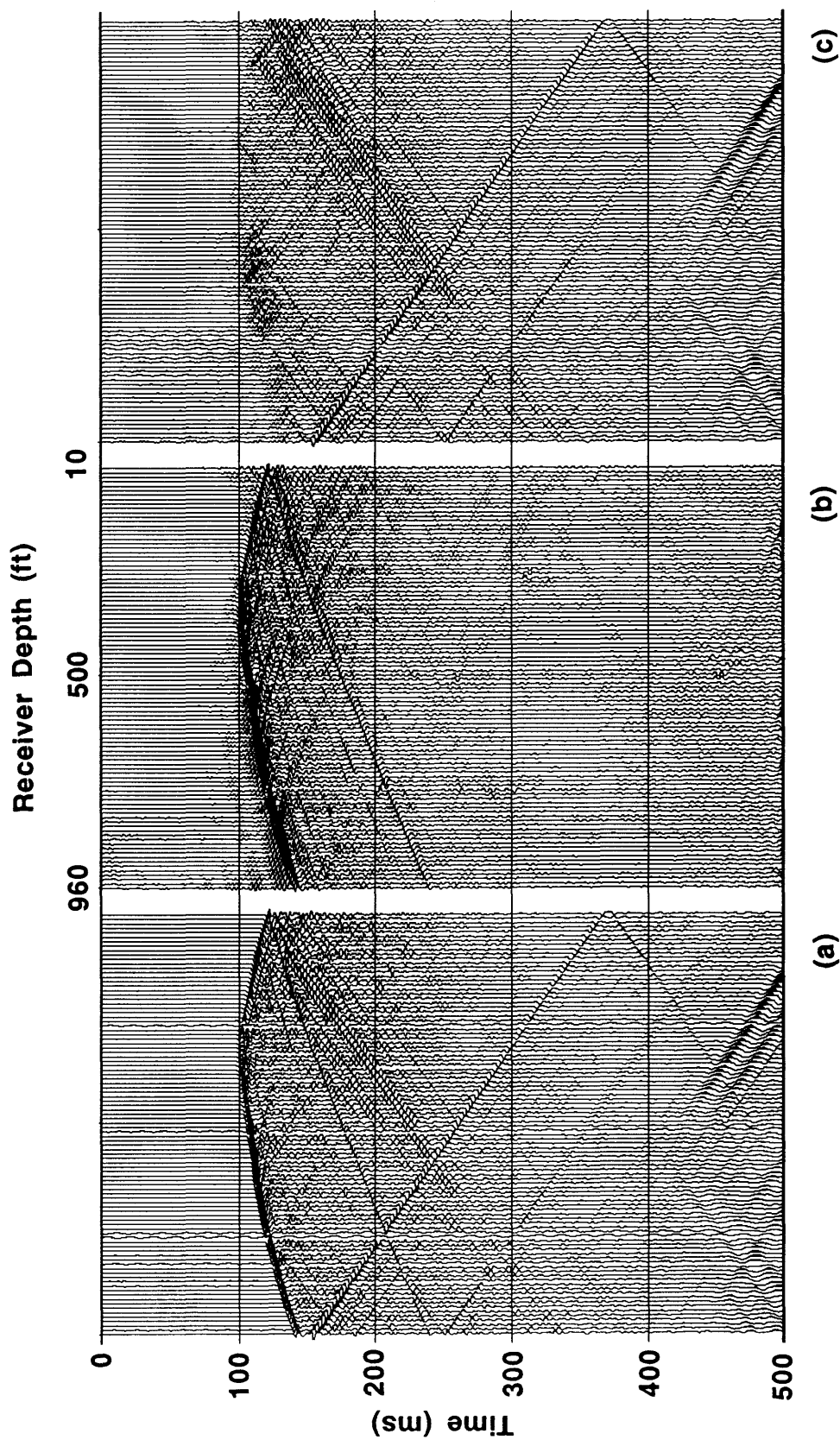
FIG. 3.6. Result of *f-k* filtering of tube waves in a crosswell shot record. (a) Input record. (b) Passed wavefield. (c) Rejected tube waves.

42

The results show that tube waves have been effectively removed from the input wavefield by the *f-k* filter. Reflections become more obvious. However, smearing of amplitudes caused by *f-k* filtering, especially around the direct arrival, is severe.

3.4.3   Median filtering

The median value of a sequence of N numbers is found by first ordering them in increasing values, then selecting the middle value of the ordered sequence when N is odd, or the mean value of the two middle numbers in the sequence when N is even. The above procedure is used to design a median filter, a type of filter that has been widely used in VSP processing to enhance desired reflections and to remove unwanted direct arrivals (Hardage, 1985; Stewart, 1985). In seismic applications, the median filter selects a median value (amplitude) from a window in the input data gather, puts it at the center of the window on the output gather, and then repeats the procedure by sliding the window to a new position along the distance (trace) direction and the time (sample) direction. The size of the window (i.e., the filter operator) is determined by the number of traces and time samples, both pre-specified. When only a line of data is involved, it is 1-D median filter, and when an area or volume is used, it becomes a 2-D or 3-D filter.

The median filters are applied to the Friendswood crosswell record to suppress the strong tube waves. The process of removing tube waves via median filtering consists of four steps. First, the time moveout of tube waves that dip in one direction is picked and removed, aligning the events. Second, the median filter is applied to enhance the aligned tube waves, and remove all other waves and noise. Third, the enhanced tube waves are subtracted from the original record of data. Fourth, a dealignment is applied to the difference record to remove the time shift applied before. These steps are then repeated for tube waves that dip in a different direction. Different operators are tested to select the optimal filter parameters that give the best tube-wave suppression result.

Figure 3.7 compares the input record (a) with outputs of the 1-D median filter (b) and the 2-D median filter (c). In the 1-D filter case, the operator is 9-traces wide. The 2-D median filter uses a 9-trace by 3-sample operator. The 1-D filter does a better job than the 2-D filter in suppressing the tube waves. Unlike the *f-k* filter, the 1-D and 2-D median filters do not cause much smearing. However, residual tube waves are still seen in the output of median filters, in particular in the 2-D filtering result.

3.4.4 Alpha-trimmed mean filtering

The alpha-trimmed mean is defined by Haldorsen and Farmer (1989) as an estimate of the mean derived from a sequence of sample values ascendingly ordered but trimmed on both sides. It can be expressed by

$$\text{Alpha-trimmed Mean} = \frac{1}{N - \alpha} \sum_{i = \alpha/2 + 1}^{N - \alpha/2} S_i \quad , \qquad (3.1)$$

where the samples S_i have been sorted in ascending value, N is the total number of samples, and α is the total number of samples rejected ($\alpha/2$ on either side of the distribution). The filter using this property is called an alpha-trimmed mean filter. The filter sorts the samples within the filter window, and averages a range of values centered about the median. The averaged value (mean) is output. Like the median filters, the alpha-trimmed mean filter can be designed in the form of 1-D or higher dimensions. The steps of applying the alpha-trimmed mean filter to remove crosswell tube waves are similar to those used for median filtering, and involve tube-wave alignment, enhancement, subtraction, and so on.

The results of alpha-trimmed mean filtering of the Friendswood crosswell record are shown in Figure 3.8. Tube waves are removed quite well by these filters. The 1-D filter yields perhaps a little less residual tube waves than does the 2-D filter. However, by

45
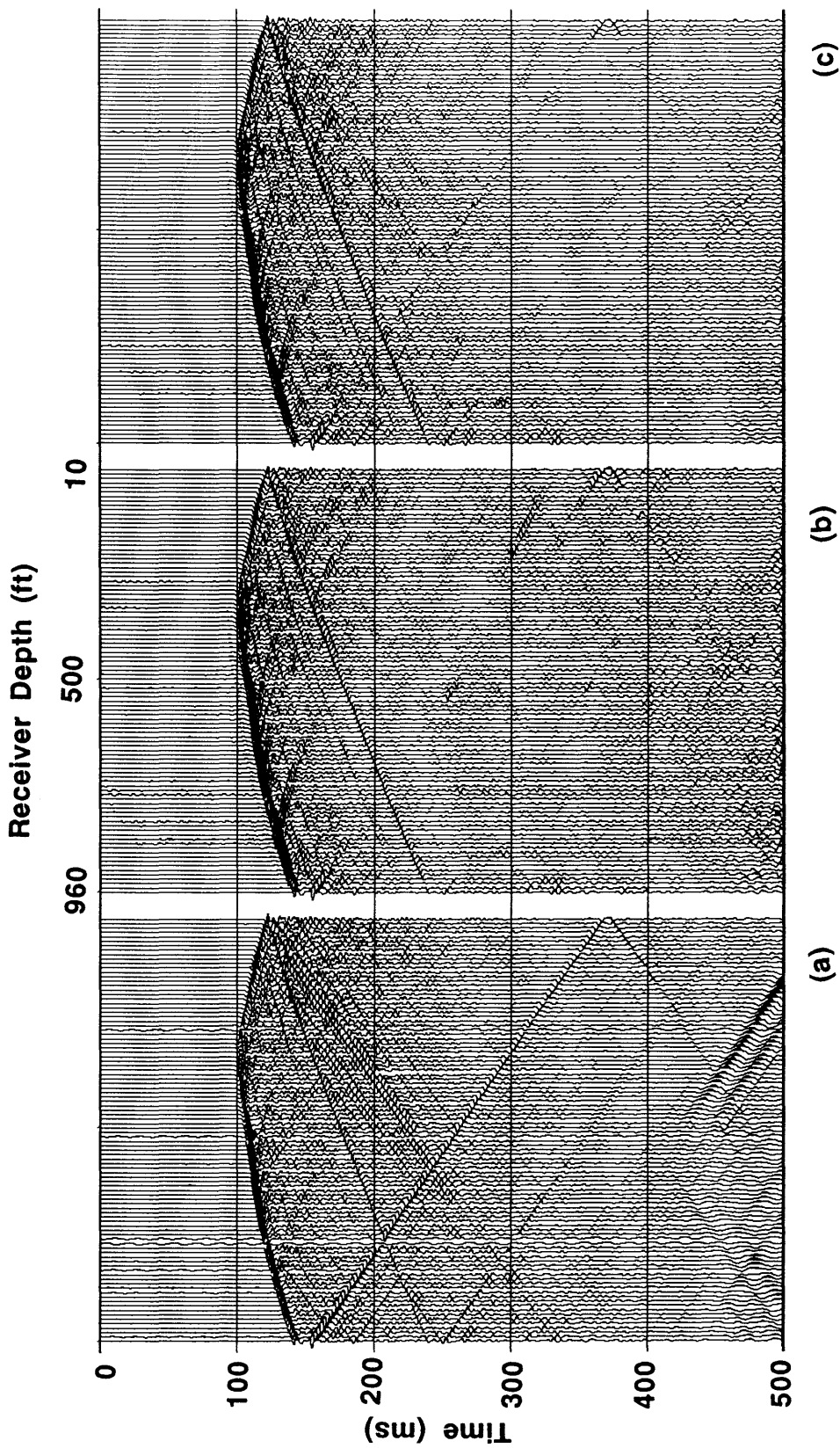
FIG. 3.7. Result of median filtering of tube waves in a crosswell shot record. (a) Input record.
(b) Output from the 1-D median filter. (c) Output from the 2-D median filter.
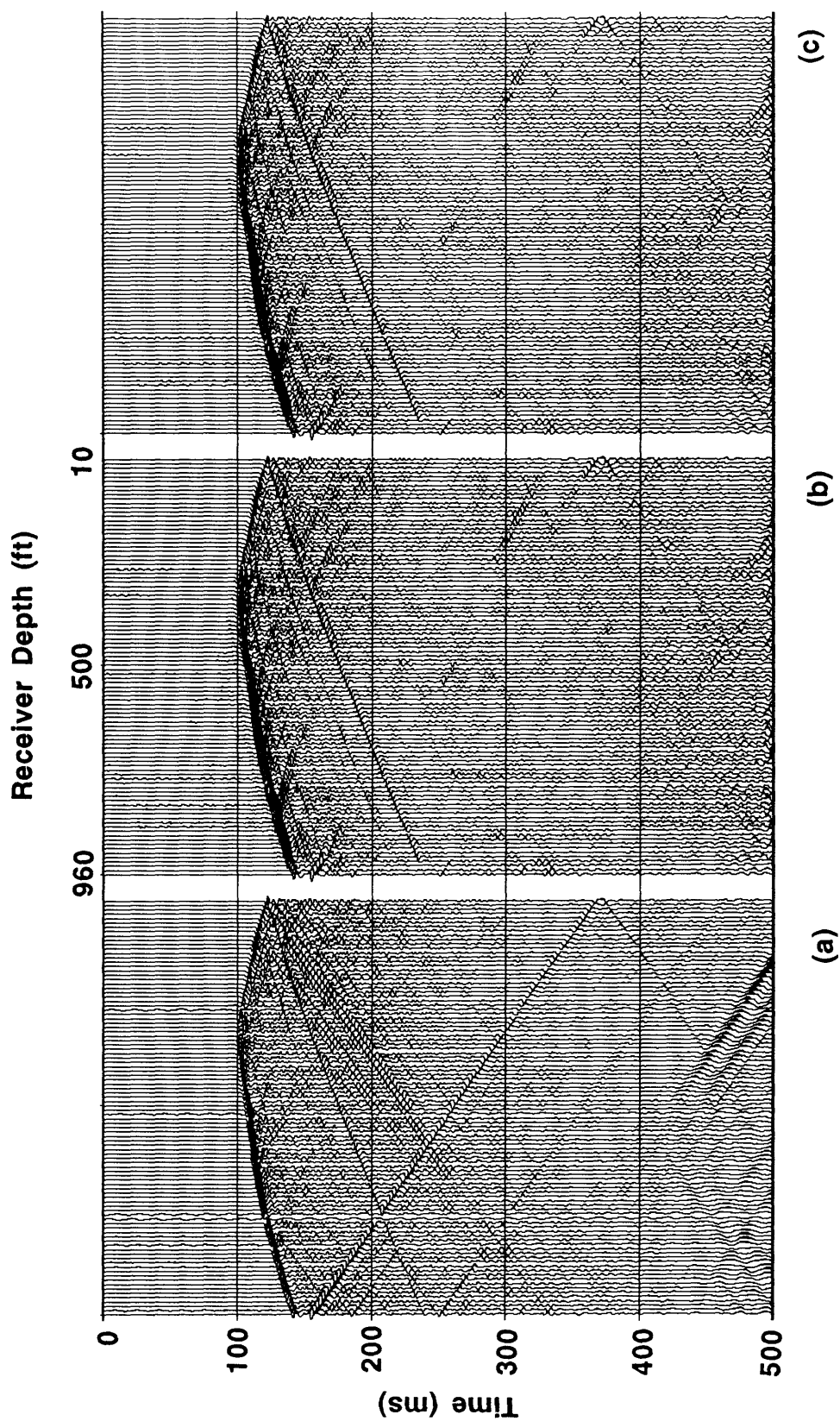
FIG. 3.8. Result of alpha-trimmed mean filtering of tube waves in a crosswell shot record. (a) Input record. (b) Output from the 1-D alpha-trimmed mean filter. (c) Output from the 2-D alpha-trimmed mean filter.

comparing Figure 3.8 with Figure 3.7, it is found that the 1-D median filter works better in removing tube waves than the other three filters.

3.5 Summary

A number of conclusions can be made from the analysis of tube waves and filtering tests in this chapter.

(1) A downhole seismic source (e.g., air gun) in a fluid-filled borehole can generate two types of energy: very strong tube wave, which accounts for a majority of the total energy produced by the source, and very weak body waves (P or S mode), which account for a very small fraction of the source energy only.

(2) Any discontinuities in the borehole such as casing changes can cause multiple reflections of the tube wave between these discontinuities and the bottom of the source or the receiver hung below it. Since these discontinuities can act as good secondary-radiation sources, the strong tube waves are found to be converted into body waves that propagate in the surrounding medium.

(3) In the crosswell data recorded in the far field, secondary radiation (that is, conversion of tube waves into body waves) can be much stronger than primary radiation (that is, body waves directly radiated from the downhole source). These converted body waves are usually strong, coherent, and linearly dipping in the far-field common-receiver gathers. They represent the major disturbing coherent noise in the crosswell data.

(4) The strong, spatially aliased tube waves in the field crosswell data can be effectively removed by digital filtering. Filters that are tested include the f-k filter, 1-D and 2-D median filters, and 1-D and 2-D alpha-trimmed mean filters. The 1-D median filter yields a better filtering result. However, limitations of all these filters exist.

Chapter 4

Automatic crosswell velocity analysis

4.1 Introduction

Many attempts have been made in the past to obtain velocity information from crosswell seismic data using tomographic inversion schemes (Bois et al., 1972; Ivansson, 1985; Peterson et al., 1985; Bregman et al., 1989; Lines and LaFehr, 1989; Abdalla et al., 1990; Lines and Tan, 1990; Stewart, 1991). However, most tomographic techniques involve time-consuming, hand-picking of traveltimes. When hundreds of crosswell shot records, for example, are available for analysis, hand-picking is clearly not efficient.

In this chapter, a new method for crosswell velocity analysis is presented. This method makes use of the basic concept of coherency-based velocity analysis widely used in conventional surface seismic data processing. The method assumes that a linear velocity-depth relationship can describe the intervening medium between two boreholes in a certain vertical region. Equations can therefore be derived to calculate theoretical traveltimes for crosswell first arrivals for each velocity guess. Within a fixed time window along the calculated traveltime trajectory, seismic traces are stacked to give the coherency (semblance value). The procedure is repeated for a range of velocity guesses. As a result, the largest semblance value corresponds to the best-fit linear velocity

function. Since the semblance analysis can be performed automatically, the hand-picking of traveltimes required by tomographic methods is not required here. In the following sections, I will describe the theoretical framework for this automatic velocity-analysis method in detail, and discuss an implementation of the algorithm. Results of testing the method with different data sets will be given.

4.2   Theory

4.2.1   Linear velocity increase with depth

For most cases in exploration seismology, it is an oversimplification to assume a constant-velocity medium. A better, but still limited, approximation to the actual Earth is that of a medium with a vertical velocity gradient; i.e., the velocity changes as a simple function of depth from a reference plane and there is no significant horizontal velocity variation. The gradient medium has been found useful in general (Helbig, 1990). In such a medium, rays are curved everywhere, but are similar for all ray parameters. Moreover, wavefronts are of similar shapes for all traveltimes.

In particular, a *linear-gradient medium* has been investigated by many geophysicists and found to be a very good approximation to the real solid earth over certain intervals. Slotnick (1959) noted that the velocity of seismic wave propagation in Tertiary basins could be approximated closely by expressing it as a linear function of depth. He gave some examples of areas, including the Gulf of Mexico, San Joaquin Valley of California, and a Venezuela basin, where "one can safely assume a linear velocity relationship with depth". After inspecting logs from Western Canada, Jain (1987) found that most logs in the Western Canadian Basin justify a linear increase in

velocity with depth down to the Paleozoic unconformity. The values of the velocity gradient he obtained from the Cretaceous section range from 0.25 to 1.0 ft/s/ft.

A commonly used expression for the linear velocity function is:

$$V(z) = V_0 + \kappa z \quad , \tag{4.1}$$

where V_0 is the initial velocity (ft/s or m/s) at the horizontal datum plane (e.g., the surface of the Earth), $V(z)$ the velocity at a depth z below the datum plane, and κ the constant gradient (ft/s/ft, or m/s/m). The value of κ indicates an increase (when κ is positive) or decrease (when κ is negative) in velocity per unit of depth. In this chapter, the case of positive velocity gradients ($\kappa \geq 0$) is considered only. For negative gradients, the method discussed below can be generalized.

Sometimes the linear velocity function is expressed in another form:

$$V(z) = V_0 \left(1 + \eta z\right) \quad . \tag{4.2}$$

Here η is called velocity gradient factor, and its dimension is (feet)$^{-1}$ [or (meters)$^{-1}$], and

$$\kappa = V_0 \eta \quad . \tag{4.3}$$

Relation (4.1) will be used below.

4.2.2 Direct waves and turning waves

Previous studies (Slotnick, 1959; Grant and West, 1965; Telford et al., 1976) show that in a medium with a linear velocity increase with depth, seismic waves propagate along a circular raypath. However, their discussions are limited to the surface

seismic case where the source and receiver are both on the surface of the Earth.

In Appendix A, a discussion of fundamental propagation characteristics of direct waves and turning waves in the linear-gradient medium is given for the case of crosswell geometry. Equations for calculating the traveltimes of these waves are derived.

Here, direct waves are defined as the waves that travel from the source directly to the receiver without a turning point (zero slope or 90° travel direction to the vertical) along its circular raypath. Turning waves are defined as the waves that travel downward from the source and then upward to the receiver so that there is a point of zero slope on its circular raypath, as indicated by the symbol Tn in Figure 4.1a. The turning point also corresponds to the maximum depth of penetration of turning waves.

As shown in Figure 4.1a, all turning waves appear in the stippled zone, and above and below this zone is the region in which direct waves occur. The upper boundary, B_1, between the direct-wave and turning-wave zones is divided by the raypath which leaves the source at a right angle to the vertical axis. The lower boundary, B_2, is given by the raypath that has a turning point just on the axis of the receiver well. Although on the boundaries, both direct and turning waves coincide, I treat them as direct waves mathematically (see Appendix A).

As the positive gradient (κ) value increases, the turning-wave raypath takes on a smaller radius of curvature, that is, the turning-wave zone expands. However, as κ approaches zero, the turning-wave zone shrinks; when κ is zero, the zone vanishes, the situation now becoming the constant-velocity case in which the direct-wave paths are straight and there is no turning wave.

In the linear-gradient medium, the crosswell first arrivals that would be recorded are composed of contributions from the turning waves (in the middle of the traveltime trajectory) and contributions from the direct waves (on both sides of the trajectory), as shown in Figure 4.1b.
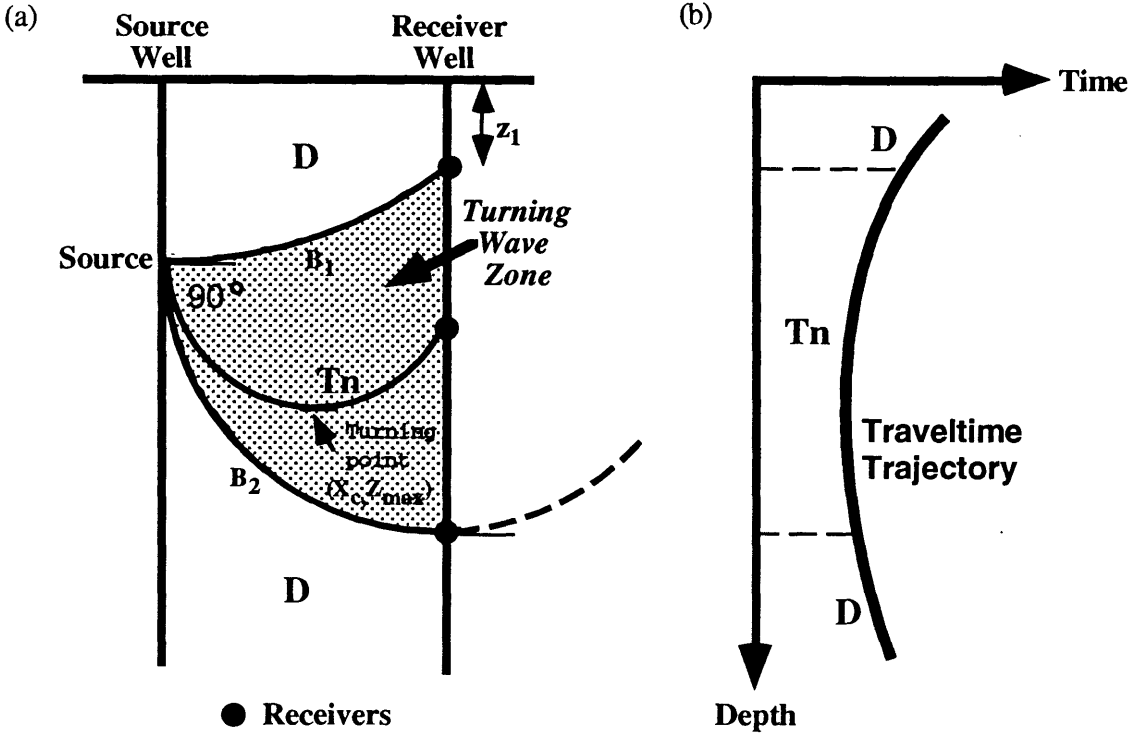
FIG. 4.1. (a) Raypaths of direct and turning waves between source and receiver wells in the medium of a linear velocity increase with depth. D represents the zone of direct waves. The stippled area is the zone of turning waves. Tn indicates a particular turning wave with turning point annotated. The curves labeled B_1 and B_2 represent the upper and lower boundaries, respectively, between the zones of direct and turning waves. (b) The traveltime trajectory of first arrivals.

4.2.3 Traveltime equations

Equations are derived in Appendix A for the theoretical traveltime trajectory of the direct and turning waves. Traveltimes for direct waves between two *vertical* boreholes can be calculated from the following equations:

$$t = \frac{1}{\kappa} \left| \ln \frac{(V_0 + \kappa z_R)\left(\sqrt{1 - p^2(V_0 + \kappa z_s)^2} + 1\right)}{(V_0 + \kappa z_s)\left(\sqrt{1 - p^2(V_0 + \kappa z_R)^2} + 1\right)} \right| , \qquad (4.4)$$

and

$$p = \cfrac{1}{\kappa \sqrt{\left[x_s - \cfrac{x_R^2 - x_s^2 + \left(z_R + \frac{V_0}{\kappa}\right)^2 - \left(z_s + \frac{V_0}{\kappa}\right)^2}{2(x_R - x_s)} \right]^2 + \left(z_s + \frac{V_0}{\kappa}\right)^2}} \quad , \qquad (4.5)$$

where t is the traveltime for direct waves, and ray parameter p is merely an intermediate variable. z_R and x_R are the depth and horizontal coordinate of the receiver, and z_s and x_s are the depth and horizontal coordinate of the source.

For turning waves, traveltimes are calculated via

$$t = \frac{1}{\kappa} \ln \frac{\sqrt{1 - p^2 (V_0 + \kappa z_s)^2} + 1}{p (V_0 + \kappa z_s)} + \frac{1}{\kappa} \ln \frac{\sqrt{1 - p^2 (V_0 + \kappa z_R)^2} + 1}{p (V_0 + \kappa z_R)} \quad . \qquad (4.6)$$

In this equation, the values of p are found from Eq. (4.5).

Appendix A gives the criterion to decide when to use equation (4.4) or (4.6). Three values need to be calculated: the receiver depth z_1 where the ray arrives, after leaving the source at a right angle to the vertical axis; the horizontal and vertical coordinates of the turning point, x_c and z_{max} (see Figure 4.1). For a certain ray arriving at a position of offset x and depth z_R, if $z_R \leq z_1$, then the direct-wave equation (4.4) should be used; if $z_1 < z_R < z_{max}$ and $x > x_c$, then the turning-wave equation (4.6) should be used; but if $z_1 < z_R \leq z_{max}$ and $x \leq x_c$, the direct-wave equation (4.4) should be used again.

4.3   Velocity analysis method

From the above discussion, given the crosswell geometry (source and receiver positions, and well separation) and the linear velocity function (initial velocity and gradient), the traveltimes of direct waves or turning waves can be calculated. These

traveltimes define a quasi-hyperbolic trajectory, as will be seen later. For a particular crosswell shot gather with known geometric parameters, changes in the values of the velocity parameters respectively will cause different traveltime trajectories, one of which may best fit the observed first arrivals. Now the question is, if we can approximate the first arrivals observed on field crosswell data with a theoretical trajectory, can we obtain an estimation of the velocity distribution? The method discussed below will answer this question.

The automatic velocity analysis method comprises two steps (see Figure 4.2). In the first step, first-arrival traveltimes are calculated for all receiver positions and one source location, using equations (4.4) or (4.6), plus (4.5). An approximate range of velocity values is guessed, resulting in many traveltime trajectories. In the second step, seismic traces in the crosswell shot gather are stacked within a time window along each traveltime trajectory calculated in the first step. Semblance values are computed from this stack. The largest semblance value, as a function of velocity, is then picked.

4.3.1 Semblance analysis

A useful measure of coherency of signals is their energy (Yilmaz, 1987; Krebes, 1989). The output energy is defined as

$$
E_{\text{out}} = \sum_{t=t(i)-\Delta t}^{t(i)+\Delta t} \left(\sum_{i=1}^{N} f_{i,t} \right)^2 \ ,
\tag{4.7}
$$

and the input energy as

$$
E_{\text{in}} = \sum_{t=t(i)-\Delta t}^{t(i)+\Delta t} \left(\sum_{i=1}^{N} f_{i,t}^2 \right) \ ,
\tag{4.8}
$$
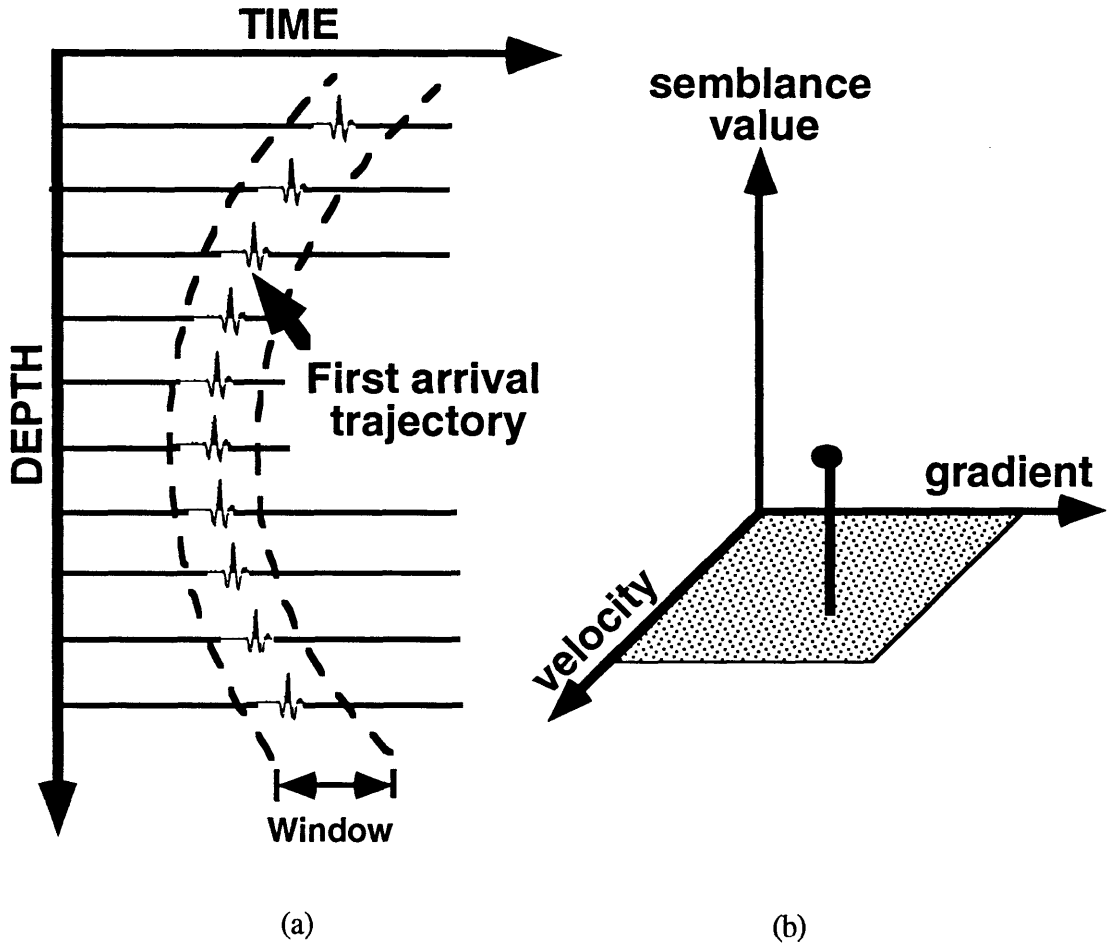
FIG. 4.2. Semblance analysis along the traveltime trajectory of first arrivals. (a) Semblance values are calculated within a time window along each trajectory calculated by guessing all velocities. (b) The largest semblance value is picked to give the best-fit velocity.

where, i - the ith seismic trace;

     $t(i)$ - the traveltime corresponding to the ith trace;

     $f_{i,t}$ - the amplitude of the ith trace at time $t(i)$ within window $[-\Delta t, \Delta t]$; and

     N - the total number of traces involved.

Therefore, the semblance value can be found from:

$$S_c = \frac{E_{out}}{N\,E_{in}}\ , \qquad 0 \le S_c \le 1 \ .$$ (4.9)

Semblance values provide a criterion for determining whether a theoretically derived traveltime curve best fits the first-arrival trajectory of the real data, and further determining whether the velocity function is the best one. The larger the semblance value, the more coherent the first arrival event of the data that has been scanned, and therefore, the better the velocity function. Accordingly, velocity parameters that correspond to the largest semblance value are selected.

4.3.2   Algorithm implementation

The algorithm has been implemented on a workstation. Shown in Figure 4.3 is the computational procedure, which is composed of the following parts:

- Enter crosswell geometry;
- Input a data gather (common source or common receiver);
- Scan through a range of κ and V_0 values;

> Calculate the traveltime, $t(i)$, for every trace i;
>
> Stack amplitudes along the calculated traveltime trajectory, within a given window $[-\Delta t, \Delta t]$;
>
> Calculate semblance value;

- Pick the velocity with largest semblance value;
- Repeat the whole procedure for a new gather from a different depth aperture, and find a new velocity function until all gathers are processed.
- Extract the final interval velocity distribution by fitting all velocity functions obtained from different depth apertures.
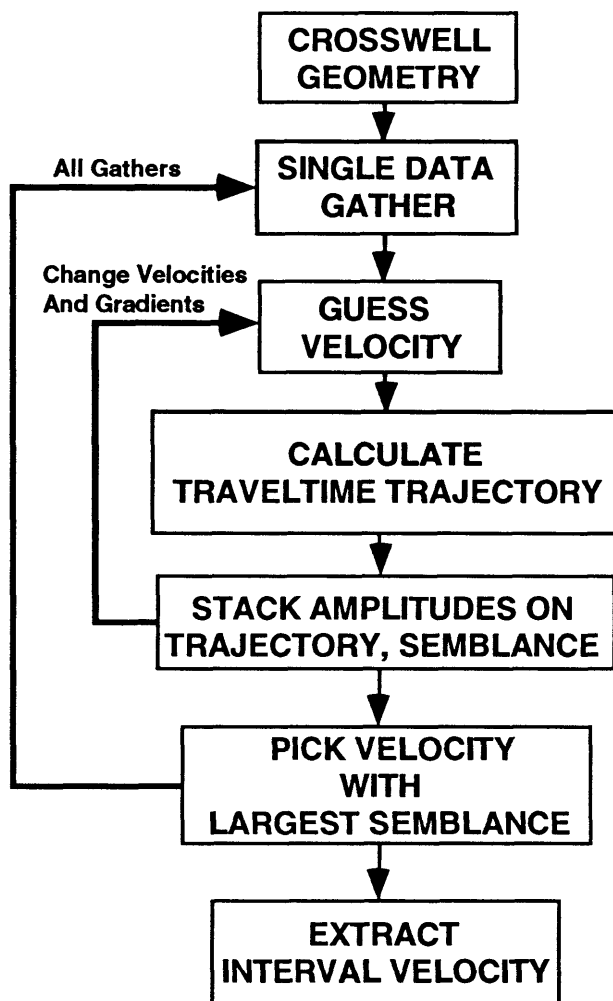
FIG. 4.3. Procedure of automatic velocity analysis for crosswell seismic data.

4.4   Tests

4.4.1 Synthetic data

Synthetic crosswell seismic data used to test the method were generated with the ray tracing program Uniseis® on the Landmark workstation. The geologic model is

shown in Figure 4.4. It is composed of 71 horizontal layers with equal thickness (20 m).
Velocity distribution in this model obeys the following linear velocity-depth relationship:

$$V = 2000 + 0.8z \quad \text{(m/s)} , \qquad\qquad (4.10)$$

but in each individual layer the velocity is constant and takes the value calculated using
Eq. (4.10) in the middle of the layer. The source was fired at various depths. Receiver
depths range from 0 m to 1200 m. So each shot gather contains 121 seismic traces. Only
rays for direct arrivals were traced. Zero-phase Ricker wavelets were used. The wavelets
were 60 ms long and had a center frequency of 40 Hz (The center frequency of a Ricker
wavelet is the frequency corresponding to the peak amplitude value in the frequency
spectrum).

Shown in Figure 4.5 is a shot gather corresponding to the source depth of 500 m,
with first arrivals displayed. Theoretical traveltimes were calculated for the first arrivals
in this gather, using equations (4.4)-(4.6). They are shown in Figure 4.6a. Their
comparison with traveltimes measured on the synthetic section (Figure 4.5) is given in
Figure 4.6b. The traveltime trajectory in Figure 4.5 has a quasi-hyperbolic shape, which
is observable on real crosswell data. Figure 4.6b reveals that the difference between the
theoretical and the ray-traced traveltimes is very small (the maximum absolute
differential time is around 3 ms), indicating that the traveltime equations I derived
provide sufficient precision. This implies that if the correct velocity is used, the
traveltime trajectory on real crosswell data can be approximated with high precision.
This provides the basis for the automatic velocity analysis.

To run the automatic velocity analysis, crosswell parameters for a shot gather
must be provided. A wide range of initial velocities and of velocity gradients is scanned
for the best selection which agrees with the largest semblance value.
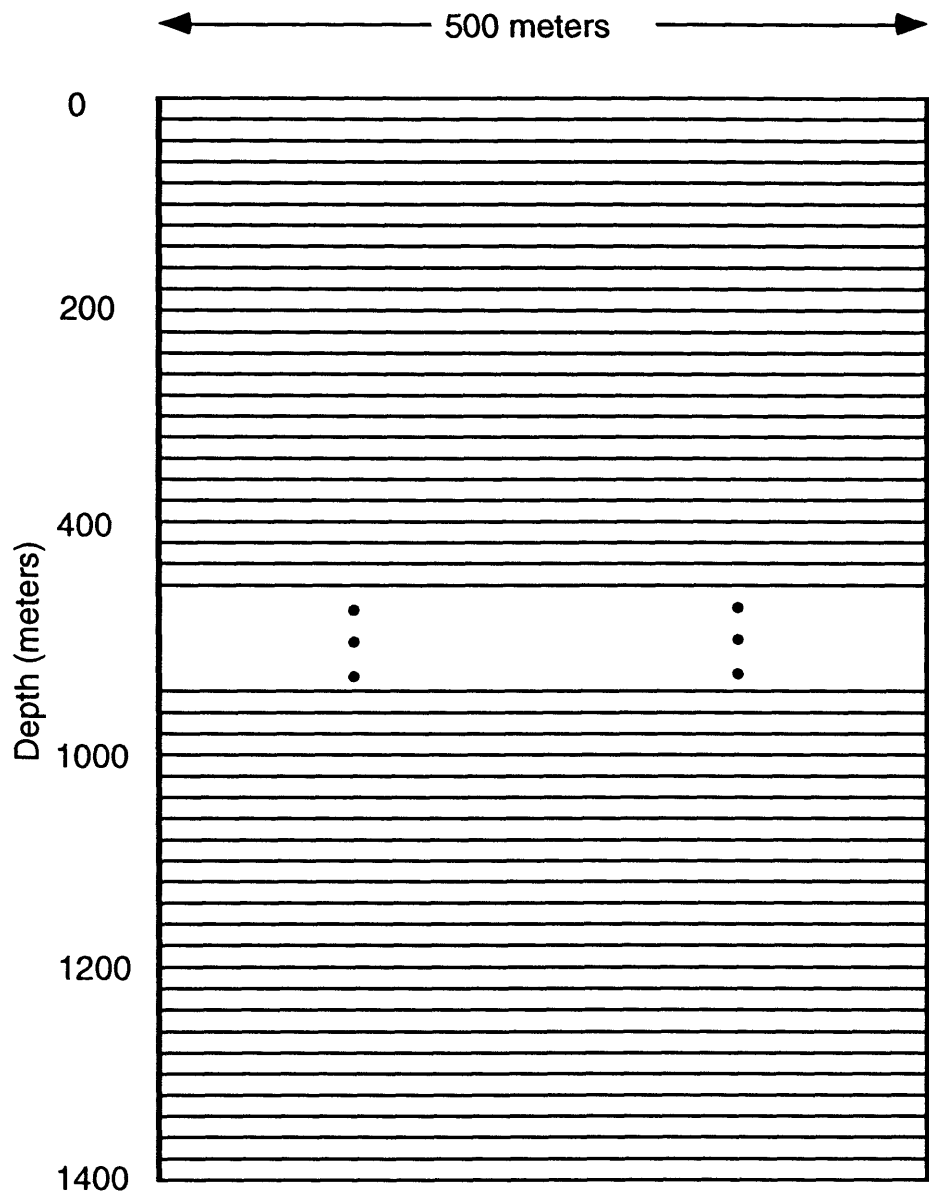
FIG. 4.4. Layered model used to generate synthetic crosswell seismic data. Each layer has the same thickness. Velocities in all layers satisfy a linear velocity-depth relationship: $V = 2000 + 0.8\,z$ (m/s).

Receiver depth (meters)
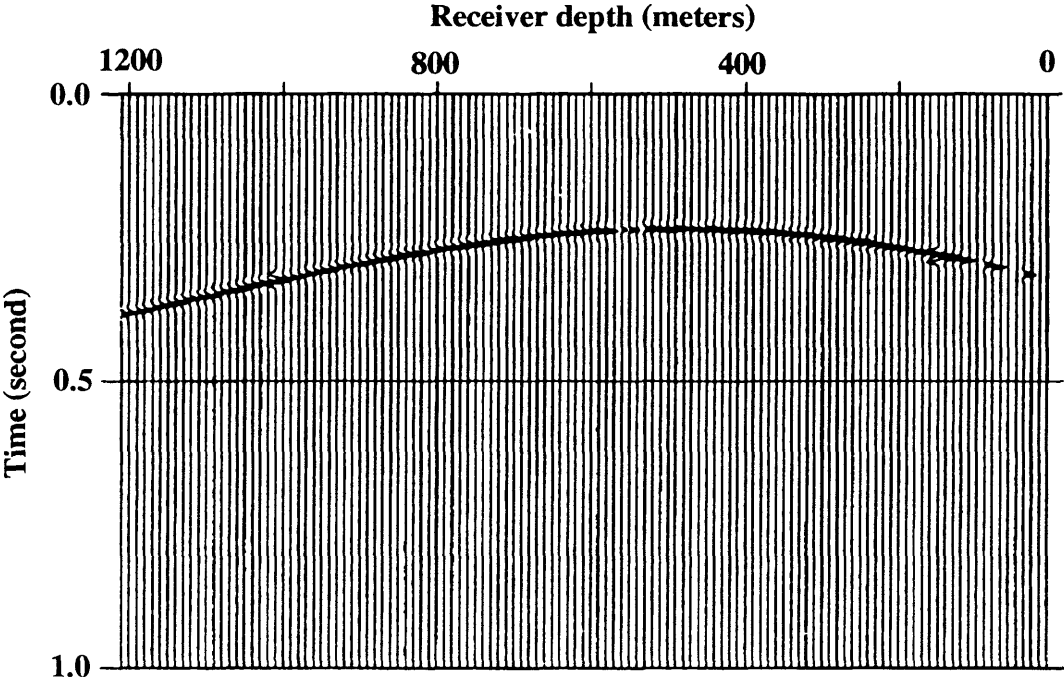
FIG. 4.5. Hyperbolic first-arrival event in a synthetic crosswell shot gather for source depth of 500 m.

For the synthetic data, I scanned for the best velocity from 1900 m/s to 2100 m/s (at intervals of 10 m/s) and for the best gradient from 0.5 m/s/m to 1.1 m/s/m (at intervals of 0.05 m/s/m). A time window equal to the width of the Ricker wavelet was used for semblance analysis. The results of semblance analysis were contoured for the ease of picking the largest values. Figure 4.7 shows the results of semblance analysis for two shot gathers. The source depths are 260 m and 500 m, respectively. In both cases, the largest semblance value appears around the point for an initial velocity of 2000 m/s and a velocity gradient of 0.8 m/s/m. The largest velocity error that can be seen is about 10 m/s. Therefore the velocity analysis has derived accurate velocity information close to that used in the geologic model.

61

THEORETICAL TRAVELTIME

DIFFERENTIAL TRAVELTIME
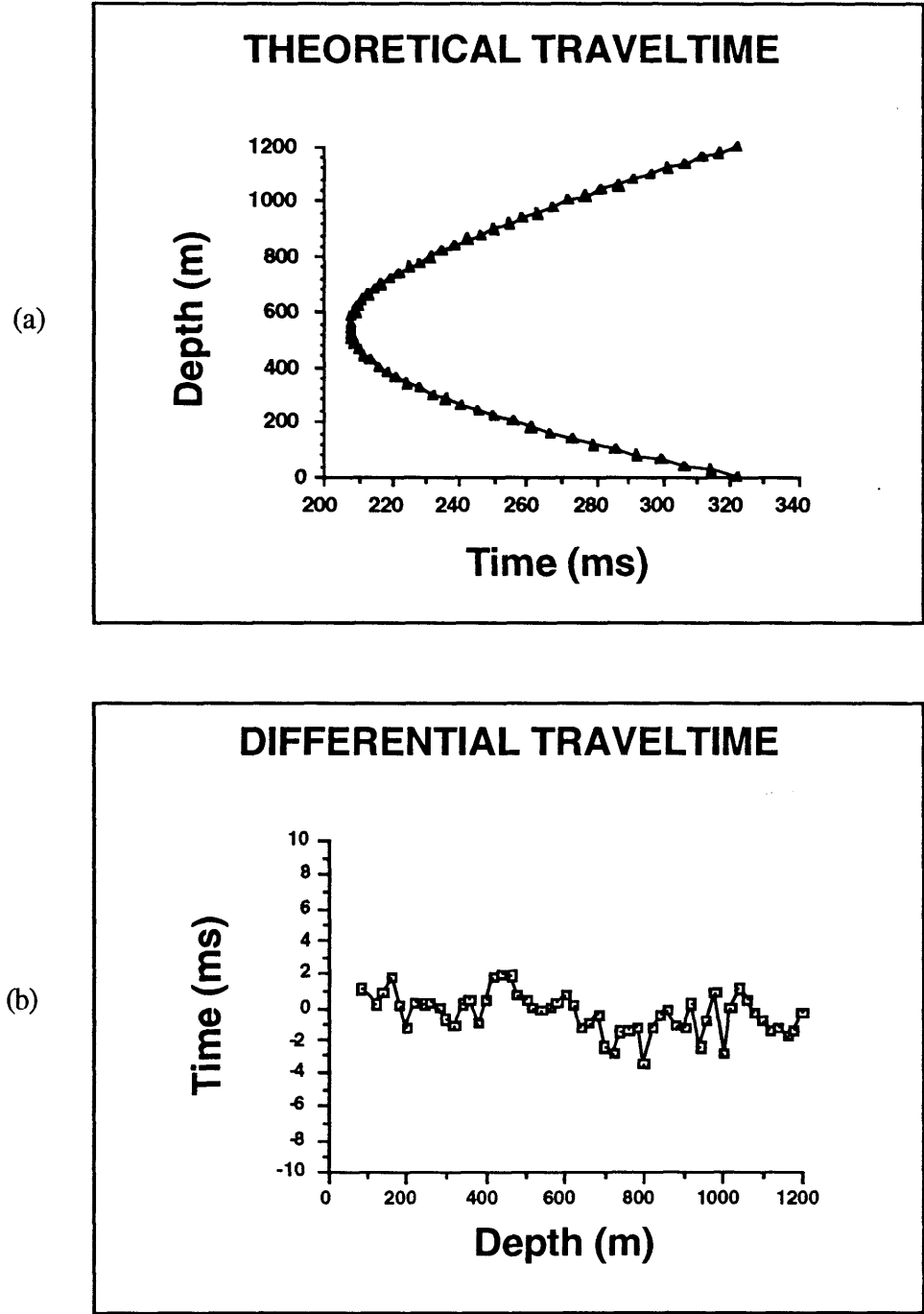
FIG. 4.6. (a) Theoretically calculated traveltimes. (b) Traveltime difference between the theoretical and ray-traced first arrival trajectories. The source depth is 500 m.
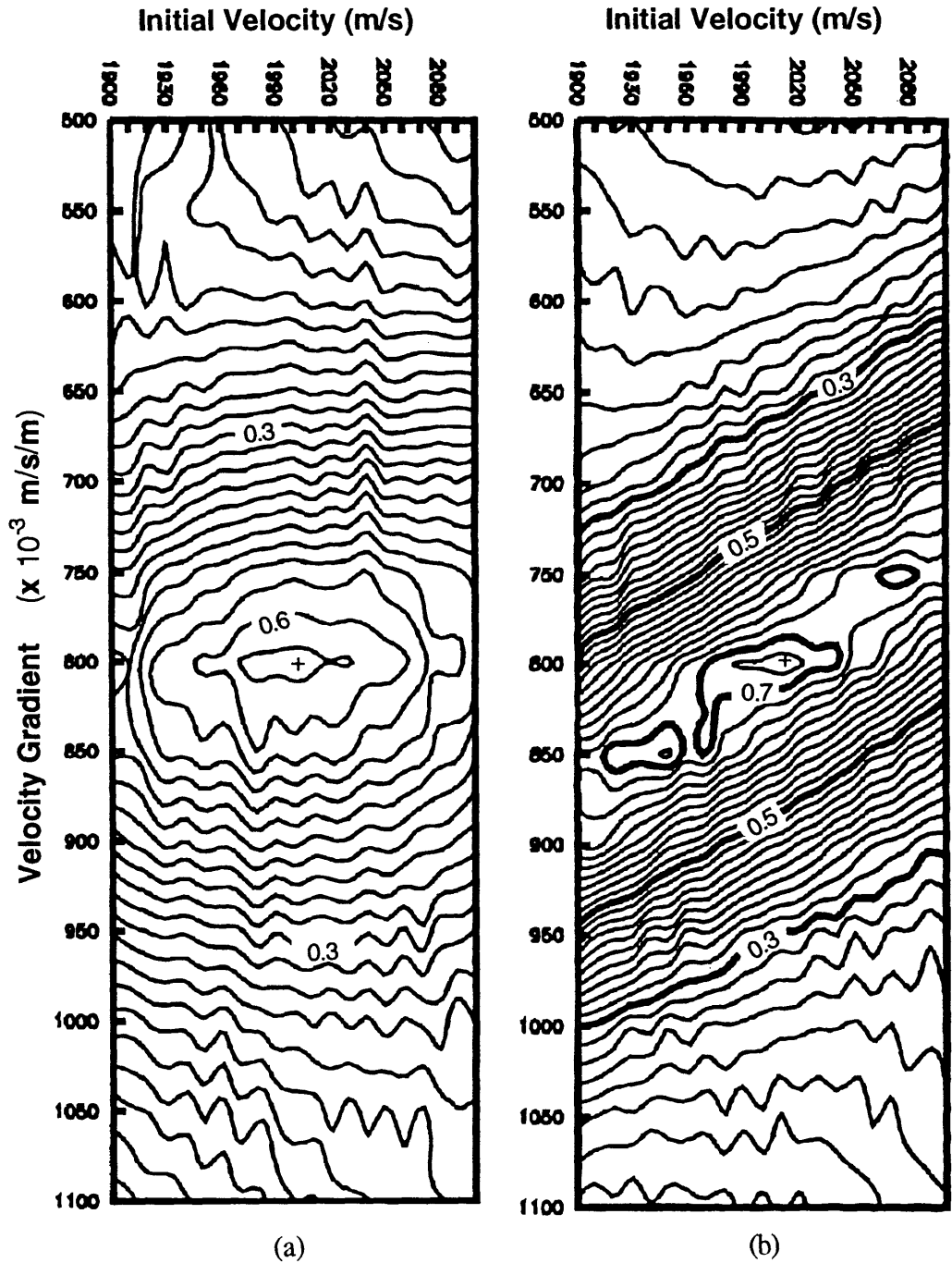
FIG. 4.7. Semblance analysis results. (a) Source depth 500 m: the largest semblance appears at a velocity of 2000 m/s and a gradient of 0.8 m/s/m. (b) Source depth 260 m: for a velocity of 2010 m/s and a gradient of 0.8 m/s/m, the semblance value is a maximum. The numbers annotated in the maps are contour intervals.

4.4.2 Physical model data

The physical model data used are from an ultrasonic borehole seismic modeling experiment accomplished by Stewart and Cheadle (1989) at the University of Calgary. Forty crosswell shot gathers, each having 40 traces, were collected in a geometry where ultrasonic source and receiver transducers were deployed along the two sides of a target model (a Teflon cylinder 3.81 cm in diameter) located in a water tank. Source spacing and receiver spacing were 50 m, and the well separation was 600 m, both scaled at a factor of 5000. One shot record with a source depth of 1000 m is shown in Figure 4.8. Note that the direct arrivals in the middle of Figure 4.8 are pulled down because the velocity of the Teflon model is lower than that of the surrounding water.

The automatic velocity analysis method was applied to three gathers for source depths of 0 m, 450 m, and 1000 m, in order to see whether or not the background velocity (that is, water velocity which is around 1490 m/s) can be inverted from direct arrivals. The guessed initial velocities range from 1000 m/s to 1800 m/s at intervals of 20 m/s. The velocity gradient was guessed between 0.00001 m/s/m and 0.01 m/s/m. The width of the wavelet, which was used for the velocity analysis window, is 30 ms.

Figure 4.9 shows the semblance analysis result for the data in Figure 4.8. The contoured values are distributed in a long and narrow zone centered at 1520 m/s. Within this zone, there are two areas with higher semblance values: one is below the gradient value of about 0.001 m/s/m, and the other above 0.005 m/s/m. The possibly picked initial velocity is 1520 m/s, 2.0% higher than the real velocity of 1490 m/s. For this constant-velocity-medium case, the semblance provides a gradient value that can be picked in a wide range, indicating that the velocity analysis method is not very sensitive to the gradient value approaching zero. The velocity gradient of 0.0065 m/s/m, corresponding to the largest semblance value, causes a velocity change of 13 m/s over a depth aperture of 2000 m. The velocity variation caused by this velocity gradient is negligible.

Receiver Depth (m)
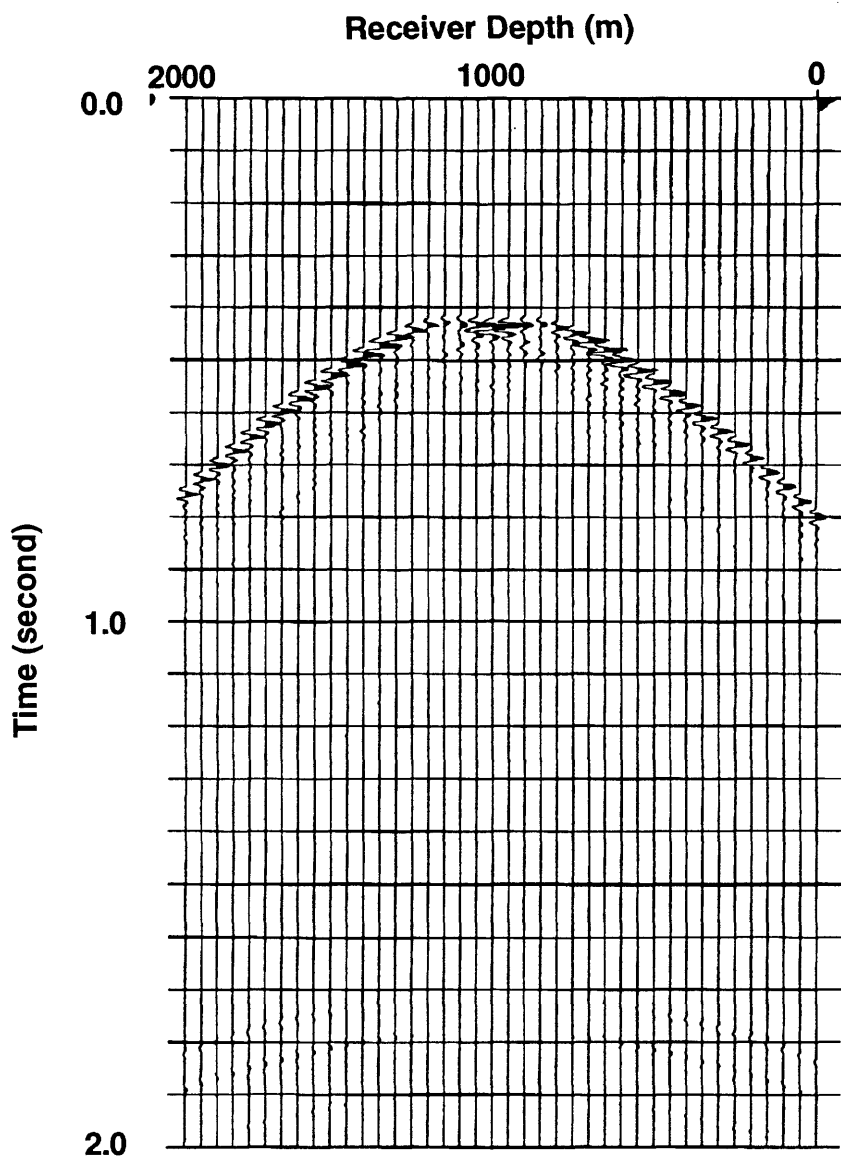
FIG. 4.8.   Shot record from an ultrasonic crosswell seismic modeling experiment in a water tank (Stewart and Cheadle, 1989). Source depth is 1000 m.
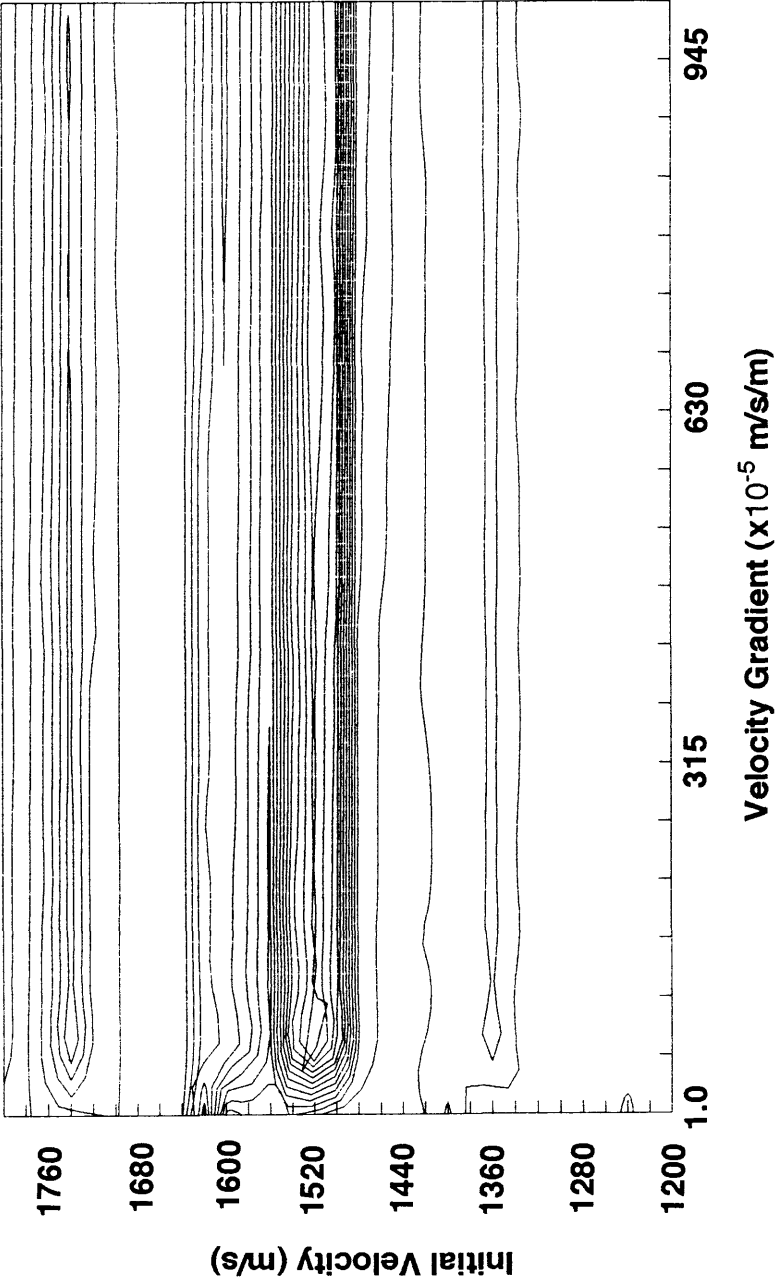
FIG. 4.9. Semblance analysis result for physical model crosswell data shown in Figure 4.8. The contoured semblance values are centered about the velocity of 1520 m/s, which may be picked as the initial velocity inverted for. The velocity gradient can be picked in a wide range in this case.

4.4.3 Field data

The field crosswell seismic data used for velocity analysis is shown in Figure 4.10. This gather is composed of 113 traces, representing a depth aperture of 300 ft (91.4 m) to 2540 ft (774.2 m). The receiver is at a depth of 1500 ft (457.2 m). Well-to-well separation is 815 ft (248.4 m). The data were sampled at a 0.25 ms interval. The P-wave direct arrival, denoted D, has a quasi-hyperbolic traveltime trajectory. It is not a symmetric hyperbola though, indicating a velocity variation with depth.

The automatic velocity analysis program searches for the optimal velocity in the given depth aperture by scanning a velocity range between 4900 ft/s (1493.5 m/s) and 16,500 ft/s (5029.2 m/s) [interval 200 ft/s (61.0 m/s)] and a gradient range from 0.045 ft/s/ft to 2.0 ft/s/ft (interval 0.1 ft/s/ft). A 14-ms time window (approximate to the wavelet width) was used to scan the traces around the direct arrival. Figure 4.11 displays the velocity analysis result. The initial velocity of 6100 ft/s (1859.3 m/s) and gradient of 0.145 ft/s/ft are picked, which correspond to the largest semblance value. From these values, the velocity field within the depth aperture of 300 ft (91.4 m) to 2540 ft (774.2 m) changes from 6143.5 ft/s (1872.5 m/s) to 6468.3 ft/s (1971.5 m/s), which appear to be reasonable for this depth aperture. Unfortunately, there is no detailed information about the velocity in this area available.

4.5   Discussion

This estimation procedure may have a non-unique answer. For example, in Figure 4.7b, there are several local highs along the central narrow belt in the semblance map. These local highs are very close in values to the one that was picked, making interpretation ambiguous. This problem arises because the combination of a smaller
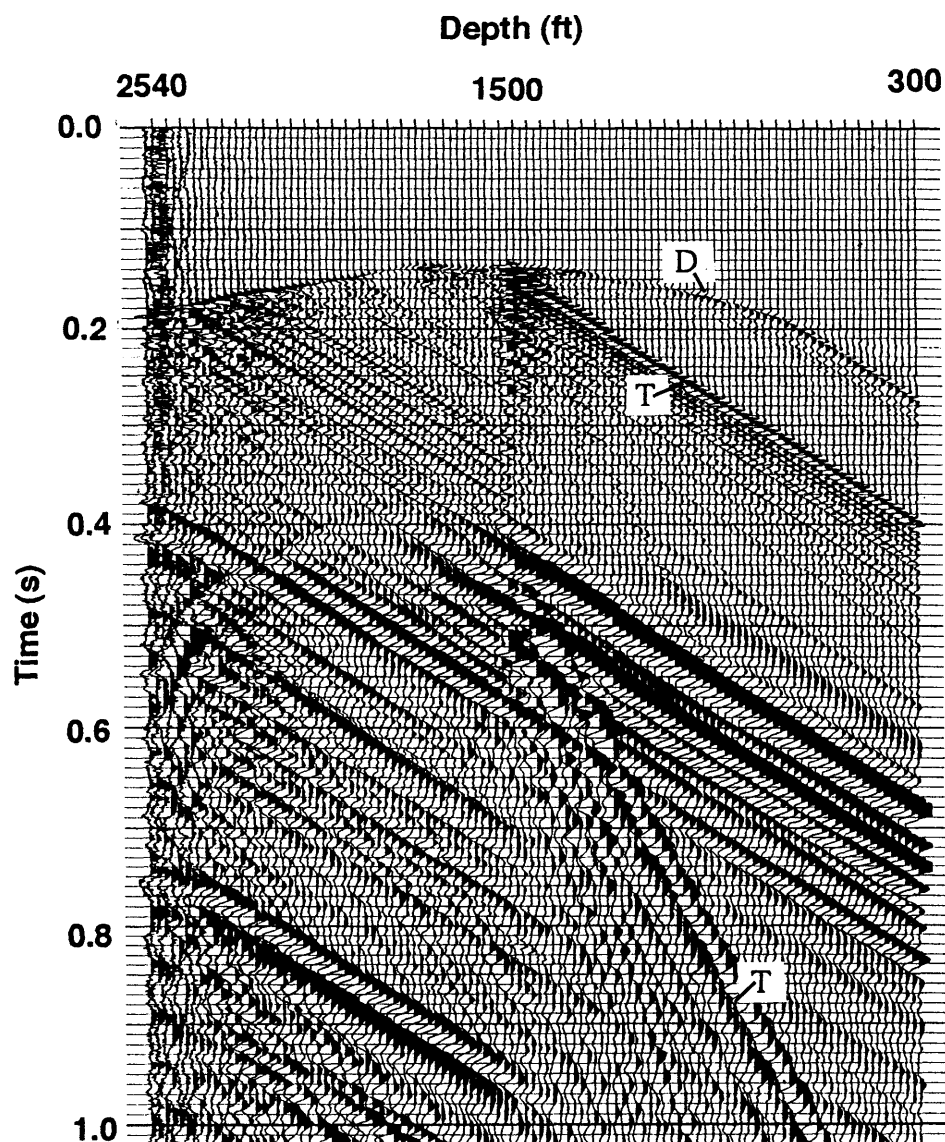
FIG. 4.10. Common-receiver gather of vertical component crosswell data, Humble, Texas. The air gun was shot in *K22* from 300 ft (91.4 m) to 2540 ft (774.2 m). The geophone was located in *C30*, 1500 ft (457.2 m) deep. The offset between the wells was 815 ft (248.4 m). *D* represents the *P*-wave first arrivals. *T* is tube waves.

68
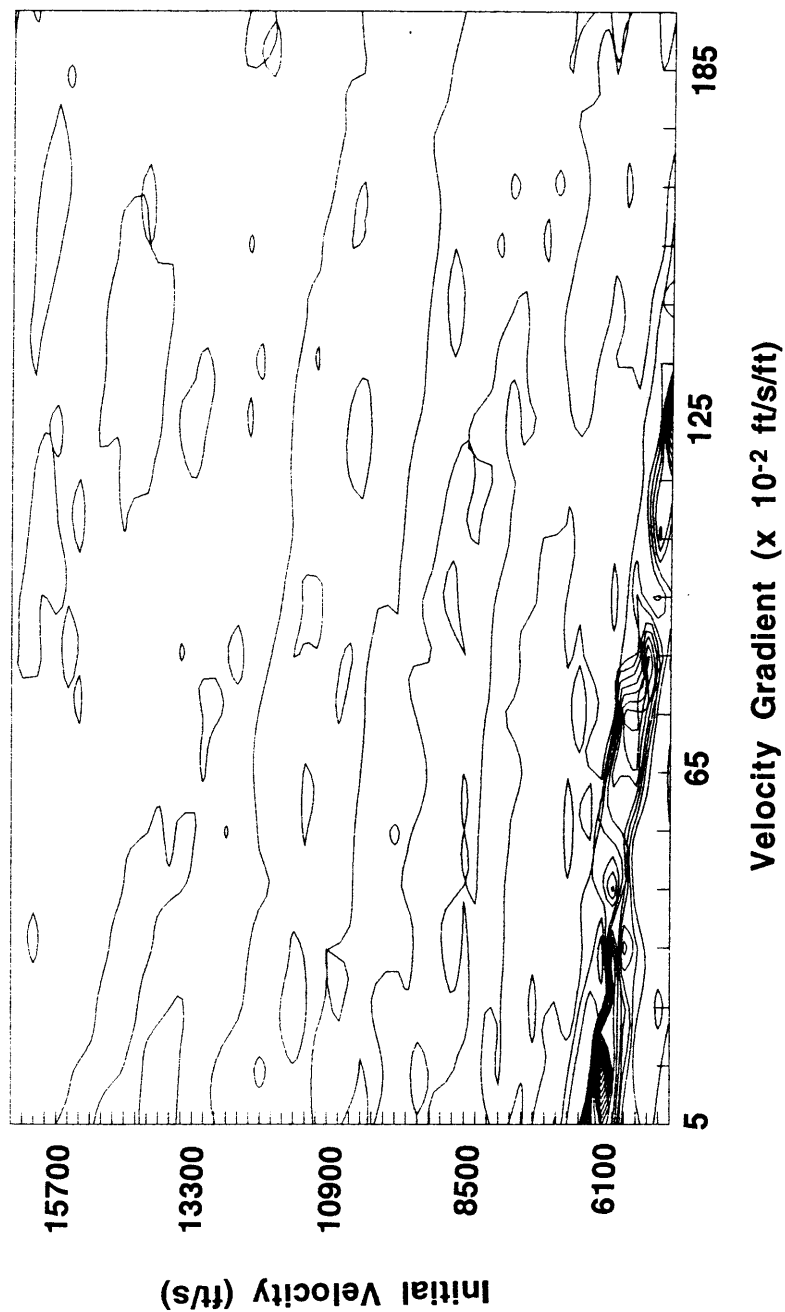
FIG. 4.11. Semblance analysis result for field crosswell data shown in Figure 4.10. The largest semblance value appears at the velocity of 6100 ft/s (1859.3 m/s) and gradient of 0.145 ft/s/ft (or m/s/m).

initial velocity and a larger gradient, or a larger initial velocity and a smaller gradient, could produce a similar result as does the combination of the correct initial velocity and gradient. Therefore, precaution must be taken in interpreting the inversion results.

Prior to velocity analysis, bandpass filtering the crosswell data to remove noise is useful. This is because noise within the given analysis window may affect the values of semblance computed. The width of the velocity analysis window is an important factor. It is found that the window close to the width of a wavelet will yield a better inversion results. It may be useful to shape the wavelets in the data such that wavelets are consistent among the traces.

Patching together various apertures should be possible to allow different velocity gradient regions. The case of negative velocity gradients, a case that may exist in some areas, is not discussed in this chapter. But it is not difficult to generalize the approach presented. For the case of deviated wells, it is feasible mathematically to generalize the method. This velocity analysis method can also be used for analyzing S-wave data.

4.6   Summary

An automatic technique has been proposed in this chapter to derive the background velocity information from crosswell first arrival traveltimes. Without having to pick the first arrivals by hand, this method computes semblance values from trace data in a searching window around the first-arrival trajectory calculated according to the theory assuming a linear velocity-depth relationship. Based on the largest semblance value, the initial velocity and gradient are picked, which form a linear velocity function. This method has been tested with a number of crosswell data gathers. The results are encouraging.

Chapter 5

Crosswell reflection imaging: Fundamental concepts and methods

5.1   Introduction

Recently, there has been considerable interest in crosswell reflection imaging. Two types of techniques, Xwell-CDP mapping (Baker and Harris, 1984; Iverson, 1988; Khalil et al., 1993) and prestack migration (Hu et al., 1988; Qin and Schuster, 1993; Zhou and Qin, 1993), have been used. In addition, Stewart et al. (1991) and Stewart and Marchisio (1991) recently proposed processing crosswell data like CDP data and developed a new crosswell processing technique, based on common mid-depth (CMD), to produce a stacked section from multi-fold crosswell data. Some of these concepts were expanded by Li and Stewart (1992).

In this chapter, fundamental concepts used in this new imaging method will be reviewed in detail. Some processing issues will be stressed. Two data domains, common-interval (CI) gather and CMD gather, are used in data processing, in addition to the traditional common-source (CS) gather and common-receiver (CR) gather. A mathematical description of these gathers will be given in this chapter. I will also discuss several

important processing steps such as direct-arrival removal, reflection-wavefield separation, velocity analysis, vertical and horizontal moveout corrections, and common-reflection-bin stacking. The important concepts and steps will be demonstrated with synthetic data. A thorough processing flow will be proposed in the summary of this chapter.

5.2   Synthetic crosswell data

To present the fundamental concepts of crosswell reflection imaging, synthetic data were generated with the Uniseis® modeling package from a simplified model shown in Figure 5.1. A constant-velocity medium, 2250 m/s with changing density, is assumed. The model consists of five flat homogeneous layers with different thicknesses and is surrounded by the free surface at the top and, at the bottom, by an infinitely thick layer that has the same velocity but a different density. This simple geology in the model gives 6 reflecting interfaces, denoted by symbols *L1* to *L6* in the Figure. The reflection from the free surface is labeled as *L1*, while reflections from the top and bottom of the zone of interest (shadowed in the Figure) are marked as *L3* and *L4*, respectively. The target horizon *L3*, at a depth of 416.5 m, is to be imaged with crosswell reflections.

The crosswell geometry used is also shown in Figure 5.1. A well-to-well distance (offset) of 55 m was used. Fifty-one sources were shot in one well at depths of between 150 m and 450 m, spaced at 6 m. In another well, receivers were positioned from 150 m to 450 m at intervals of 3 m. A 100-Hz zero-phase Ricker wavelet was used in generating seismic traces, and only *P*-wave primary reflections and direct arrivals were simulated. The record length was 600 ms with a sample interval of 1 ms.

A total of 51 shot gathers were recorded, each having 101 traces. Figure 5.2 shows two typical common-source gathers corresponding to depths of 240 m and 360
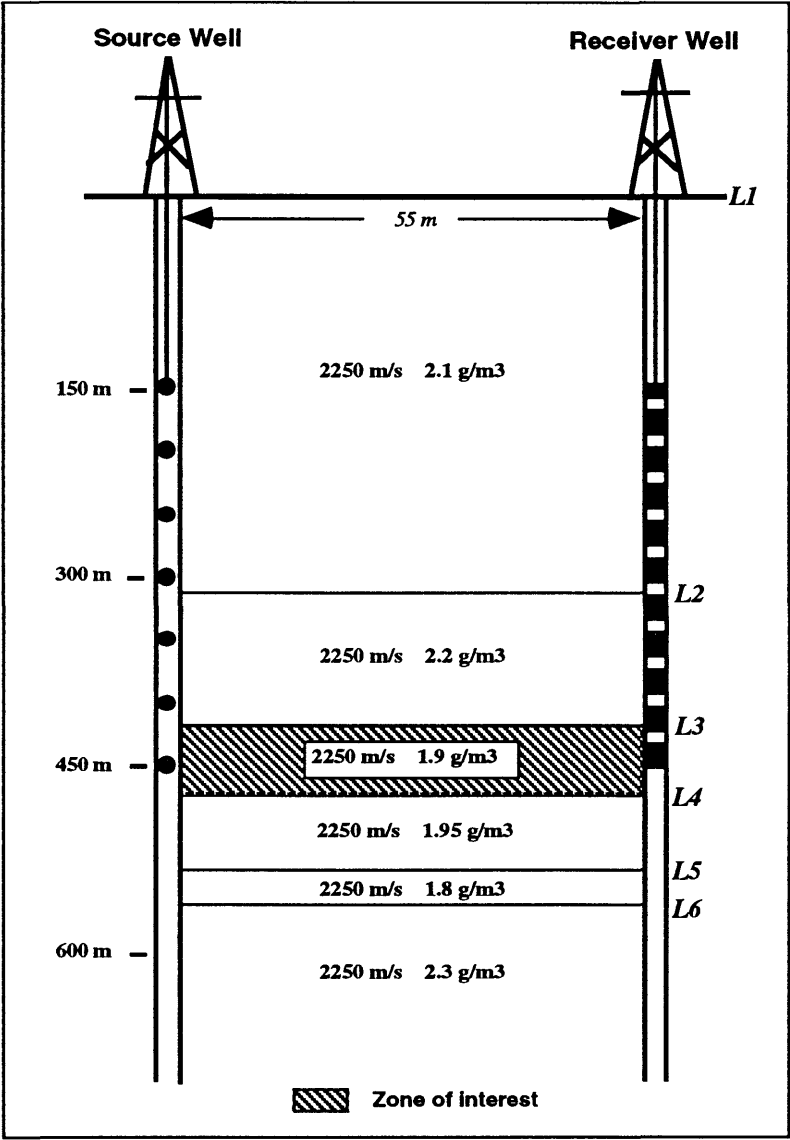
FIG. 5.1. Crosswell survey geometry and Earth model used to generate synthetic crosswell seismic data. Separation between boreholes is 55 m. The source is shot from 150 m to 450 m, spaced at 6 m, while geophones are deployed between 150 m and 450 m, at intervals of 3 m. Six reflectors, from the top to the bottom, are numbered *L1* to *L6*, respectively. The target zone is the shadowed layer, bounded by horizons *L3* and *L4*. Its top (*L3*), at a depth of 416.5 m, is to be imaged.

73
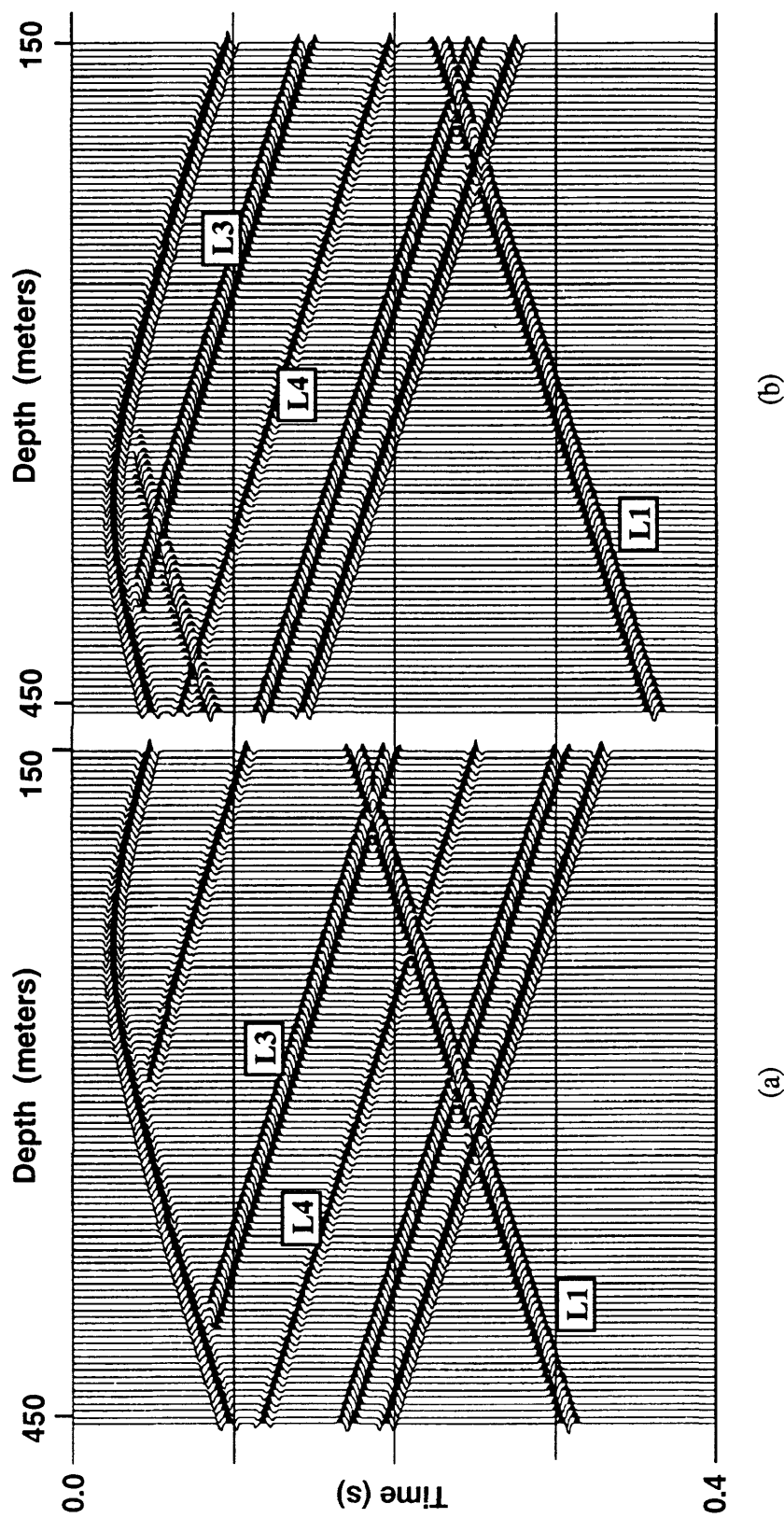
FIG. 5.2. Common-source gathers generated from the crosswell geometry in Figure 5.1. The source depths are (a) 240 m and (b) 360 m, respectively. Each gather has 101 traces, representing receiver depths from 150 m to 450 m at intervals of 3 m. Events such as *L3* and *L4* are upgoing reflections, while events like *L1* are downgoing reflections. The hyperbolic event is the direct arrival. *L1* is a reflection from the top horizon, *L3* and *L4* are reflections from the top and bottom of the shadowed zone in Figure 5.1.

m, respectively. Only 0.4 seconds of data are displayed. In the Figure, a few reflections are marked. A hyperbolic direct arrival and a number of nearly linear reflections can be seen. The downgoing reflections have a down-to-left moveout whereas the upgoing reflections exhibit a down-to-right pattern. All of the 51 shot gathers were used in data processing and the results will be demonstrated in the following sections.

5.3 Data sorting domains

Figure 5.3 shows a basic relationship among all elements existing in a typical crosswell geometry. Suppose the source S is located at depth s, the receiver G at depth g, and the wells offset by x. There is a representative flat reflector at depth r in a constant-velocity (V) medium. Two relations can be derived from Figure 5.3.

In the crosswell case, traveltime for a reflected wave can be expressed as a function of variables s, g, and r:

$$t = t(s, g, r) = \frac{1}{V} \sqrt{[(r-s) + (r-g)]^2 + x^2} \quad . \tag{5.1}$$

In the above expression, x is constant. Equation (5.1) is valid for both upgoing and downgoing reflections. For a direct wave, the traveltime is determined by

$$t = t(s, g) = \frac{1}{V} \sqrt{(s-g)^2 + x^2} \quad . \tag{5.2}$$

It is independent of the reflector depth r. It will be seen later that equations (5.1) and (5.2) constitute the basis for crosswell data sorting.
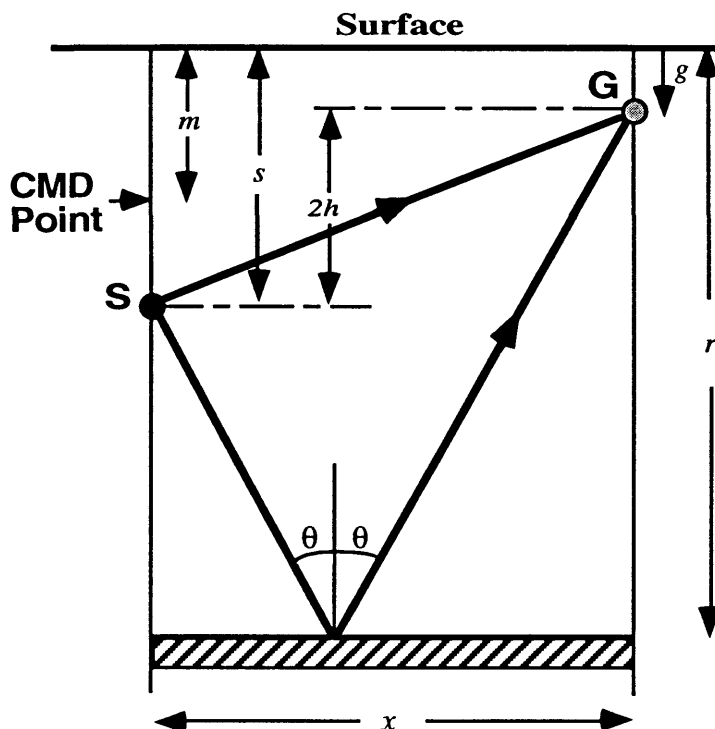
FIG. 5.3. Relationship among the coordinates used in crosswell geometry. s is source depth, g is receiver depth, and x is well separation. The common mid-depth (CMD) is given by $m = (s + g)/2$, and common interval by $2h = (s - g)$.

One characteristic of the new crosswell reflection imaging procedure is the use of various coordinate domains to sort seismic trace data. In seismic terminology, such a domain is also called a gather. Four types of gathers, CS, CR, CI, and CMD, will be described below in mathematical terms. A common-interval gather is also known as a common-offset gather. These gathers are schematically shown in Figure 5.4.

5.3.1 Common-source gather

A CS gather is a collection of seismic traces that originate from the same source location but are recorded at various receivers. In equation (5.1), variable s now is a

Common Source

Common Receiver

Common Interval

Common Mid-Depth

● **Source**   ■ **Receiver**
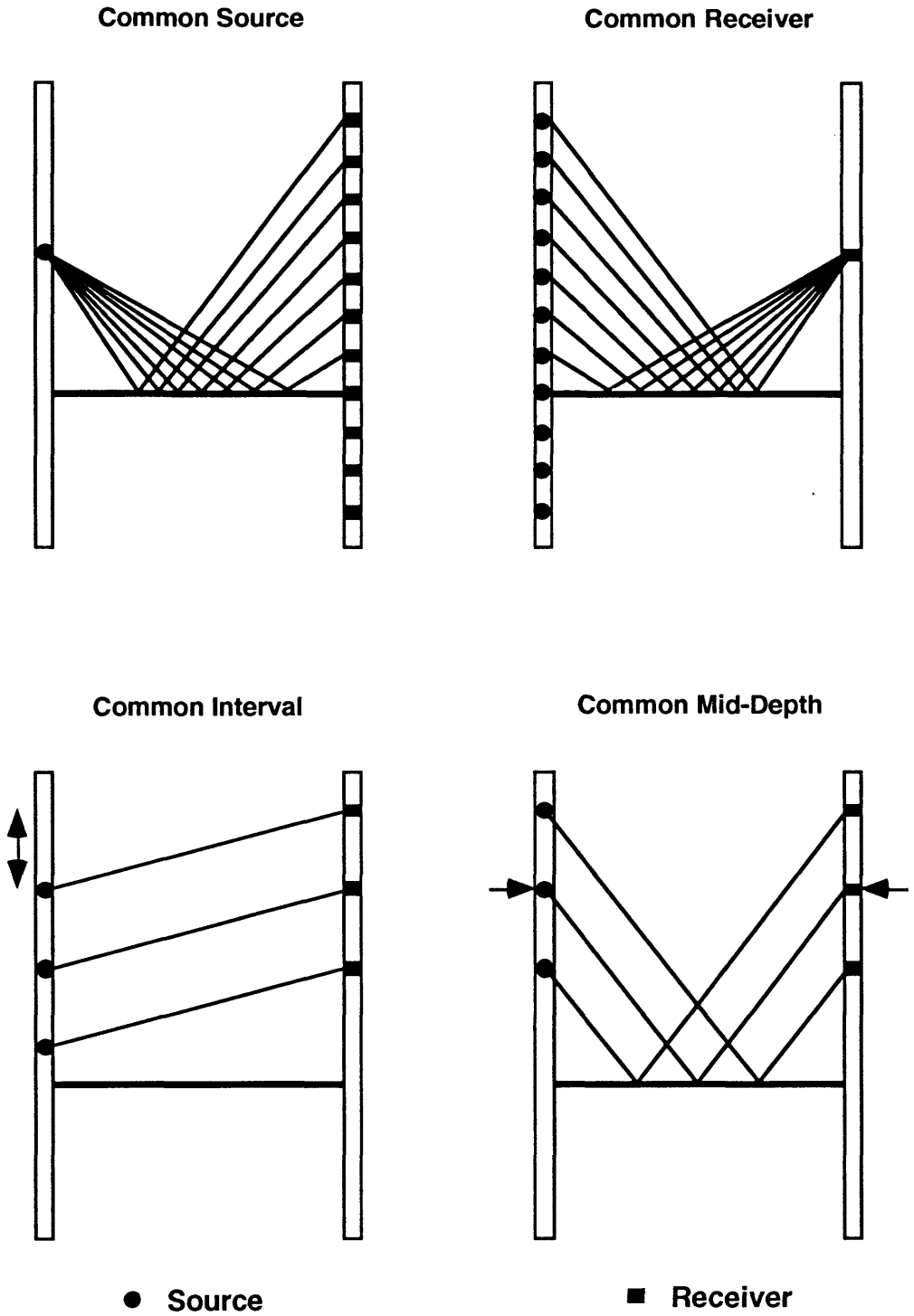
FIG. 5.4. Domains of sorting crosswell seismic data (after Stewart, 1991).

constant. Assuming a known reflector depth r, the reflection time is a function of receiver depth g only. That is,

$$t = t(g) = \frac{1}{V} \sqrt{(u - g)^2 + x^2} \quad , \tag{5.3}$$

where $u = 2r - s$ is a constant. Equation (5.3) can be rewritten as

$$\frac{t^2}{\left(\frac{x}{V}\right)^2} - \frac{(g - u)^2}{x^2} = 1 \quad . \tag{5.4}$$

It describes a hyperbolic curve in the (t, g) plane. So equation (5.4) suggests that reflections in a CS gather have a hyperbolic shape, whose apex is at $(x/V, \pm u)$ in the (t, g) domain ($\pm u$ are respectively for upgoing and downgoing reflections).

For direct arrivals, equation (5.2) becomes

$$\frac{t^2}{\left(\frac{x}{V}\right)^2} - \frac{(g - s)^2}{x^2} = 1 \quad , \tag{5.5}$$

which is also a hyperbola, with its apex at $(x/V, s)$.

Synthetic examples of crosswell CS gathers were shown in Figure 5.2. Although the direct arrival is an obvious hyperbola, the reflections appear to be linear (see events L1, L3, and L4, for example). This is because the reflections shown are only from the small portion of a large hyperbola, whose apex is far beyond the depth range displayed.

In CS gathers, reflections often have larger moveout than direct arrivals, a useful characteristic that has been exploited in separating direct waves from reflections by velocity filtering (Abdalla et al., 1990). However, applying a velocity filter in CS gathers to suppress direct arrivals sometimes may cause damages to reflections. Figure 5.5 shows

such a case. There are two reflections below the hyperbolic direct-arrival event: the downgoing reflection *L2* and the upgoing reflection *L3*. Note that, above the source depth, reflection *L3* has a moveout similar to that of the direct arrivals. It has been found (Iverson, 1988; and Pratt and Goulty, 1991) that this effect often occurs when both the source and the receiver are on the same side of the reflector and the receiver is farther away from the reflector than the source is, as indicated in Figure 5.5.

Applying a velocity filter to remove the direct arrivals from the CS gather in Figure 5.5 would affect not only the direct arrivals but also the reflections with similar moveout, such as event *L3*, therefore resulting in a greatly damaged reflection wavefield. A remedy to overcome this problem is to use common-interval gathers.

5.3.2 Common-receiver gather

Similarly, a CR gather is a collection of traces which are from different source locations but recorded at the same receiver. In this case,

$$u = 2r - g \quad , \tag{5.6}$$

is a constant. So equation (5.1) becomes

$$t = t(s) = \frac{1}{V} \sqrt{(u - s)^2 + x^2} \quad . \tag{5.7}$$

This equation can be rewritten in the form of a hyperbolic equation:

$$\frac{t^2}{\left(\frac{x}{V}\right)^2} - \frac{(s - u)^2}{x^2} = 1 \quad . \tag{5.8}$$

Therefore, the reflection in a CR gather is also a hyperbolic event whose apex is at
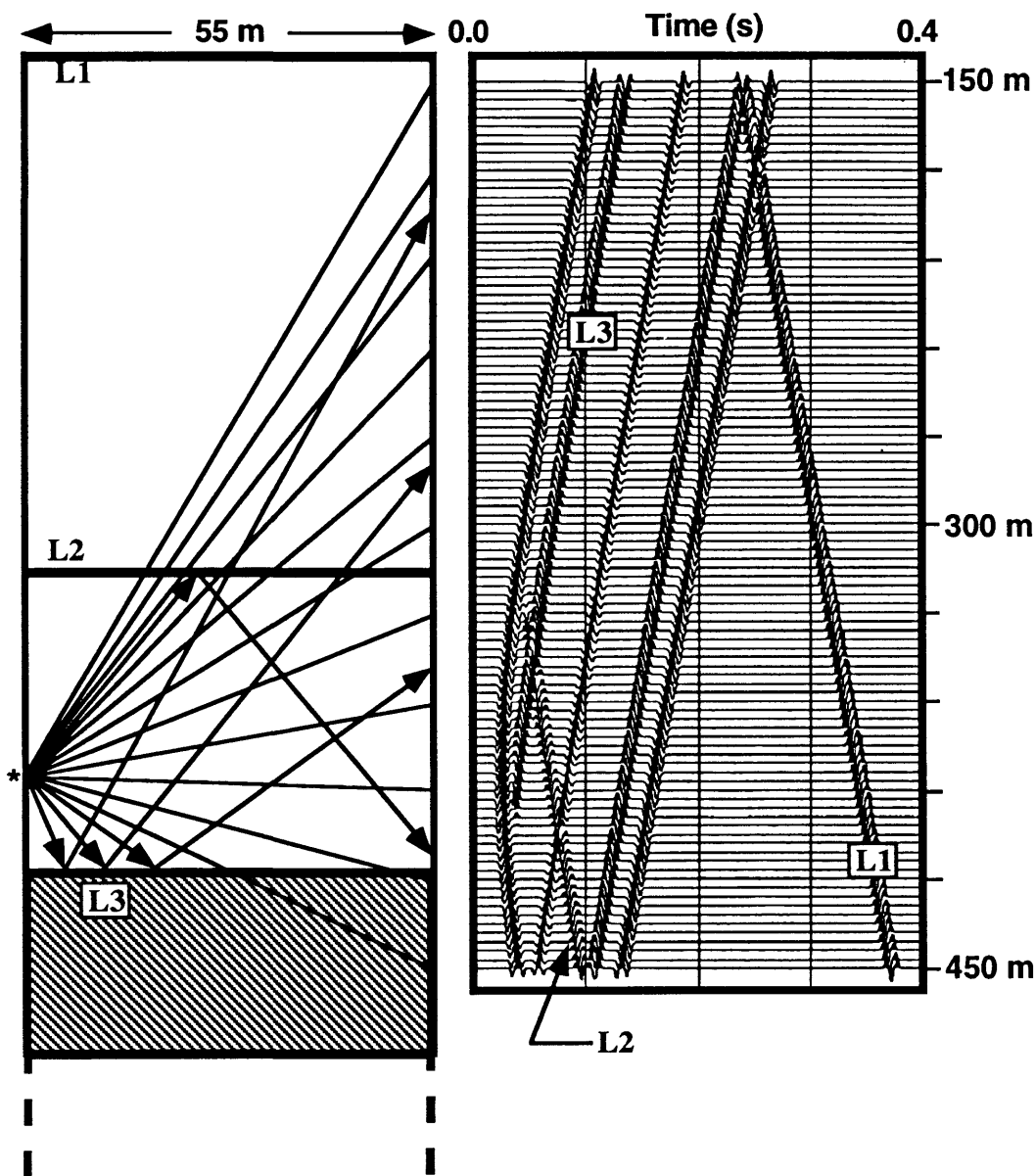
FIG. 5.5. When both source and receiver are on the same side of the reflector, and when the receiver is farther away from the reflector than the source, part of the hyperbolic direct wave will have a moveout similar to those of reflection events such as L3. In this case, applying velocity filters to remove the direct wave would damage the reflections.

$(x/V, \pm u)$ in the (t, s) domain.

Direct arrivals in a CR gather are hyperbolic as well, and described by

$$\frac{t^2}{\left(\frac{x}{V}\right)^2} - \frac{(s-g)^2}{x^2} = 1 \quad . \tag{5.9}$$

Characteristics of CR gathers are shown in Figure 5.6, where three synthetic CR gathers are displayed. The receiver depths are 150 m in (a), 312 m in (b), and 387 m in (c). Each gather has 51 traces. The reflections that ought to be hyperbolic are almost linear, for the same reason as given before for CS gathers.

In early crosswell work (Baker and Harris, 1984; Abdalla et al., 1990), CS gathers or CR gathers are the only data domain used for reflection imaging.

5.3.3 Common-interval gather

CI gathering is a new idea of sorting crosswell data. A CI gather collects traces with a constant vertical interval between the source and receiver depths (see Figures 5.3 and 5.4). Mathematically,

$$s - g = 2h \quad , \tag{5.10}$$

where h is a constant. Therefore, for direct arrivals,

$$t = \frac{1}{V} \sqrt{4h^2 + x^2} = \text{constant} \quad , \tag{5.11}$$

and for reflections,
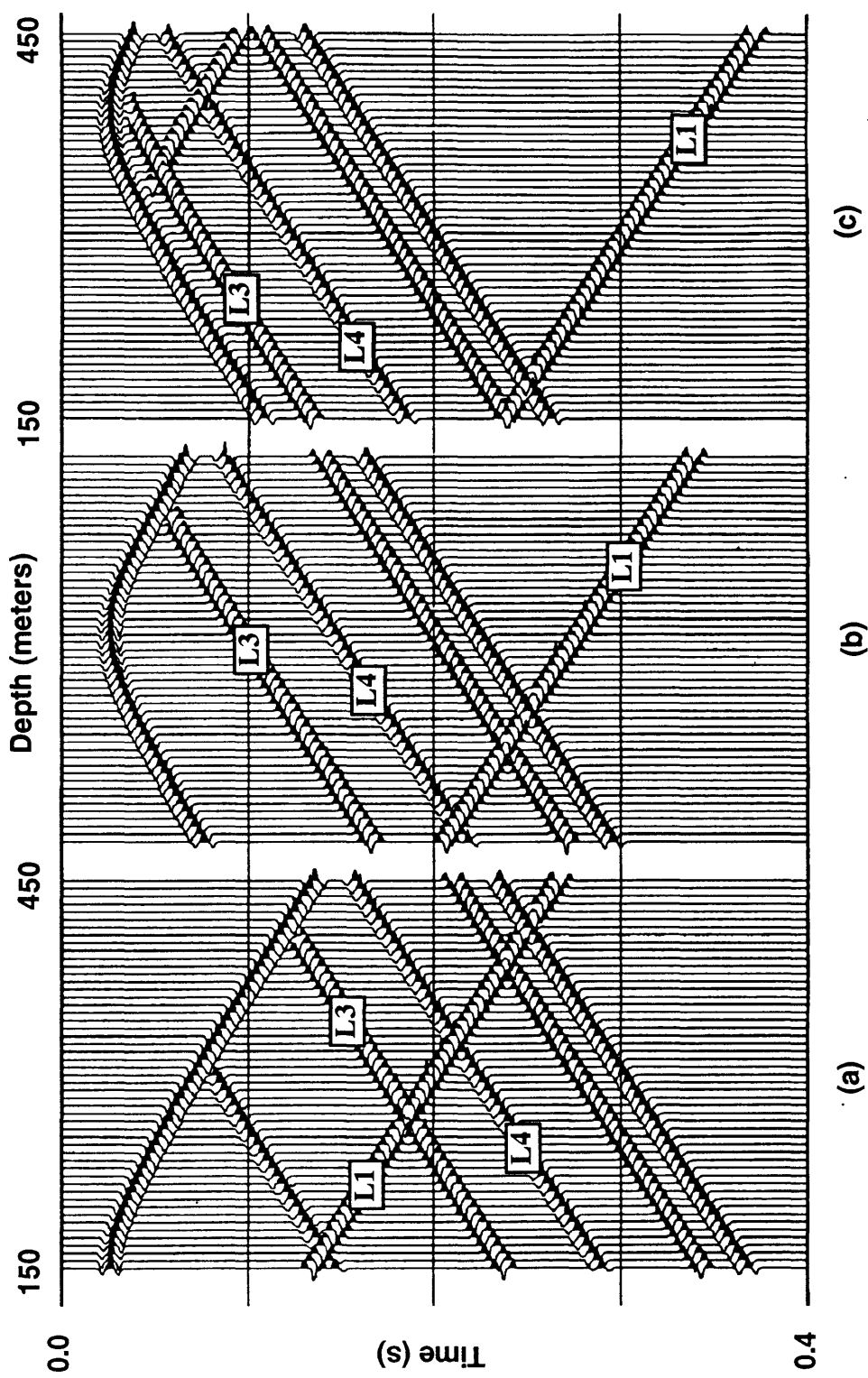
FIG. 5.6. Common-receiver gathers of synthetic crosswell seismic data. The receiver depths are (a) 150 m, (b) 312 m, and (c) 387 m, respectively.

$$\frac{t^2}{\left(\frac{x}{V}\right)^2} - \frac{(u-s)^2}{\left(\frac{x}{2}\right)^2} = 1 \quad , \tag{5.12}$$

where $u = r + h$. Equations (5.11) and (5.12) imply that for a constant-velocity medium, direct arrivals in a CI gather lead to a flat event, while reflections give hyperbolae. This is confirmed in Figure 5.7, where three CI gathers are shown. Immediately above upgoing and downgoing reflections, which have opposite dips, is the direct arrival that is perfectly aligned. More importantly, notice the sharp (large-angle) termination of reflections against the direct arrival. This is a useful characteristic possessed by CI gathers that can be employed in data processing. For example, I use CI gathers to remove direct arrivals from the total wavefield. Also, direct arrivals in CI gathers may be a useful indicator of velocity variation with depth for field crosswell seismic data, because in real cases velocity change with depth will affect the traveltimes of direct waves, thus affecting their flatness in CI gathers (see Chapter 7).

5.3.4 Common mid-depth gather

CMD gathering is also a new concept first introduced by Whiteley et al. (1990) into crosswell reflection processing. For a CMD gather,

$$s + g = 2m \quad , \tag{5.13}$$

where constant m is the mid-depth between the source and receiver. Hence, the traveltime equation for reflections is

$$t = \frac{1}{V}\sqrt{4(r-m)^2 + x^2} = \text{constant} \quad , \tag{5.14}$$

83
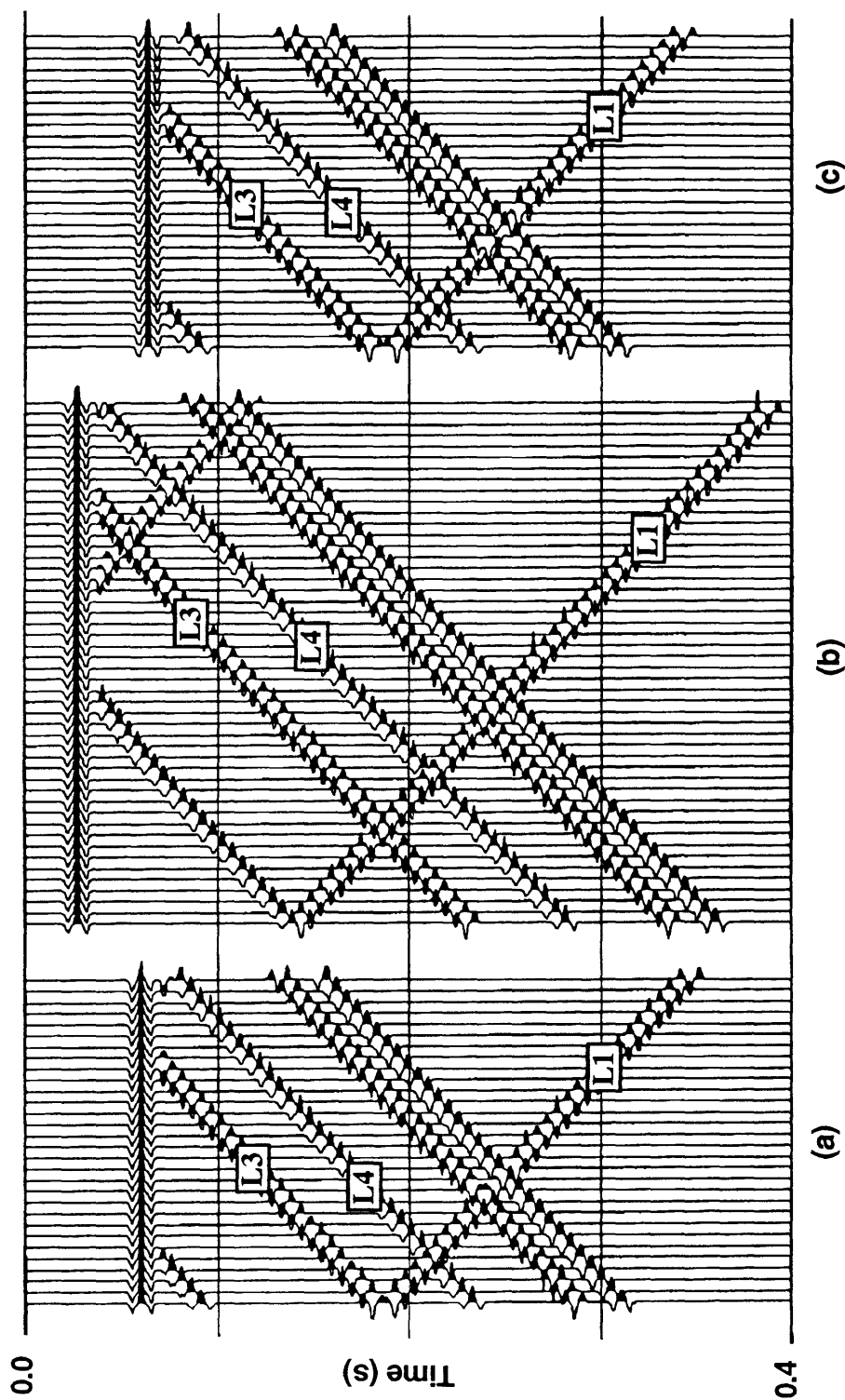
FIG. 5.7. Common-interval gathers of synthetic crosswell seismic data. The vertical intervals between the source and the receiver for the gathers are (a) 123 m, (b) 18 m, and (c) -132 m, respectively.

and, for direct arrivals,

$$\frac{t^2}{\left(\frac{x}{V}\right)^2} - \frac{(s-m)^2}{\left(\frac{x}{2}\right)^2} = 1 \quad .$$ (5.15)

So for a constant-velocity medium, reflections from a flat layer in a CMD gather are a flat event and, by contrast, direct arrivals are hyperbolic and symmetric about the mid-depth m. This is proven by synthetic CMD gathers in Figure 5.8. The three gathers represent 3 different mid-depths. Upgoing and downgoing reflections are all flat. The apex of the hyperbolic direct arrivals corresponds to the mid-depth m. Between CMD gathers, the same reflection events have different traveltimes. In some CMD gathers, upgoing and downgoing reflections partially coincide or interfere with each other. CMD gathers provide partial images of reflectors, can be used as an intermediate step to enhance reflected arrivals, or can be a starting point for a mapping procedure (Stewart, 1991). Whether or not reflection events in CMD gathers are flat may be meaningful in determining homogeneity of the real medium in which crosswell data are recorded, and examining whether the reflectors are flat or dipping. Note that crosswell CMD gathers are different than the surface seismic CDP gathers in that reflections in a CMD gather actually come from different points along a reflector, even if it is flat.

The inter-relationship of the four types of gathers, as discussed above, and their fold can also be seen in a crosswell stacking chart (Figure 5.9) provided by Stewart (1991) in a special case. This chart is similar, in many aspects, to the stacking chart often used in surface seismic data processing (see Yilmaz, 1987).

85
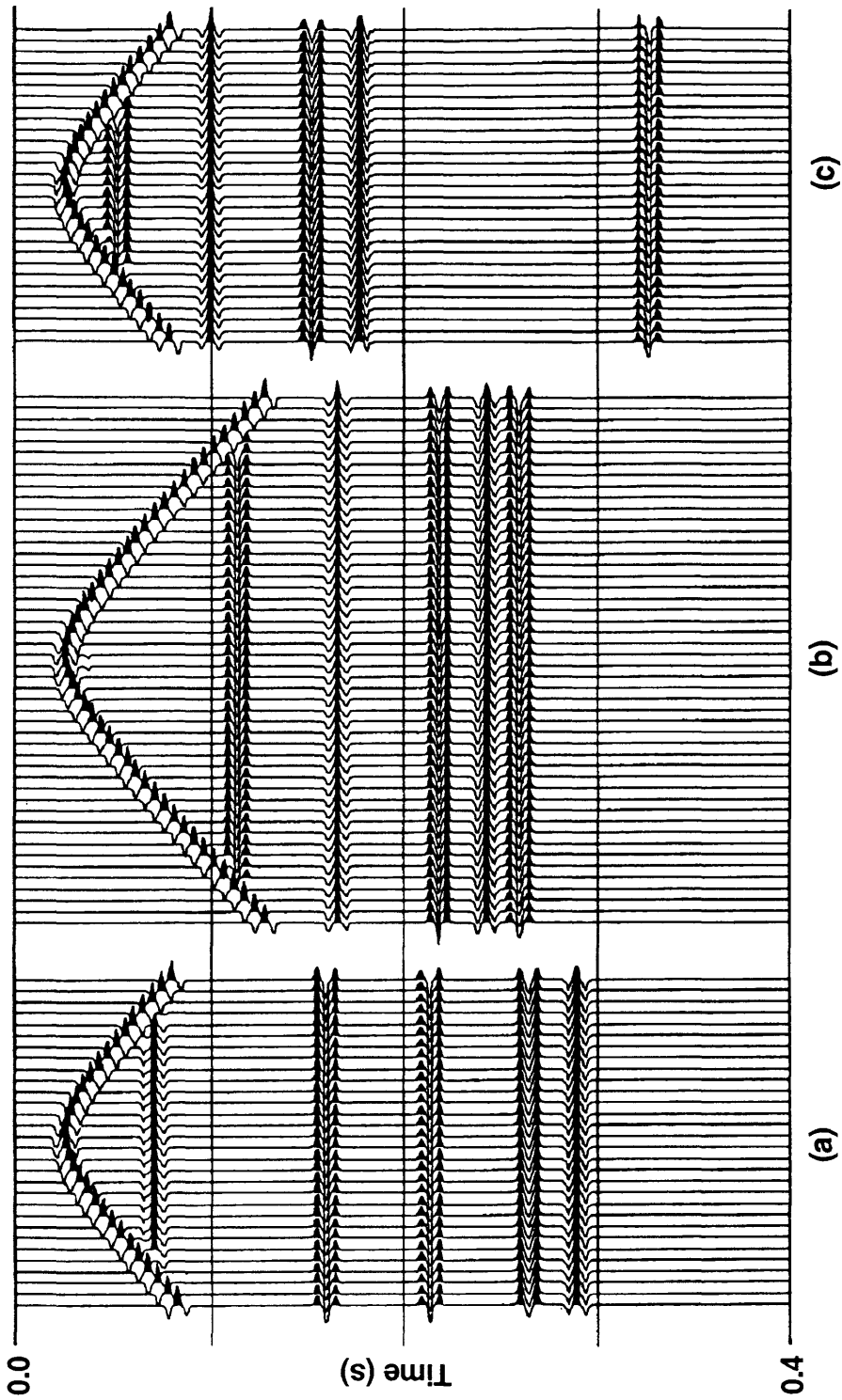
FIG. 5.8. Common mid-depth gathers of synthetic crosswell seismic data. The CMD depths for the gathers are (a) 238.5 m, (b) 291 m, and (c) 366 m. The flat events are reflections, while the hyperbolic wave is the direct arrivals.

Receiver depth (m)
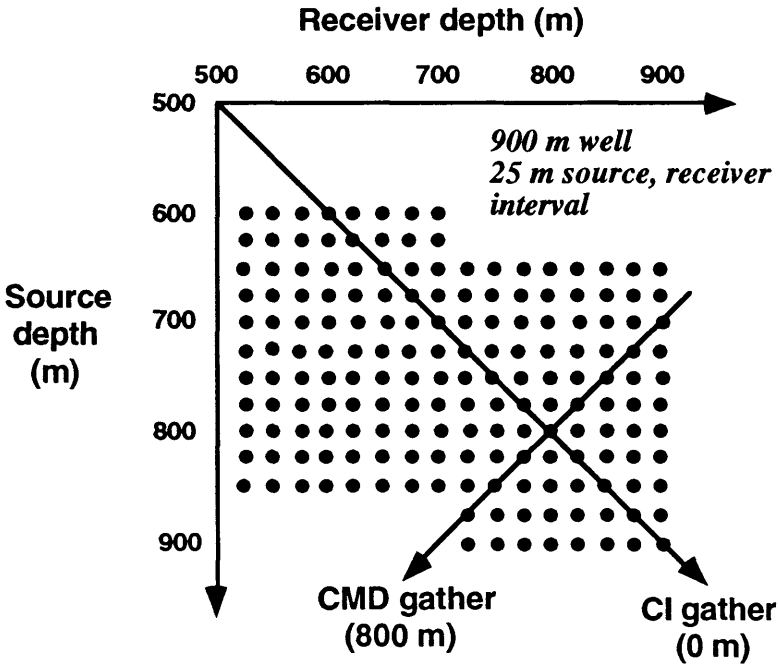
FIG. 5.9. Crosswell stacking chart (after Stewart, 1991)

5.4 Wavefield separation

The wavefield contained in borehole seismic data is often very complex. In the VSP case, one important processing step is to separate downgoing direct arrivals from upgoing reflections. In a shot (or receiver) gather, the direct arrivals have an apparent dip opposite to those of upgoing reflected events. So the wavefield is separated by designing a dip filter in the *f-k* domain (Hardage, 1985), or alternately, by running a median filter in the time-depth domain (Hardage, 1985; Stewart, 1985).

Crosswell wavefield could be separated the same way as in VSP data processing. However, crosswell seismic data usually consist of a more complex wavefield. Crosswell data contain downgoing *and* upgoing direct arrivals and primary reflections. Downgoing

primary reflections are useful for crosswell imaging. Although a velocity filter might be used to separate direct arrivals from reflections in CS or CR gathers, this could be a problem when reflections and direct arrivals have similar moveouts. The potential of different crosswell data gathers should be exploited for wavefield separation. In the following section, I will sort the data from CS gathers into CI gathers, where I perform median filtering to remove direct arrivals. As a further step, upgoing and downgoing reflections are separated by applying an *f-k* filter after sorting data back to CS or CR gathers.

5.4.1 Direct-arrival removal

In the case of a constant-velocity medium, crosswell direct arrivals are flat in CI gathers (as shown in Figure 5.7), and reflections have a sharp angle against them. This characteristic enables us to apply a median filter to remove these direct arrivals easily. The procedure is the following: By median filtering in each CI gather, the direct-arrival event is enhanced and other waves removed; then the enhanced event is subtracted from the total wavefield. Figure 5.10 shows reflections retained after removing direct waves (Figure 5.11) from those CI gathers in Figure 5.7. A median filter, whose operator is 11 traces long, was used. By comparing these figures, it can be seen that the direct arrivals have been removed nicely. Median filtering may cause some high-frequency glitches, which appear in the gathers in Figure 5.10. This problem can be overcome by running a high-cut filter after the median operation (Stewart, 1985).

The CS gather in Figure 5.5 is re-displayed in Figure 5.12, but now contains reflections only. The dashed curve represents the original position of the direct arrivals removed by median filtering in CI gathers. Note that median filtering causes no damage to the reflections, proving the advantage of using CI gathers to separate direct arrivals and reflections.

88
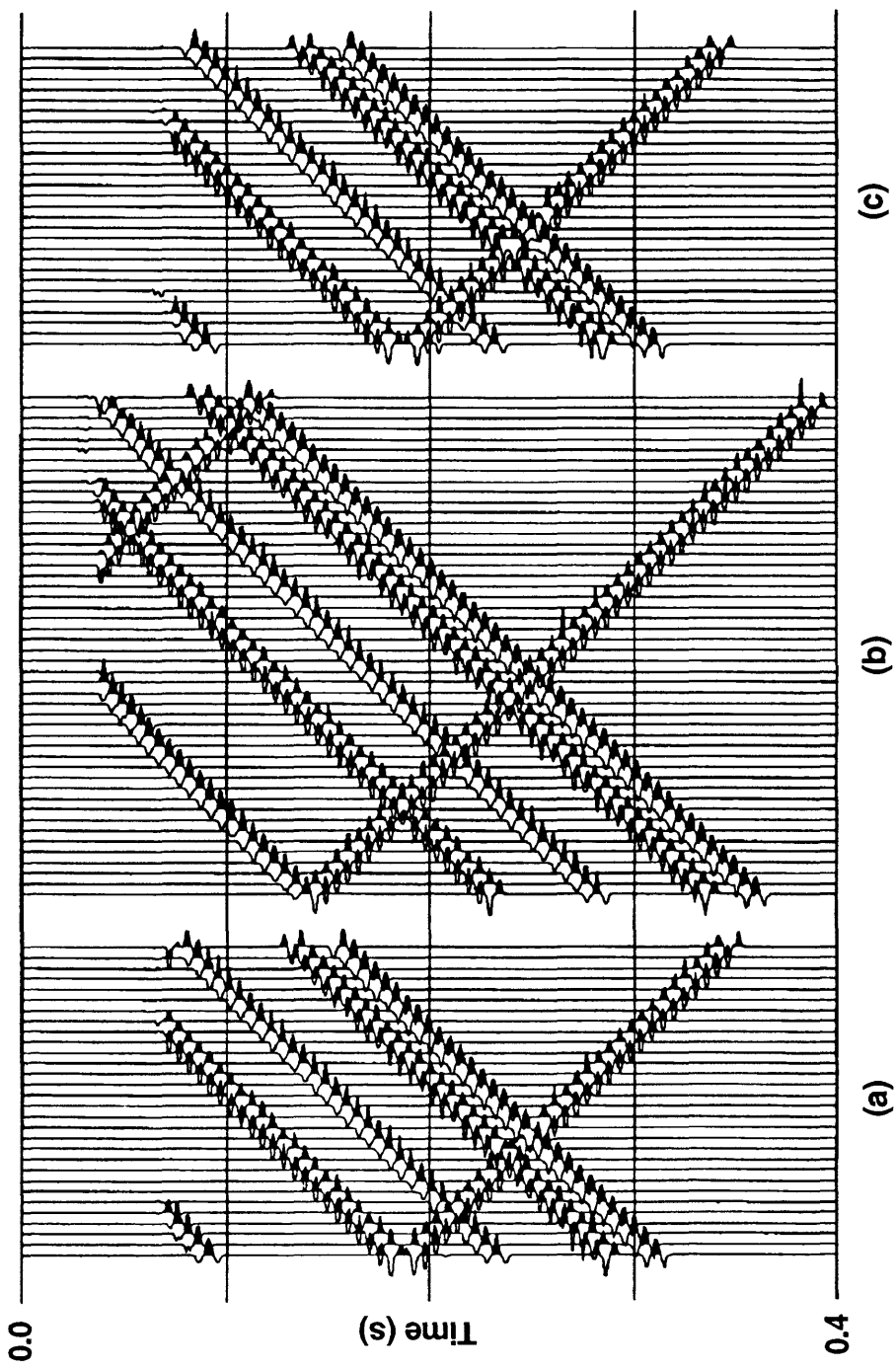
FIG. 5.10. Reflection data after removing direct arrivals by applying a median filter to the CI gathers in Figure 5.7. Gathers (a), (b), and (c) correspond to source-receiver intervals of 123 m, 18 m, and -132 m, respectively.

89
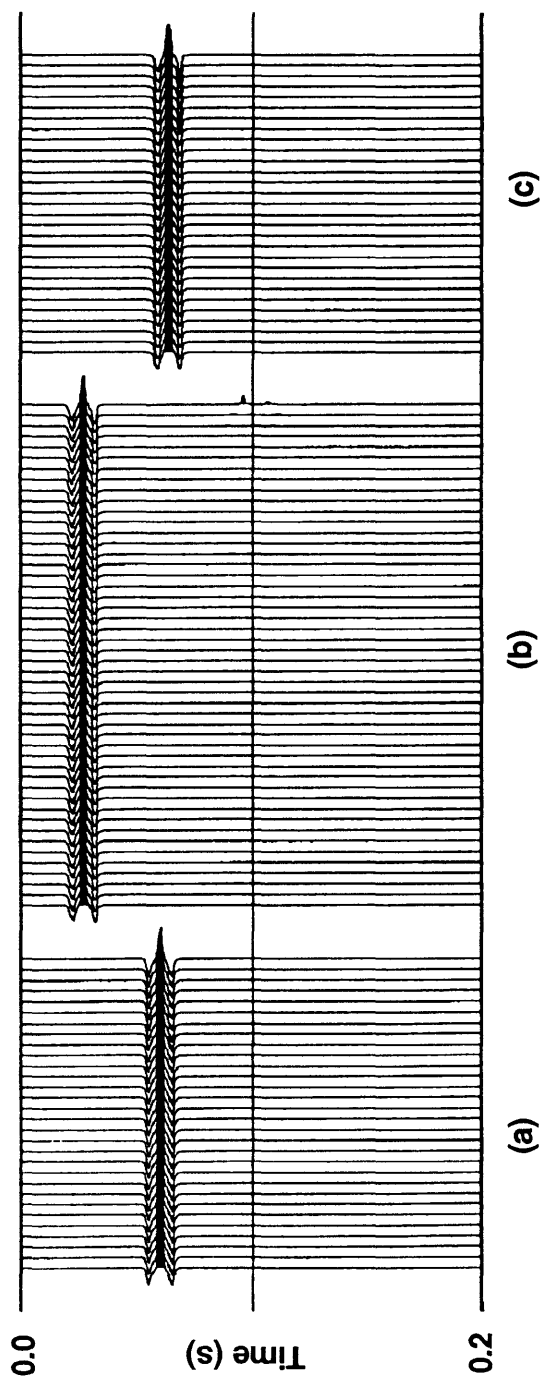
FIG. 5.11. Direct arrivals removed from the total wavefield in Figure 5.7, by running a median filter in the CI gathers. The filter operator length is 11 traces. Gathers (a), (b), and (c) correspond to source-receiver intervals of 123 m, 18 m, and -132 m, respectively.
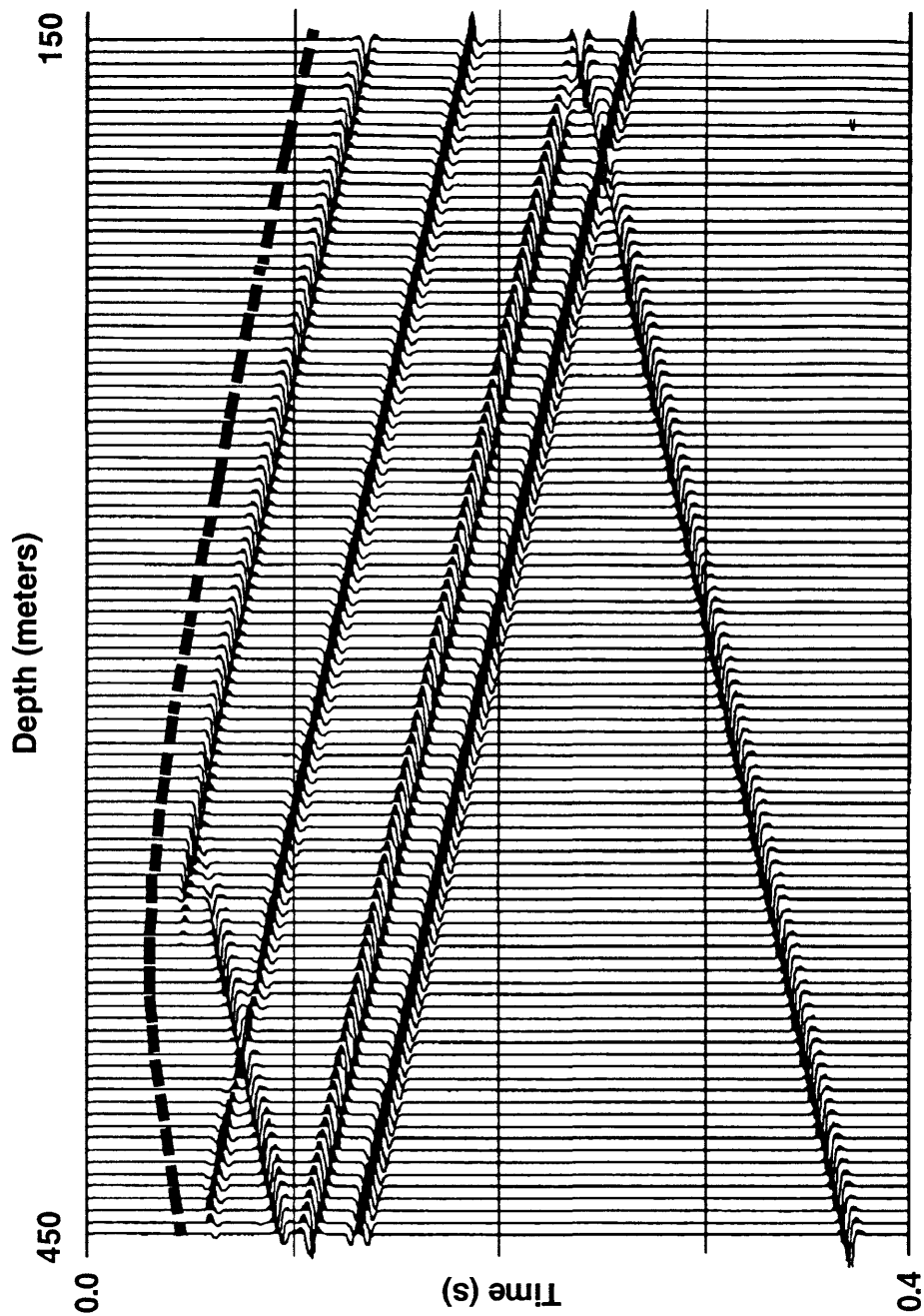
FIG. 5.12. Common-source gather of reflection data, with the direct arrivals (the dashed line) removed by median filtering in common-interval gathers.

5.4.2 Reflection-wavefield separation

After direct-arrival removal, the filtered CI gathers are sorted back into CS gathers. An f-k filter could have been applied in the CI gathers to separate upgoing and downgoing reflections, because of their opposite apparent dips. However, as the vertical source-receiver interval becomes larger, there are fewer traces contained in a CI gather. Also the events might be aliased. Therefore, it is not recommended to separate upgoing and downgoing reflections in the CI gathers.

Wavefield separation can be done in CS gathers. Multichannel velocity filters such as an f-k filter can be used. Other filters like a median filter can also be applied but it involves time-consuming event picking. In this case, I chose to use the f-k filter. Figures 5.13 and 5.14, respectively, show the upgoing and downgoing reflections separated from the same CS gather as in Figure 5.12. As can be seen, the f-k filter did a very good job. After the wavefield separation, further processing leading to image reconstruction can be performed on the separated reflection data.

5.5   Velocity analysis and moveout corrections

Further processing that leads to a final image is mainly performed in CMD gathers, because in these gathers, reflected waves are flat, assuming a constant-velocity medium. This is similar to the surface seismic case where reflection events in CDP gathers are flattened after a normal moveout (NMO) correction is applied. However, differences exist between the surface and crosswell cases. First, a reflection across a CDP gather is from the same point on a subsurface reflector, if it is flat. But in a CMD gather, the same reflection event is from different lateral points, even though the reflector is flat. Second, before a moveout correction is ever applied, reflections in CMD gathers are already flat.
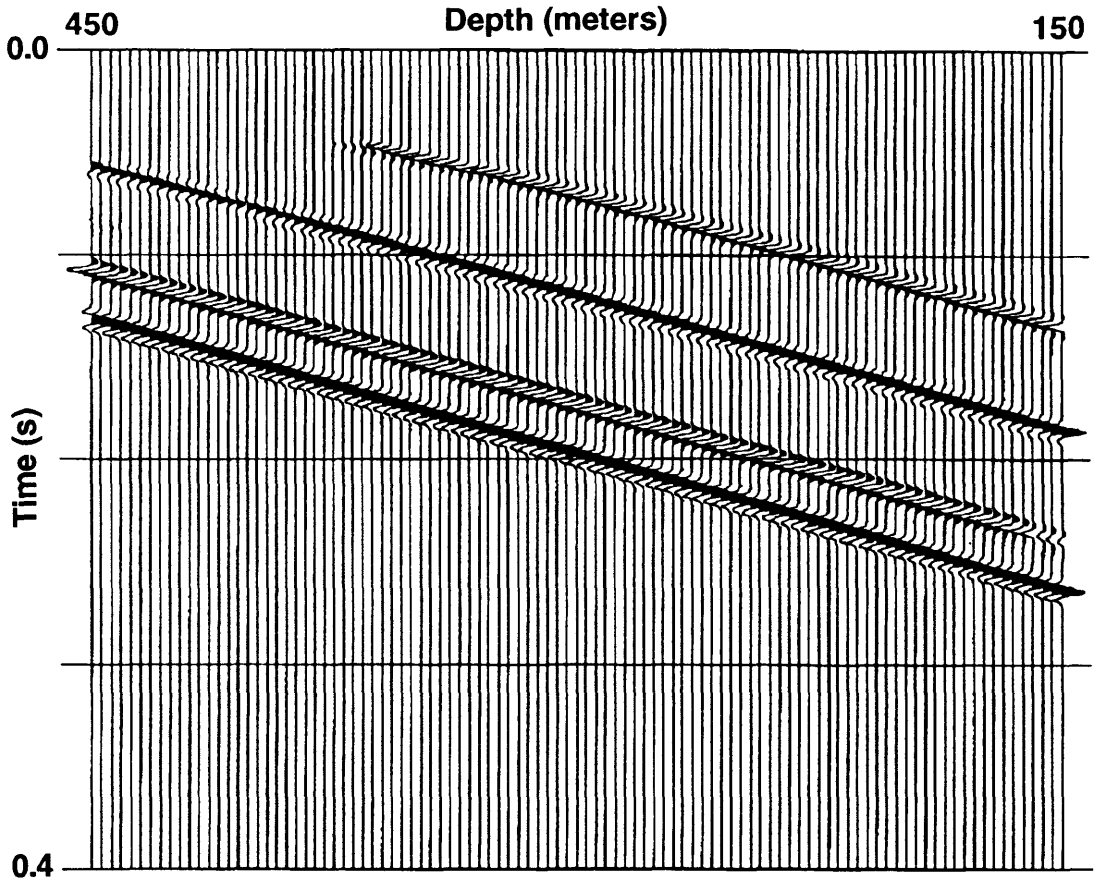
FIG. 5.13. Upgoing reflections in a common-source gather, obtained from *f-k* filtering.

Apparently, special efforts in data processing are necessary for crosswell reflection imaging.

Now, upgoing and downgoing reflection data are separately sorted into CMD gathers. Three of them are shown in Figures 5.15 and 5.16 for upgoing and downgoing waves. It is noted that for the same reflection event, there is a non-linear time shift between gathers. This shift is caused by moveout. Two types of moveout have to be considered, including vertical moveout (VMO) and horizontal moveout (HMO). VMO is the moveout
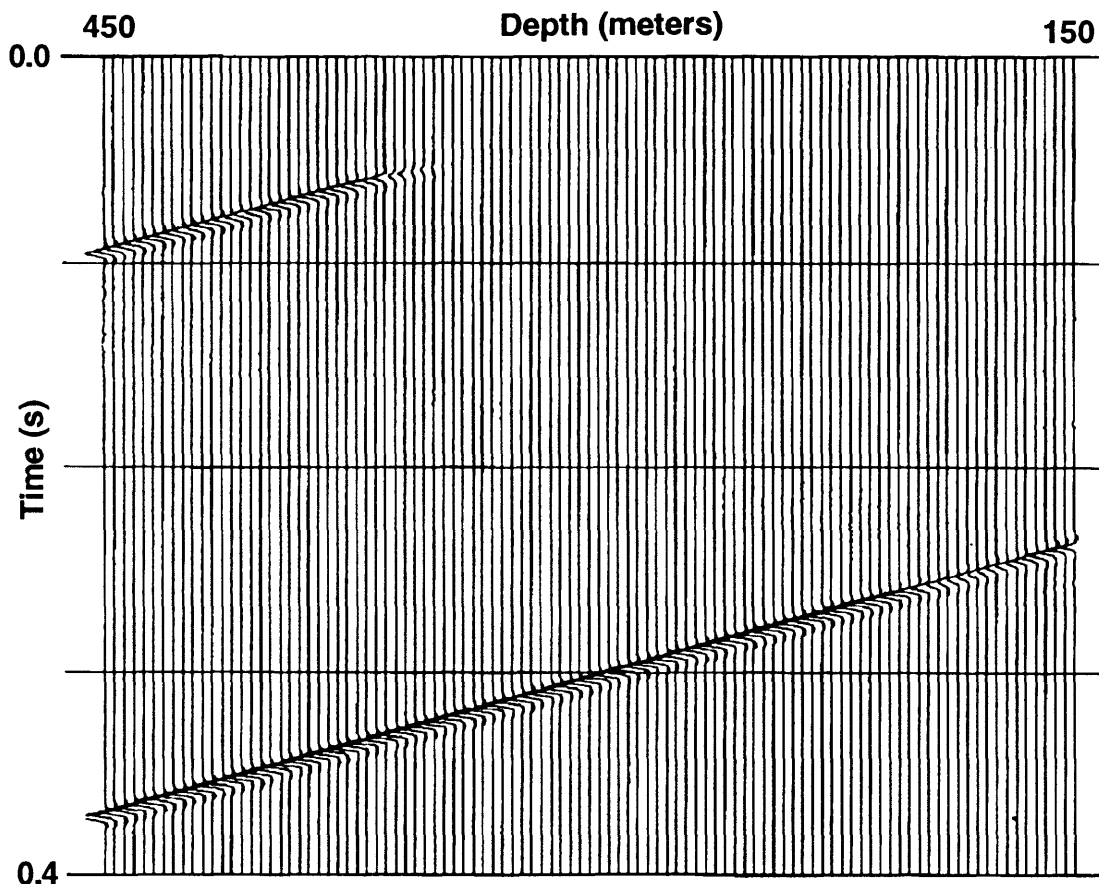
FIG. 5.14. Downgoing reflections in a common-source gather, obtained from *f-k* filtering.

due to difference between CMD depths, while HMO refers to the moveout caused by the offset distance between the source and receiver wells. As will be shown shortly, both VMO and HMO moveout are a function of distance. Since they will be corrected in the time domain, velocity information is needed. I will show next that such information can be obtained from a zero-interval gather by a velocity scanning procedure similar to that used in CDP data processing. Velocity information obtained this way is applied to VMO and HMO corrections.
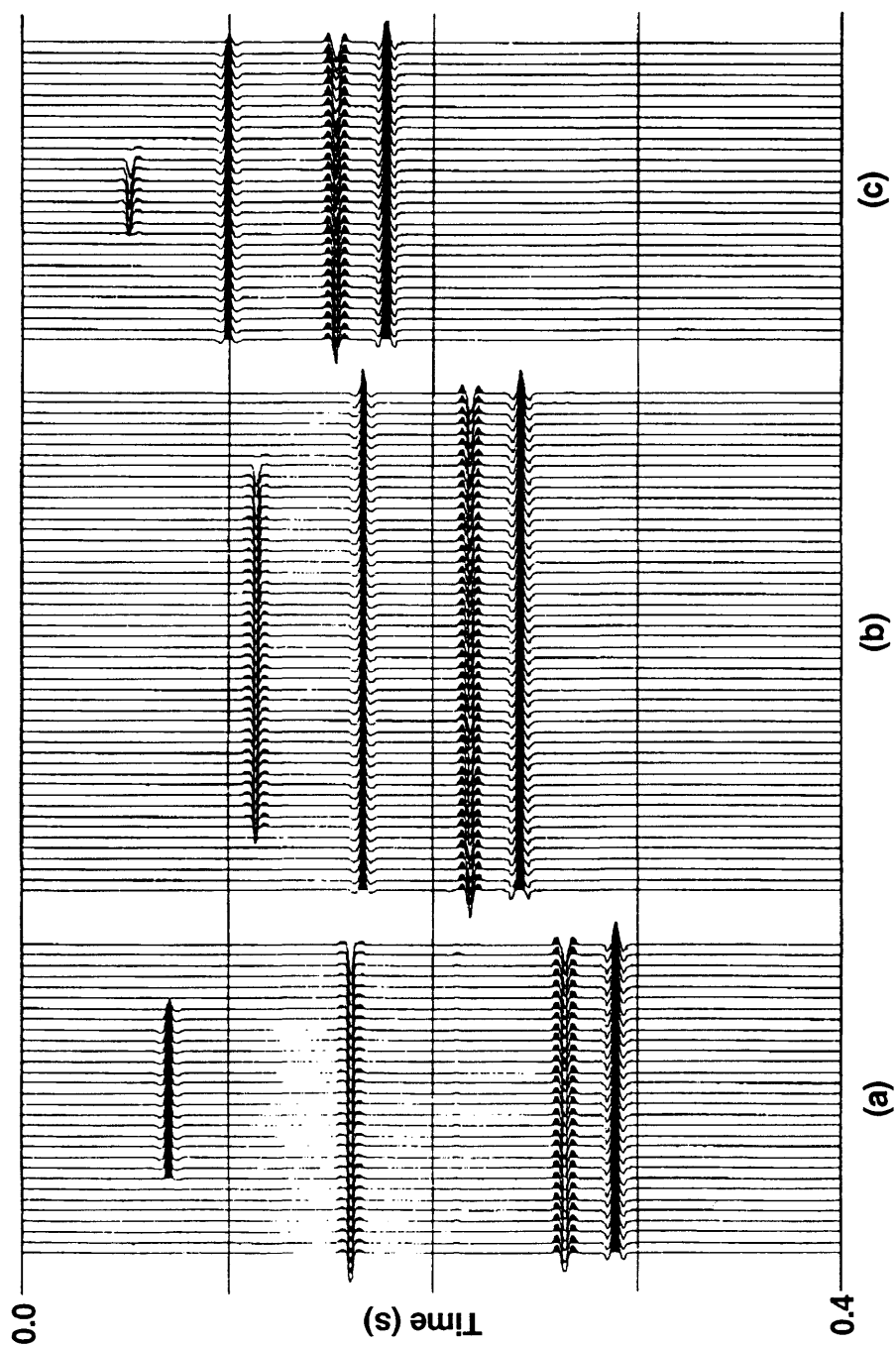
94

FIG. 5.15. Separated upgoing reflections in common mid-depth gathers (a) 238.5 m, (b) 291 m, and (c) 366 m, respectively.
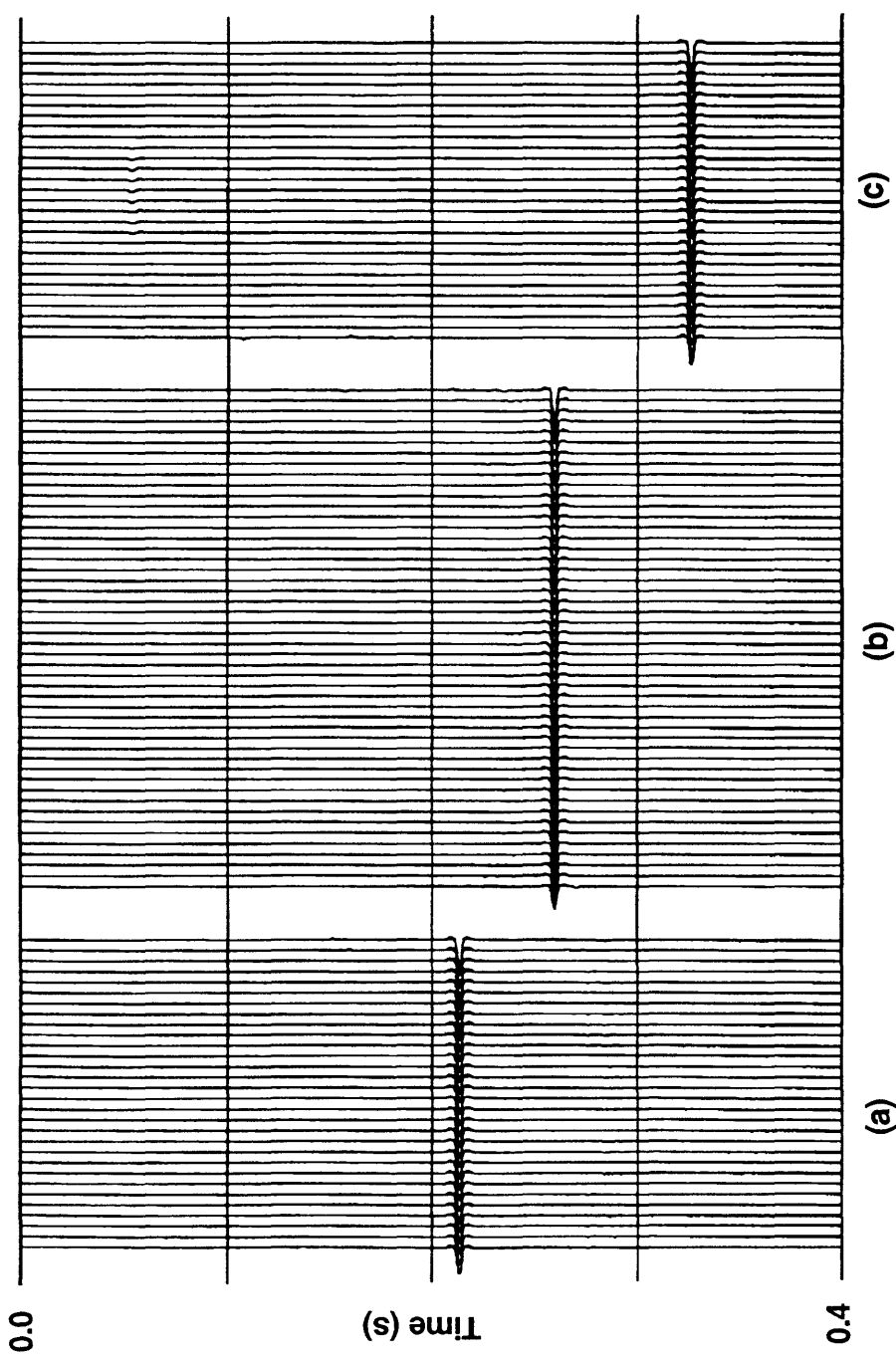
FIG. 5.16. Separated downgoing reflections in common mid-depth gathers (a) 238.5 m, (b) 291 m, and (c) 366 m, respectively.

5.5.1 Zero-interval velocity analysis

A zero-interval gather is a set of traces whose vertical interval between source and receiver is equal to zero. Thus a zero-interval gather is the special case of a CI gather. An example of the zero-interval gather is shown in Figure 5.17. In this Figure, both upgoing and downgoing reflections are displayed for the purpose of illustration, although in velocity analysis, use of only one type is sufficient. The upgoing reflection was actually used.

To derive formulae for velocity analysis and moveout correction, let us consider the raypath of reflections from a single flat reflector in a constant-velocity medium, shown in Figure 5.18a. Figure 5.18b shows the corresponding time-depth curve for this zero-interval gather. There is moveout between traces because of the difference in distance traveled by each reflected wave. In the case of Figure 5.18a, the moveout is caused mainly by the difference in vertical distance.

It is easy to find that the distance difference between adjacent traces is actually the difference between adjacent CMD depths. The traveltime of an upgoing reflection recorded at some depth z, is given by

$$t = \frac{2}{V} \left\{ \left(\frac{x}{2}\right)^2 + (r - z)^2 \right\}^{1/2} \quad , \tag{5.16}$$

where V is the medium velocity, x the well offset and r the reflector depth. Here, V and r are unknowns. The moveout for that reflection, with respect to a reference time t_r (to which the data will be VMO corrected), is calculated using

$$\Delta t = t - t_r \quad . \tag{5.17}$$

The reference time t_r is arbitrarily chosen. As an example, the known time for the reflection from the first trace (depth z_1) in the zero-interval gather can be chosen as the reference time.
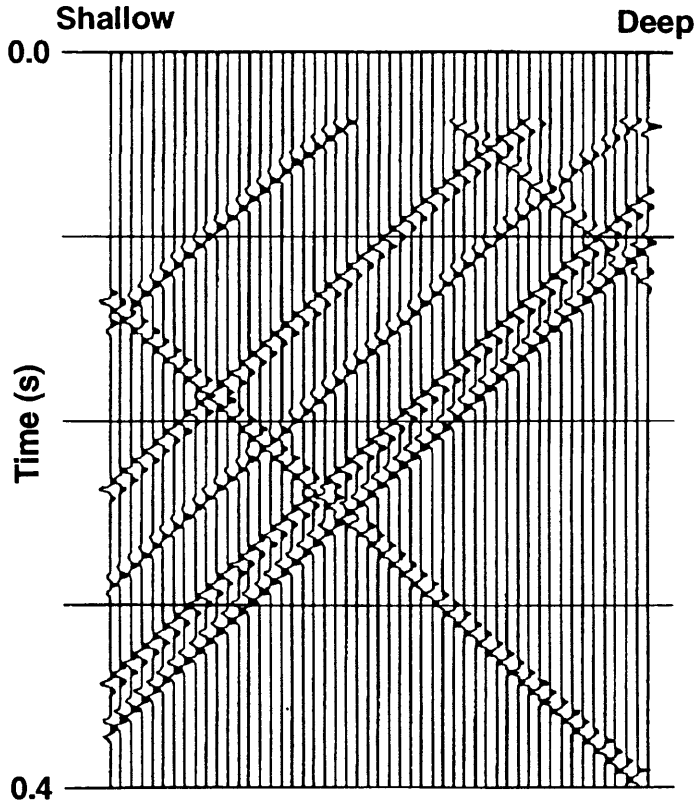
FIG. 5.17. A zero-interval CI gather with both up- and downgoing reflections displayed.

Hence,

$$t_r = \frac{2}{V} \left\{ \left(\frac{x}{2}\right)^2 + (r - z_1)^2 \right\}^{1/2} \quad , \tag{5.18}$$

from which the reflector depth r can be found:

$$r = \left\{ \left(\frac{V t_r}{2}\right)^2 - \left(\frac{x}{2}\right)^2 \right\}^{1/2} + z_1 \quad . \tag{5.19}$$

Upon substitution, we obtain a formula for VMO correction in the zero-interval gather:
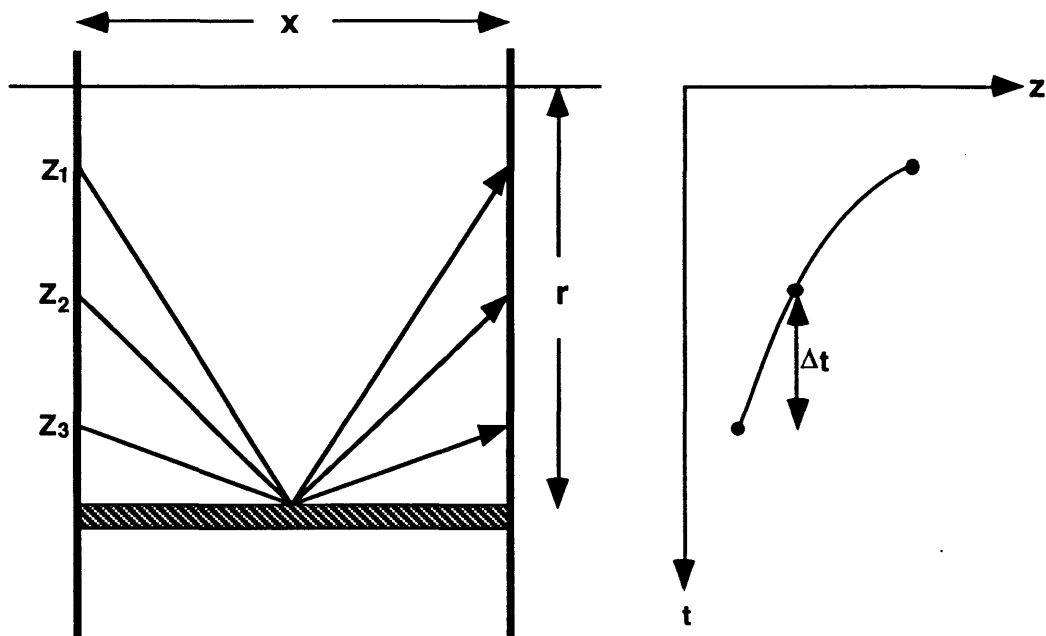
FIG. 5.18. (a) Raypaths for upgoing reflections in a zero-interval gather; (b) A time-depth representation of the zero-interval gather.

$$\Delta t = \frac{2}{V}\left\{\left(\frac{x}{2}\right)^2 + \left[\sqrt{\left(\frac{V\,t_r}{2}\right)^2 - \left(\frac{x}{2}\right)^2} + z_1 - z\right]^2\right\}^{1/2} - t_r \quad.$$ (5.20)

In this equation, the only unknown is the velocity V.

The VMO correction is a process of mapping data from $P(t, z)$ to $P(t_r, z)$, through equation (5.20). Using different velocities in equation (5.20) will produce different VMO correction amounts. So by scanning a range of possible velocities, the best velocity can be selected that yields the optimal VMO correction: This best velocity should flatten the reflection event. This process is illustrated in Figure 5.19. The zero-interval gather was scanned with many different velocities, and the results from 8 velocities scanned are displayed in panels (a) through (h). The event being considered is horizon $L3$ (pointed out by the arrow). In each panel, the $L3$ event has been VMO-corrected differently due to the
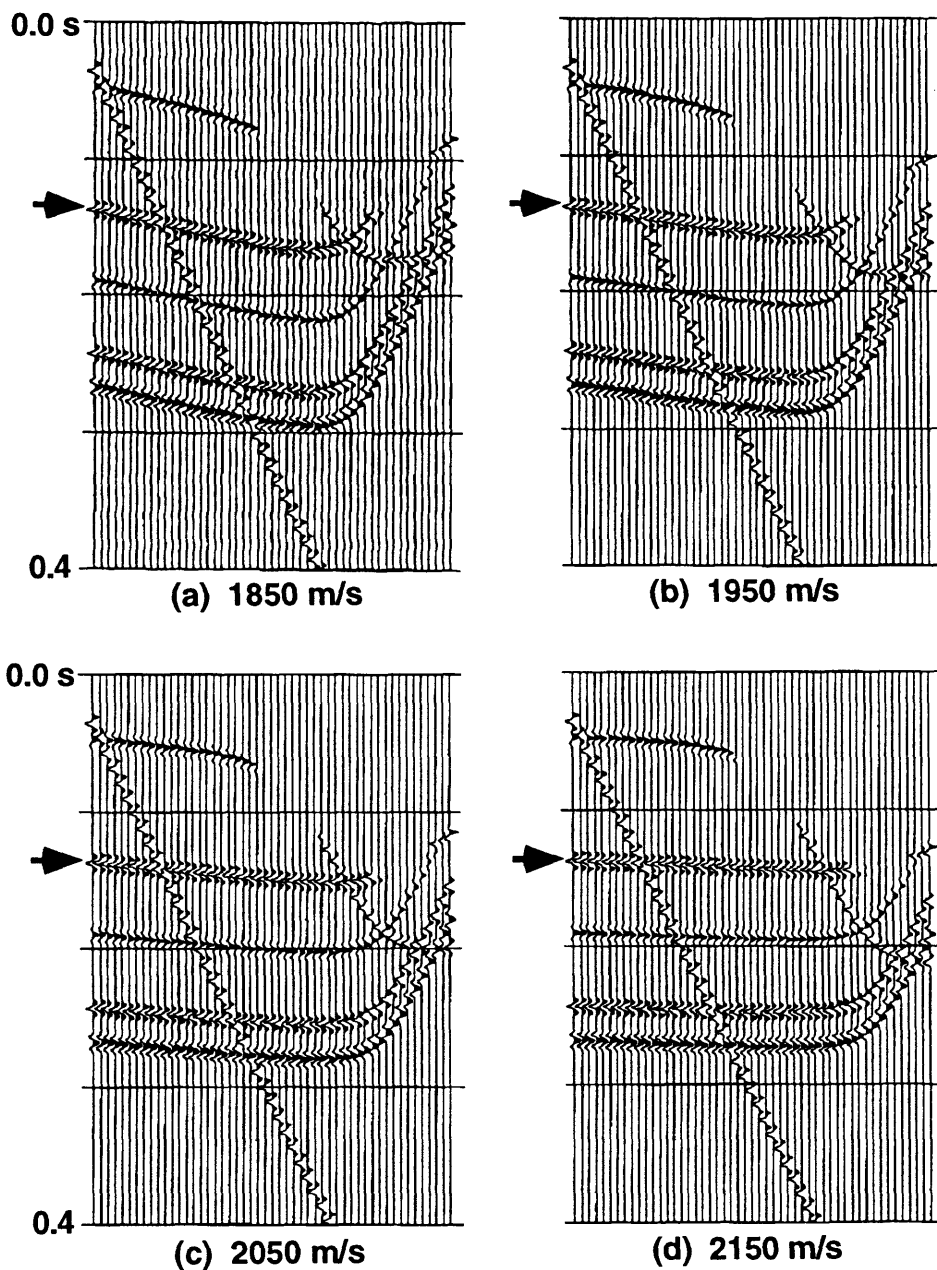
FIG. 5.19. Constant-velocity scan in a zero-interval CI gather for finding the best velocity for moveout corrections. Displayed in this page are the four velocities that were scanned, (a) to (d), and the other four, (e) to (h) shown in next page. The medium velocity, i.e., 2250 m/s, would produce the best moveout correction for the event of interest indicated by the arrow.

(e) 2250 m/s

(f) 2350 m/s

(g) 2450 m/s

(h) 2550 m/s
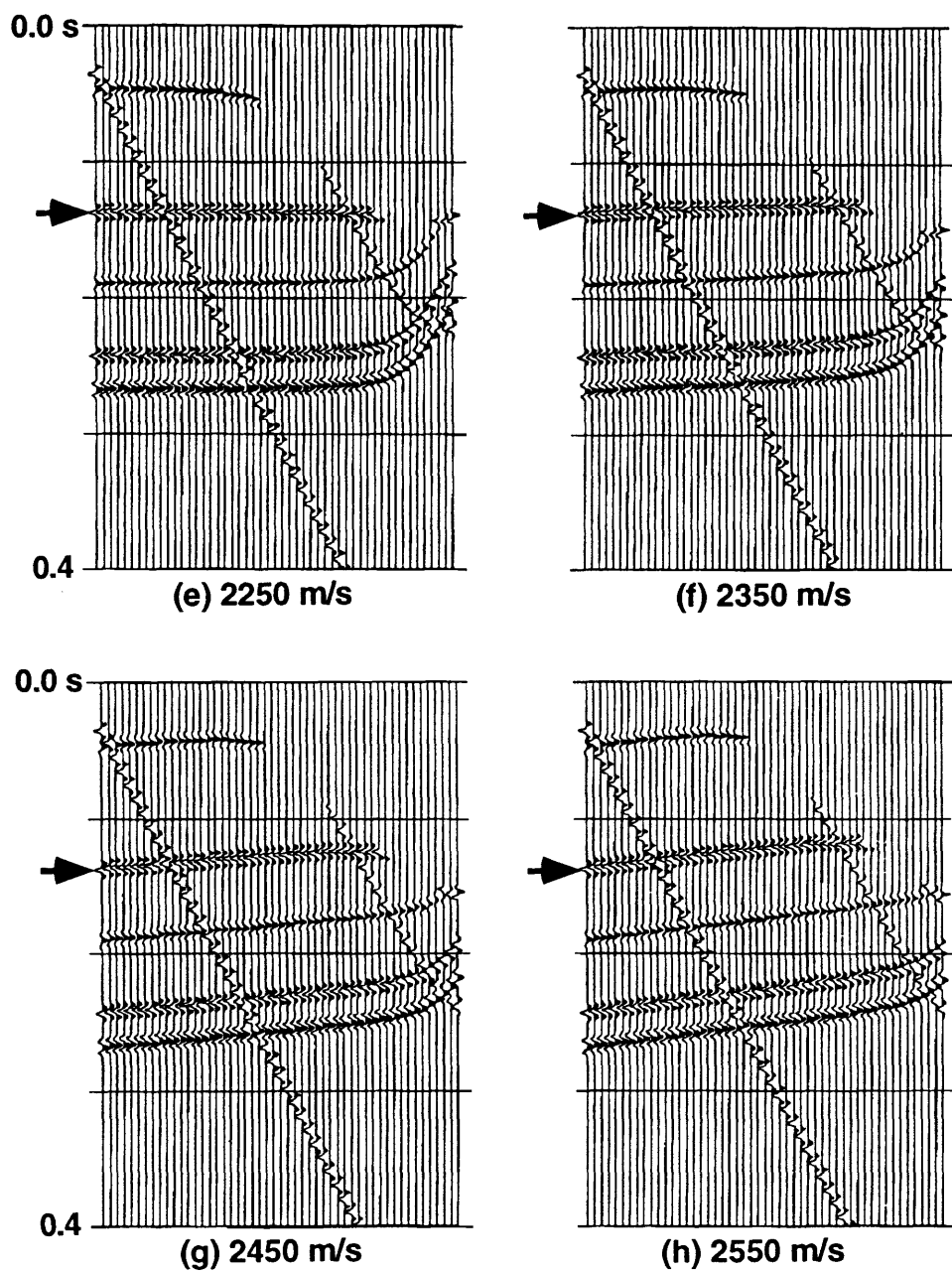
FIG. 5.19. Continued

use of different velocities. It is found that the velocity of 2250 m/s produces the best VMO correction for this event, which now becomes flat. Recall that 2250 m/s is indeed the medium velocity used in the model. That means, in a constant-velocity medium, the medium velocity is the optimal moveout-correction velocity. When the scanned velocity is below 2250 m/s, the same event is undercorrected. On the other hand, however, if a velocity higher than 2250 m/s is used, the *L3* event will be overcorrected.

Note that the moveout-correction velocity is dependent upon the reflector depth. From Figure 5.19e, it is seen that although 2250 m/s is the best velocity for the *L3* horizon, it causes undercorrection for the shallower event and overcorrection for the deeper reflection events. Also, note that reflections on the deeper traces (on the right side of each panel in Figure 5.19) are more affected by the scanning velocities than the shallower traces (on the left side), until the velocity being used more closely approaches the best velocity. This can be confirmed, for example, by comparing the *L3* event in all velocity panels.

5.5.2 Vertical moveout correction

The problem of VMO correction can be illustrated by the diagrams in Figure 5.20. In diagram (a), the shadowed columns represent two CMD gathers, whose depths are m_r and m, respectively. The solid horizontal bar in each gather symbolizes the reflection event that is generated from the same reflector, as shown in diagram (b), where the rays for two reflections at depths m_r and m are shown. In the CMD gather representative of depth m_r, the reflection event has a two-way traveltime of t_r. The reflection in the other gather should be shifted by a time determined by the VMO.

The purpose of the VMO correction is to remove the moveout from the data and relocate the reflections in each CMD gather to a *known* reference time. A general formula for VMO correction is developed from equation (5.20) and given by:

(a)   (b)
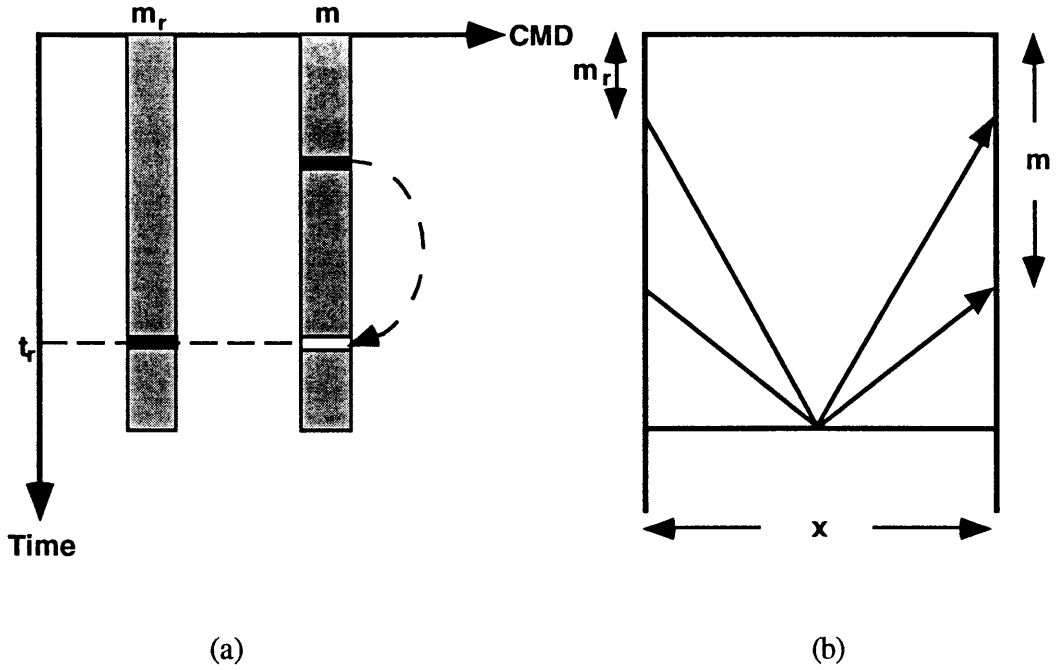
FIG. 5.20. Diagrams illustrating the process of VMO correction.

$$t_m^2 = t_r^2 + \frac{4(m - m_r)^2}{V_{\text{vmo}}^2} - \frac{4(m - m_r)}{V_{\text{vmo}}}\sqrt{t_r^2 - \left(\frac{x}{V_{\text{vmo}}}\right)^2} \quad , \tag{5.21}$$

where t_m is reflection time in an arbitrary CMD gather, whose depth is denoted by m, and t_r is the reference time corresponding to CMD depth m_r, which is to be chosen. The VMO velocity was derived in the previous section, based on zero-interval gather velocity scan. In equation (5.21), time t_m is a function of the CMD difference, m-m_r. Stewart et al. (1991) performed VMO corrections by assuming that VMO is linearly related to the CMD depth. However, this linear relationship is valid only for small CMD depths. When the CMD depth is large, the relationship becomes nonlinear.

After VMO correction, the reflection in the CMD gather at depth m will be relocated to the reference time t_r. This is indicated by the dashed arrow in Figure 5.20a. At this point, reflections in all CMD gathers will have been adjusted to the same time level, if they are from the same reflector. The synthetic upgoing reflection data in Figure 5.15 were corrected for VMO. The result is shown in Figure 5.21. For VMO correction, a velocity of 2250 m/s was used. The reference time was 0.238 second, which is the time of the reflection corresponding to reflector $L3$, in the shallowest CMD gather (refer to the first trace of the zero-interval gather in Figure 5.17). This time can be readily picked from the time section. It is seen from Figure 5.21 that, after VMO correction, the same reflection event in all CMD gathers is aligned horizontally.

A similar process can also be applied to the downgoing reflection data. Figure 5.22 shows the result of applying VMO correction to the downgoing reflection data in three CMD gathers. For the downgoing waves, a reference time was chosen at 0.4 second for the reflection on the deepest CMD gather (or last trace in Figure 5.17), which corresponds to the downgoing reflection from the free surface. Therefore, all the reflection in other CMD gathers are corrected to that time level.

5.5.3 Horizontal moveout correction

To this point, the effect of horizontal moveout (HMO) due to borehole separation distance still exists in the reflection data and has to be corrected for. The derivation of the expression for HMO moveout is simple, and the equation for upgoing reflection is

$$t^2 = \left(t_0 - \frac{2m_r}{V_{\text{hmo}}}\right)^2 + \left(\frac{x}{V_{\text{hmo}}}\right)^2 \quad , \tag{5.22}$$

and for downgoing reflection, is

104
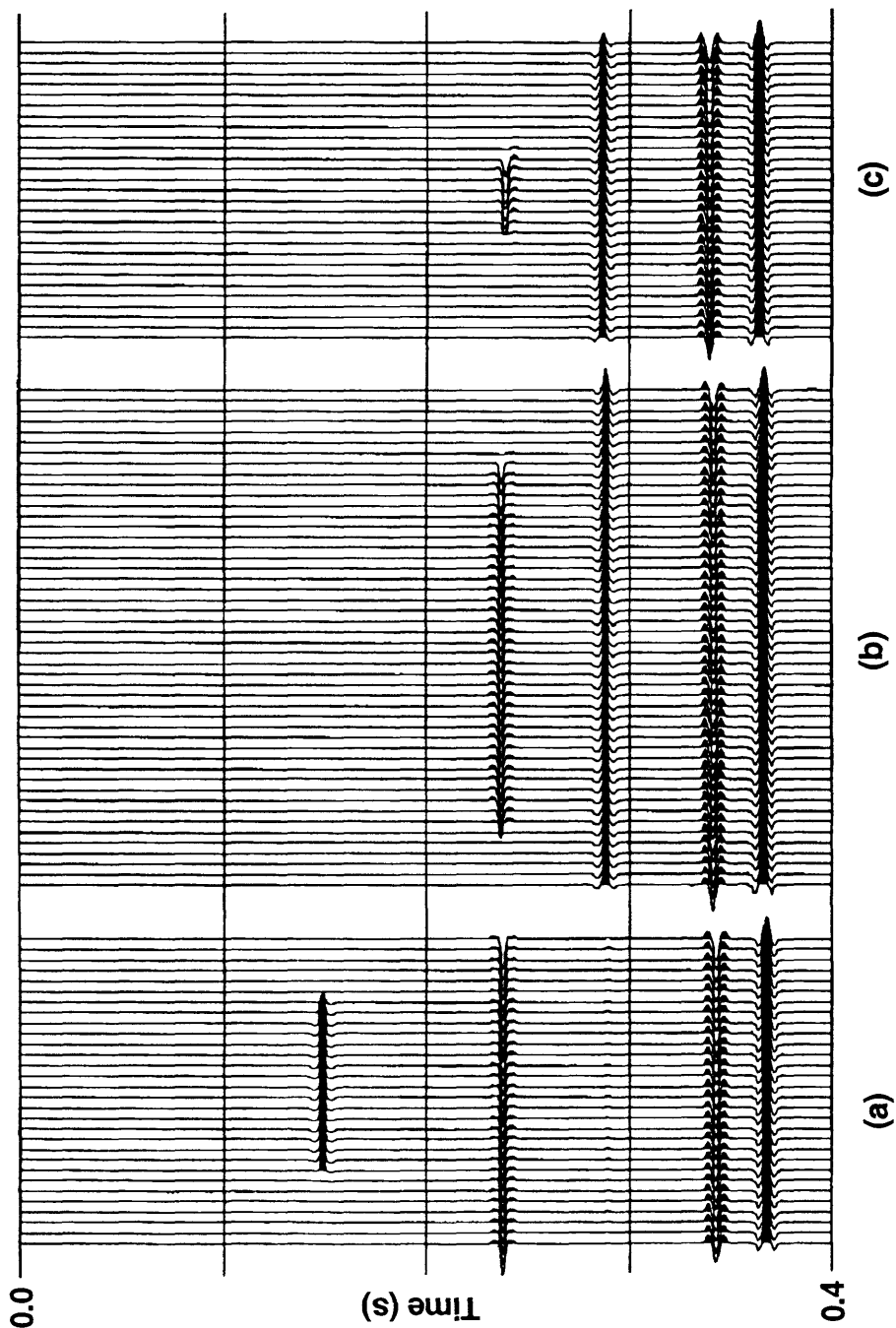
FIG. 5.21. Upgoing reflection data in CMD gathers, after VMO correction has been applied. The CMD depths for the gathers are (a) 238.5 m, (b) 291 m, and (c) 366 m.
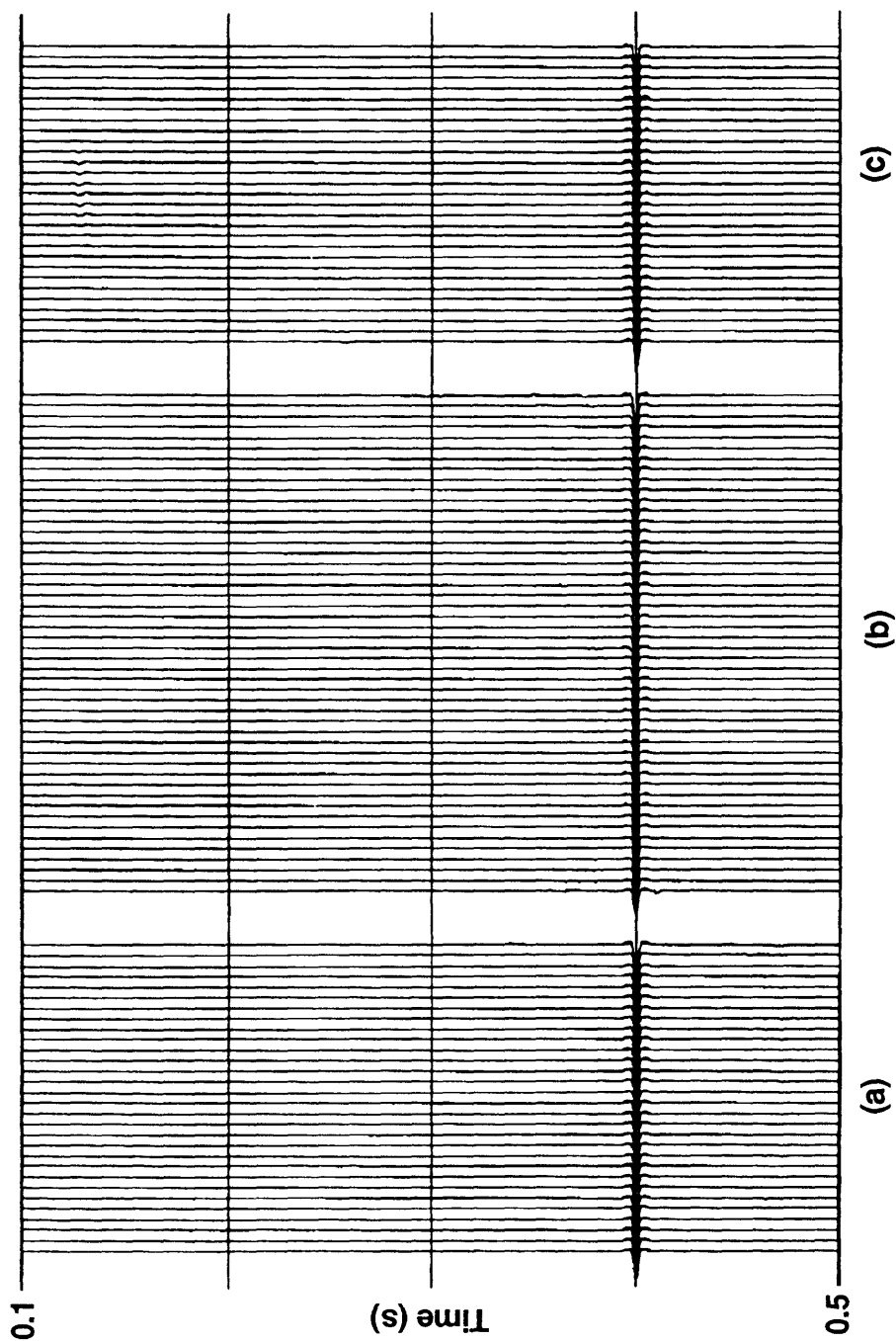
FIG. 5.22. Downgoing reflection data in CMD gathers, after VMO correction has been applied. The CMD depths for the gathers are (a) 238.5 m, (b) 291 m, and (c) 366 m.

$$t^2 = \left(\frac{2m_r}{V_{hmo}} - t_0 \right)^2 + \left(\frac{x}{V_{hmo}} \right)^2 . \tag{5.23}$$

In both equations, t is two-way traveltime in the VMO-corrected CMD gather, t_0 is two-way vertical traveltime from the reflector to the free surface, m_r is the known reference CMD depth in Figure 5.20. The HMO velocity V_{hmo} here is set to the medium velocity in the constant-velocity medium case. To correct for HMO moveouts, a process of mapping from $P(t, z)$ to $P(t_0, z)$ must be performed, where z is the trace depth.

The HMO corrections were applied to the upgoing reflection data in Figure 5.21 and to the downgoing reflection data in Figure 5.22. The results after HMO corrections are displayed in Figures 5.23 and 5.24, respectively. Note that for the upgoing reflection data, there is some difference between pre-HMO and post-HMO corrections, due to the effect of the 55-m well separation. However, for the downgoing reflections, the HMO correction has not only corrected for the effect of the well separation, but also put the reflections into their correct positions. In this case, the free-surface reflection at 0.4 second in the VMO-corrected CMD gathers (Figure 5.22) has been positioned correctly to time zero in the HMO-corrected CMD gathers (Figure 5.24), while a shallower reflection in Figure 5.22c now becomes a deeper reflection in Figure 5.24c, which is actually from the reflector below the free surface in the geologic model in Figure 5.1.

After VMO and HMO corrections, the reflections are equivalent to those that would have traveled vertically from a surface source and back to the detector at the same surface location as the source.
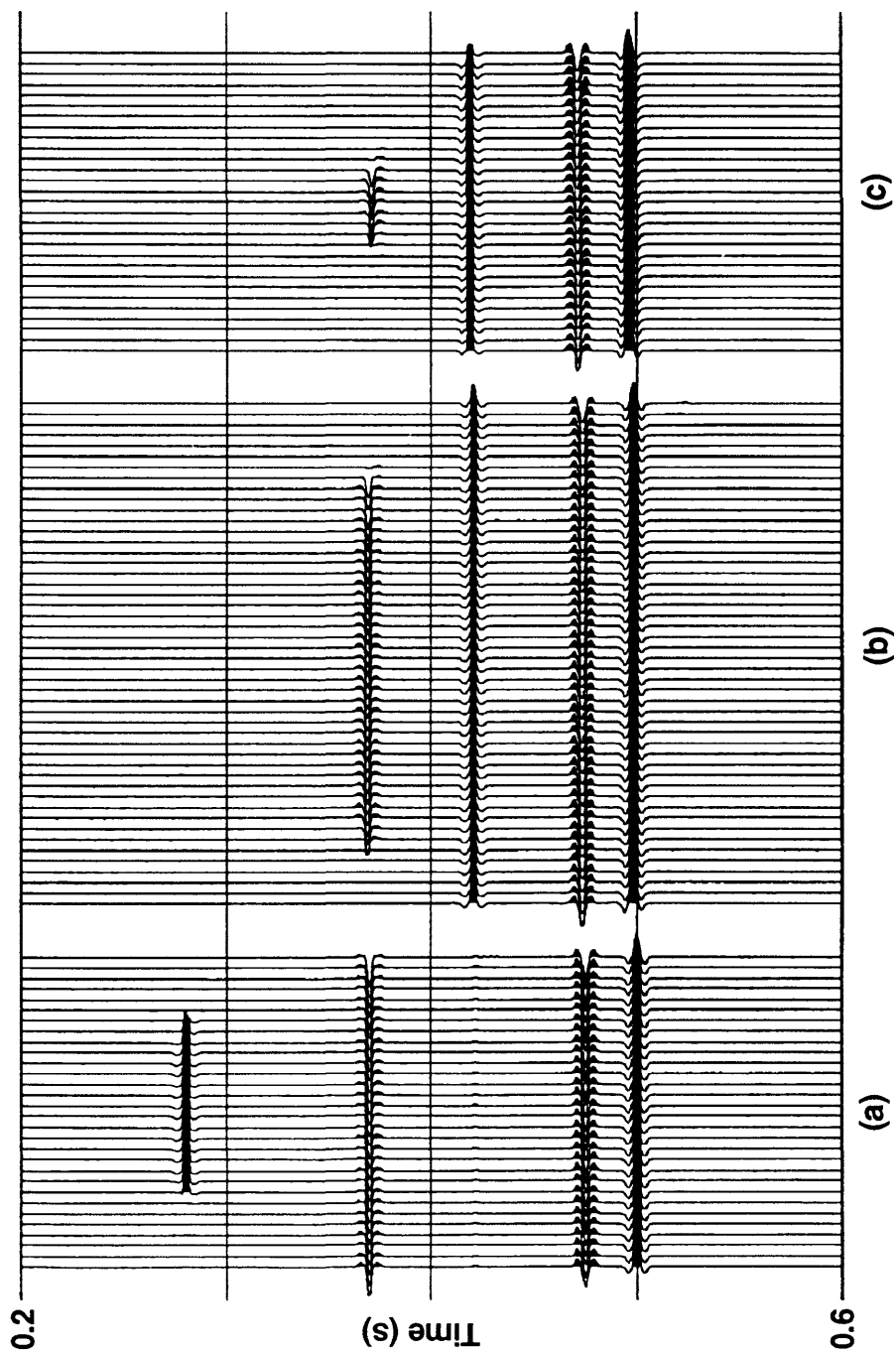
FIG. 5.23. Upgoing reflection data in CMD gathers, after HMO correction has been applied. The CMD depths for the gathers are (a) 238.5 m, (b) 291 m, and (c) 366 m.
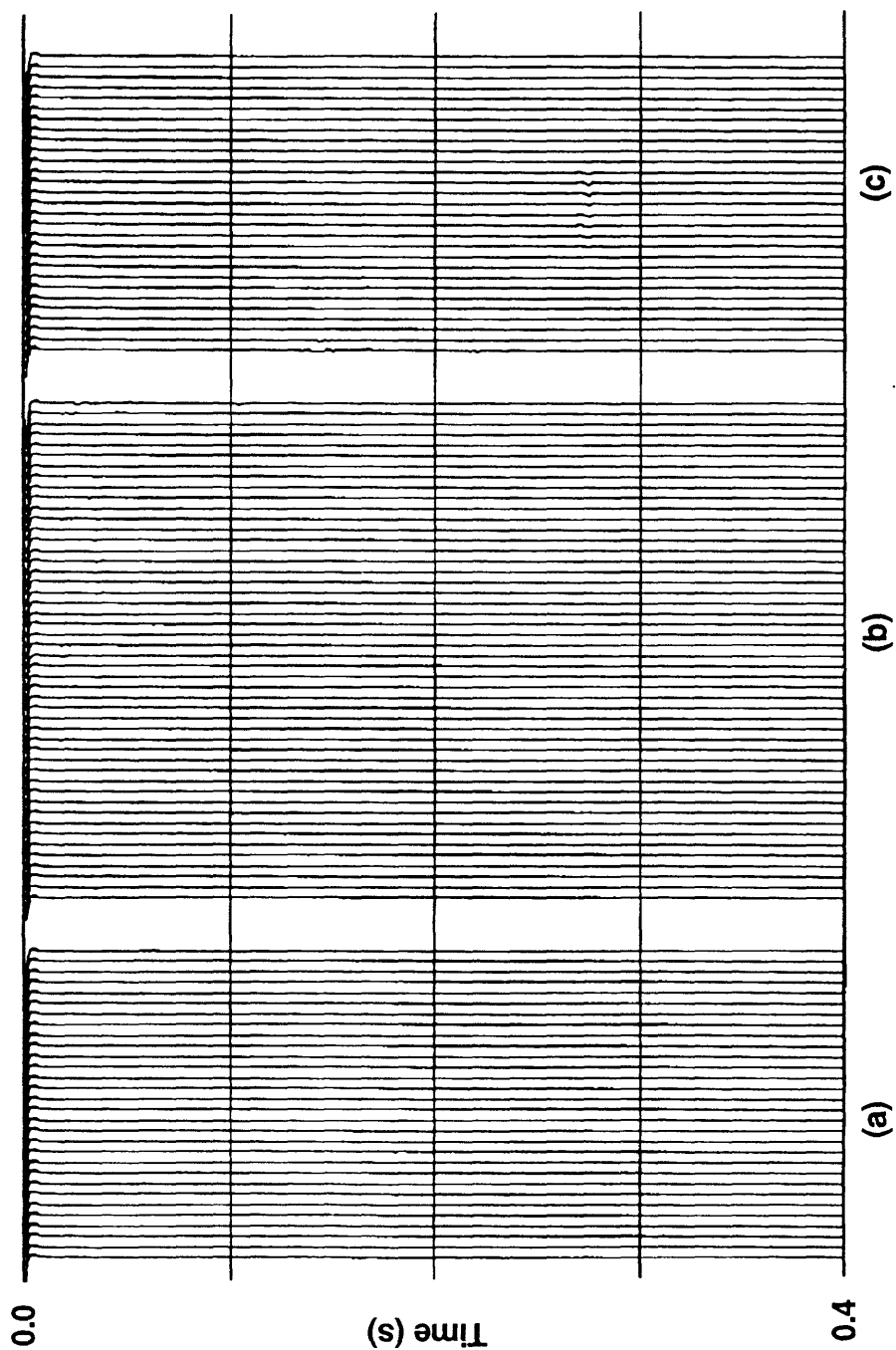
FIG. 5.24. Downgoing reflection data in CMD gathers, after HMO correction has been applied. The CMD depths for the gathers are (a) 238.5 m, (b) 291 m, and (c) 366 m.

5.6 CRB gathering, stacking and imaging

5.6.1 CRB gathering

Crosswell reflections in CMD gathers after corrections represent the energy vertically reflected from different positions along the reflector. In order to produce a stacked section, traces need to be re-ordered into common-reflection-point gathers. So it is essential to find the reflection points for each trace.

Figure 5.25 schematically shows the lateral location of two reflection points. In a constant-velocity medium, the lateral dispersal of the reflection point from the point half-way between the wells is given by:

$$\Delta x = \frac{x}{4} \frac{g - s}{r - m} \quad , \tag{5.24}$$

where r is depth of the target reflector, which can be found from equation (5.19), and m is the CMD depth. The distance from the source well to the reflection point is

$$L = \frac{x}{2} \left(1 + \frac{1}{2} \frac{g - s}{r - m} \right) \quad . \tag{5.25}$$

To ensure that each gather has sufficient fold, common reflection bins (CRBs) should be used, instead of common reflection points. The interwell region is divided into a number of bins with a certain width. The bin size depends on the desired fold. For each trace, a location of the reflection point for a target reflector is found according to equation (5.25). Traces that fall within the same bin are collected into a CRB gather. Traces in each CRB gather are then summed to yield a stacked trace.

Figure 5.26 shows the upgoing reflection data in two CRB gathers. For both gathers, the bin size was 0.5 m, and the data were gathered according to the depth of
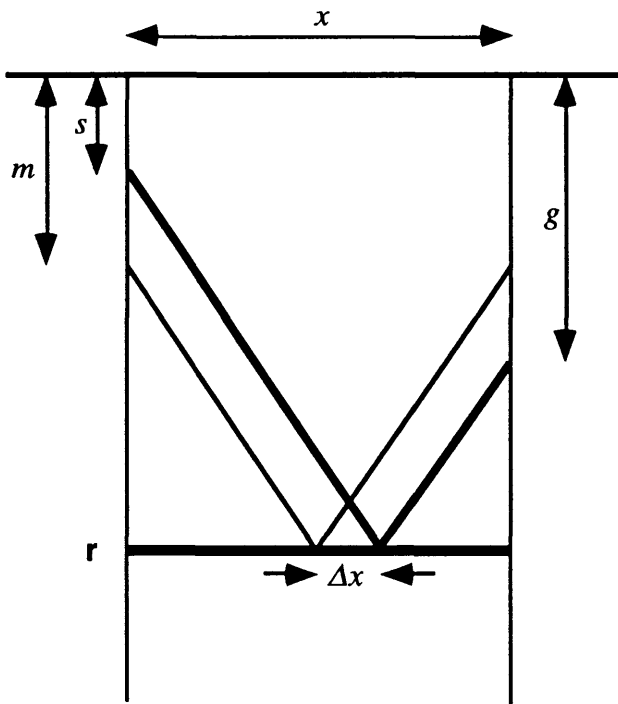
FIG. 5.25. Diagram showing the lateral position of
reflection points.

horizon *L3*. For gather (a), the lateral distance of the reflection point is 24 m away from

the source well, and the fold (traces per CRB gather) is 48. For gather (b), the reflection

point is 25 m away from the source well, and a fold of 50 is achieved. Generally, CRB

gathers from the middle reflection bins have higher fold. In the gathers, there exist some

residual statics between traces. The holes appearing on some events are the result of

separating the upgoing and downgoing reflections which interfere with each other at their

intersection points, because of the limitation of the modeling program used to generate the

synthetic data. Shown in Figure 5.27 is a CRB gather for downgoing refection. The data

were gathered with reference to the free surface. The bin size used is 0.5 m. The reflection

bin is 25 m away from the source well. This gather has a fold of 150.

111
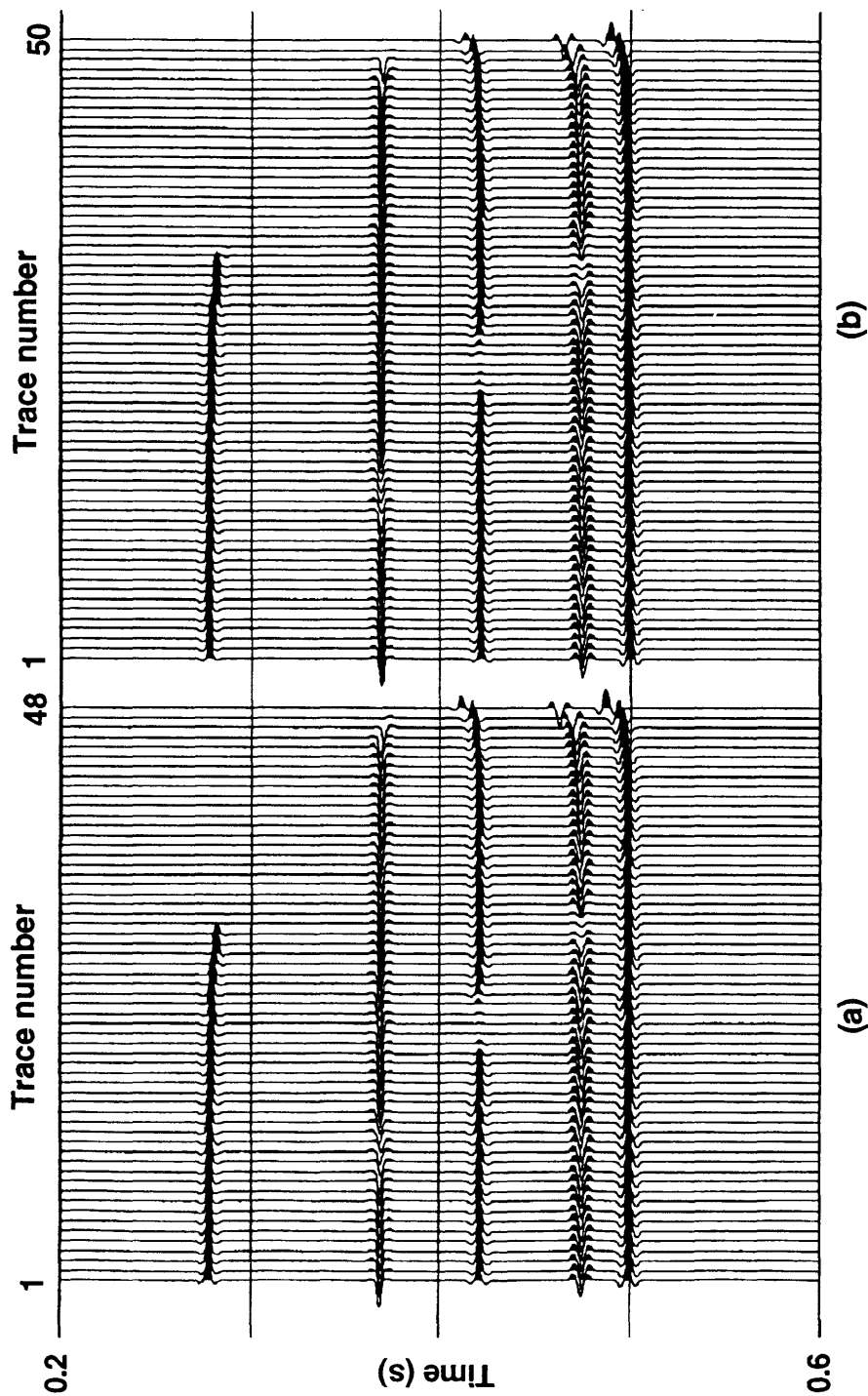
FIG. 5.26. Upgoing reflection data in common-reflection-bin gathers. Bin size used is 0.5 m. The depth of layer *L3* is used for the imaging depth. For gather (a), the offset from the source is 24 m, and fold is 48. For gather (b), the offset is 25 m and fold is 50.
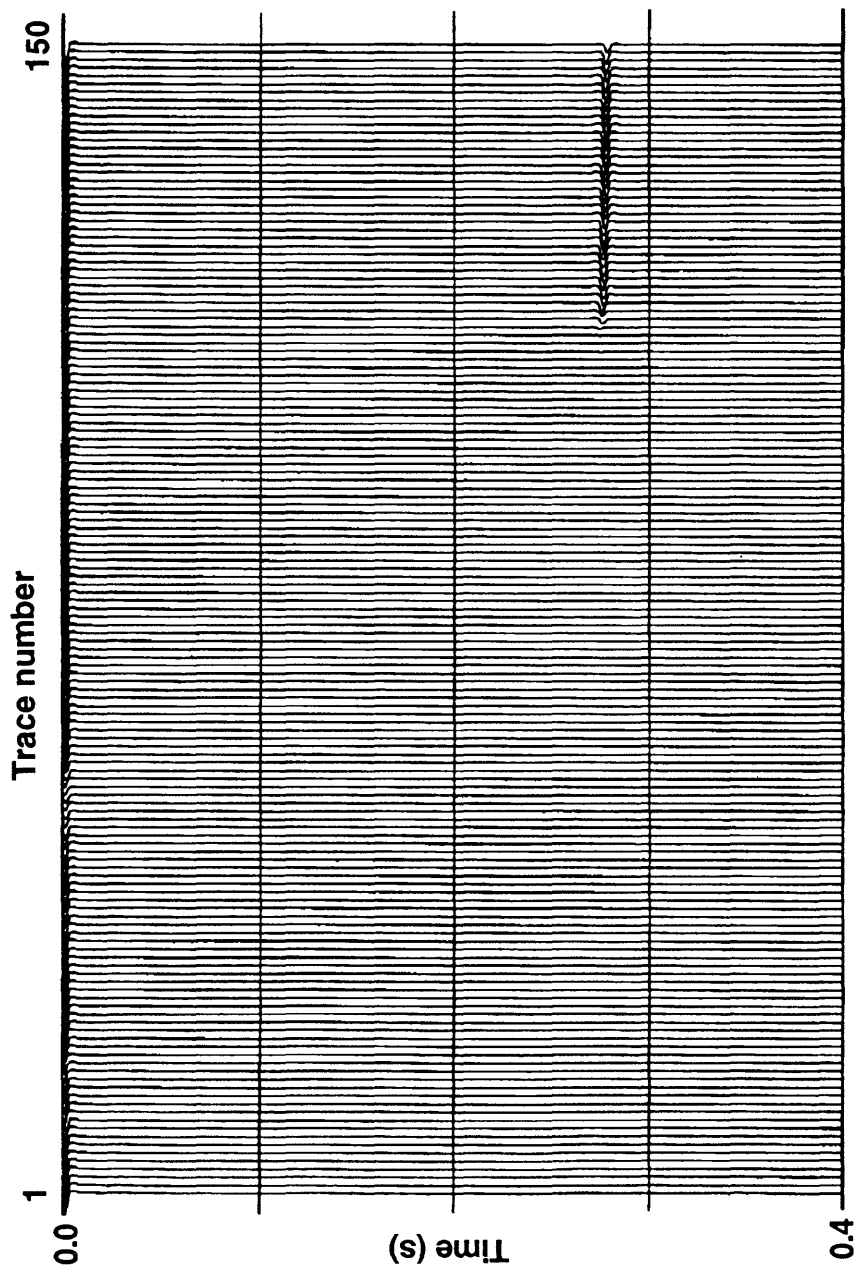
FIG. 5.27. Downgoing reflection data in a common-reflection-bin gather. Bin size used is 0.5 m. The offset from the source well is 25 m. For this gather, a fold of 150 is achieved.

5.6.2 Imaging via stacking

A stacked section can be generated by summing traces in each CRB gather. Since upgoing and downgoing reflection data are processed separately, there should be two stacked sections. Eventually, the two sections need to be combined to get a final stacked section.

Shown in Figure 5.28 is a time section of upgoing reflection data. Since both VMO and HMO corrections have been applied, the data are displayed in two-way vertical traveltime. The horizontal axis of the section is the bin number, representing the horizontal distance of each reflection bin to the source well. In the upgoing reflection case, the bin number starts from 2, and ends at 109, indicating a range of 53.5 m between the boreholes that has been imaged. In the section, five reflection events are seen, representing reflectors *L2* to *L6*, from shallow to deep. Most reflectors except the shallowest event (*L2*) are well imaged. Note the lateral extent of the top and bottom (*L3* and *L4*) of the zone of interest. The stacked section for downgoing waves is given in Figure 5.29, where reflections from the free surface (*L1*) and the reflector *L2* are imaged, with a negative polarity. It is seen that the shallow horizons are less imaged by downgoing reflections than the deep horizons by upgoing reflections. When combining both up- and downgoing reflection data in order to construct a final time section, it is necessary to reverse the polarity of the downgoing reflection data.

The final stacked time section, containing both up- and downgoing reflections, is displayed in Figure 5.30. A depth section can also be obtained if time-depth conversion is carried out. The depth section is given in Figure 5.31, along with the model used. The medium velocity was used in time-depth conversion. A trace balancing was applied to the section. From either time or depth section, it is seen that an image of all layers in the geologic model has been reconstructed. Although the shallow reflectors are less imaged because of the limited coverage of the rays emitted from the crosswell geometry, deep
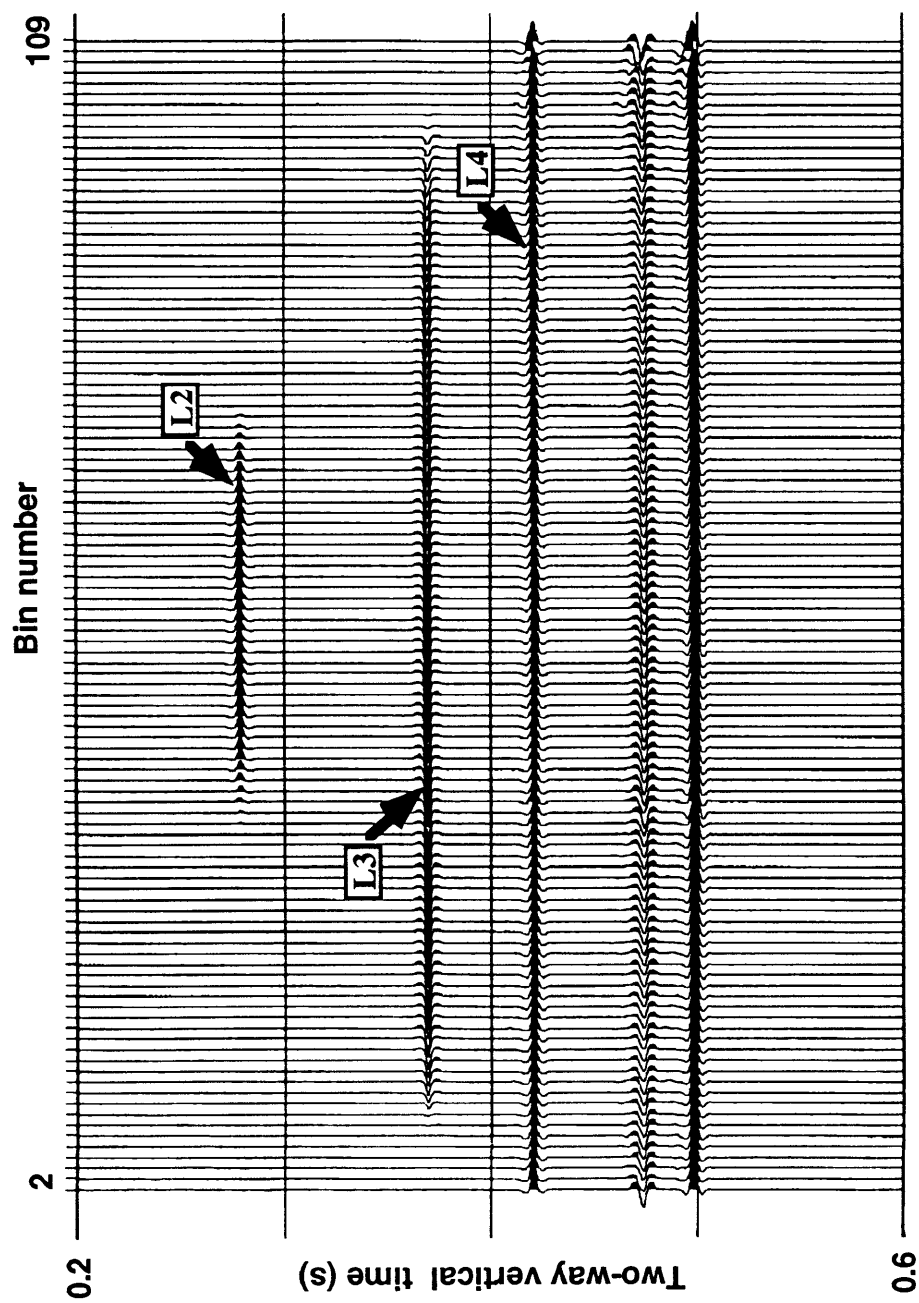
FIG. 5.28. Stacked time section for upgoing reflection data.
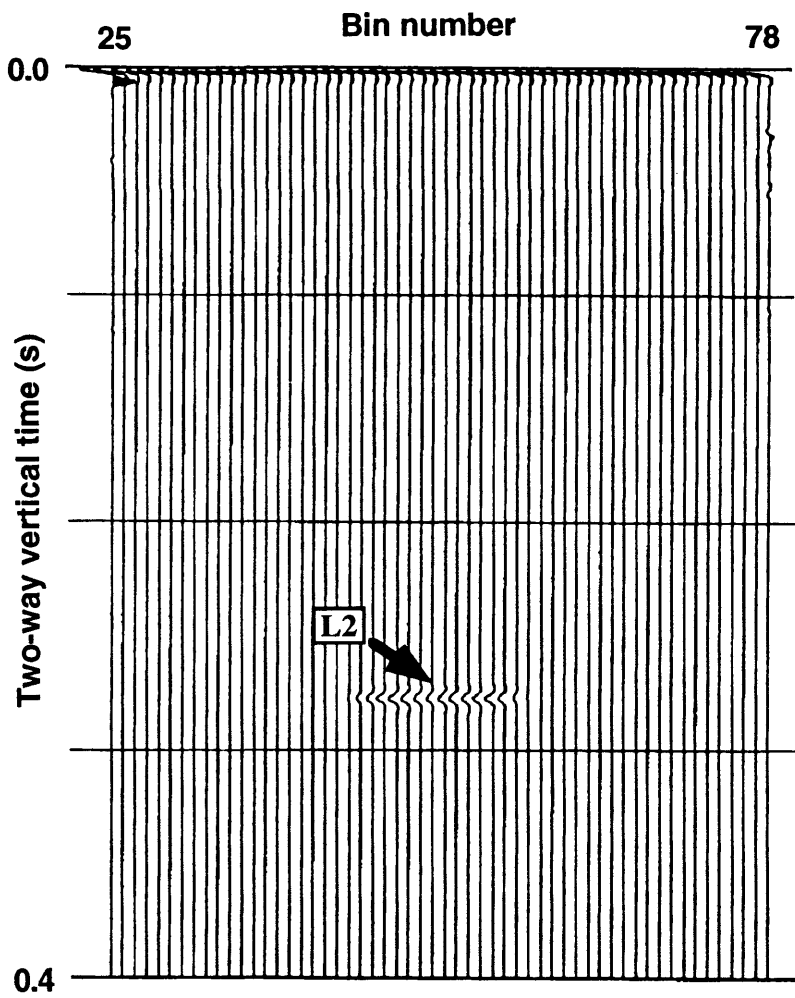
FIG. 5.29. Stacked time section for downgoing reflection data.

reflectors are well imaged. This indirectly shows the advantage of imaging horizons around and below the bottom of drilled wells with crosswell reflections.

116
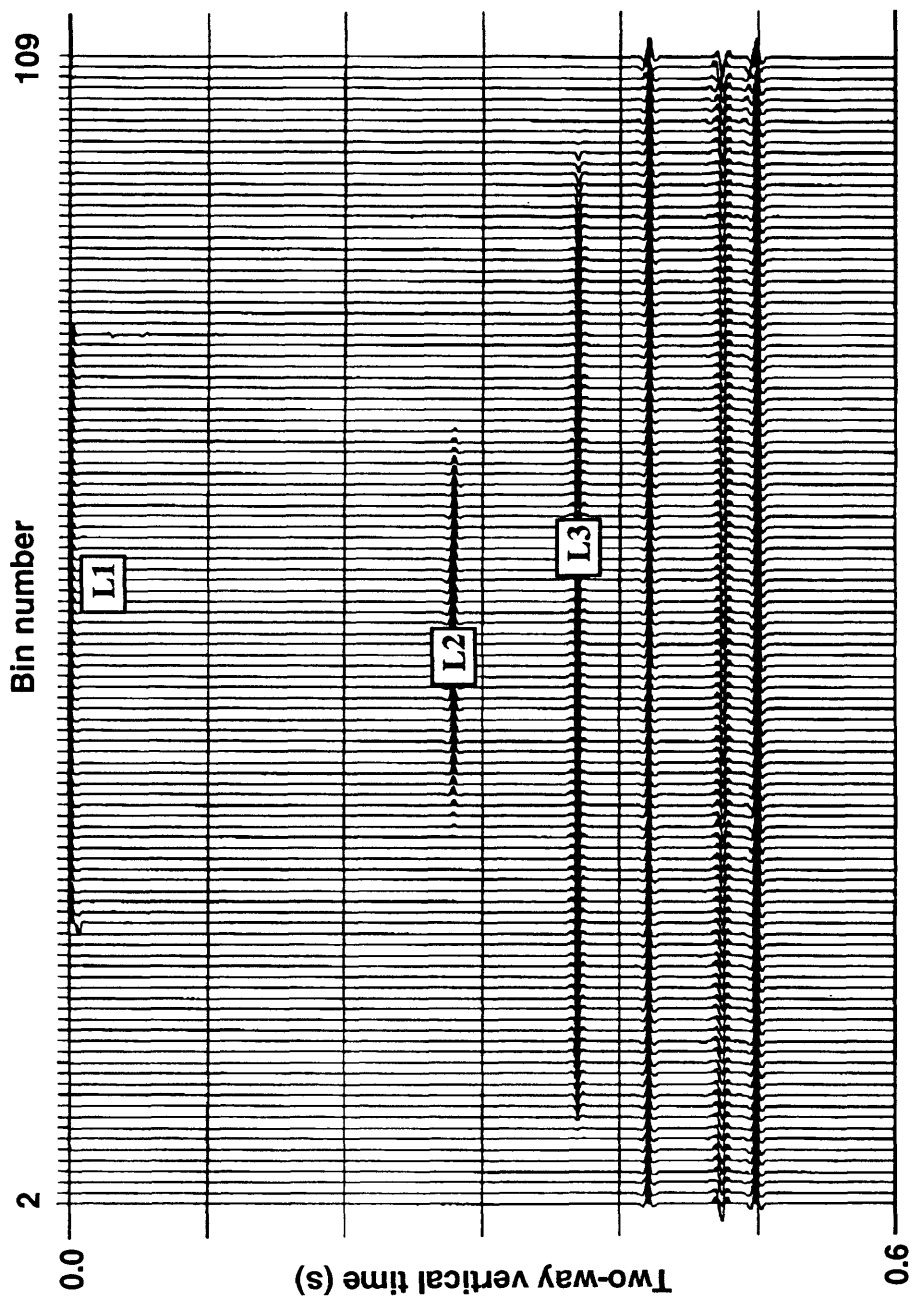
FIG. 5.30. Final stacked time section.

117

Depth (m)

0

200

400

600

54.0

Distance to source well (m)

L1

L3
L4

0.5

R

S

55 m

2250 m/s 2.1 g/m3

2250 m/s 2.2 g/m3

2250 m/s 1.9 g/m3

2250 m/s 1.95 g/m3

2250 m/s 1.8 g/m3

2250 m/s 2.3 g/m3
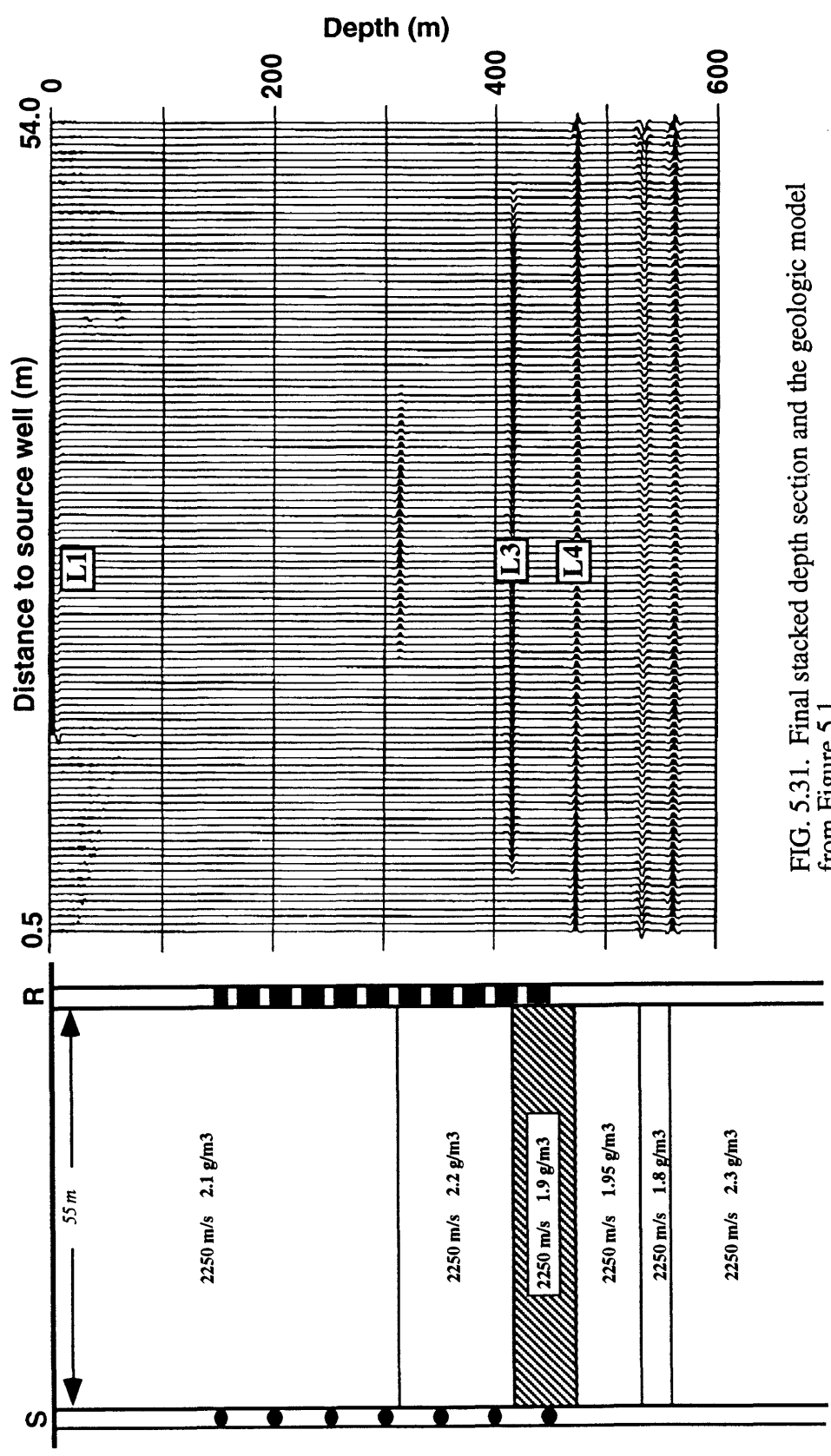
FIG. 5.31. Final stacked depth section and the geologic model
from Figure 5.1.

5.7 Summary

In this chapter, the fundamental concepts in crosswell reflection data processing and imaging have been discussed, and a procedure of crosswell data processing that leads to a final stacked depth section has been outlined. Different data sorting domains can be used, including common-source gather, common-receiver gather, common-interval gather, and common mid-depth gather. Each gather has its specific uses during data processing. For instance, CI gathers are useful in separating direct arrivals and reflections. The zero-interval CI gather can be used to derive velocity information for vertical and horizontal moveout corrections. The CS or CR gather is the place where up- and downgoing waves can be effectively separated through multichannel filtering. CMD gathers provide a partial image of the subsurface, and can be used to apply VMO and HMO corrections. After these corrections, reflection data are sorted into common-reflection-bin gathers and then stacked to yield a stacked time section, or through a time-depth conversion, a final depth section. All the important processing steps that have been discussed in this chapter can be summarized by a flow given in Figure 5.32. With synthetic crosswell reflection seismic data, I have shown the effectiveness of the crosswell reflection imaging method.
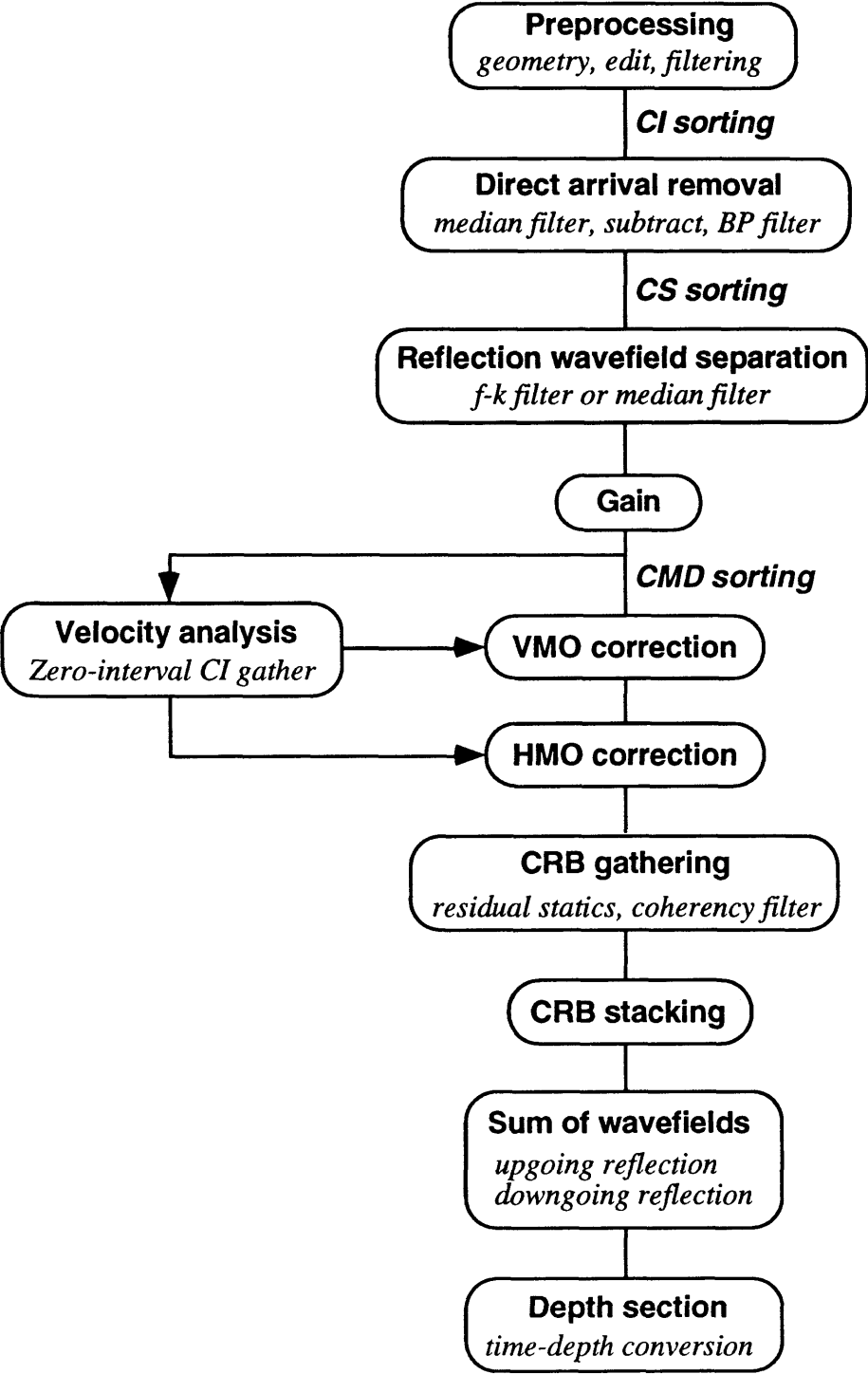
FIG. 5.32. CMD-based processing flow for crosswell reflection imaging.

Chapter 6

Crosswell reflection imaging: Common reflection point stacking method

6.1   Introduction

In Chapter 5, I have presented the CMD-based imaging technique. One characteristic of this method is that, after reflection-wavefield separation, data are sorted into common mid-depth (CMD) gathers, where vertical and horizontal moveout corrections are applied with velocity information derived from a zero-interval gather. Based on the moveout-corrected CMD gathers, data are grouped into common-reflection-bin gathers and stacked to obtain a final stacked section.

It is found, however, that reflection data can be directly sorted into common-reflection-point (CRP) gathers without using the CMD gathers. In the CRP gathers, horizontal and vertical moveouts are corrected respectively, followed by trace stacking. This leads to a new crosswell reflection imaging technique, here referred to as the CRP stacking method, which is the subject of this chapter. I will first introduce the concepts of the CRP stacking method. These concepts will be illustrated with synthetic data examples. A complete processing flow will be developed that may be used in processing

field crosswell data. An idea of composite stacking will be examined. I will conclude this chapter with a summary. Application of the CRP stacking method to field crosswell seismic data can be found in Chapter 7.

6.2   Concepts

The CRP stacking method is illustrated schematically in Figure 6.1. The key to this method is to sort upgoing (or downgoing) reflection seismic traces into a new data domain according to their common reflection point position, as shown in Figure 6.1a. For any trace in the CRP gather, the CRP position along a flat reflector in a constant-velocity (V) medium is given by

$$L = \frac{x}{2}\left(1 + \frac{1}{2}\frac{g-s}{r-m}\right) , \tag{6.1}$$

where L is distance of the CRP measured from source well S, x is horizontal distance between S and R (the receiver well), g is receiver depth, s is source depth, r is reflector depth, and m is mid-depth for that trace (i.e., half of the sum of g and s). When g and s are equal, the CRP is half way between the two boreholes. Equation (6.1) is actually equivalent to equation (5.25). In processing, a bin of a certain size is assigned to each CRP so that all traces falling into the same CRP bin are grouped to form a CRP gather, and every such gather has enough fold. Figure 6.1a illustrates the geometry of a CRP gather of N traces and Figure 6.1b shows the traveltime vs mid-depth curve of a reflection event from that gather.

From the geometry shown, a relation between time and depth can be derived:
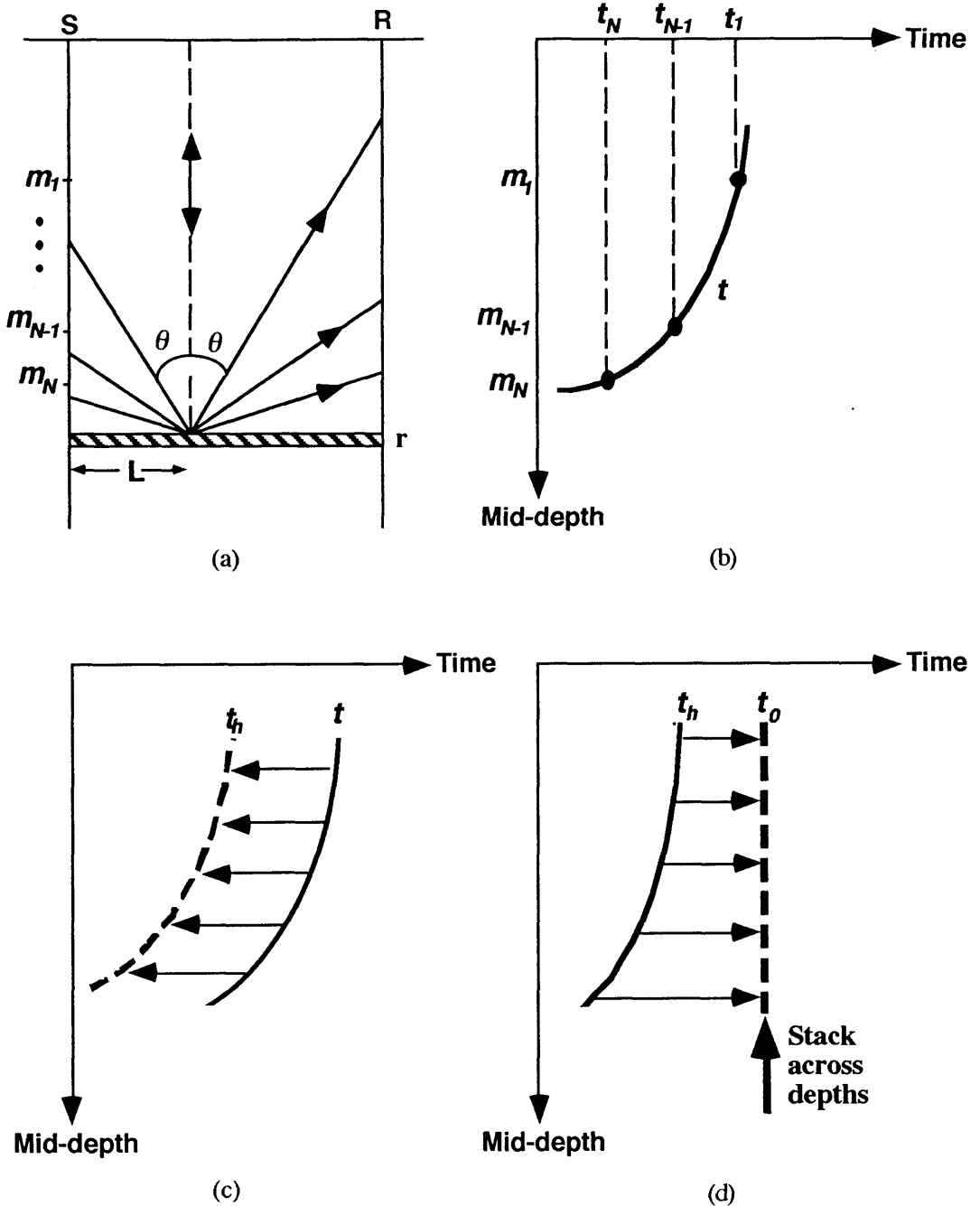
FIG. 6.1. The common-reflection-point stacking method. (a) CRP gathering; (b) traveltime-depth relation; (c) horizontal moveout correction (from t to t_h); and (d) vertical moveout correction (from t_h to t_0) and stacking across the gather.

$$t^2 = \left(t_0 - \frac{2m}{V}\right)^2 + \left(\frac{x}{V}\right)^2 \quad ,$$ (6.2)

where t_0 is two-way *vertical* time from the reflector to the free surface indicated by the dashed line in Figure 6.1a. Equation (6.2) is very similar to the standard NMO equation used for surface seismic data, and implies that reflections in a CRP gather have a hyperbolic pattern.

The second term on the right side of equation (6.2) is a constant since x is constant for the crosswell geometry and V is assumed the constant velocity. This term constitutes a time shift (from t to t_h) which corrects for horizontal moveout (HMO) due to the well separation distance x. If we make the following substitution in equation (6.2):

$$t_h = t_0 - \frac{2m}{V} \quad ,$$ (6.3)

then we have

$$t^2 = t_h{}^2 + \left(\frac{x}{V}\right)^2 \quad .$$ (6.4)

So applying an HMO correction is equivalent to mapping the data from $P(t, m)$ to $P(t_h, m)$ as shown in Figure 6.1c.

After HMO correction, the effect of vertical moveout (VMO) defined by the term $2m/V$ still exists in the data. Therefore, the next step is VMO correction. The VMO correction is calculated through the relation

$$t_0 = t_h + \frac{2m}{V} \quad .$$ (6.5)

The process of VMO correction is shown in Figure 6.1d. After applying both HMO and

VMO corrections, the reflection event is flattened. Then the traces are stacked across mid-depths to obtain a stacked section.

Based on the above analysis, the CRP stacking method is composed of four steps: 1) Sorting reflection data into CRP gathers; 2) Correcting for horizontal moveout; 3) Correcting for vertical moveout; and 4) Stacking. Figure 6.2 describes a processing flow, which is a modification of the processing procedure shown in Figure 5.32.

6.3   Synthetic example

I will use the same synthetic data as used in Chapter 5 to demonstrate the concepts of the CRP stacking method. To avoid repetition, I will skip all processing steps up to reflection-wavefield separation. Velocity analysis in the zero-interval gather is still useful, and will also be part of the CRP stacking method. Again, I will not repeat this step. However, the result from the previous velocity analysis will be simply used here.

The separated reflection data are sorted into CRP gathers, according to their common reflection points determined by equation (6.1). Figure 6.3 displays two CRP gathers of upgoing reflection data. During CRP gathering, the bin size was 0.5 m, and the reflector depth for horizon *L3* was used in equation (6.1). In Figure 6.3, the horizontal axis is mid-depth and the vertical axis is two-way traveltime. Bin numbers for the two gathers are respectively 49 and 51, representing a lateral distance of 24 m and 25 m, measured from the source borehole. Both gathers contain five reflection events. The event from the top of the target zone is marked with *L3*. From this Figure, it is seen that as predicted, each reflection event shows a hyperbolic shape and that deeper events have larger moveouts than shallower events. The moveouts include the vertical and horizontal moveouts. In this Figure, the holes seen on the reflections are caused for the same reason

```
            ┌─────────────────────────────┐
            │       Preprocessing         │
            │  geometry, edit, filtering  │
            └─────────────────────────────┘
                        │ CI sorting
            ┌─────────────────────────────────────┐
            │      Direct arrival removal          │
            │ median filter, subtract, BP filter   │
            └─────────────────────────────────────┘
                        │ CS sorting
            ┌──────────────────────────────────────┐
            │   Reflection wavefield separation     │
            │       f-k filter or median filter     │
            └──────────────────────────────────────┘
                        │
                   ┌─────────┐
                   │  Gain   │
                   └─────────┘
```

Preprocessing
geometry, edit, filtering

CI sorting

Direct arrival removal
median filter, subtract, BP filter

CS sorting

Reflection wavefield separation
f-k filter or median filter

Gain

CRP gathering

Velocity analysis
Zero-interval CI gather

HMO correction

VMO correction

CRP stacking

Sum of wavefields
upgoing reflection
downgoing reflection

Depth section
time-depth conversion

FIG. 6.2. Processing flow chart for the common-reflection-point stacking method.

126
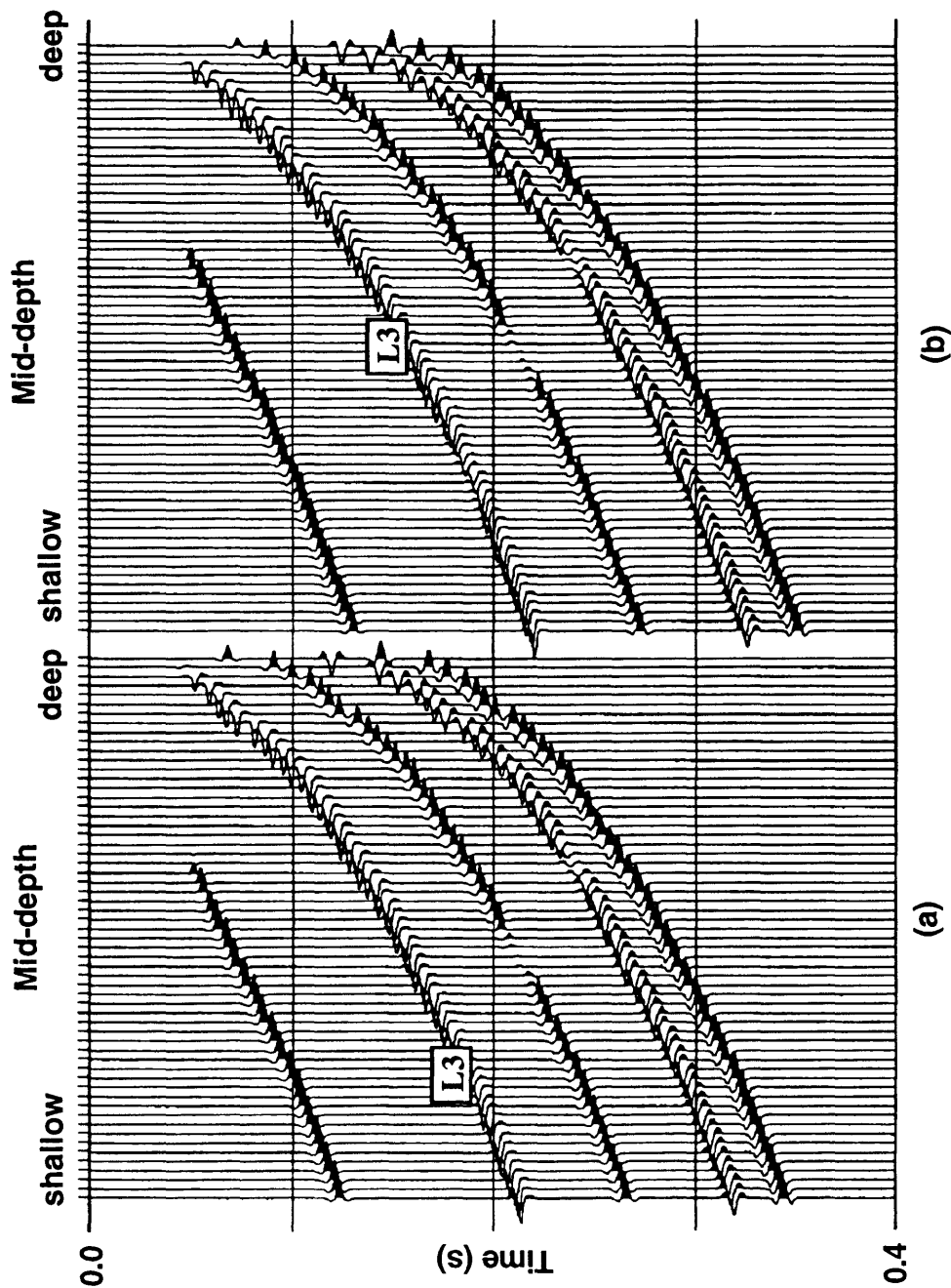
FIG. 6.3. Common-reflection-point gathers of synthetic crosswell upgoing reflection data. The CRP bin width is 0.5 m. For gathers (a) and (b), the bin number is 49 and 51 respectively, representing a horizontal distance of 24 m and 25 m measured from the source well. The horizon labeled *L3* is the top of the target zone.

as that in Chapter 5.

Shown in Figure 6.4 is a CRP gather of downgoing reflection data, whose bin number is 49. The bin size used when gathering the data is also 0.5 m, so the bin number of 49 is equal to a horizontal distance of 24 m from the source well. The depth of the first reflector $L1$, i.e., the free surface of the geologic model in Figure 5.1, was used. In this case, it is zero. The downgoing reflection gather includes only two reflection events, one from $L1$, and the other from $L2$. $L1$ is marked in Figure 6.4. Notice that in the time-depth domain, the $L1$ event is deeper than $L2$, even though in the depth model $L2$ is deeper than $L1$. Both reflection events will be correctly re-positioned after vertical and horizontal moveout corrections are applied. Note also a partial coverage of event $L2$. The hyperbolic pattern of the downgoing-reflection events, like those of upgoing reflections, does agree with the theoretical prediction.

Recall that equation (6.1), which determines CRP positions, is dependent upon the reflector depth, r. This depth dependence determines, in turn, the dependence of CRP gathering on reflector depths. Therefore, in each CRP gather, only one reflection event is actually from the same reflection point. In the case of Figures 6.3 and 6.4, the CRP gathering is true only for event $L3$ (upgoing) and for event $L1$ (downgoing). The rest of events in both figures are indeed *not* from the same reflection points. This problem is a limitation of the method being discussed.

HMO correction removes the effect of the horizontal distance between the source and receiver boreholes. The amount for HMO correction is determined by equation (6.4). Borehole offset is $x = 55$ m. The velocity for HMO correction was derived in Chapter 5, and it is 2250 m/s. Figures 6.5 and 6.6 respectively show the results of HMO correction for upgoing and downgoing reflection data in Figures 6.3 and 6.4. The difference between pre-HMO and post-HMO gathers is small though, because the borehole offset of
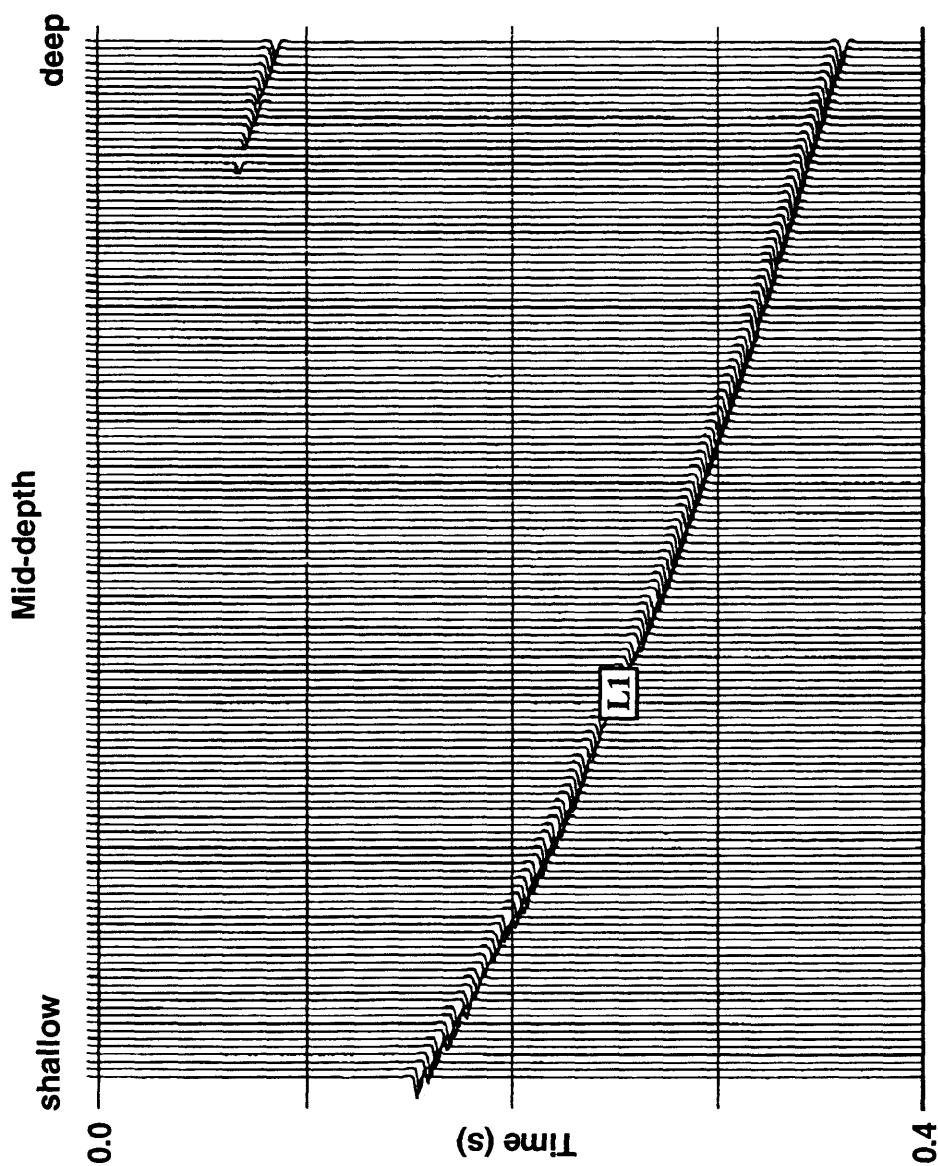
FIG. 6.4. Common-reflection-point gather of synthetic crosswell downgoing reflection data. The CRP bin width is 0.5 m. For this gather, the bin number is 49, representing a horizontal distance of 24 m measured from the source well. The horizon marked *L1* is from the free surface of the geologic model.
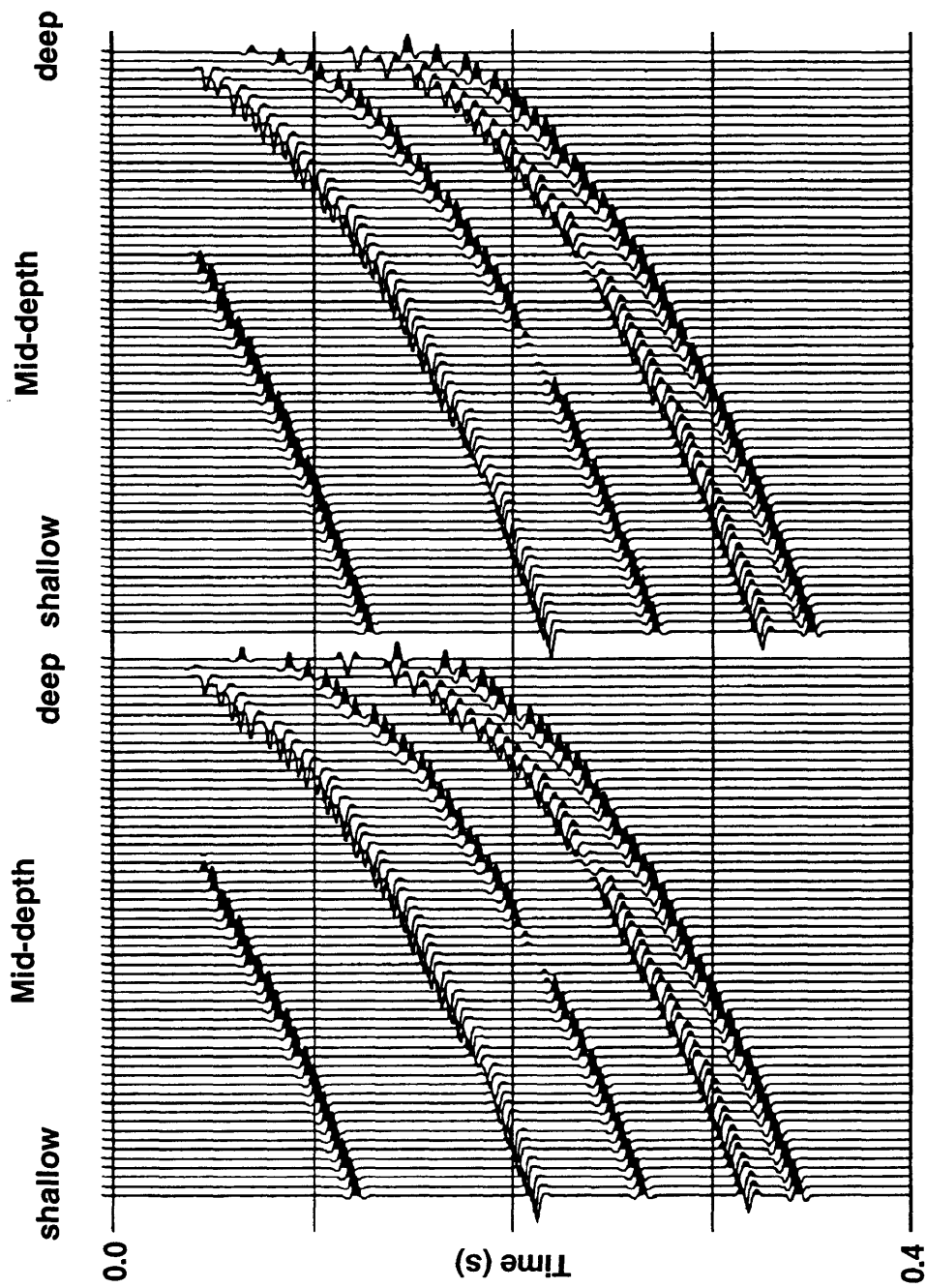
FIG. 6.5. Common-reflection-point gathers of upgoing reflection data after horizontal moveout correction.
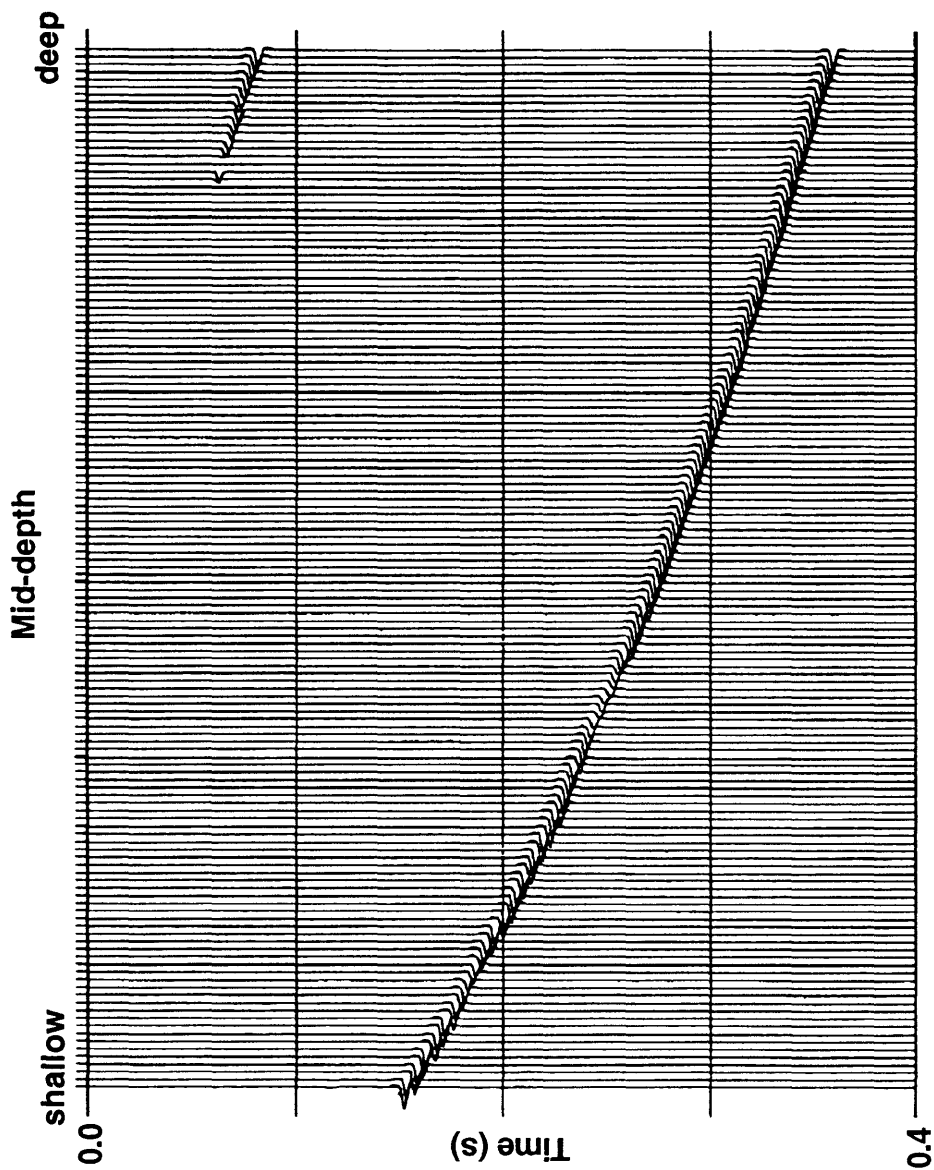
FIG. 6.6. Common-reflection-point gather of downgoing reflection data after horizontal moveout correction.

55 m causes a minor moveout in the data.

Figures 6.7 and 6.8 show the same CRP gathers after vertical moveout has been corrected. The VMO velocity of 2250 m/s was used in equation (6.5). After VMO correction, all reflection events are flattened, as expected by the theory. Applying both HMO and VMO corrections to the upgoing reflection data is equivalent to moving the source and receiver to a coincident location on the surface where reflection signals traveling vertically, as shown by the dashed line in Figure 6.1a, would have been recorded. This process is analogous to the NMO-corrected CDP gather case. A similar explanation can be made for the downgoing reflection situation. In the downgoing reflection gather, note that the relative position between horizons $L1$ and $L2$ has now been corrected. By VMO correction, a deeper reflection of $L1$ now becomes a flat reflection event appearing at the time of zero, corresponding to the free surface.

In Figure 6.7, there are no residual statics on the upgoing reflections as were seen in Figure 5.26. More importantly, unlike the HMO and VMO processes discussed in Chapter 5, which are dependent on the reflector depth, the HMO and VMO corrections described in this chapter are independent of the reflector depth. Looking back at equations (6.4) and (6.5), we see that all that is required in both moveout corrections is an input trace (time t), its mid-depth m, borehole offset x, and velocity V. The only dependence on reflector depth appears in equation (6.1) for the CRP location. Therefore, it makes the imaging method simpler and more reliable.

The final step in processing is a straightforward horizontal stacking of the moveout-corrected CRP gathers across the mid-depths. The examples of the stacked time sections are given in Figure 6.9 for upgoing reflections and in Figure 6.10 for downgoing reflections. The vertical axis for the stacked sections is two-way vertical time, and the horizontal axis is horizontal distance of each CRP location from the source well, expressed by bin number. The final stacked time section, combining up- and downgoing
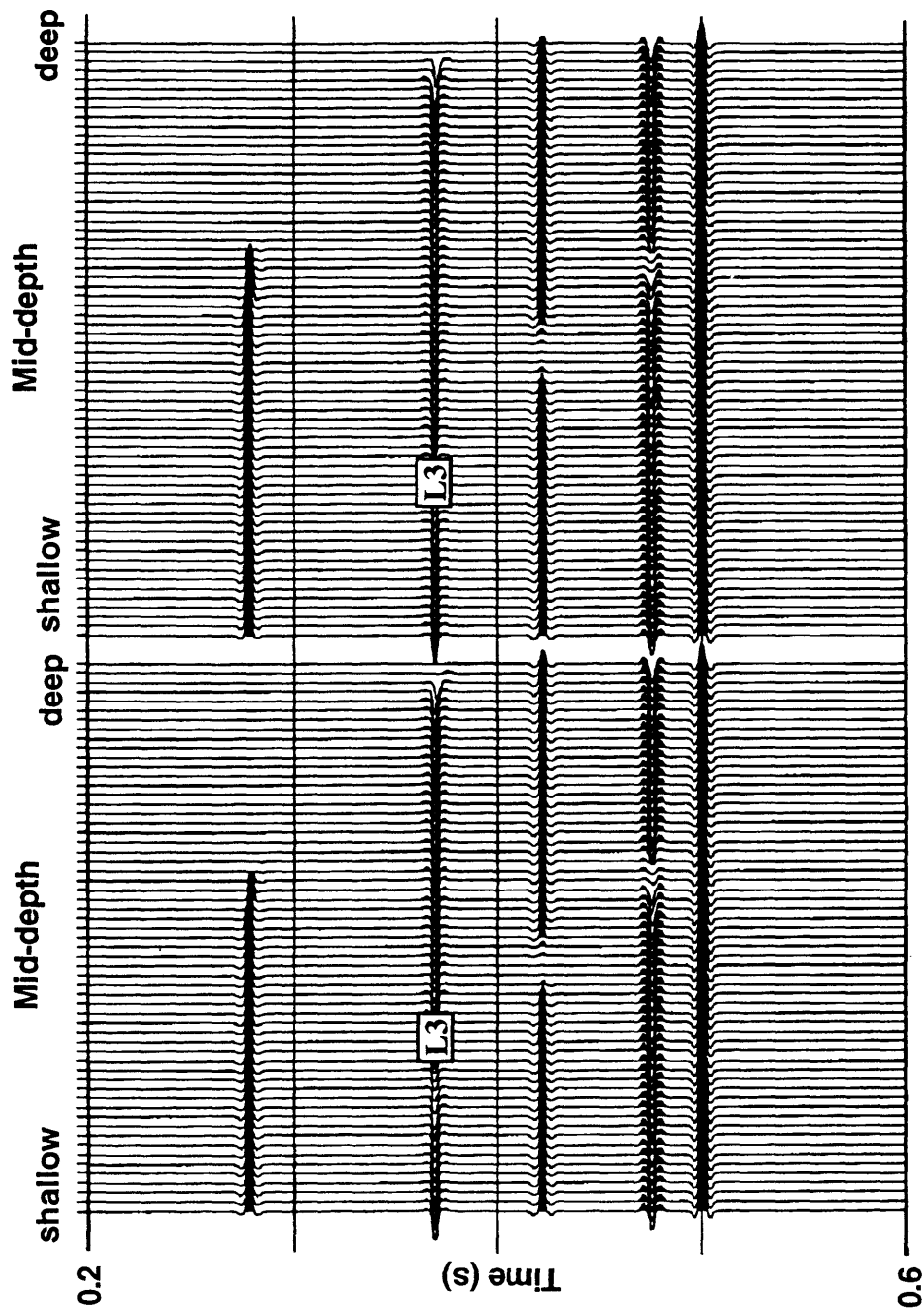
FIG. 6.7. Common-reflection-point gathers of upgoing reflection data after vertical moveout correction, which flattens the reflection events.
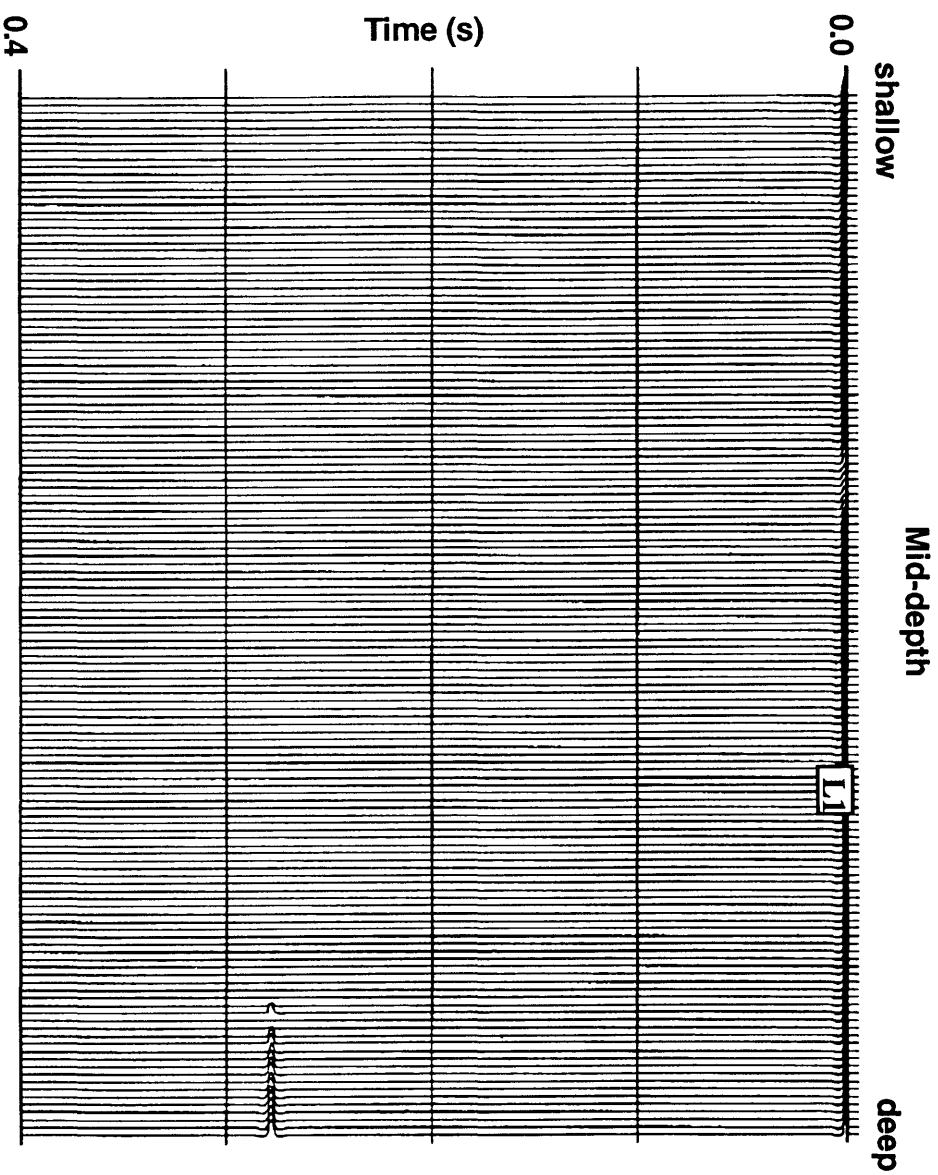
FIG. 6.8. Common-reflection-point gather of downgoing reflection data after vertical moveout correction, which flattens the reflection events and moves them into their correct positions.
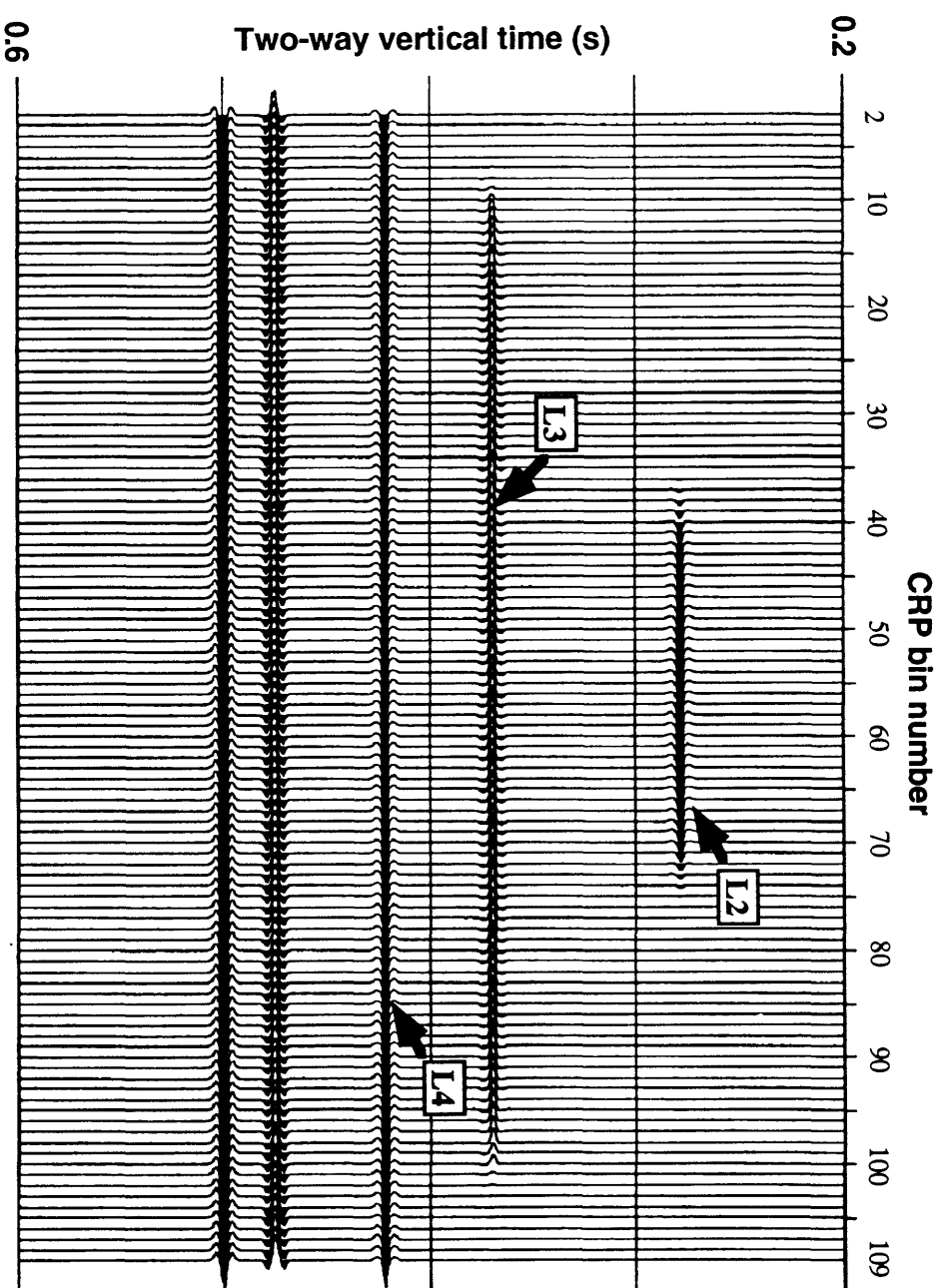
FIG. 6.9. Stacked time section of upgoing reflection data.

CRP bin number
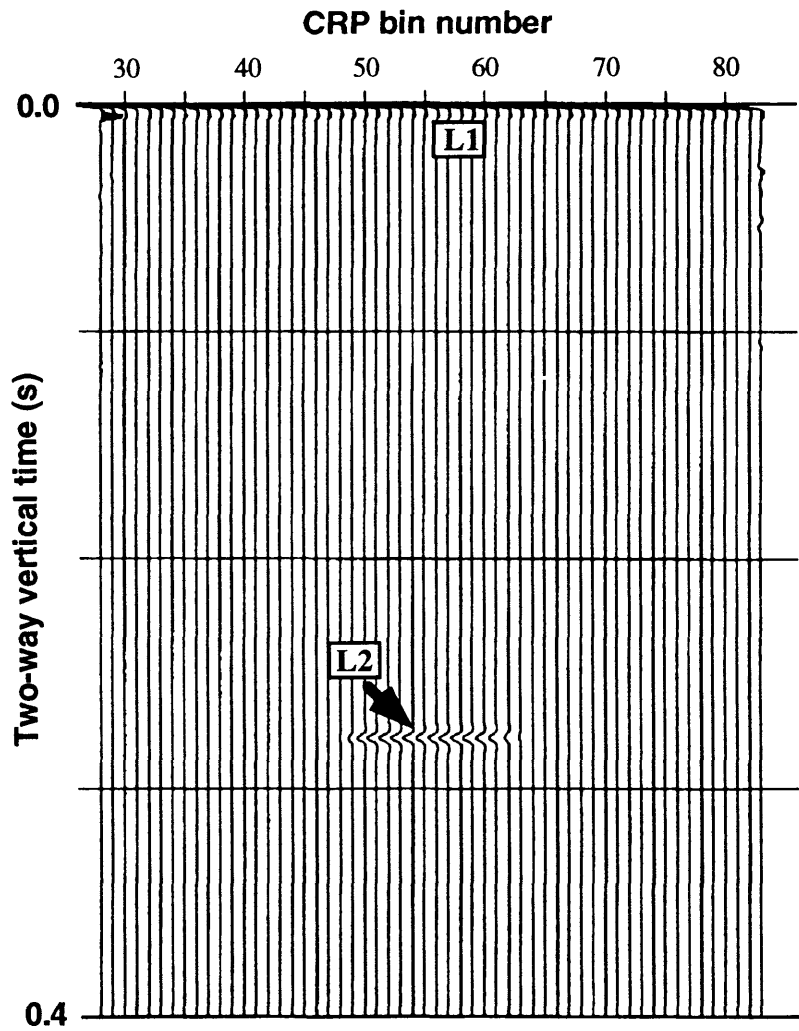
FIG. 6.10. Stacked time section of downgoing reflection data.

reflections, is given in Figure 6.11, with the first three reflectors marked. By comparison, it is easily seen that this stacked section is almost identical to the one given in Figure 5.30. This indicates that the imaging method works well.

136

CRP bin number

2 10 20 30 40 50 60 70 80 95 100 109

L1

L2

L3

Two-way vertical time (s)

0.0

0.6
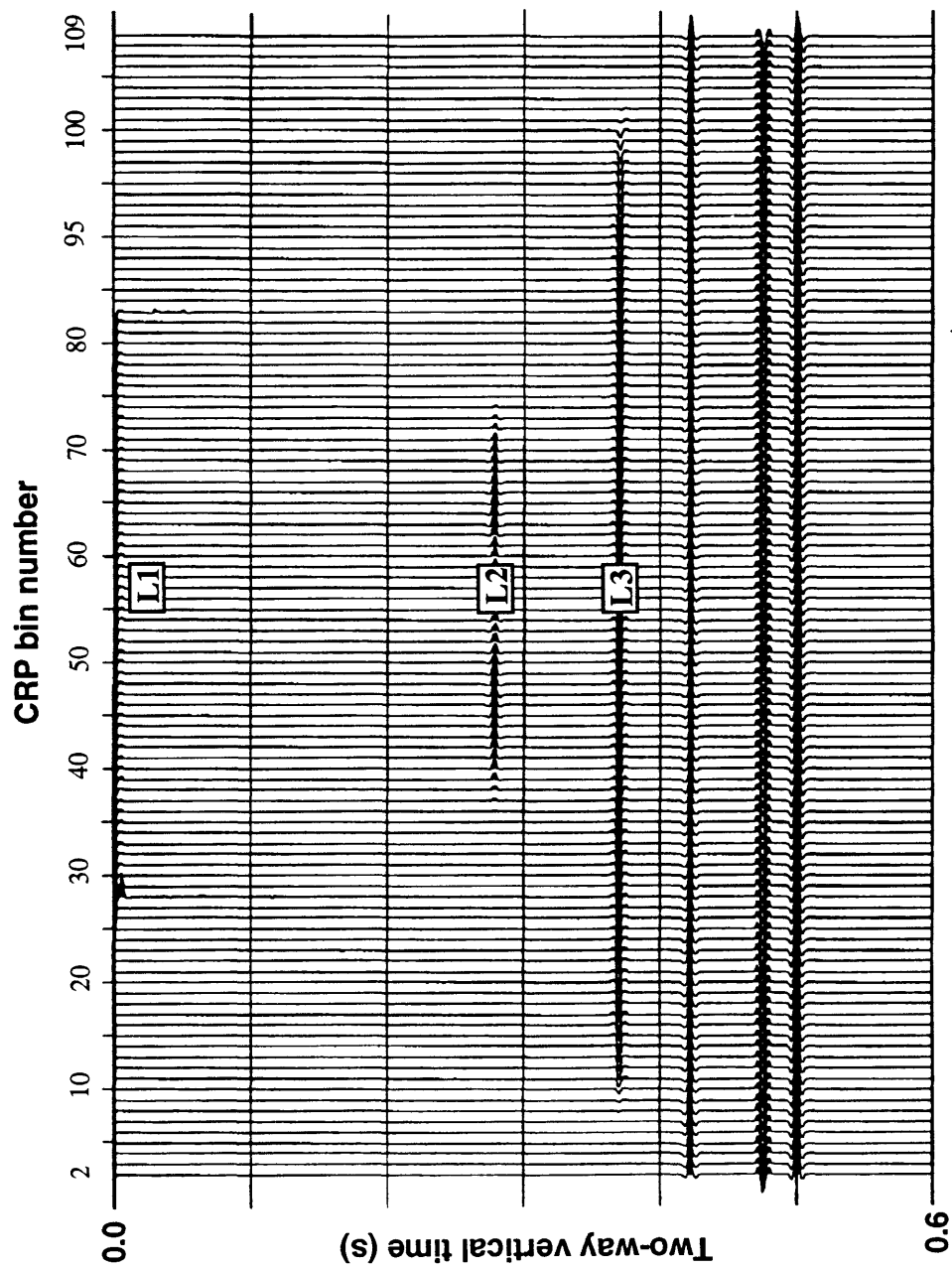
FIG. 6.11. Stacked time section containing upgoing and downgoing reflection data.

6.4   Composite stack

The above imaging procedure has a dependence on the target reflector depth, i.e., r in equation (6.1). To overcome this problem, images may be obtained for many different reflector depths (perhaps, in consecutive steps) and combined so that a composite stacked section is generated. Figure 6.12 shows an example of the composite stacked section. In this case, two depths from reflectors $L2$ and $L3$ were used. Note the broader lateral extent of these horizons in the composite section than the equivalent horizons in the CMD-based image in Figure 5.31. Caution should be taken because, when producing the composite stack, individual images may cause a sudden boundary between them, which is not desirable.

6.5   Summary

A processing flow based on the common-reflection-point stacking method has been outlined. Several kinds of gathers, including common-source, common-interval, and common-reflection-point gathers are used in the procedure. The CRP stacking method is simple and easy to implement. This method allows us to process crosswell reflection data in an even closer manner to the surface reflection seismic data analysis. After wavefield separation, reflection data are sorted into CRP gathers, corrected for horizontal and vertical moveout, and then stacked. A composite stacked section may be produced to overcome dependence of the imaging procedure on a single target depth. Tests with synthetic data have shown that the CRP stacking method is an effective imaging procedure.

138
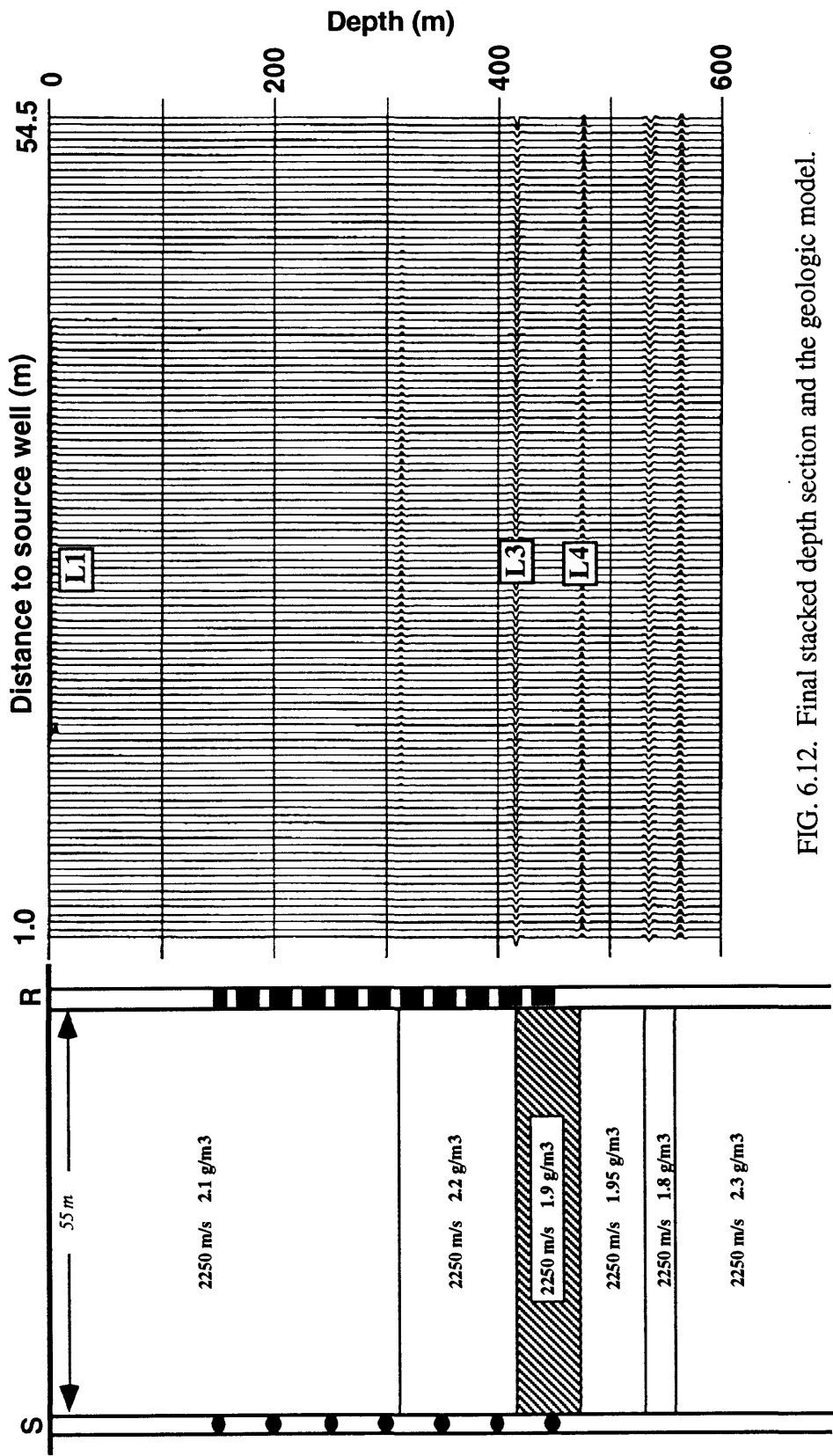
FIG. 6.12. Final stacked depth section and the geologic model.

Chapter 7

Field data example: Friendswood, Texas

7.1 Introduction

The emphasis in this chapter will be placed on the application of the theory and methods of crosswell reflection processing and imaging discussed in the previous chapters to field crosswell data. The field data to be used are from the combined surface-borehole seismic survey carried out near Friendswood, Texas, which was described in Chapter 2. In that chapter, the recorded data were analyzed with a typical shot record shown as an example. This same shot record is also displayed in Figure 7.1 and will be used for comparisons in this chapter.

The field crosswell data comprise a complicated wavefield. The common-source gather contains a clear direct wave, a number of strong tube-wave packages, upgoing and downgoing reflections, and random noise. Compared with the tube waves, the reflections are so weak that it is very difficult to image with them without proper processing. A processing sequence similar to the one proposed in Chapter 6 is used to process the field data. The initial steps during data processing are designed to achieve the objectives of
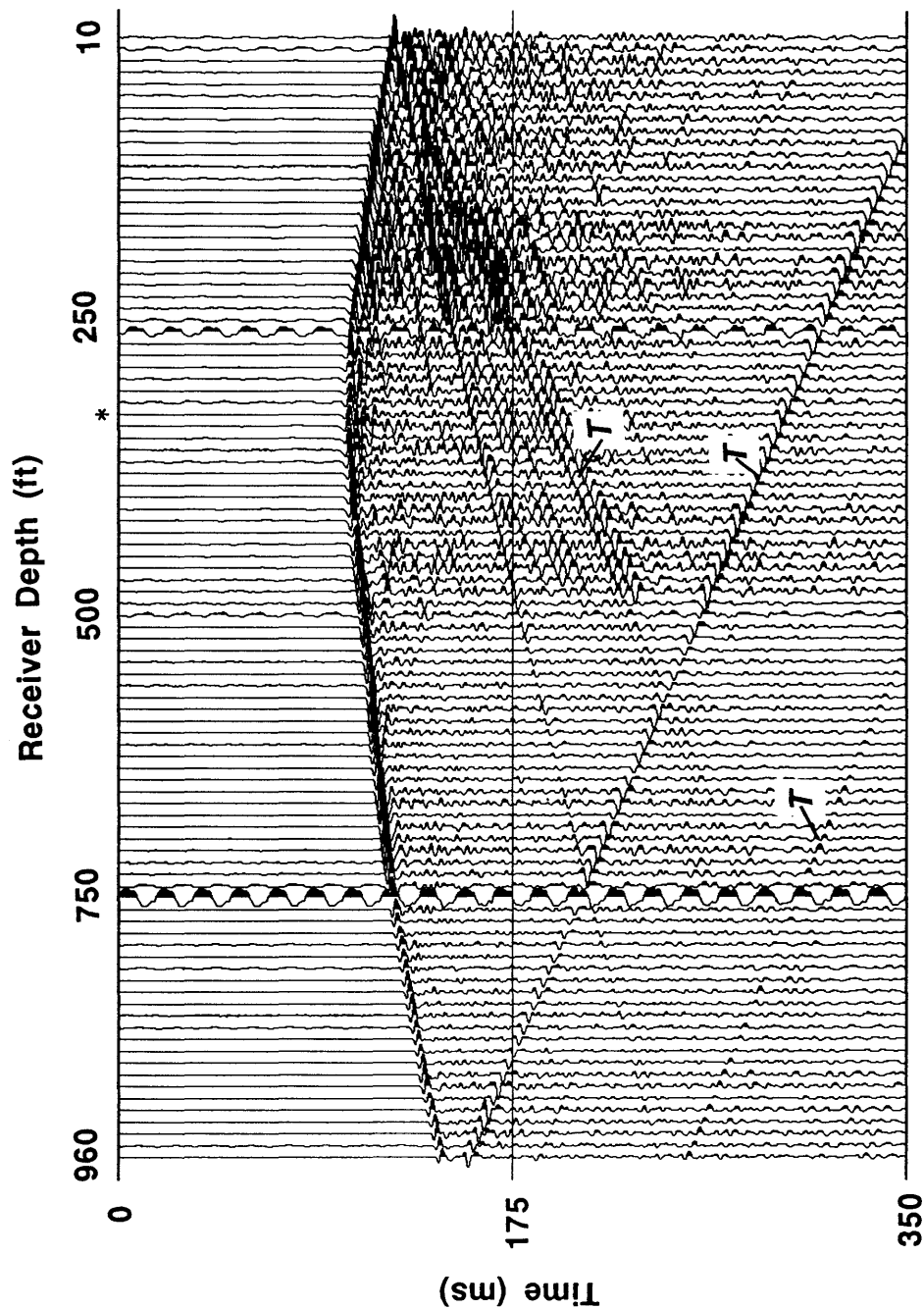
FIG. 7.1. Raw crosswell data in a common-source gather from the Friendswood crosswell survey. The source is located at a depth of 330 ft (100.6 m) (indicated by the symbol *). Tube waves are indicated by T.

reducing coherent and incoherent noise in the data and of extracting reflections from the complex wavefield. For this purpose, the procedure prior to imaging consists of preprocessing, tube-wave suppression, direct-wave removal, and reflection-wavefield separation. This procedure is similar to those of Stewart and Marchisio (1991) and Cai and Schuster (1993).

Following noise attenuation and wavefield separation, reflection imaging is performed through steps such as common-reflection-point (CRP) gathering, moveout corrections, and stacking. Results from each major processing step will be shown. In the end of this chapter, the final images obtained will be briefly analyzed and compared with a reverse VSP section, surface seismic data, synthetic seismograms, and crosswell prestack migrated reflection data, all from the same survey site.

7.2 Extraction of reflections

7.2.1 Preprocessing

Preprocessing is composed of geometry setup, trace editing, spectral analysis, bandpass filtering and trace balancing. Bad traces may be edited and energy bursts may be surgically muted. Spectral analysis of shot records (Figure 2.7) is useful in determining filter parameters. For the data being considered, a bandpass filter of 70-620 Hz was applied to common-source gathers in order to filter out low-frequency and high-frequency noise. After filtering, a trace balancing is performed to equalize amplitude energy in traces.

7.2.2 Tube-wave suppression

The Friendswood crosswell data contain strong tube waves. Since these tube waves are present as linear events in the common-source gathers, they are suppressed in

these gathers by applying velocity filters. In this study, a median filter was applied (see Chapter 3). Because the tube waves exhibit two opposite apparent dips, the median filter had to be run twice. The tube waves were aligned, enhanced via median filtering, and then subtracted from the original wavefield. There is a trade-off between good filtering performance and reflection preservation, due to the nature of this kind of filter. Short filter operators suppress tube waves more effectively than longer operators, but they may distort reflections more severely. On the other hand, a longer operator preserves reflections better, but leaves behind more unfiltered component of the tube waves. The operator length of 9 traces was found best for this data set from parameter testing. After median filtering, a bandpass filter (70-620 Hz) was applied to eliminate higher-frequency glitch noise caused by the median filter. Figure 7.2 shows the same common-source gather as in Figure 7.1, after removing tube waves. A 500-ms AGC was applied for display. There are still some residual tube waves existing. Nevertheless, downgoing and upgoing reflections now become more obvious.

7.2.3 Direct-wave removal

With synthetic data, I have demonstrated in Chapter 5 that applying a velocity filter in common-source gathers to remove direct waves may very likely cause damage to reflections, because the reflections may have similar moveout to that of the direct waves. It was thus suggested to use common-interval (CI) gathers when removing direct waves.

Ideally, in a constant-velocity medium, the direct waves should be flat in the CI gather, as they travel the same distance from the source to the receiver. However, the real Earth is rarely constant-velocity. Instead, a velocity variation with depth is expected. In some cases, anisotropy of the velocity may also be present. This introduces some complexity into methods of removing direct arrivals. Figure 7.3 shows a CI gather of the Friendswood data. This gather consists of 77 traces. For all traces, the interval between
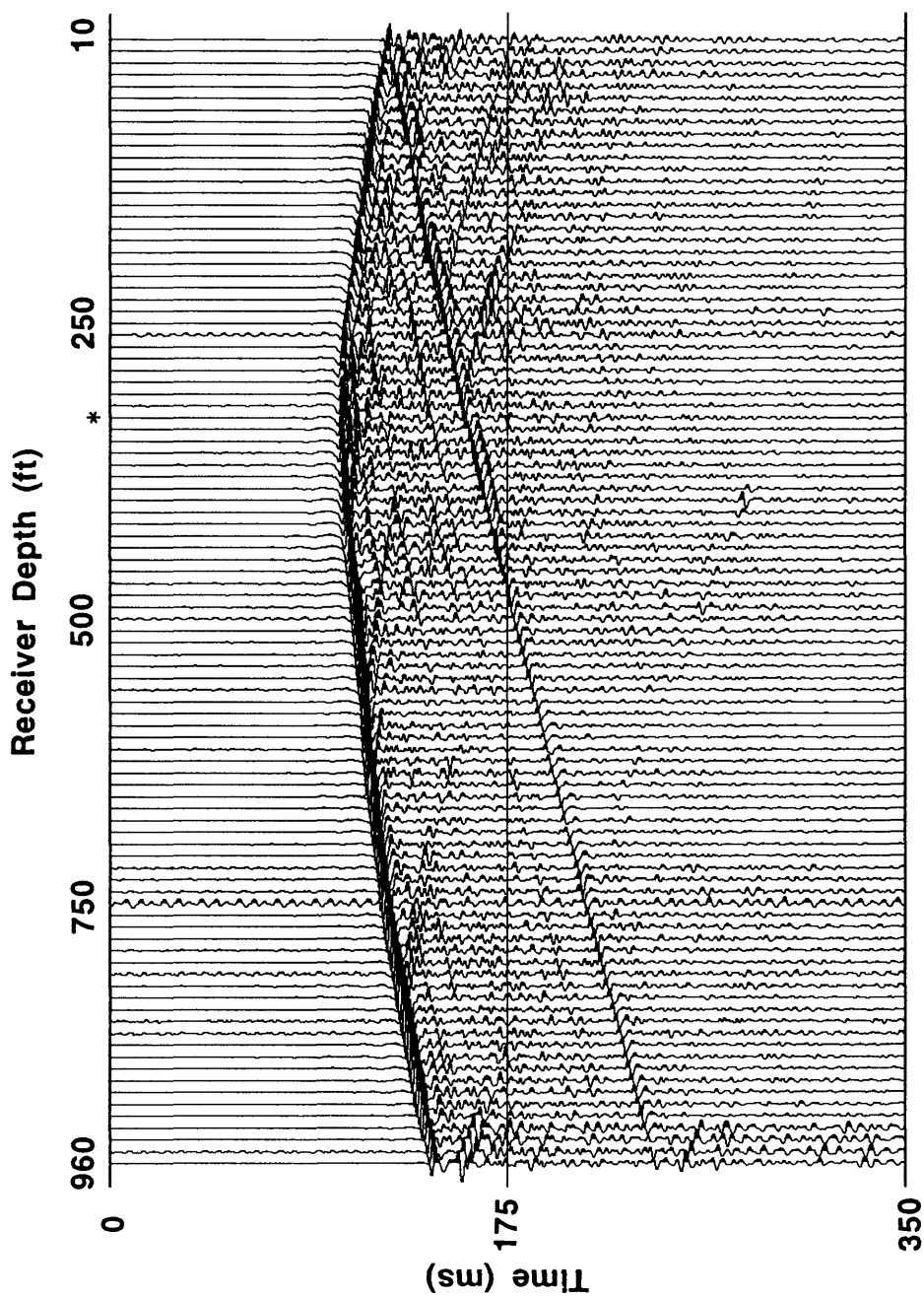
FIG. 7.2. The Friendswood crosswell common-source gather, after removing tube waves by median filtering. The symbol * represents the source position.
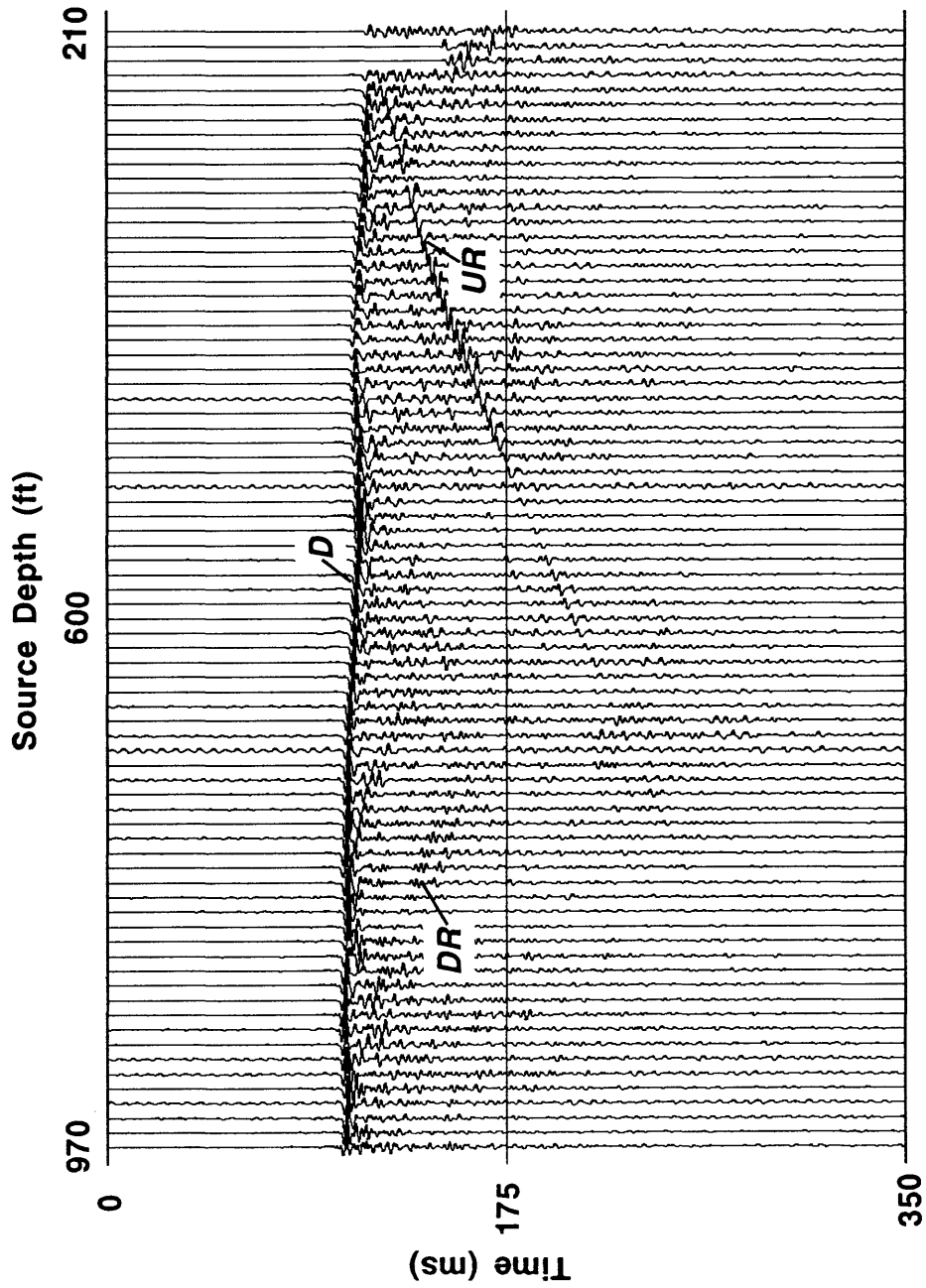
FIG. 7.3. Common-interval gather of the Friendswood crosswell data. The vertical interval between the source and receiver positions for this gather is 200 ft (61.0 m). *D* represents the direct *P* wave, *DR* downgoing reflections, and *UR* upgoing reflections.

the source and the receiver is 200 ft (61.0 m). A few events, including the direct wave, downgoing and upgoing reflections, are indicated in the Figure. It can be seen that, although the direct wave is nearly flat and its shape does not change dramatically, there is some difference in traveltime across the gather, indicating some velocity variation with depth.

Note that, in the real data case, the relationship of large-angle termination of both upgoing and downgoing reflections against the direct wave above them is still very clear in the CI gather. This relationship is an important characteristic of the CI gather that makes possible the effective removal of direct waves via velocity filtering without damage to the reflection wavefield. Also note that upgoing and downgoing reflections have opposite dips in the CI gathers.

A median filter of 9 traces was used in the CI gather to remove the direct wave, which was aligned beforehand. Figure 7.4 displays the result of applying the median filter, followed by a high-cut filter. The direct wave has been removed nicely, and the reflections preserve a good shape in positions where they contacted the direct wave. A detailed comparison of a portion of the data in Figures 7.3 and 7.4 is given in Figure 7.5.

7.2.4 Reflection-wavefield separation

Wavefields for upgoing and downgoing reflections are separated through f-k dip filtering of common-source gathers. Upgoing and downgoing reflections occupy different quadrants in the f-k domain. The zone to pass reflections is selected for either upgoing or downgoing waves. An example of the separated reflections from a common-source gather is displayed in Figures 7.6 (upgoing) and 7.7 (downgoing), respectively. Despite some smearing, the f-k filter performed well. Indeed, the Friendswood crosswell seismic data contain many good reflections. They are generated from layers at various depths, as indicated by the shot gather in Figures 7.6 and 7.7.
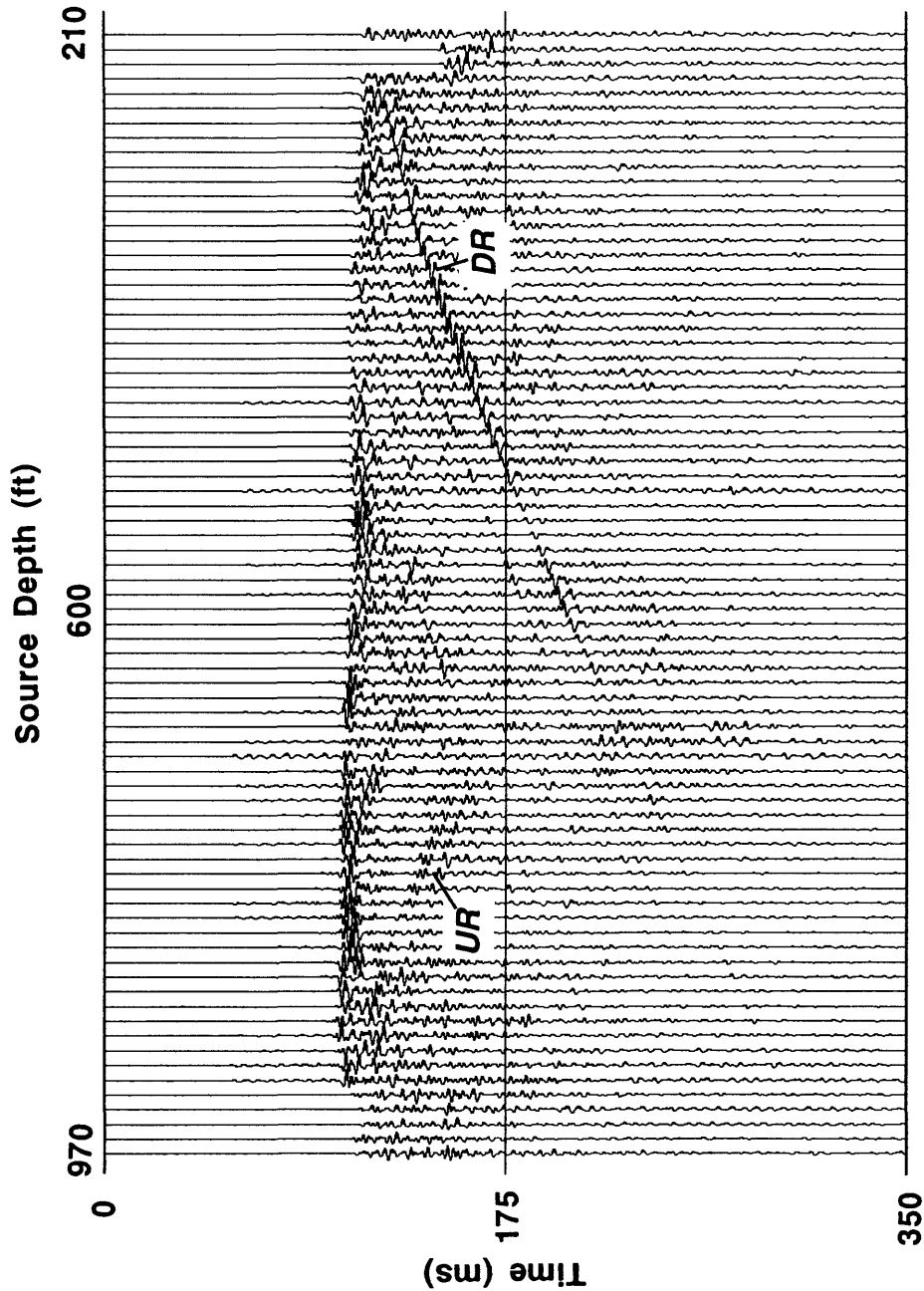
FIG. 7.4. The same common-interval gather as in Figure 7.3, but after removing the direct *P* wave.
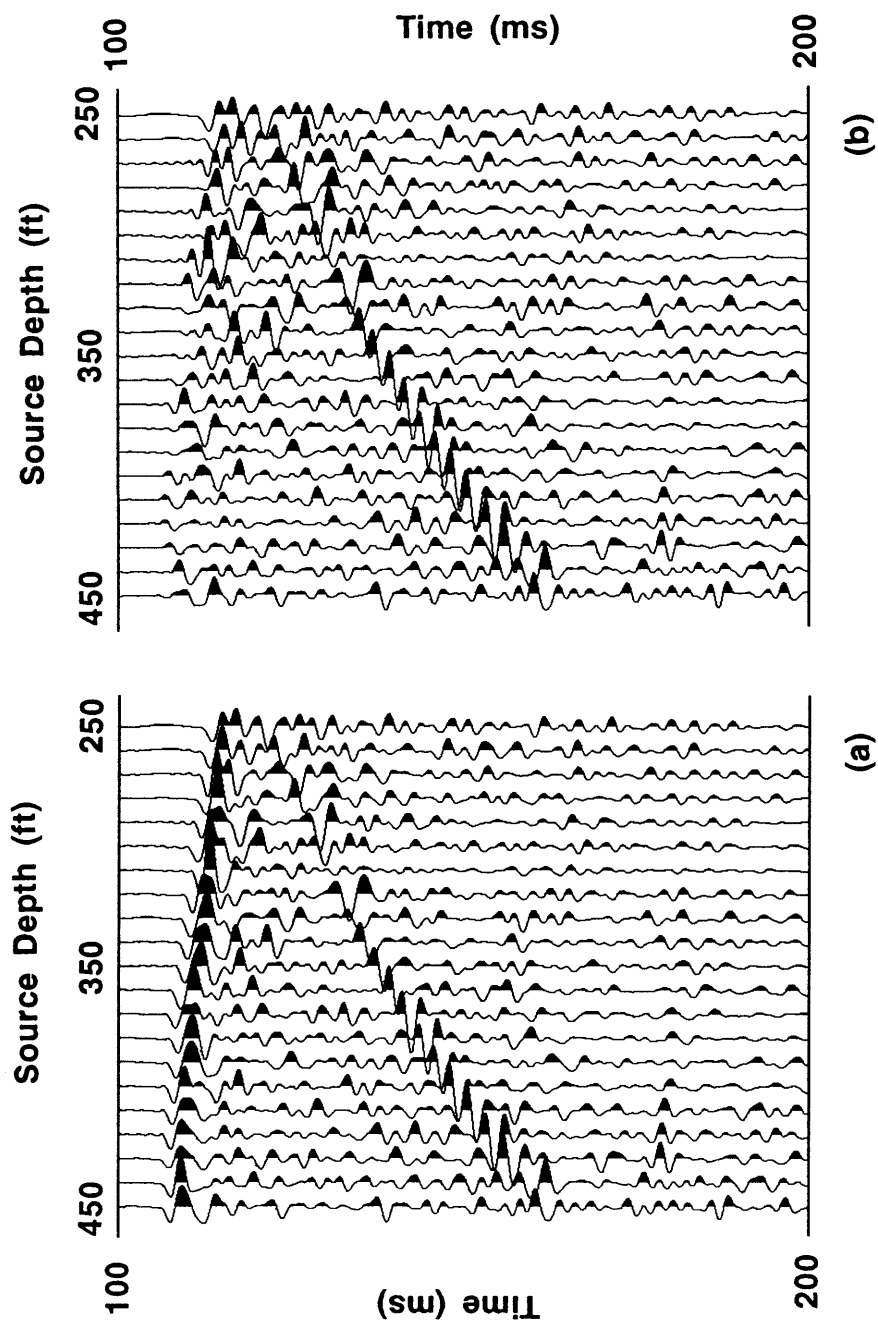
FIG. 7.5. An expanded view of part of the common-interval gather (a) before and (b) after removing the direct P wave.

148
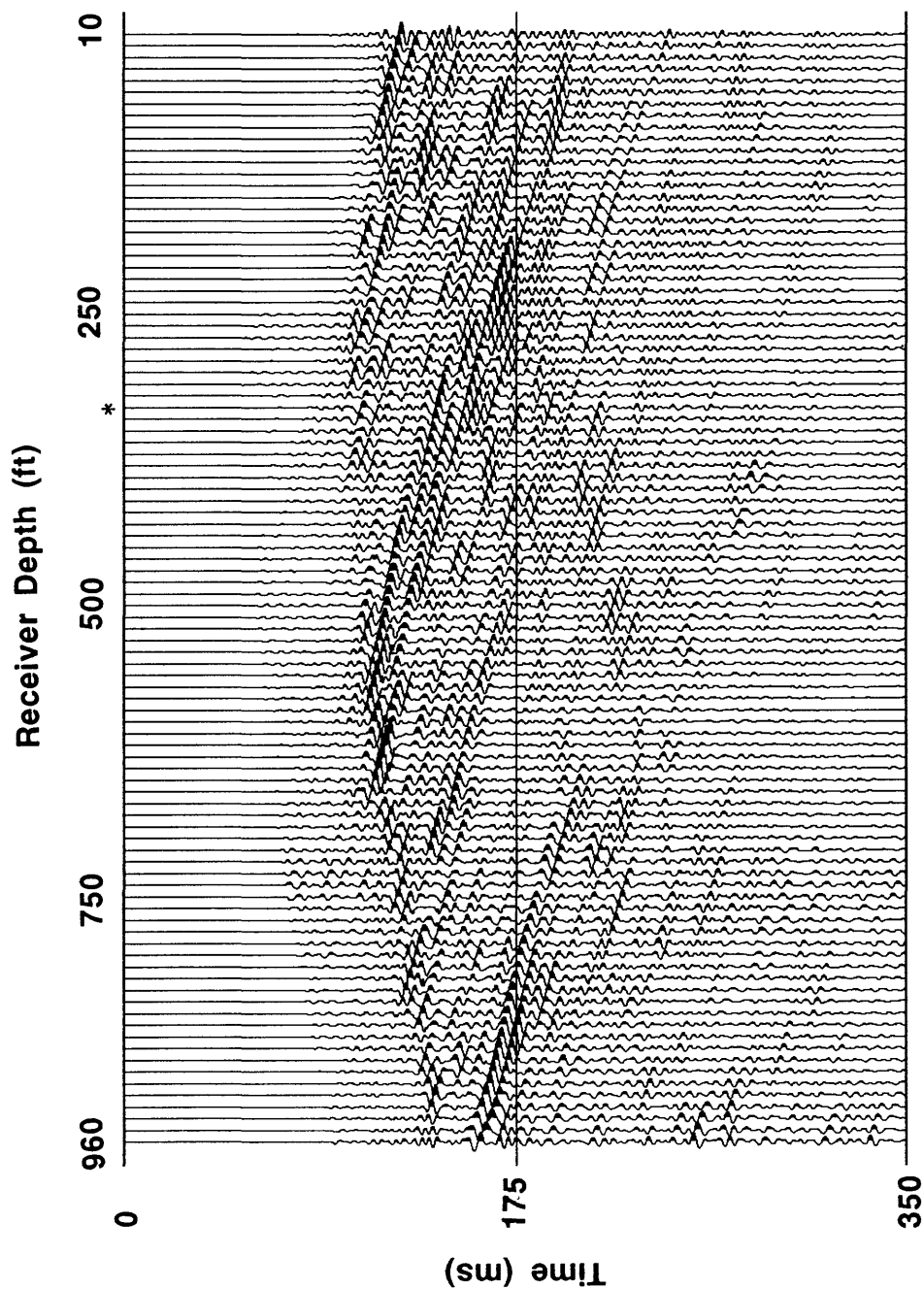
FIG. 7.6. Upgoing reflections in the common-source gather. The symbol * represents the source position.

149
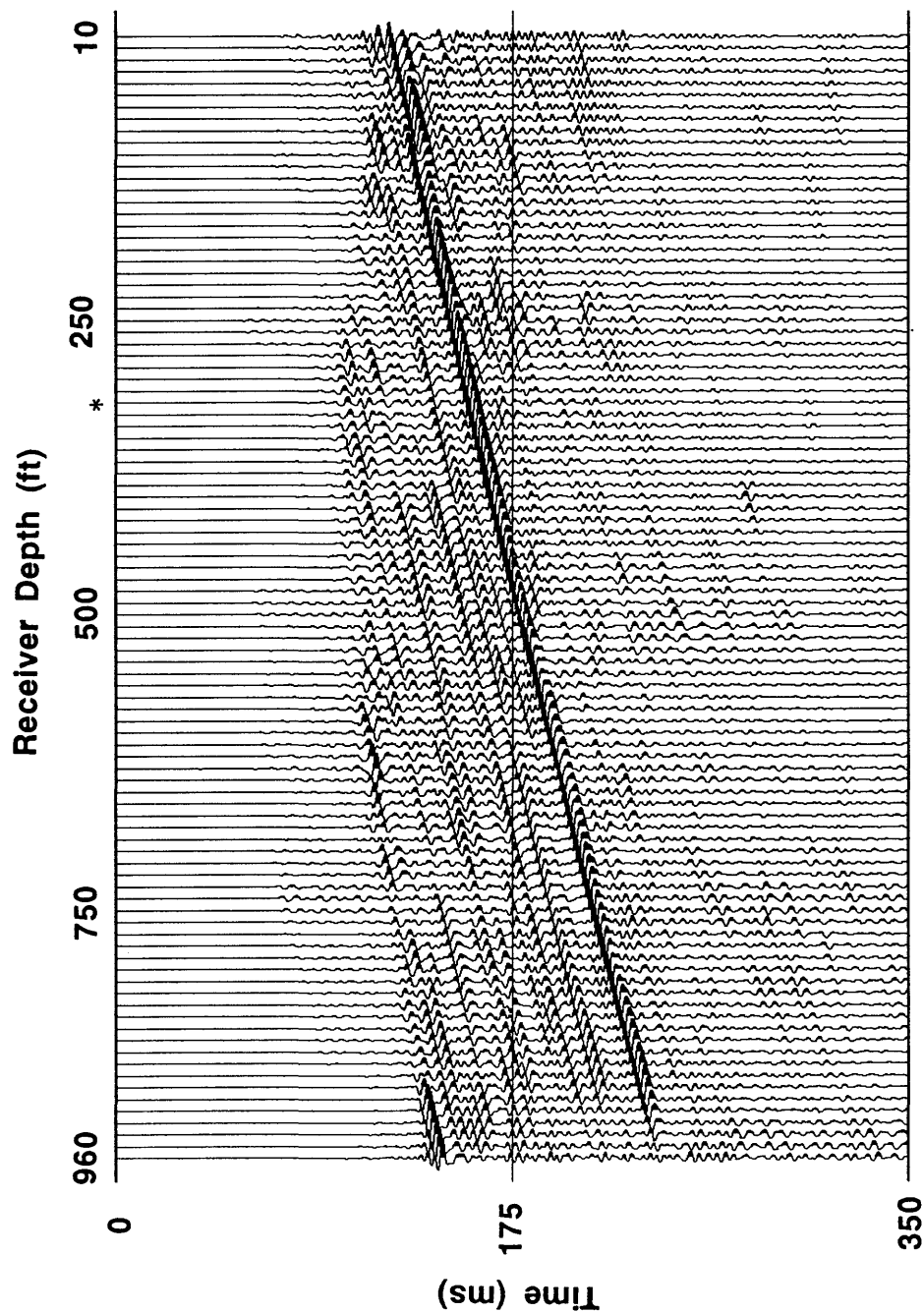
FIG. 7.7. Downgoing reflections in the common-source gather. The symbol * represents the source position.

7.3 Reflection imaging

For imaging, the common-reflection-point stacking method is used. The imaging involves a few steps: zero-interval-gather velocity analysis, CRP gathering, moveout corrections, and CRP stacking.

7.3.1 Zero-interval-gather velocity analysis

The zero-interval CI gather provides a data domain for velocity analysis. For a constant-velocity case, a zero-interval gather is a true CRP gather, since reflections contained in this gather are all from the same subsurface location. The horizontal moveout in the gather is constant, while vertical moveout caused by the difference in vertical distance between traces is a function of velocity. Therefore, if a correct velocity is used, the reflection events should be flat after moveout corrections.

Figure 7.8 shows the zero-interval gather of upgoing reflection data. There are many visible reflection events. They all exhibit a hyperbolic shape and have a different moveout from one to another. Correction of the moveouts with different velocities should give rise to different effects on these events. To find the best velocity I use the velocity scanning method discussed in Chapter 5. Because of the limitation of the CRP stacking method, I presently have to focus on only one reflection event to which the best velocity will be applied. In this particular case, the event of interest around 0.25 second, indicated by an arrow on the right side of the section, is examined. A velocity range from 4000 ft/s (1219.2 m/s) to 8000 ft/s (2438.4 m/s), incremented at 50 ft/s (15.2 m/s), was scanned. A few velocities scanned are displayed in Figure 7.9.

The zero-interval gather is affected differently by the scanning velocities. The velocity of 5100 ft/s (1554.5 m/s) gives the best moveout correction of the event indicated by the arrow (Figure 7.9b). Velocities below 5100 ft/s (1554.5 m/s) cause the event to be
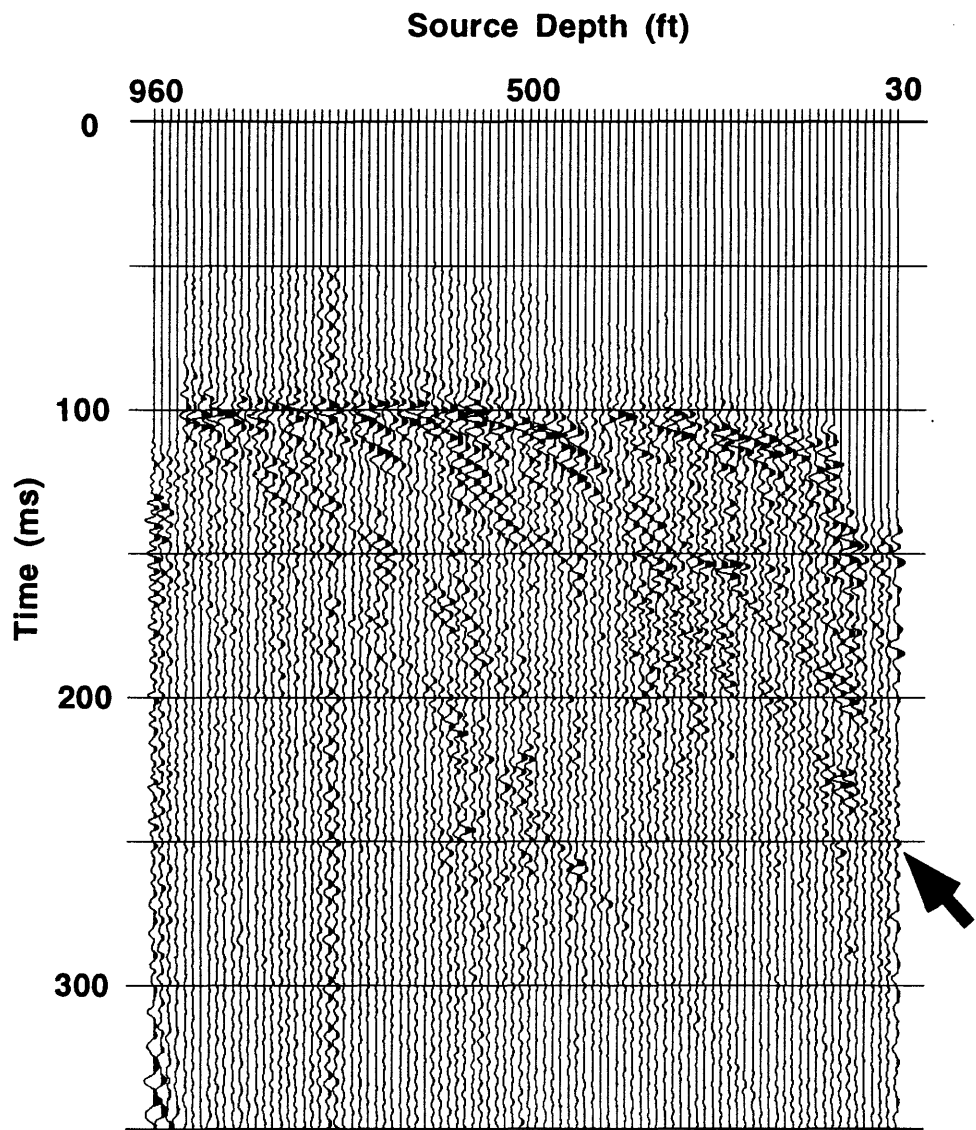
FIG. 7.8. Upgoing reflections in a zero-interval gather. This gather will be used for velocity analysis. The arrow indicates the reflection from the zone of interest.
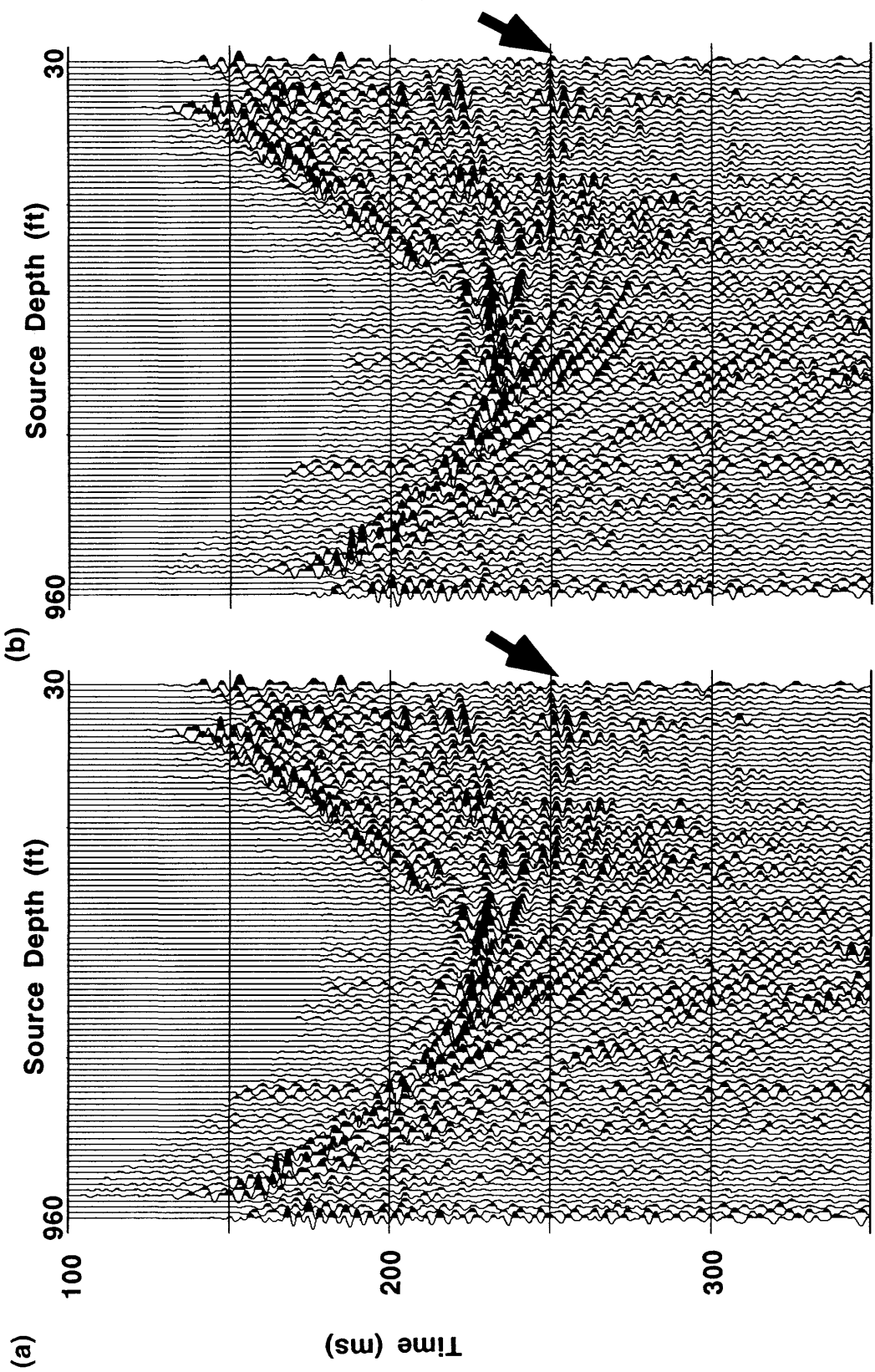
FIG. 7.9. Results of velocity scanning in the zero-interval gather. The arrow indicates the reflection from the zone of interest. Velocities scanned are (a) 4800 ft/sec (1463.0 m/s); (b) 5100 ft/s (1554.5 m/s). (To be continued on next page)
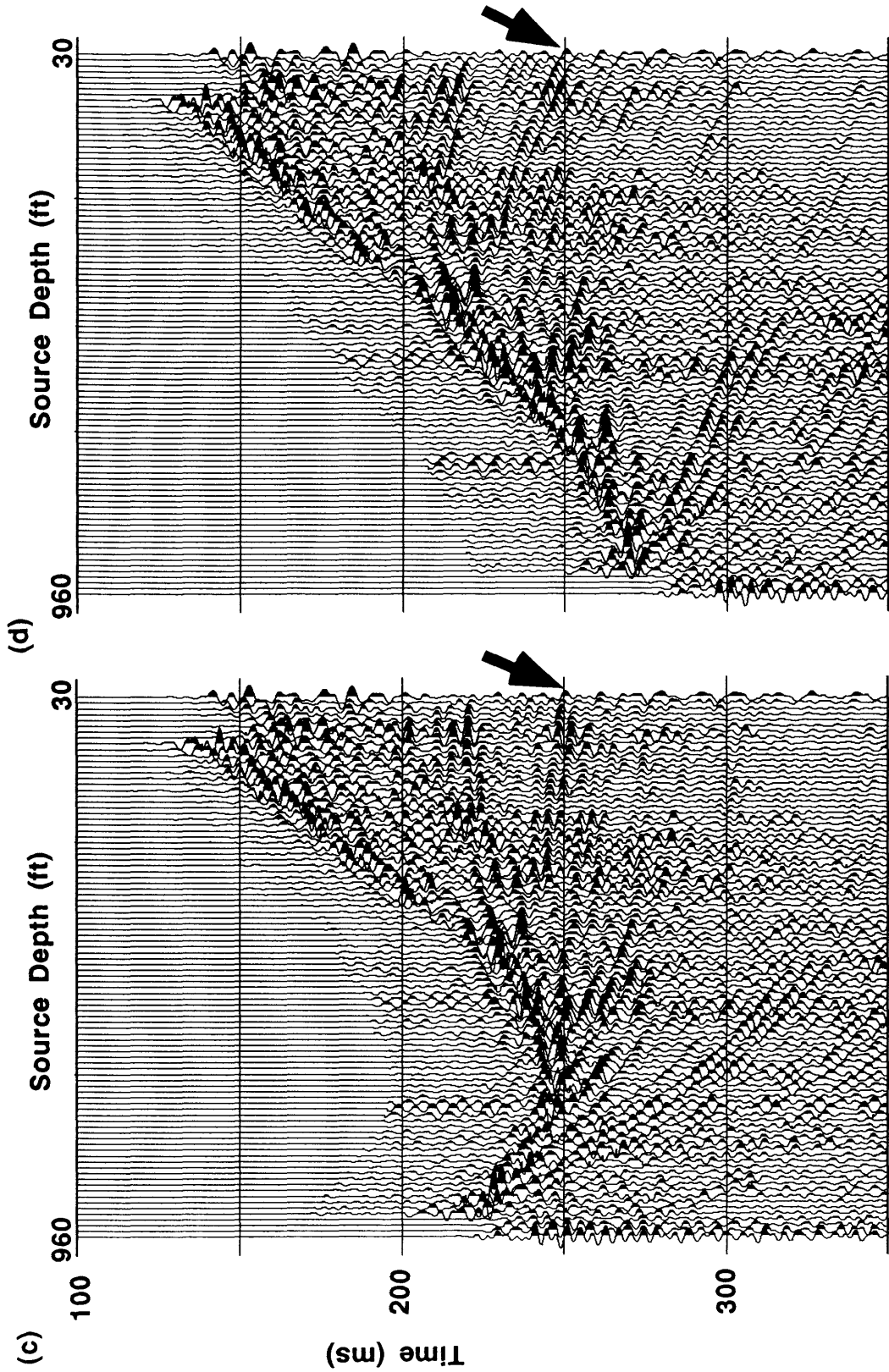
FIG. 7.9. (Continued.) (c) 5800 ft/s (1767.8 m/s); (d) 7400 ft/s (2255.5 m/s).

under-corrected (Figure 7.9a). On the other hand, however, velocities higher than 5100 ft/s (1554.5 m/s) make the event overcorrected (Figures 7.9c and 7.9d). So for the event of interest, 5100 ft/s (1554.5 m/s) is the best velocity for moveout corrections.

The zero-interval-gather velocity analysis is actually sensitive to depths. It is possible to extend the analysis to a velocity that varies with depth. For example, for events above the zone of interest but below 0.2 second, a higher velocity, say 5800 ft/s (1767.8 m/s), would be the best velocity. For very deep reflections, a velocity higher than 7400 ft/s (2255.5 m/s) would be appropriate. In short, this velocity analysis method provides a useful tool to quickly extract velocity information from crosswell reflection seismic data.

7.3.2 CRP gathering

All the seismic traces are grouped into CRP gathers, according to their subsurface reflection points, determined by equation (6.1). An example CRP gather of upgoing reflection data is shown in Figure 7.10a.

When gathering, an assumed target reflector depth of 650 ft (198.1 m) was used. The CRP bin size was 3 ft (0.9 m). The fold in CRP gathers varies. For this particular gather in Figure 7.10a, the fold is 14. However, the maximum fold achievable for the Friendswood data is 74 if the same bin size and the reflector depth are used.

Although the hyperbolic shape of the reflection events are not obvious, they do have moveout. The moveout is a function of mid-depths.

7.3.3 Moveout corrections

The moveout corrections include two parts: one for horizontal moveout, and the other for vertical moveout. The horizontal moveout correction is to remove the moveout caused by the horizontal distance between the boreholes, which is constant for all traces, while the vertical moveout correction is to eliminate the moveout due to the difference in

155
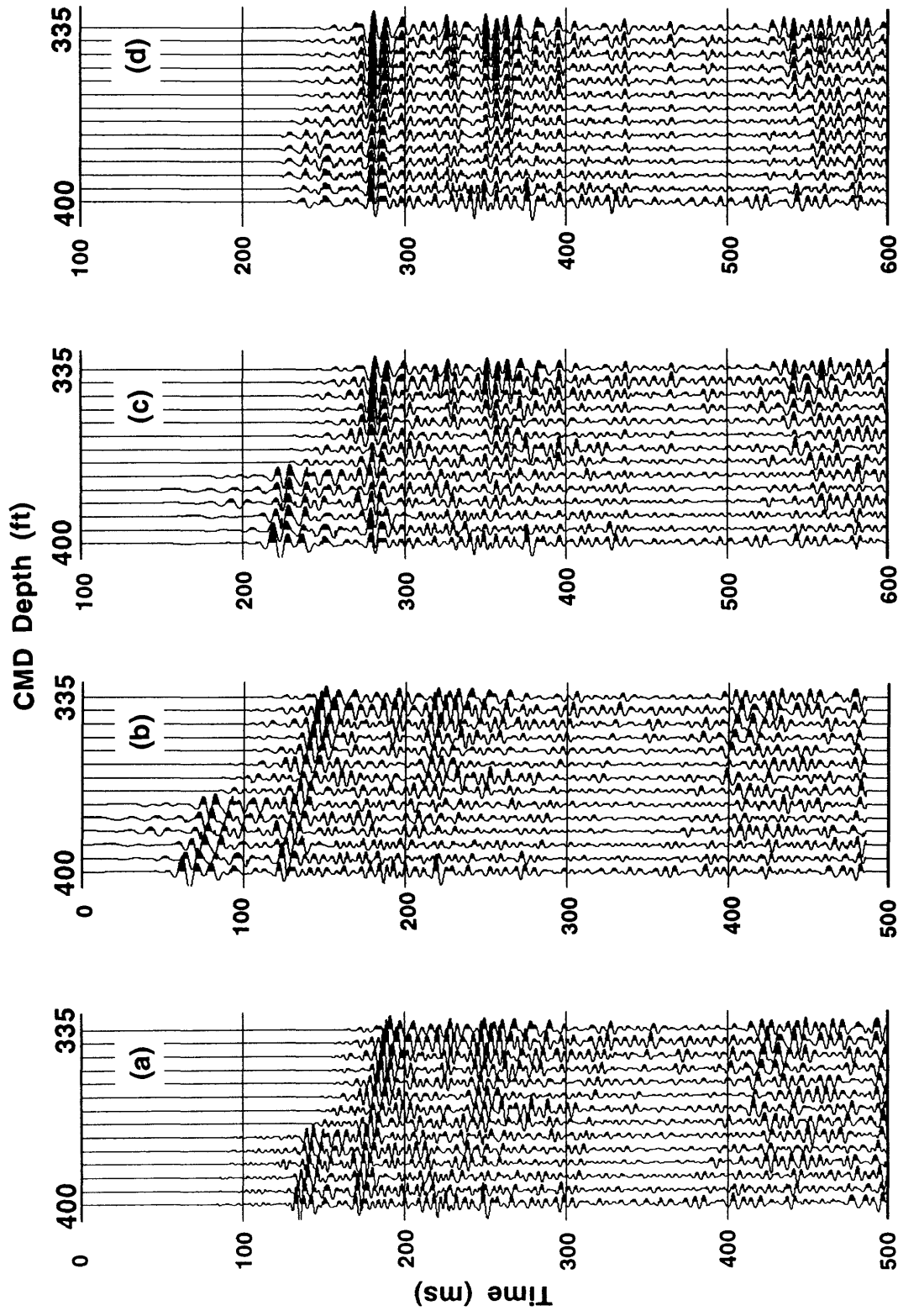
FIG. 7.10. (a) CRP gathered upgoing reflections. After (b) HMO and (c) VMO correction. (d) Enhanced reflections after trim statics and filtering. The CRP bin width is 3 ft (0.9 m). The reflector depth is 650 ft (198.1 m). The fold is 14.

vertical distance (interval) for each source-receiver pair. The mathematical basis for these corrections has been given in Chapter 6.

Velocity information needs to be derived to correct for these two types of moveouts. A velocity of 5100 ft/s (1554.5 m/s) obtained from the velocity analysis described above was used. Figures 7.10b and 7.10c show the CRP gather after HMO and VMO corrections, respectively.

All events in the HMO-corrected gather are shifted upwards. The HMO correction causes the shallow reflections to be stretched, especially on those traces of larger CMD depths, which correspond to wide-angle reflections. These distorted wavelets on the stretched events need to be muted.

After the VMO correction, all the reflection events are well flattened, in agreement with the theoretical prediction. A little bit of residual moveout exists in the gather, largely because of the spatial variability of the real velocity, as opposed to the constant-velocity model that was used in processing. Note that the time axis for the gather now is two-way *vertical* time, referred to the surface.

Using a ProMAX® program, a correlation-based trim statics was applied to the VMO-corrected gather to eliminate the residual moveout. Then, a carefully selected trace mixing was performed to remove the dipping events appearing in the gather (Figure 7.10c), believed to be residual tube waves surviving from median filtering. The most severely stretched shallow data were also muted. The result is shown in Figure 7.10d. Now the reflections become better aligned and the gather has a higher S/N ratio.

7.3.4 CRP stacking

Figure 7.11 shows a time section which stacks horizontally seismic traces in all moveout-corrected CRP gathers, like the one in Figure 7.10d. For display purposes, a 50-ms AGC was applied. This section contains a wealth of upgoing reflection information

Offset (ft)

FIG. 7.11. Stacked time section of crosswell upgoing reflection data. The horizontal axis indicates the distance of each reflection point from the source well, whereas the vertical axis is two-way traveltime from the surface to the reflectors.

which describes subsurface reflectors at various depths. The horizontal axis is the offset distance from the reflection points to the source well location, and the vertical axis is the two-way vertical time from the free surface to each reflector. The shallow mute zone for stretched data is obvious in this section.

The stacked section can also be displayed in depth, if a time-depth conversion is applied. Upgoing and downgoing reflections may be combined into a single section. In Figure 7.12, a stacked depth section is shown. For the time-depth conversion, a single velocity of 5100 ft/s (1554.5 m/s) was used. The position for joining upgoing and downgoing data is clearly indicated by the mute pattern around the depth of 350 ft (106.7 m). Above the joint position is the contribution from the downgoing reflections and below it is the contribution from the upgoing reflections.

7.4   Results

The most noticeable feature in Figures 7.11 and 7.12 is that the images provided by crosswell reflection stacking can cover a large interwell space bounded by the boreholes. Specifically, the region that has been imaged by the crosswell reflections is about 580 ft (176.8 m) wide [from offset of 10 ft (3.0 m) to 590 ft (179.8 m)], compared to the entire borehole spacing of 600 ft (182.9 m). The time section in Figure 7.11 and the depth section in Figure 7.12 both contain many continuous, coherent reflection events. The events in the middle portion of the sections exhibit better coherency and S/N ratio than the events on both sides. The reason for this is simple: the middle CRP gathers generally have a higher fold than those on the sides. One usual case in oilfield development is that the reservoirs are situated between the wells. The major objective of crosswell reflection imaging is to provide a reliable image of the reservoirs, and the crosswell reflection

159
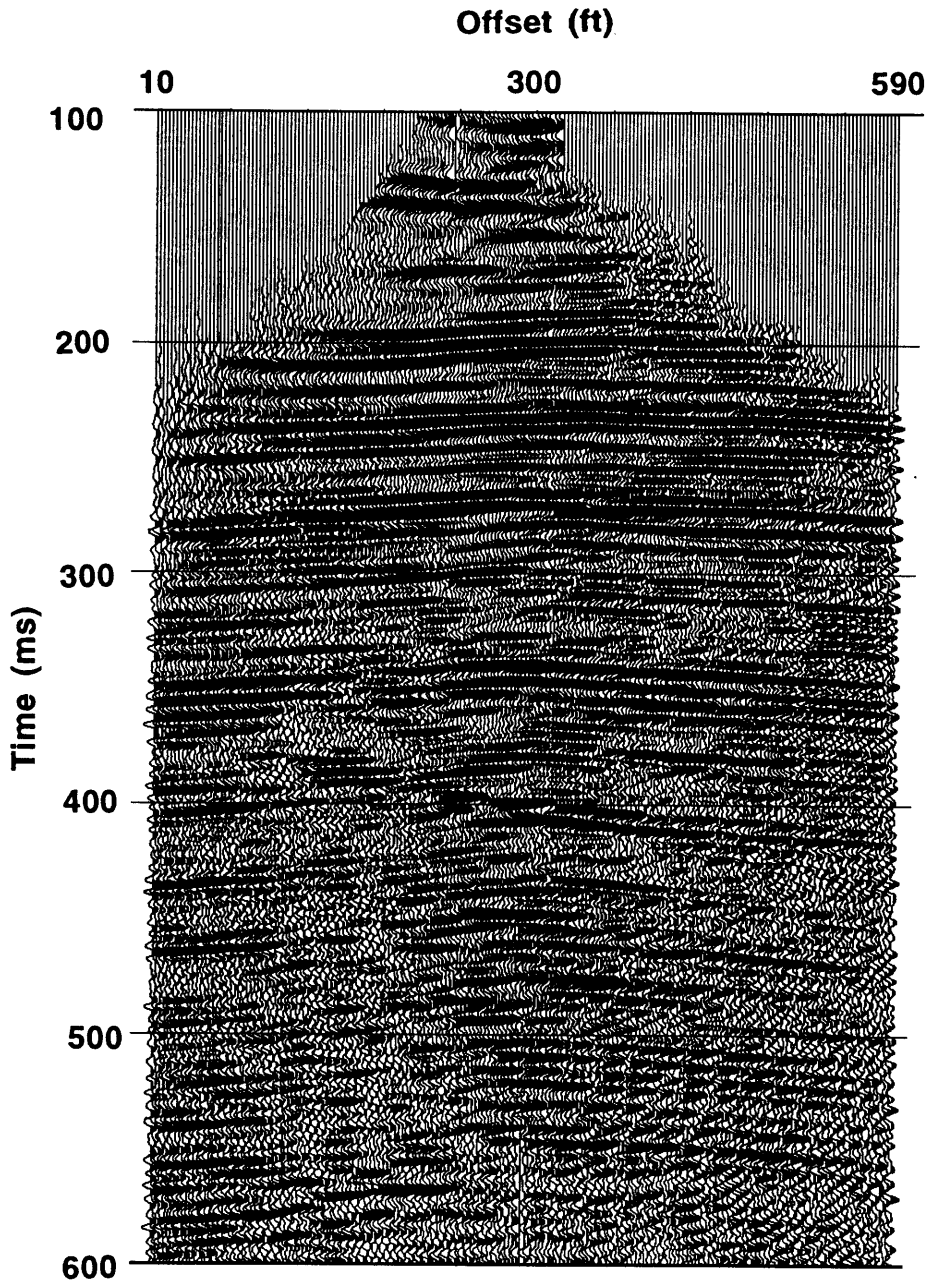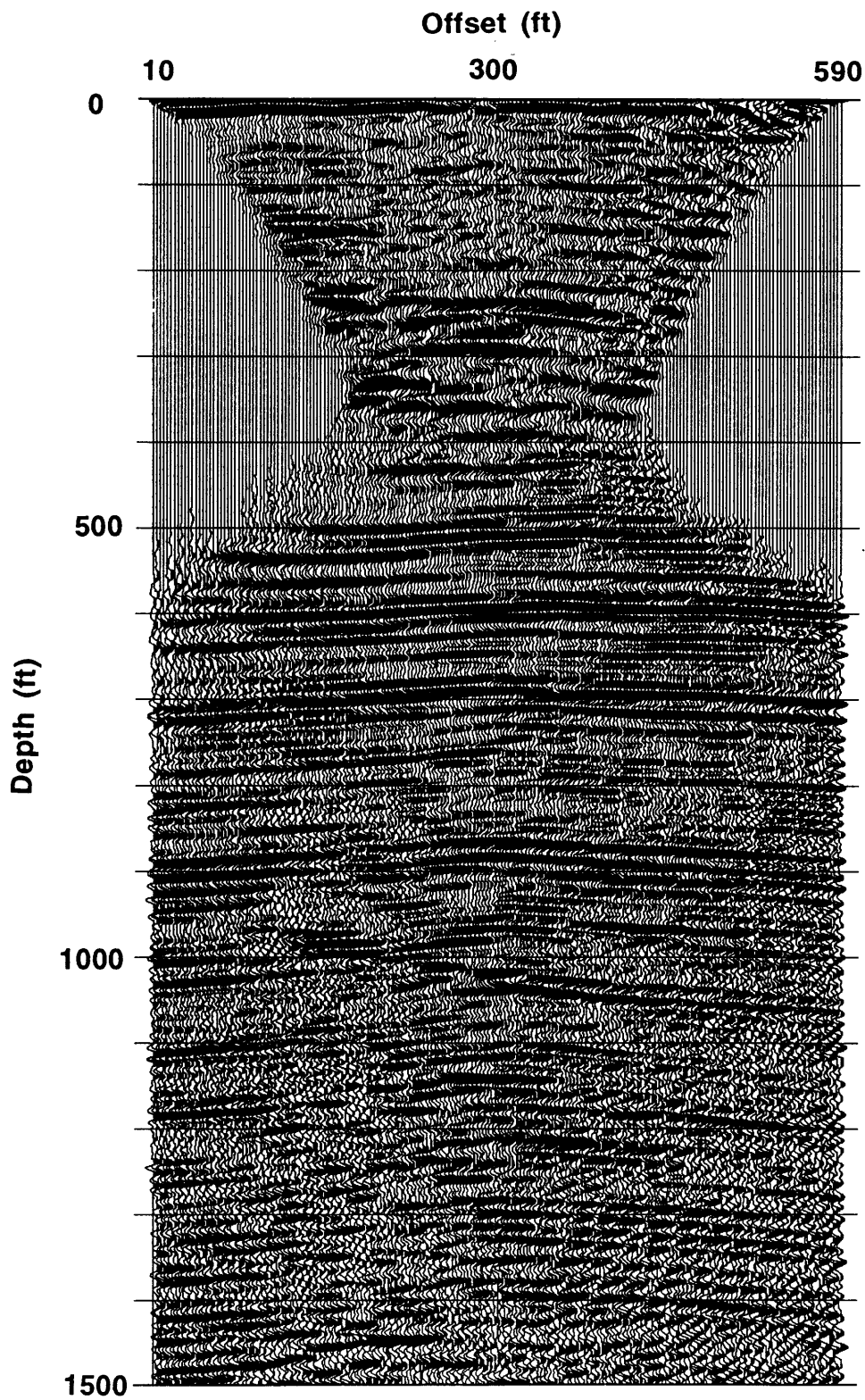

FIG. 7.12. Stacked depth section of crosswell reflection data. The horizontal axis is the distance of each reflection point from the source well, whereas the vertical axis is the depth from the surface to the reflectors.

stacking methods obviously have the advantage of achieving the objective. The image near the source well (on left side) is better than the image near the receiver well (on right side). The image between depths 500 ft (about 200 ms) to 1000 ft (about 400 ms) shows better reflection events, while the image resulting from below 1000 ft (304.8 m) (the total borehole depths) is generally less continuous and noisier. This can be explained by certain facts, including: (i) the imaging procedure via reflection stacking was focusing on the target reflector assumed at a depth of 650 ft (198.1 m); (ii) the Friendswood crosswell survey was designed for the traveltime tomographic inversion study (Chen et al., 1990), but might not have been designed optimally for reflection imaging; therefore no optimal reflection coverage below the borehole depths could be achieved; (iii) because of longer traveltimes, the deep wavefield often suffers more from noise disturbance than the shallower wavefield.

Another feature is the weakness of the reflections in the very shallow section [above 200 ft (61.0 m)], where irregular, unconsolidated sediments often occur. However, boundaries between the reflection events are still clear, although these weak events are not so continuous as those in the deeper section.

The techniques introduced in this thesis represent a very new area in crosswell seismology. Noticeable artifacts still exist in the images produced by these techniques. For example, an inspection of the images in Figures 7.11 and 7.12 reveals some unexpected structural highs (pull-ups) on the reflection events in the middle of the sections. These features are more severe on deep events than on shallow ones. An analysis of these artifacts will be given in the next section.

The Friendswood crosswell data have been processed before by other researchers for different purposes. Chen et al. (1990) and Squires et al. (1992) studied the traveltime tomographic inversion for the interwell velocity distribution. The reflection data were migrated using different prestack migration algorithms such as the Kirchhoff migration (Qin and Schuster, 1993) and reverse-time migration (Zhou and Qin, 1993). However, the

sections presented here represent the first of the stacked sections of this kind ever produced from field crosswell data.

Let us now turn to comparisons of the stacked sections with the results of crosswell migrated reflection data, as well as the surface seismic data, and the reverse VSP data, both from the same survey location as the crosswell data.

Figure 7.13 compares the crosswell stack (in the middle) with the sonic log and synthetic seismograms (on the left) and the migrated section (on the right). The sonic log was obtained from the source well in the Friendswood survey. The synthetic seismic traces were generated by Qin and Schuster (1993) from this log, using the frequency band of the crosswell data. The migrated section was produced through prestack Kirchhoff migration (Qin and Schuster, 1993). Only panels cut from the middle of the stacked and the migrated sections are shown in Figure 7.13. It could take intensive CPU time on a supercomputer to generate such a migrated section. By contrast, producing a stacked section, starting from the step of CRP gathering, takes only a few hours of connect time on a SUN SPARC-2 workstation.

There is a reasonable overall correlation between the synthetic and the stack, and between the stack and the migration. Most horizons existing on the synthetic due to lithologic changes also appear in the stacked and migrated sections. For example, the sonic log shows a quiet zone between 350 ft (106.7 m) and 500 ft (152.4 m). This results in a few very weak events on the synthetic. This feature appears in the stacked and migrated sections as well. There is a large impedance contrast at 400 ft (121.9 m), which gives rise to a strong event on the synthetic. This event is very weak on the left side of the stacked and migrated sections, but began to appear more strongly on the right side of both sections. Below this event is another horizon appearing on both stacked and migrated sections, but very weak on the synthetic. Conclusions may be drawn. First, there is a noticeable lithologic change near the source well around 400 ft (121.9 m); it becomes less significant
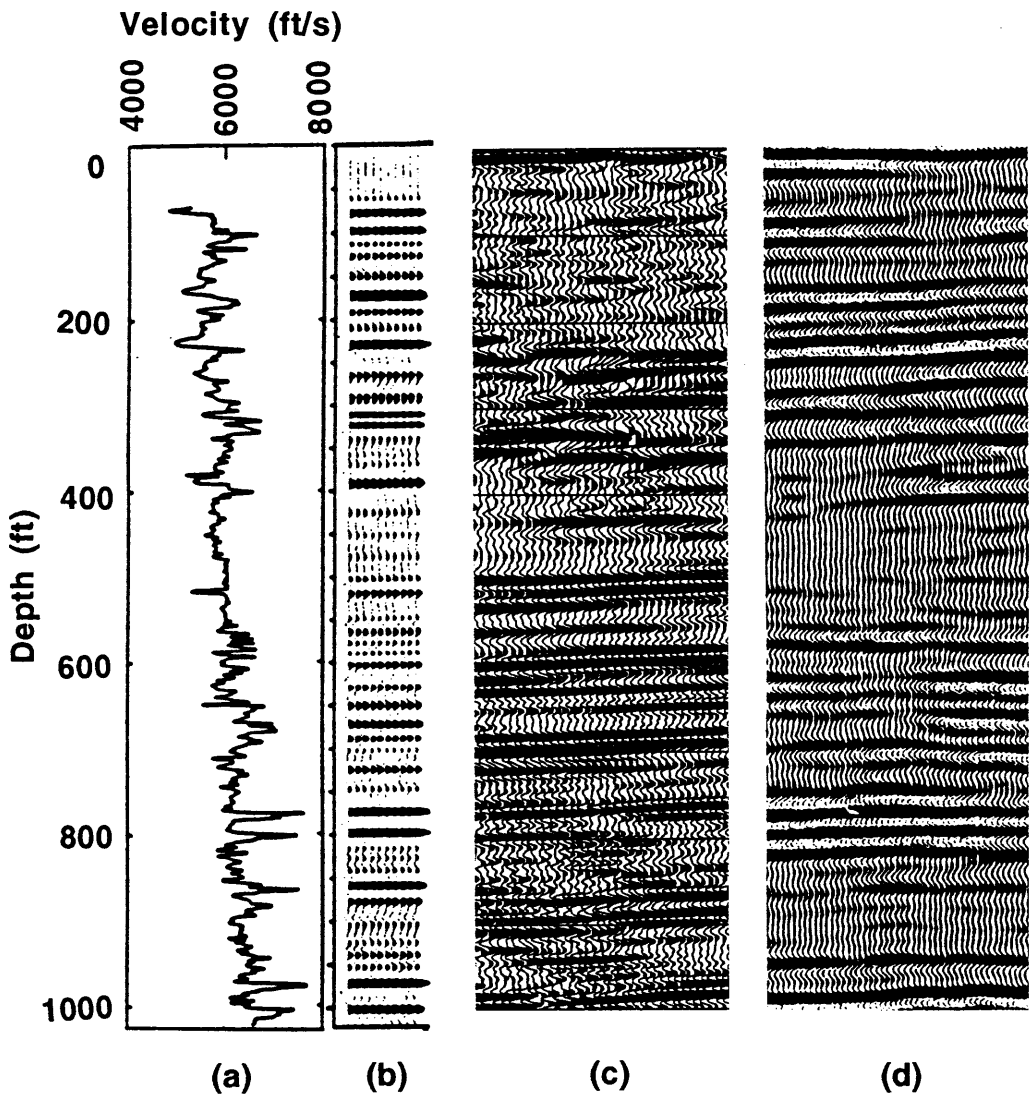
FIG. 7.13. Comparison of the crosswell stacked section with other types of data. (a) A sonic log from the source well; (b) Synthetic seismograms generated from the sonic log; (c) Crosswell stacked section; and (d) Crosswell prestack migrated section (after Qin and Schuster, 1993).

when away from the well, and it appears again when close to the receiver well. Second, in the middle region of the interwell space, there seems to be a strong lithologic change below 400 ft (121.9 m), but it does not appear significantly near the source well. Below 500 ft (152.4 m), the lithology changes dramatically with depth, which causes strong coherent reflection events on all three sections. Especially below 500 ft (152.4 m) and above 800 ft (243.8 m), there is a fairly good correlation between the stack and the synthetic, and between the stack and the migrated section, with an exception, that is, events near 500 ft (152.4 m) show up on the synthetic and stack, but very weakly and less continuously on the migrated section. Above 200 ft (61.0 m), the stacked section shows reflections that are not as strong as those on the synthetic and the migrated data.

Figure 7.14 shows a comparison of the crosswell stack with the reverse VSP section (in the middle) and the surface seismic section (on the right), both published by Chen et al. (1990). The crosswell section defines shallow horizons (above 200 ms) much better than either of the RVSP and surface sections. Actually, it is hard to follow the shallow horizons on the RVSP data because of the noise problem, except for a few horizons around time 100 ms which are comparable to the crosswell data. On the other hand, the shallow horizons in the surface seismic data are generally traceable but very noisy. Below 200 ms, horizons are continuous on all sections, but the crosswell section shows a better resolution than the RVSP and surface sections.

A close-up comparison between the crosswell section and the surface 2-D line is given in Figure 7.15, within the depth interval of 0 ft (0.0 m) to 1000 ft (304.8 m). The crosswell reflections have a much higher resolution than the surface seismic data. For example, major events on the 2-D line near 520 ft (158.5 m), 650 ft (198.1 m), and 900 ft (274.3 m) are indeed the composite of a number of well-defined reflections on the crosswell data. Besides, strong reflections appearing in the crosswell section between 200
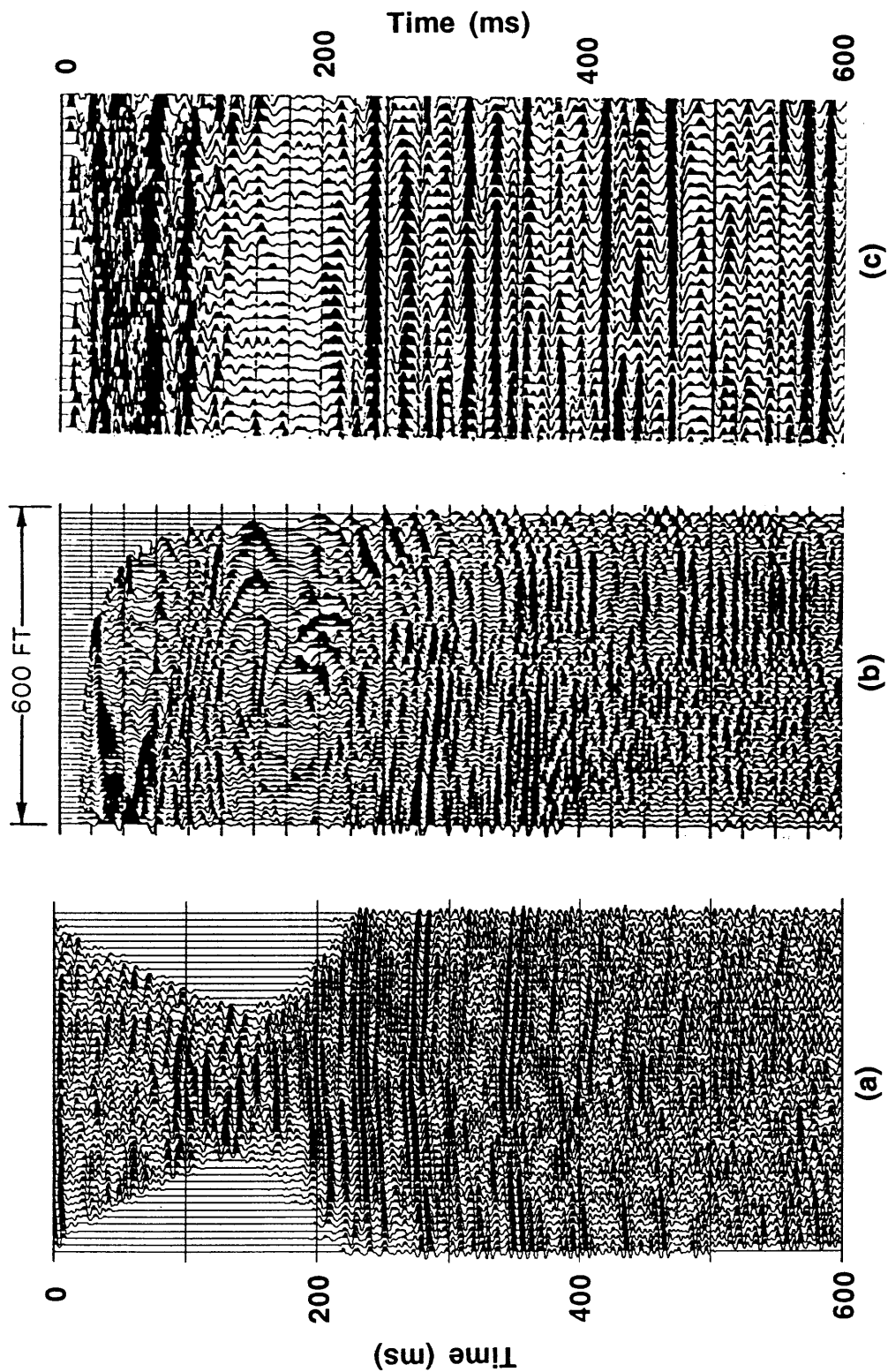
FIG. 7.14. Comparison of (a) the crosswell stacked section with (b) the reverse VSP section and (c) the surface 2-D seismic section published by Chen et al. (1993).
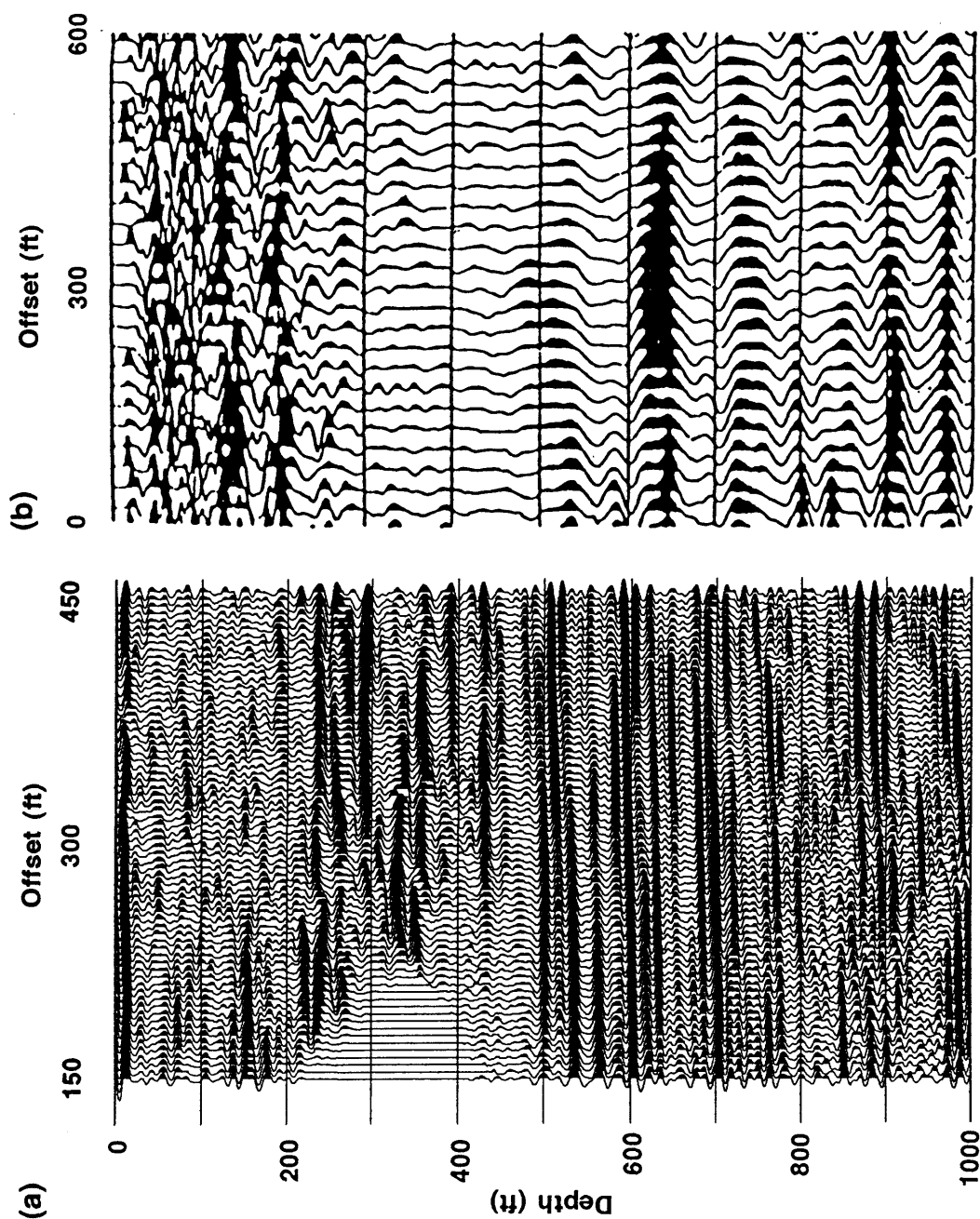
FIG. 7.15. Comparison of (a) the crosswell stacked section with (b) the surface 2-D seismic section from Chen et al. (1993).

ft (61.0 m) and 350 ft (106.7 m) correspond to large acoustic impedance contrasts on the sonic log (Figure 7.13), but show very little on the surface seismic section.

To summarize, the crosswell stacked section shows many major reflections that show up on the crosswell migrated section, reverse VSP section, and surface 2-D seismic section. These reflection events are caused by significant acoustic impedance contrasts that correspond to the lithologic changes shown on the sonic log and confirmed by the synthetic seismograms. The crosswell reflections provide much higher resolution than the surface seismic data. Also, the crosswell stacked sections define the subsurface image better than the reverse VSP in terms of continuity and resolution of the reflectors.

7.5   Limitations

The CRP stacking method is based on equation (6.1) for CRP gathering and equation (6.2) for moveout correction, for which three assumptions are made: (1) a constant-velocity medium; (2) flat layers; and (3) imaging one target reflector only. In reality, these conditions may be difficult to meet. Clearly, further research is required to relax one or all of the assumptions. In this section, an analysis is given to the errors in the Friendswood crosswell reflection images due to these assumptions.

Despite local velocity variations along the depth axis, the sonic log in Figure 7.13 indicates an average background velocity of 5800 ft/s (1767.8 m/s) above 550 ft (167.6 m) and 6100 ft/s (1859.3 m/s) below that depth. The overall average velocity may be around 6000 ft/s (1828.8 m/s). Although the velocity of 5100 ft/s (1554.5 m/s) that was used before for moveout corrections is quite different from the average velocity of 6000 ft/s (1828.8 m/s) in the medium, the assumption of a constant-velocity medium may still be weakly valid. However, local interval velocity variations in each layer may have caused

errors that are related to the structural artifacts which are seen in the crosswell stacked sections. The tomographic inversion study of the Friendswood crosswell direct-arrival traveltimes by Chen et al. (1990) shows not only a velocity change with depth, but also a large lateral velocity variation, especially in the lower half of the interwell region. A similar crosswell inversion study by Squires et al. (1992) finds that the large lateral velocity change seen by Chen et al. (1990) is actually caused largely by a static problem, but their study also shows some horizontal variation of the velocity field. The vertical and horizontal velocity changes both introduce errors in the amount of moveout correction applied to the crosswell reflection data.

Let us take a look at the CRP gather in Figure 7.10. The dipping reflection events have been nicely aligned after the VMO correction using a constant velocity (Figure 7.10c), suggesting that the VMO correction is not very sensitive to errors due to the velocity variations.

Let us also take a look at the geometry of CRP gathering (Figure 6.1a). When the reflection points are close to the middle of the interwell zone, the CRP gathers consist of traces from the sources and receivers at various depths. However, when the reflection points are close to the source well or the receiver well, the situation is very different. Near the source well, the CRP gathers are composed of traces from the sources close to the reflectors and from the receivers far away from the reflectors. On the other side, when the reflection points are near the receiver well, the CRP gathers are comprised of traces from the sources far away from the reflectors and from the receivers close to the reflectors. The difference in travel paths for different CRP-gathered traces may be susceptible to the effect of the velocity variations. For example, each gather at a different location may need to be corrected for HMO by a different amount using a variable velocity instead of the constant velocity. This may partially explain why the reflection events in the stacked sections are

convex upwards in the middle. The use of the single constant velocity in the time-depth conversion may have caused errors as well.

The second assumption of flat layers may be acceptable in the Friendswood data case. The CDP stacked section from the surface 2-D line (Figure 7.14c) shows that most horizons are flat. However, in the presence of dipping layers, dip moveout (DMO) may need to be applied to the crosswell data before stacking. (DMO is not discussed in this thesis.)

Imaging through crosswell reflection stacking is so far dependent on the target reflector depth, because this depth is assumed to be known in equation (6.1). One possible solution to overcome this problem is the composite stack, which has been discussed in Chapter 6. In this method, images are made for consecutive reflector depths, and all such images are finally summed. But for real data, how to smooth the boundary between neighboring images remains a problem.

Some other issues such as tube wave suppression may be related, to some extent, to the artifacts and noise problems in the crosswell images as well. Perhaps, the most effective digital filters to be used in removing strong spatially aliased tube waves are yet to be developed.

7.6   Summary

Crosswell stacked sections in time and depth were produced by processing the field crosswell reflection data from the Friendswood survey, and applying the imaging technique based on the common-reflection-point stacking method. The processing sequence similar to those proposed in previous chapters was used, including preprocessing, tube-wave suppression, direct-arrival removal, reflection-wavefield separation, velocity analysis in

zero-interval gather, CRP gathering, vertical and horizontal moveout correction, and stacking.

The images generated from stacking multi-fold crosswell reflection data contain many reflection events of high S/N ratio and coherency, which are comparable to those on the synthetic seismograms and the crosswell prestack migrated section. Moreover, the crosswell stacked sections provide high-resolution reflection information that is difficult to obtain in the surface seismic data and the reverse VSP data both shot in the same site.

The real-data study in this chapter has proven that the imaging method presented in this thesis provides a novel and rapid way to process large crosswell seismic data sets, although a few recognized limitations require more research work.

Chapter 8

Conclusions

8.1 Thesis summary

In this thesis, a comprehensive study of crosswell reflection seismic data analysis and processing has been presented. Three representative field crosswell seismic surveys have been described and the wavefields of the typical data from each survey have been analyzed for a recognition of reflections and noise such as tube waves. Digital filtering techniques have been tested for suppressing strong tube waves, which severely obscure useful reflections. A technique for automatically deriving velocity information from first-arrival traveltimes has been proposed and tested with various types of data. As the main objective of this thesis, different methods for processing crosswell reflection data have been discussed, major processing steps have been illustrated in detail with synthetic and field data, and a complete processing sequence has been developed. A number of significant conclusions can be drawn as follows.

Field crosswell seismic data contain much reflection information useful in imaging the geologic objects between and below the boreholes. The crosswell reflections carry a very broad frequency band with high frequency that is usually not obtainable in other seismic data (surface seismic or VSP). The rich frequency content makes crosswell

seismology a potential high-resolution tool desirable in petroleum seismic exploration and development.

Reflections in recorded crosswell data are usually very weak, and sometimes hardly visible, because quite often tube waves dominate the wavefield. Tube waves seen in this thesis are strong, coherent, non-attenuative, and low-velocity. They are largely low-frequency but can have frequency as high as that of reflections. Tube waves can be generated in the source well and propagate into the surrounding medium in the form of body waves, or they can be converted from body waves propagating in the surrounding medium and travel in the receiver well. Where there are inhomogeneities in the boreholes, tube waves can be reflected more than once. It is important to effectively suppress tube waves before reflection imaging can be done. Velocity filters such as f-k filter, median filter, and alpha-trimmed mean filter, work quite well in suppressing tube waves, with median filters performing the best in the cases here.

An approximate 1-D velocity distribution can be derived automatically from traveltimes of first arrivals without picking them. Given the possible velocity range and velocity-gradient variation range, first-arrival traveltimes can be calculated with reasonable accuracy and, based on the calculations, semblance analysis yields a best velocity fit. However, non-uniqueness may be a problem. The linear-velocity-gradient assumption may not be applicable in some geologic areas.

Common-interval gathers are useful in removing direct arrivals from the whole crosswell wavefield. In these gathers, reflection events and direct arrivals often have an obvious difference in moveout. The direct arrivals are nearly flat, while reflections are dipping with a large angle. This feature makes feasible median filtering of direct arrivals, without damaging reflections as in common-source gathers.

In common mid-depth gathers, reflections are flat while direct arrivals are hyperbolic. However, unlike the CRP gathers, a flat reflection event in CMD gathers

does not represent the same reflection point, but actually the reflection on different traces are from many different reflection points along the reflector.

As in the surface seismic exploration case, the multi-fold coverage of the subsurface horizons by crosswell reflections is very useful in enhancing signals (reflections) and suppressing noise. The common-reflection-point stacking technique, developed in this thesis, fully takes advantage of the high-fold coverage of crosswell reflection seismic data. This method is very similar, in many aspects, to the CDP stacking procedure used in surface seismic data processing. It sorts the reflection data into CRP gathers, applies moveout corrections, and stacks reflections. For the Friendswood crosswell data considered in this thesis, the fold in CRP gathers varies from 14 to 74.

Stacked sections produced from the Friendswood crosswell reflection data, using the CRP stacking method, are easily interpretable and correlatable to other types of seismic data (surface 2-D line or RVSP) and geologic information (sonic log or synthetic seismogram). Reflection events in the crosswell stacked sections are comparable to equivalent events present on the synthetic seismograms in the same frequency band and on the prestack migrated crosswell section, but have higher resolution than the 2-D surface seismic line and RVSP data. Presently, the CRP stacking technique is limited by its dependence on the target reflector depth, simple velocity model and the assumption of flat reflectors.

8.2   Future work

This thesis has introduced some important ideas and useful techniques that can be used in crosswell reflection seismic data processing and imaging. However, more

research is required in the future for these ideas and techniques to become sophisticated. Specifically, a few things in the following are worth some additional effort.

It may be meaningful to derive a depth-variable velocity function from a layered earth model for the crosswell case. Application of such a velocity function in moveout correction and time-depth conversion may reduce residual moveout and some structural artifacts that were seen before.

In the dipping-layer case, applying a dip-moveout (DMO) process to crosswell reflection data may be helpful in correctly imaging and preserving relative amplitudes. As the computer technology is getting cheaper, prestack migration may be the best solution to the crosswell reflection imaging problem in presence of dipping layers and vertical/lateral velocity variations. However, edge effects and dipping artifacts caused by existing migration algorithms need to be solved.

Not much attention has been given to the relationship of reflection amplitude and phase variation with angles. In the crosswell case, there exist wide-angle reflections that may have different characteristics than those reflections from small angles. Study of crosswell amplitude variation with offsets (AVO), or amplitude variation with angles (AVA) may provide useful information in exploration and development.

The automatic crosswell velocity analysis method needs to be generalized. In some geologic areas, the existence of multiple velocity gradients within different depth intervals may cause direct arrivals to behave differently than what has been dealt with in this thesis. Therefore, multiple velocity scan may be necessary in every sub-aperture, within which velocity analysis is conducted using the method described. Results from these sub-apertures are finally combined into a unified velocity function. Besides, it is worth investigating other velocity-depth relationships which may be more accurate and more suitable to describe subsurface velocity patterns than the one used in this thesis.

References

Abdalla, A. A., and Stewart, R. R., 1989, Reflection processing of synthetic crosshole seismic data: CREWES Project Research Report, The University of Calgary, 1, 225-244.

Abdalla, A. A., Stewart, R. R., and Henley, D. C., 1990, Traveltime inversion and reflection processing of cross-hole seismic data: 60th. Ann. Internat. Mtg., Soc. Expl. Geophys., Expanded Abstracts, 47-50.

Baerg, J. R., 1985, Analysis of cocrust seismic refraction and wide angle reflection experiments from southern Saskatchewan and Manitoba: M. Sc. thesis, The University of Western Ontario.

Baker, L. J., and Harris, J. M., 1984, Cross-borehole seismic imaging: 54th. Ann. Internat. Mtg., Soc. Expl. Geophys., Expanded Abstracts, 23-25.

Barton, D. C., 1929, The seismic method of mapping geologic structure: Geophys. Prosp., 1, 572-624.

Bernabini, M., and Borelli, G. B., 1974, Methods for determining the average dynamic elastic properties of a fractured rock mass and the variations of these properties near excavations: Proc. 3rd. Cong. Int. Soc. Rock Mech., Denver, 2, Part A, 393-397.

Beydoun, W. B., Delvaux, J., Mendes, M., Noual, G., and Tarantola, A., 1989, Practical aspects of an elastic migration/inversion of crosshole data for reservoir characterization: A Paris basin example: Geophysics, 54, 1587-1595.

Bois, P., La Porte, M., Lavergne, M., and Thomas, G., 1972, Well-to-well seismic measurements: Geophysics, **37**, 471-480.

Bregman, N. D., Hurley, P. A., and West, G. F., 1989, Seismic tomography at a fire-flood site: Geophysics, **54**, 1082-1090.

Cai, W., and Schuster, G. T., 1993, Processing Friendswood cross-well seismic data for reflection imaging: 63rd. Ann. Internat. Mtg., Soc. Expl. Geophys., Expanded Abstracts, 92-94.

Chen, S. T., and Eriksen, E. A., 1989, Experimental studies of downhole seismic sources: 59th. Ann. Internat. Mtg., Soc. Expl. Geophys., Expanded Abstracts, 62-64.

Chen, S. T., Zimmerman, L. J., and Tugnait, J. K., 1990, Subsurface imaging using reversed vertical seismic profiling and crosshole tomographic methods: Geophysics, **55**, 1478-1487.

Dines, K. A., and Lytle, R. J., 1979, Computerized geophysical tomography: Proc. of IEEE., **67**, 1065-1073.

East, R. J. R., Worthington, M. H., and Goulty, N. R., 1988, Convolutional back-projection imaging of physical models with crosshole seismic data: Geophys. Prosp., **36**, 139-148.

Eastwood, J., Lebel, P., Dilay, A., and Blakeslee, S., 1994, Seismic monitoring of steam-based recovery of bitumen: The Leading Edge, **13**, No. 4, 242-251.

Fehler, M., and Pearson, C., 1984, Cross-hole seismic surveys: Applications for studying subsurface fracture systems at a hot dry rock geothermal site: Geophysics, **49**, 37-45.

Findlay, M. J., Goulty, N. R., and Kragh, J. E., 1991, The crosshole seismic reflection method in opencast coal exploration: First Break, **9**, 509-514.

Grant, F. S., and West, G. F., 1965, Interpretation theory in applied geophysics: McGraw-Hill Book Company, New York.

Haldorsen, J. B. U., and Farmer, P. A., 1989, Suppression of high-energy noise using an alternative stacking procedure: Geophysics, **54**, 181-190.

Hardage, B. A., 1985, Vertical seismic profiling, Part A - Principles: 2nd Ed., Geophysical Press.

Hawkins, L. V., Whiteley, R. J., Holmes, W. H., and Dowle, R., 1982, Downhole-crosshole high resolution seismic reflection profiling to resolve detailed coalseam structure: 52nd. Ann. Internat. Mtg., Soc. Expl. Geophys., Expanded Abstracts, 423-426.

Helbig, K., 1990, Rays and wavefront charts in gradient media: Geophys. Prosp., **38**, 189-220.

Ho-Liu, P., Montagner, J., and Kanamori, H., 1989, Comparison of iterative back-projection inversion and generalized inversion without blocks: case studies in attenuation tomography: Geophys. J. R. astr. Soc., **97**, 19-29.

Hu, L., McMechan, G. A., and Harris, J. M., 1988, Acoustic prestack migration of cross-hole data: Geophysics, **53**, 1015-1023.

Ivansson, S., 1985, A study of methods for tomographic velocity estimation in the presence of low-velocity zones: Geophysics, **50**, 969-988.

Iverson, W. P., 1988, Crosswell logging for acoustic impedance: Journal of Petroleum Technology, January, 75-82.

Jain, S., 1987, Amplitude-vs-offset analysis: A review with reference to application in western Canada: J. Can. Soc. Expl. Geophys. **23**, 23-27.

Khalil, A. A., Stewart, R. R., and Henley, D. C., 1993, Full-waveform processing and interpretation of kilohertz cross-well seismic data: Geophysics, **58**, 1248-1256.

Krebes, E. S., 1989, Geophysical data processing: Course Notes, The University of Calgary.

Laine, E. F., 1987, Remote monitoring of the steam-flood enhanced oil recovery process: Geophysics, **52**, 1457-1465.

Lazaratos, S. K., Rector, J. W. III, Harris, J. M., and Van Schaack, M., 1993, High-resolution, cross-well reflection imaging: Potential and technical difficulties: Geophysics, **58**, 1270-1280.

Lee, M. W., and Balch, A. H., 1982, Theoretical seismic wave radiation from a fluid-filled borehole: Geophysics, **47**, 1308-1314.

Lee, M. W., Balch, A. H., and Parrott, K. R., 1984, Radiation from a downhole air gun source: Geophysics, **49**, 27-36.

Li, G., and Stewart, R. R., 1992, Imaging the subsurface using crosswell reflection data: A synthetic study: Presented at the CSEG National Convention, Calgary, Alberta.

Lines, L. R., and LaFehr, E. D., 1989, Tomographic modeling of a cross-borehole data set: Geophysics, **54**, 1249-1257.

Lines, L. R., and Tan, H., 1990, Cross-borehole analysis of velocity and density: 60th. Ann. Internat. Mtg., Soc. Expl. Geophys., Expanded Abstracts, 34-36.

Lo, T., Toksöz, M. N., Xu, S., and Wu, R., 1988, Ultrasonic laboratory tests of geophysical tomographic reconstruction: Geophysics, **53**, 947-956.

Macrides, C. G., Kanasewich, E. R., and Bharatha, S., 1988, Multiborehole seismic imaging in steam injection heavy oil recovery projects: Geophysics, **53**, 65-75.

Mason, I. M., 1981, Algebraic reconstruction of a two-dimensional velocity inhomogeneity in the High Hazles seam of Thoresby colliery: Geophysics, **46**, 298-308.

McDonal, F. J., Angona, F. A., Hills, R. L., Sengbush, R. L., Van Nostrand, R. G., and White, J. E., 1958, Attenuation of shear and compressional waves in Pierre shale: Geophysics, **23**, 421-439.

Peterson, J. E., Paulsson, B. N. P., and McEvilly, T. V., 1985, Applications of algebraic reconstruction techniques to crosshole seismic data: Geophysics, **50**, 1566-1580.

Pratt, R. G., and Goulty, N. R., 1991, Combining wave-equation imaging with traveltime tomography to form high-resolution images from crosshole data: Geophysics, **56**, 208-224.

Pratt, R. G., and Worthington, M. H., 1988, The application of diffraction tomography to cross-hole seismic data: Geophysics, **53**, 1284-1294.

Qin, F., and Schuster, G. T., 1993, Constrained Kirchhoff migration of cross-well seismic data: 63rd. Ann. Internat. Mtg., Soc. Expl. Geophys., Expanded Abstracts, 99-102.

Ricker, N., 1953, The form and laws of propagation of seismic wavelets: Geophysics, **18**, 10-40.

Slotnick, M. M., 1959, Lessons in seismic computing, Ed. by R. A. Geyer, Soc. Expl. Geophys.

Squires, L. J., Blakeslee, S. N., and Stoffa, P. L., 1992, The effects of statics on tomographic velocity reconstructions: Geophysics, **57**, 353-362.

Stewart, R. R., 1985, Median filtering: review and a new F/K analogue design: J. Can. Soc. Expl. Geophys., **21**, 54-63.

Stewart, R. R., 1991, Exploration seismic tomography: Fundamentals, Course Notes, Soc. Expl. Geophys.

Stewart, R. R., and Cheadle, S. P., 1989, Ultrasonic modeling of borehole seismic surveys: CREWES Project Research Report, The University of Calgary, **1**, 206 - 224.

Stewart, R. R., and Marchisio, G., 1991, Cross-well seismic imaging using reflections: 61st. Ann. Internat. Mtg., Soc. Expl. Geophys., Expanded Abstracts, 375-378.

Stewart, R. R., Marchisio, G., and Li, G., 1991, Crosswell seismic imaging: Fundamentals and a physical modeling study: Presented at the 1991 Ann. Nat. Mtg., Can. Soc. Expl. Geophys.

Telford, W. M., Geldart, L. P., Sheriff, R. E., and Keys, D. A., 1976, Applied Geophysics: Cambridge University Press.

Whiteley, R. J., Holmes, W. H., and Dowle, R. D., 1990, A new method of downhole-crosshole seismics for geotechnical investigation: Exploration Geophysics, **21**, 83-89.

Williamson, P. R., 1991, A guide to the limits of resolution imposed by scattering in ray tomography: Geophysics, **56**, 202-207.

Winbow, G. A., 1989, Seismic sources in open and cased boreholes: 59th. Ann. Internat. Mtg., Soc. Expl. Geophys., Expanded Abstracts, 8-10.

Wong, J., Bregman, N., West, G., and Hurley, P., 1987, Cross-hole seismic scanning and tomography: The Leading Edge, **6**, No. 1, 36-41.

Wyatt, K. D., and Wyatt, S. B., 1984, Determining subsurface structure using the vertical seismic profiling: in Vertical Seismic Profiling, Part B: Advanced Concepts, edited by M. N. Toksöz and R. R. Stewart, Geophysical Press.

Yilmaz, O., 1987, Seismic data processing: Soc. Expl. Geophys.

Zhou, C., and Qin, F., 1993, Real data crosshole reverse-time migration: 63rd. Ann. Internat. Mtg., Soc. Expl. Geophys., Expanded Abstracts, 103-105.

Zhu, X., and McMechan, G. A., 1988, Acoustic modeling and migration of stacked cross-hole data: Geophysics, **53**, 492-500.

Appendix A:

Wave propagation in a medium with velocity increasing linearly with depth

In this appendix, I discuss the propagation of a seismic wave between two boreholes within the medium of a linear velocity relationship of $V(z) = V_0 + \kappa z$, where z is the depth, V_0 is the initial velocity, and κ is the velocity gradient. Here, only the case of positive gradients (i.e., $\kappa \geq 0$) is considered. The case of negative velocity gradients ($\kappa < 0$) can be examined in a similar way. The typical crosswell geometry of both vertical source and receiver wells is assumed.

In an orthogonal coordinate system, let the horizontal axis x represent the distance on the flat surface of the Earth, the vertical axis z represent the depth along the source well, and the origin be at the well head (Figure A-1). Suppose there is a seismic wave traveling from the source point S at $(0, z_s)$ to an arbitrary receiver point R at (x, z), along a curved raypath $\overset{\frown}{SR}$. The angle of ray emission from the source is α_0.

Let us consider an infinitesimal segment of the raypath, dl. It makes an angle α with the z-axis. Its vertical and horizontal components are dz and dx, respectively. The following relations hold:

$$\frac{dx}{dz} = \tan \alpha \,, \quad dl = \frac{dz}{\sqrt{1 - (\sin \alpha)^2}} \,, \quad dt = \frac{dl}{V} \,. \tag{A-1}$$

The ray parameter p is related to the depth-dependent angle α through Snell's law:

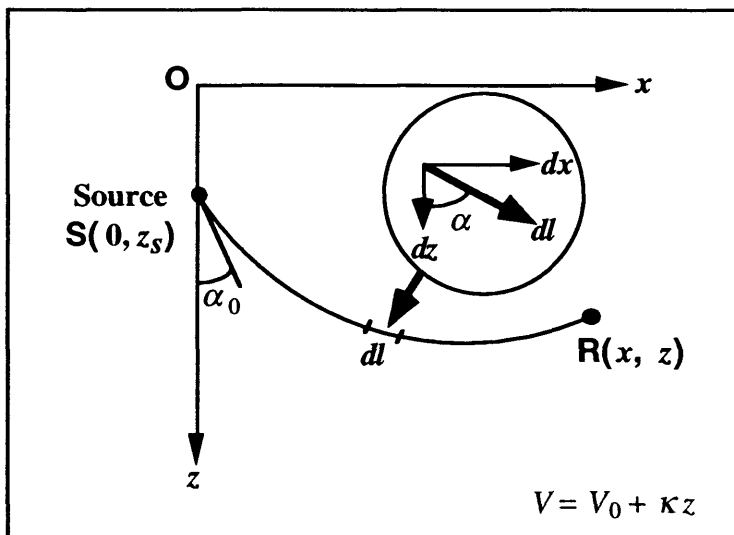$$p = \frac{\sin \alpha}{V} \,, \tag{A-2}$$

FIG. A-1. Geometry illustrating a seismic ray leaving the source at an angle $\leq 90^{\circ}$ and traveling in a medium with velocity increasing linearly with depth.

where V is medium velocity. Snell's law governs wave propagation along a least-time path. By substituting equation (A-2) into (A-1) and then integrating equation (A-1), the total horizontal distance traveled x and total traveltime t can be obtained from the following equations:

$$x = \int_{z_s}^{z} \frac{pVdz}{\sqrt{1 - p^2V^2}} \, , \tag{A-3a}$$

and

$$t = \int_{z_s}^{z} \frac{dz}{V\sqrt{1 - p^2V^2}} \, . \tag{A-3b}$$

Equations (A-3a) and (A-3b) are both parameterized in terms of p. Equation (A-3a) describes a family of curved raypaths in the x-z plane characterized by ray parameter p. For different p values, the raypaths will be different, and thus the traveltime given by (A-3b) for each raypath will be different.

The source S will radiate rays in all directions. For crosswell geometry, useful emission angles of the rays are only between $0°$ and $180°$. Since turning waves are expected to occur when the angle is less than $90°$, the two cases, $\alpha_0 \leq 90°$ and $\alpha_0 > 90°$ will be discussed separately.

A.1 Direct waves

Equations (A-3a) and (A-3b) are derived for the case of $\alpha_0 \leq 90°$. Let us now substitute the velocity relationship of $V(z) = V_0 + \kappa z$ into Eq. (A-3). After some mathematics, we have the following solutions:

$$x = \frac{1}{\kappa p}\left(\sqrt{1 - p^2(V_0 + \kappa z_s)^2} - \sqrt{1 - p^2(V_0 + \kappa z)^2}\right) , \qquad \text{(A-4a)}$$

$$t = \frac{1}{\kappa}\ln\frac{(V_0 + \kappa z)\left(\sqrt{1 - p^2(V_0 + \kappa z_s)^2} + 1\right)}{(V_0 + \kappa z_s)\left(\sqrt{1 - p^2(V_0 + \kappa z)^2} + 1\right)} . \qquad \text{(A-4b)}$$

Formulas (A-4a) and (A-4b) can be expressed in a different manner (Telford et al., 1976; Baerg, 1985). The raypath is circular in the x-z plane. This can be seen by rearranging formula (A-4a) into

$$\left[x - \frac{\sqrt{1 - p^2(V_0 + \kappa z_s)^2}}{\kappa p}\right]^2 + \left(z + \frac{V_0}{\kappa}\right)^2 = \frac{1}{\kappa^2 p^2} . \qquad \text{(A-5)}$$

The center of the circular raypath is at (x_c, z_c), where

$$x_c = \frac{\sqrt{1 - p^2(V_0 + \kappa z_s)^2}}{\kappa p} \quad , \qquad\qquad\qquad \text{(A-6a)}$$

$$z_c = -\frac{V_0}{\kappa} \quad , \qquad\qquad\qquad\qquad \text{(A-6b)}$$

and the radius R is

$$R = \frac{1}{\kappa p} \quad . \qquad\qquad\qquad\qquad \text{(A-7)}$$

Therefore, in the linear-velocity-gradient medium, direct waves travel along circular raypaths characterized by equation (A-5). Figure A-2 shows a seismic ray leaving the source at the angle α_0 and traveling along a circular path. The center of the circular raypath lies above the Earth's surface a distance of V_0/κ.
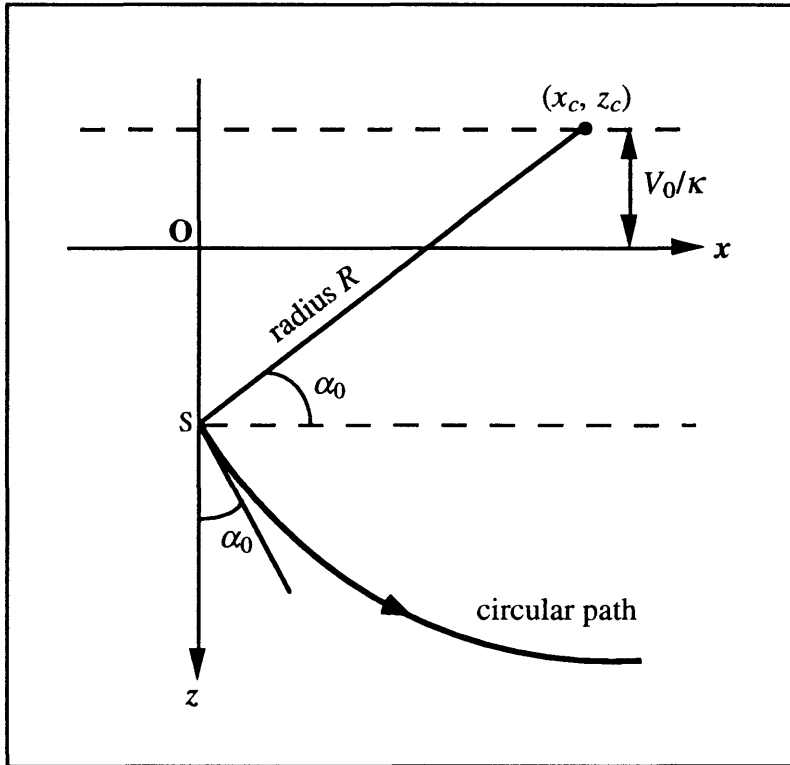

FIG. A-2. Circular raypath leaving the source S at the angle α_0.

It is found, in equation (A-6b), that the vertical coordinate of the center, z_c, is independent of α_0. The value of z_c is determined by the given velocity function alone and thus is a constant. This means that the centers of all circular raypaths lie on the same horizontal line. This line is located where the velocity would be zero if the velocity function were extrapolated up to the elevation of $z = - V_0/\kappa$ (Telford et al., 1976).

Furthermore, since parameters V_0 and κ, and ray parameter p, are positive values, the centers of those raypaths are all located within the $(+ x, - z)$ quadrant of the coordinate system. Equation (A-7) indicates that the radius of the circular path depends upon the ray parameter p. Figure A-3 shows schematically some of the circular raypaths whose radii are different.
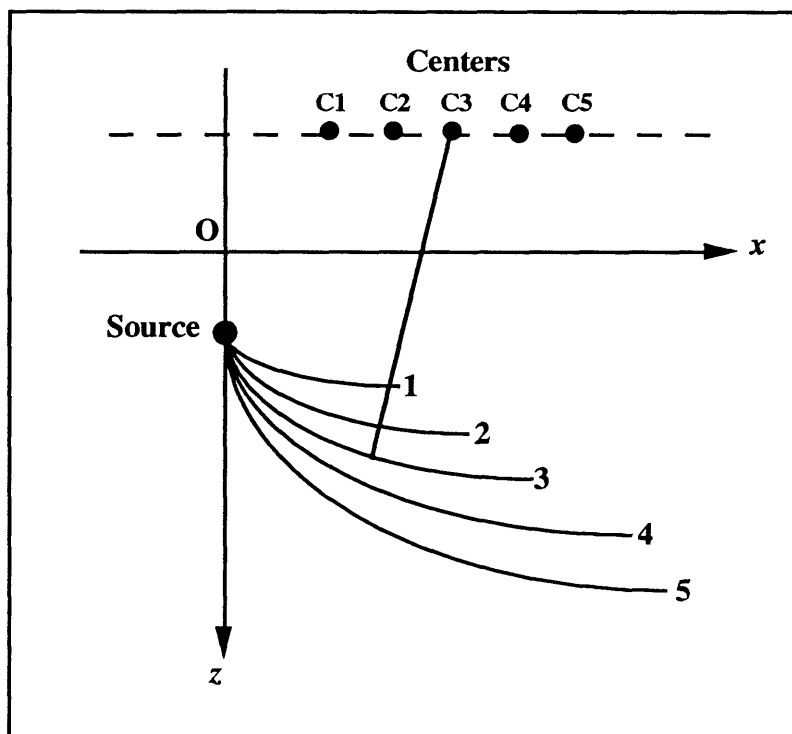

FIG. A-3. Circular raypaths with different radii and centers.

According to equation (A-6a), the horizontal coordinates of the centers of the circular rays are the non-negative values, x_c. When the emission angle is $\alpha_0 = 90°$, the raypath is such a circular arc whose center is at $(0, z_c)$. This can be shown by substituting:

$$p = \frac{\sin \alpha_0}{V_0 + \kappa z_s} = \frac{\sin 90°}{V_0 + \kappa z_s} = \frac{1}{V_0 + \kappa z_s} \ ,$$ (A-8)

into equation (A-6a). This situation is shown in Figure A-4.

For a ray emission angle larger than 90°, the direct wave travels upward along a curved raypath as shown in Figure A-5. The derivation of formulae for the raypath and traveltime of the direct wave can be accomplished in a similar approach as before. But note that in this case, the angle α is always greater than 90° everywhere along the raypath. From Figure A-5, we see that
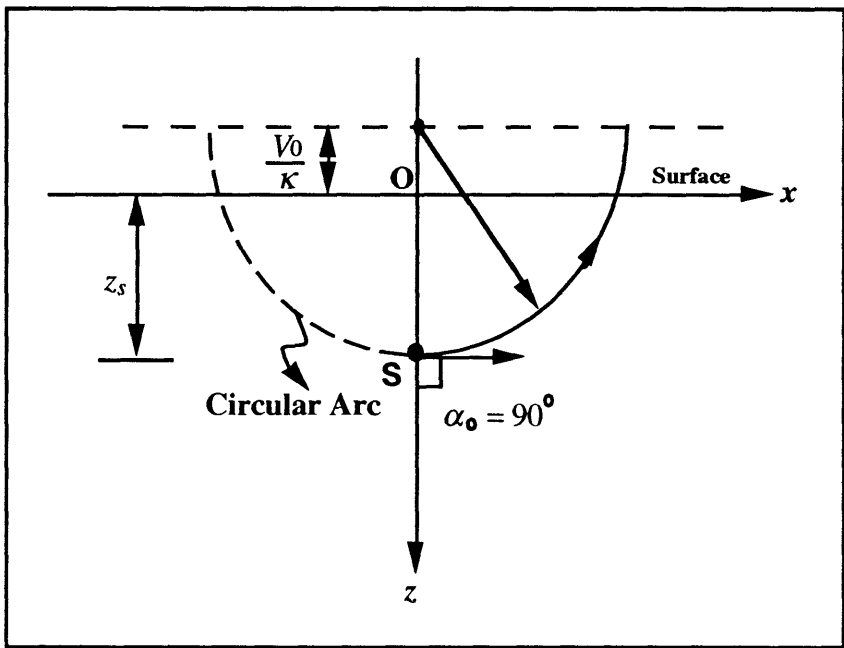

FIG. A-4.   When the emission angle of the ray is $90°$, the center of the circular raypath is on the vertical axis.
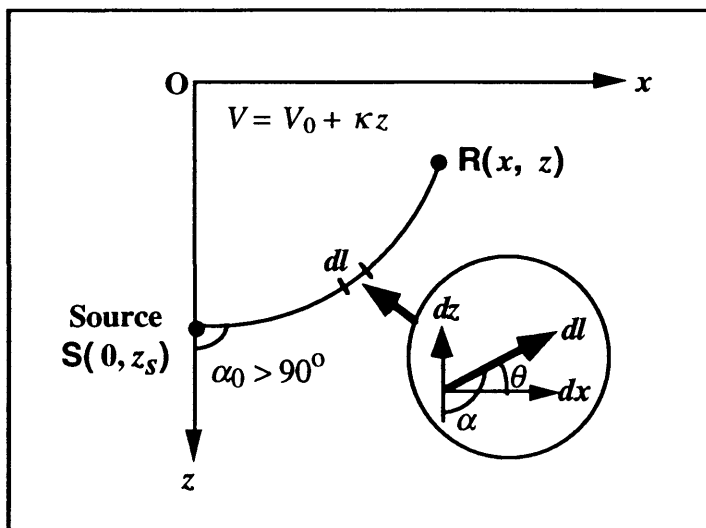
FIG. A-5. Geometry showing a seismic ray leaving the source at an angle $> 90^\circ$ and traveling upward in a medium with velocity increasing linearly with depth.

$$\theta = \alpha - 90^\circ \quad , \tag{A-9}$$

therefore,

$$\frac{dx}{dz} = \cot \theta = \cot (\alpha - 90^\circ) = -\tan \alpha = -\frac{\sin \alpha}{\sqrt{1 - (\sin \alpha)^2}} \quad , \tag{A-10a}$$

$$dt = \frac{dl}{V} = \frac{\sqrt{(dx)^2 + (dz)^2}}{V} \quad . \tag{A-10b}$$

Using Snell's law of Eq. (A-2) and the linear velocity function, and integrating equations (A-10a) and (A-10b), we get the following relations:

$$x = \frac{1}{\kappa p}\left(\sqrt{1 - p^2(V_0 + \kappa z)^2} - \sqrt{1 - p^2(V_0 + \kappa z_s)^2}\right) \quad , \tag{A-11a}$$

$$t = \frac{1}{\kappa} \ln \frac{(V_0 + \kappa z_s)\left(\sqrt{1 - p^2(V_0 + \kappa z)^2} + 1\right)}{(V_0 + \kappa z)\left(\sqrt{1 - p^2(V_0 + \kappa z_s)^2} + 1\right)} \quad . \tag{A-11b}$$

Rearranging the terms in equation (A-11a), we have

$$\left[x + \frac{\sqrt{1 - p^2(V_0 + \kappa z_s)^2}}{\kappa p} \right]^2 + \left(z + \frac{V_0}{\kappa} \right)^2 = \frac{1}{\kappa^2 p^2} \quad . \tag{A-12}$$

Equation (A-12) shows that the resulting raypath is a circular arc, whose center and radius are, respectively,

$$\text{Center at: } \left(-\frac{\sqrt{1 - p^2(V_0 + \kappa z_s)^2}}{\kappa p} , \ -\frac{V_0}{\kappa} \right) \quad ,$$

and

$$\text{Radius: } R = \frac{1}{\kappa p} \quad .$$

As can be seen, for velocity gradient $\kappa > 0$, the center of the circular path is always located within the coordinate quadrant $(-x, -z)$. The vertical coordinate of the center is independent of ray parameter p while the radius varies with it. Again, the centers of all possible rays lie on the same horizontal line above the x-axis (the Earth's surface) by a certain distance. Figure A-6 shows some raypaths and their center positions.

The traveltime equations for the direct waves in all directions, Eq. (A-4b) and Eq. (A-11b), can be combined into one unified expression, which reads:

$$t = \frac{1}{\kappa} \left| \ln \frac{(V_0 + \kappa z_R)\left(\sqrt{1 - p^2(V_0 + \kappa z_s)^2} + 1\right)}{(V_0 + \kappa z_s)\left(\sqrt{1 - p^2(V_0 + \kappa z_R)^2} + 1\right)} \right| \quad , \tag{A-13}$$
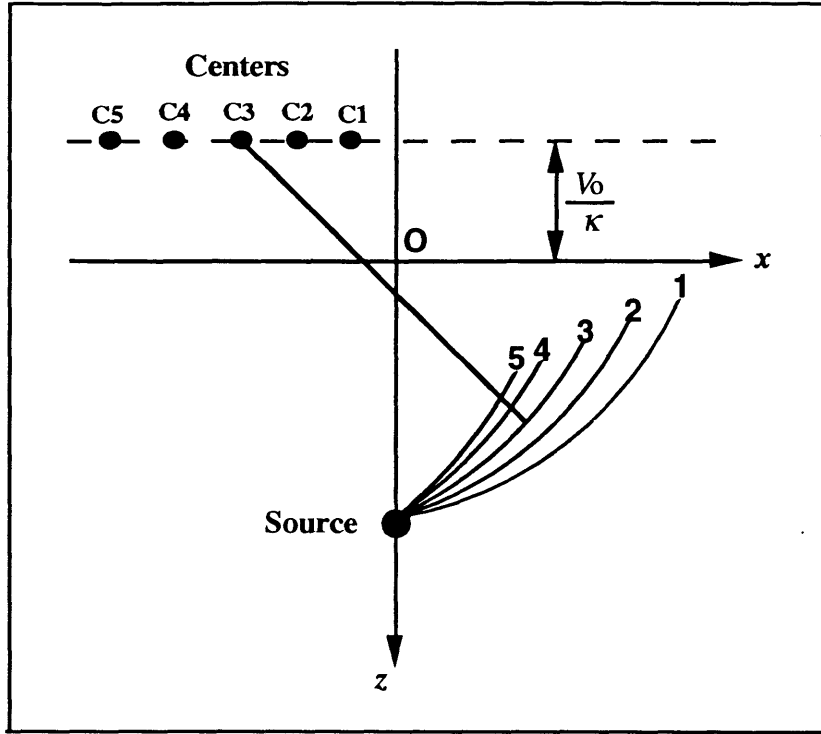
FIG. A-6. Circular raypaths and their centers.

where receiver depth z_R is used to replace z.

In equation (A-13), there is an unknown, the ray parameter p . However, since direct waves travel along circular raypaths in the linear-gradient medium between the wells, their paths must satisfy the equation for a circle. Mathematically, two points (i.e., the pair of source and receiver positions) are not sufficient to determine a circle uniquely. But it is known from the above discussion that the vertical coordinate of the center of a circular raypath is a constant and determined by the parameters in the given velocity relationship. Hence, for a particular raypath connecting the source (x_s, z_s) and the receiver (x_R, z_R),

$$(x_s - x_c)^2 + (z_s - z_c)^2 = R^2 \quad, \tag{A-14a}$$

and

$$(x_R - x_c)^2 + (z_R - z_c)^2 = R^2 \quad , \tag{A-14b}$$

where x_c and z_c specify the center of this circular raypath, whose radius is R. Solving (A-14) results in

$$x_c = \frac{x_R^2 - x_s^2 + (z_R - z_c)^2 - (z_s - z_c)^2}{2(x_R - x_s)} \quad , \tag{A-15}$$

and

$$R = \sqrt{(x_s - x_c)^2 + (z_s - z_c)^2} \quad . \tag{A-16}$$

So the ray parameter p for this particular circular locus is given by:

$$p = \frac{1}{R\kappa} \quad . \tag{A-17}$$

After some algebra, the following formula is obtained:

$$p = \frac{1}{\kappa \sqrt{\left[x_s - \dfrac{x_R^2 - x_s^2 + \left(z_R + \frac{V_0}{\kappa}\right)^2 - \left(z_s + \frac{V_0}{\kappa}\right)^2}{2(x_R - x_s)} \right]^2 + \left(z_s + \frac{V_0}{\kappa}\right)^2}} \quad . \tag{A-18}$$

When $x_s = 0$, $x_R = x$, where x is the interwell spacing between the wells. Equations (A-13) and (A-18) constitute the formulae for calculating the traveltimes of direct arrivals in the crosswell geometry in the medium of a linear velocity gradient.

A.2 Turning waves

If the initial emission angle of the ray is $\alpha_0 < 90^0$, we need to take into account the effect of turning waves, whose definition was given in Chapter 4. One method (as used by Slotnick, 1959) is to find the deepest ray penetration point (turning point) and integrate the traveltime from the source to this point and then from this point to the receiver. The turning point is at the intersection of the circular raypath with a vertical line that goes through the center of the circle. So the depth of the turning point can be found by setting $x = x_c = \left[1 - p^2 (V_0 + \kappa z_s)^2 \right]^{1/2} / \kappa p$ in equation (A-5); thus

$$z_{max} = \frac{1}{\kappa p} - \frac{V_0}{\kappa} \; .$$

(A-19)

Here, p is given in Eq. (A-18). Now, the traveltime can be calculated via

$$t = \int_{z_s}^{z_{max}} \frac{dz}{(V_0 + \kappa z)\sqrt{1 - p^2 (V_0 + \kappa z)^2}} - \int_{z_{max}}^{z_R} \frac{dz}{(V_0 + \kappa z)\sqrt{1 - p^2 (V_0 + \kappa z)^2}}$$

$$= \frac{1}{\kappa} \ln \frac{(V_0 + \kappa z_{max})\left(\sqrt{1 - p^2 (V_0 + \kappa z_s)^2} + 1\right)}{(V_0 + \kappa z_s)\left(\sqrt{1 - p^2 (V_0 + \kappa z_{max})^2} + 1\right)}$$

$$+ \frac{1}{\kappa} \ln \frac{(V_0 + \kappa z_{max})\left(\sqrt{1 - p^2 (V_0 + \kappa z_R)^2} + 1\right)}{(V_0 + \kappa z_R)\left(\sqrt{1 - p^2 (V_0 + \kappa z_{max})^2} + 1\right)} \; .$$

(A-20)

This equation can be reduced, by substituting equation (A-19), to

$$t = \frac{1}{\kappa} \ln \frac{\sqrt{1 - p^2 (V_0 + \kappa z_s)^2} + 1}{p (V_0 + \kappa z_s)} + \frac{1}{\kappa} \ln \frac{\sqrt{1 - p^2 (V_0 + \kappa z_R)^2} + 1}{p (V_0 + \kappa z_R)} \; .$$

(A-21)

When $z_R = z_s$, we have

$$t = \frac{2}{\kappa} \ln \frac{\left(\sqrt{1 - p^2 (V_0 + \kappa z_s)^2} + 1\right)}{p(V_0 + \kappa z_s)} . \tag{A-22}$$

Slotnick (1959) and Grant and West (1965) obtained a similar result for the case of $z_R = z_s = 0$.

A.3 Turning or direct wave: criterion

From the above discussion, seismic waves propagate along circular raypaths in a medium where velocity increases linearly with depth. When the emission angle α_0 is equal to or greater than 90°, we will have direct waves. No turning wave will occur in this area. When $\alpha_0 < 90°$, both direct waves and turning waves may occur. Turning waves have a turning point on their raypath, which corresponds to the maximum ray penetration depth. When the turning point is on the axis of the receiver well, the turning wave and the direct wave coincide. There are two boundaries between the direct-wave zone and the turning-wave zone. The upper boundary is determined by the raypath which leaves the source at a 90° angle. The lower boundary is decided by the turning point which is located on the axis of the receiver well. The region above the upper boundary or below the lower boundary belongs to direct waves. In this region, Eq. (A-13) should be used to calculate the traveltimes for direct waves. The region between the upper and lower boundaries contains the turning waves. Within this zone, Eq. (A-21) should be used for turning-wave traveltime calculation. Figure 4.1 summarizes the cases discussed above.

To determine the upper boundary, the receiver depth corresponding to the ray leaving the source at a right angle needs to be found by setting $p = 1/(V_0 + \kappa z_s)$ for $\alpha_o = 90°$ into equation (A-5), yielding:

$$x^2 + \left(z + \frac{V_0}{\kappa}\right)^2 = \left(\frac{V_0 + \kappa z_s}{\kappa}\right)^2 \quad , \tag{A-23}$$

where x is the known interwell spacing, and z_s is the source depth. So the depth is given by

$$z_1 = \sqrt{\left(\frac{V_0 + \kappa z_s}{\kappa}\right)^2 - x^2} - \frac{V_0}{\kappa} \quad . \tag{A-24}$$

The lower boundary is given by the coordinates of the turning point of the turning waves, i.e., x_c and z_{max} in equations (A-6a) and (A-19).

The criterion is the following: for a ray arriving at a position of offset x and depth z_R, if $z_R \leq z_1$, then the direct-wave equation (A-13) should be used; if $z_1 < z_R < z_{max}$ and $x > x_c$, then the turning-wave equation (A-21) should be used; but if $z_1 < z_R \leq z_{max}$ and $x \leq x_c$, then the direct-wave equation (A-13) should be used again.